DOCTORATE DISSERTATION NO. 2022:12

College of Science

THE DESIGN, SYNTHESIS, AND CHARACTERIZATION OF COPPER-BASED METAL-ORGANIC FRAMEWORKS FOR THEIR INVESTIGATION AGAINST CANCER AND THEIR EFFECT AS ANTI-MICROBIAL AGENTS

Sandy Elmehrath
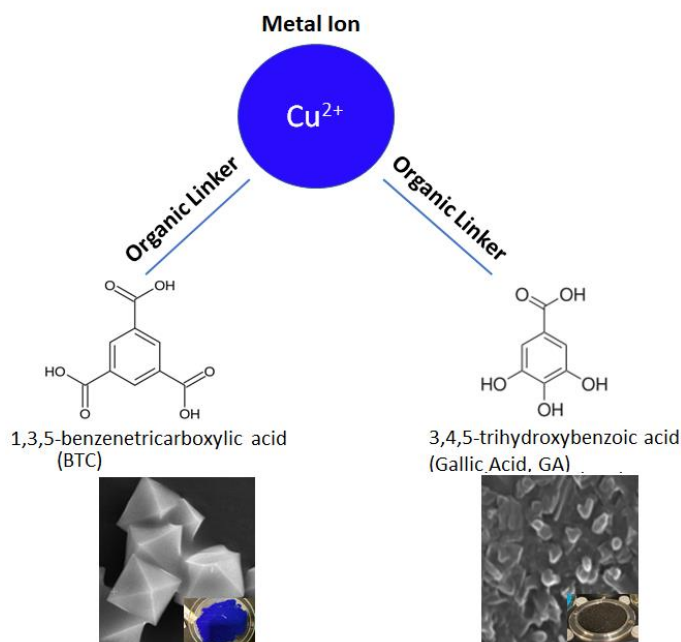
June 2022

United Arab Emirates University

College of Science

THE DESIGN, SYNTHESIS, AND CHARACTERIZATION OF COPPER-BASED METAL-ORGANIC FRAMEWORKS FOR THEIR INVESTIGATION AGAINST CANCER AND THEIR EFFECT AS ANTI-MICROBIAL AGENTS

Sandy Elmehrath

This dissertation is submitted in partial fulfillment of the requirements for the degree of Doctor of Philosophy in Chemistry

Under the Supervision of Professor Yaser Greish

June 2022

Declaration of Original Work

I, Sandy Elmehrath, the undersigned, a graduate student at the United Arab Emirates University (UAEU), and the author of this thesis/dissertation titled *"The Design, Synthesis, and Characterization of Copper-based Metal-Organic Frameworks for Their Investigation Against Cancer and Their Effect as Anti-microbial Agents"*, hereby, solemnly declare this is the original research work done by me under the supervision Professor Yaser Greish, in the College of Science at UAEU. This work has not previously been presented or published, or formed the basis for the award of any academic degree, diploma or a similar title at this or any other university. Any materials borrowed from other sources (whether published, or unpublished) and relied upon or included in my thesis/dissertation have been properly cited and acknowledged in accordance with appropriate academic conventions. I further declare that there is no potential conflict of interest with respect to the research, data collection, authorship, presentation and/or publication of this thesis/dissertation.

Student's signature: Date: June 28, 2022

Advisory Committee

1) Advisor: Yaser Greish

Title: Professor

Department of Chemistry

College of Science

2) Co-Advisor: Sherif Karam

Title: Professor

Department of Anatomy

College of Medicine and Health Sciences

3) Member: Amr Amin

Title: Professor

Department of Biology

College of Science

4) Member: Soleiman Hisaindee

Title: Associate Professor

Department of Chemistry

College of Science

Approval of the Doctorate Dissertation

This Doctorate Dissertation is approved by the following Examining Committee Members:

1) Advisor (Committee Chair): Yaser Greish

   Title: Professor

   Department of Chemistry

   College of Science

   Signature_____   Date_28.06.2022

2) Member: Sulaiman Al-Zuhair

   Title: Professor

   Department of Chemical and Petroleum Engineering

   College of Engineering

   Signature_____   Date_28.06.2022

3) Member: Iltaf Shah

   Title: Associate Professor

   Department of Chemistry

   College of Science

   Signature_____   Date 28/06/22

4) Member (External Examiner): Kyriaki Polychronopoulou

   Title: Professor

   Department of Mechanical Engineering

   Khalifa University of Science, Technology and Research, UAE

   Signature_____   Date_28.06.2022

This Doctorate Dissertation is accepted by:

Dean of the College of Science: Professor Maamar Benkraouda

Signature _Maamar Benkraouda_   Date August 19,2022

Dean of the College of Graduate Studies: Professor Ali Al Marzouqi

Signature Ali Hassan   Date   19/08/2022

Abstract

A wide range of nanomaterials have been developed for biomedical applications, such as drug delivery, biomedical imaging, and sensors. Nanomaterials can include nanoparticles (NPs) and nanofibers with various dimensions that are both natural and synthetic. A successful nanomaterial, for use in biological applications, is characterized by its biocompatibility, biodegradability, intrinsic high surfaces area, high interconnected porosity and functionality. These features were achieved with the development of metal-organic framework (MOF) nanostructures. MOFs are assemblies of metal ions and organic linkers that are built into different geometries and can exist in all dimensions (up to 3-D). The choice of linkers with well-defined shapes and connectivity to secondary building units (SBUs) allows for the desired design of MOF structures. Furthermore, these reticular materials can be post-synthetically modified and fine-tuned for specific biological properties. BioMOFs have proven their effective delivery of various molecular drug entities, however, a focus on these materials as a stand-alone treatment is needed. The intrinsic peroxidase activity of Cu^{2+} and its ability to cause oxidative stress in cancer and bacterial cells sparked our interest in studying and further evaluating the efficacy of copper-based MOFs as anti-cancer and anti-bacterial stand-alone treatments. Gallic Acid (GA), an edible phytochemical found in nature, can exhibit pro-oxidant and antioxidant properties by causing reactive oxidative species (ROS) accumulation while decreasing glutathione (GSH) levels in tumor cells. In this work, the effectiveness of Cu-BTC and Cu-GA MOFs were evaluated in gastric and colon cancer cell lines. The bacterial inhibition of gram-negative and gram-positive bacteria was also examined with both pristine MOFs. In addition, Cu-BTC, a microporous MOF, was chosen for the

development of a hierarchical structure containing both micro-and mesopores for the intended encapsulation and loading of larger drug molecular compounds. Lastly, a MOF core-shell nanoflower was formed for the enhanced stability and release of Cu^{2+} from the Cu-BTC MOF structure.

Keywords: Metal-Organic Framework (MOF), secondary building units (SBUs), nanoparticle (NP), biocompatibility, reactive oxidative species (ROS), nanoflowers (NFs), hierarchical MOF structure

Title and Abstract (in Arabic)

تصميم وتوليف وتوصيف الأطر المعدنية القائمة على النحاس من أجل إستخداماتها ضد السرطان وكعوامل مضادة للميكروبات

الملخص

تم تطوير مجموعة واسعة من المواد النانوية للتطبيقات الطبية الحيوية، مثل توصيل الأدوية، والتصوير الطبي الحيوي، وأجهزة الاستشعار. يمكن أن تشتمل المواد النانوية على الجسيمات النانوية (NPs) والألياف النانوية بأبعاد مختلفة طبيعية وصناعية. تتميز المادة النانوية الناجحة، لاستخدامها في التطبيقات البيولوجية، بتوافقها الحيوي، وقابليتها للتحلل البيولوجي، ومساحة الأسطح العالية الجوهرية، والمسامية والوظائف العالية المترابطة. تم تحقيق هذه الميزات من خلال تطوير الهياكل النانوية للإطار المعدني العضوي (MOF). الأطر العضوية المعدنية هي تجمعات من الأيونات المعدنية والروابط العضوية المبنية في أشكال هندسية مختلفة ويمكن أن توجد في جميع الأبعاد (حتى 3-D). يسمح اختيار الروابط ذات الأشكال المحددة جيدًا والاتصال بوحدات البناء الثانوية (SBUs) بالتصميم المطلوب لهياكل الأطر المعدنية. علاوة على ذلك، يمكن تعديل هذه المواد الشبكية بعد التصنيع وضبطها لخصائص بيولوجية محددة. أثبتت BioMOFs تقديمها الفعال للعديد من كيانات الأدوية الجزيئية، ومع ذلك، هناك حاجة إلى التركيز على هذه المواد كعلاج مستقل. أثار نشاط البيروكسيديز الجوهري لـ Cu^{2+} وقدرته على التسبب في الإجهاد التأكسدي في السرطان والخلايا البكتيرية اهتمامنا بدراسة وتقييم فعالية الأطر العضوية المعدنية القائمة على النحاس باعتبارها علاجات قائمة بذاتها مضادة للسرطان والبكتيريا. حمض الغال (GA)، وهو مادة كيميائية نباتية صالحة للأكل توجد في الطبيعة، يمكن أن تظهر خصائص مؤيدة للأكسدة ومضادة للأكسدة عن طريق التسبب في تراكم الأنواع المؤكسدة التفاعلية (ROS) مع تقليل مستويات الجلوتاثيون (GSH) في الخلايا السرطانية. في هذا العمل، تم تقييم فعالية Cu-BTC و Cu-GA MOFs في خطوط خلايا سرطان المعدة والقولون. تم فحص التثبيط البكتيري للبكتيريا سالبة الجرام والبكتيريا موجبة الجرام أيضًا مع كل من الأطر العضوية العضوية البكر. بالإضافة إلى ذلك، تم اختيار Cu-BTC، وهو إطار عضوي صغير يسهل اختراقه، لتطوير هيكل هرمي يحتوي على كل من الثقوب الصغيرة والمتوسطة الحجم للتغليف المقصود وتحميل المركبات الجزيئية للدواء الأكبر. أخيرًا، تم تشكيل زهرة نانوية من MOF لتحسين الاستقرار وإطلاق Cu^{2+} من هيكل Cu-BTC MOF.

مفاهيم البحث الرئيسية: الإطار المعدنى العضوى، وحدات البناء الثانوية، الجسيمات النانونية، التوافق الحيوى، الأنواع المؤكسدة التفاعلية، الزهور النانونية، هياكل الأطر المعدنية العضوية الهرمية.

Acknowledgments

A PhD journey is one that is full of diversions, revelations and obstacles that make the ending seem almost unsurmountable. However, the benevolent influences along the way make it possible; therefore, I would like to take this moment to thank and acknowledge those who made this dissertation happen. I would like to begin with my family. They have endured many years without my presence but always showed their continuous support. Thank you for always believing in me and allowing me to grow and flourish into the woman that I needed to become.

My advisor, Professor Yaser Greish. At the beginning of it all, you understood my vision and gave me the opportunity to create and be curious throughout the years. The foundation and guidance you provided were the pillars to completing this dissertation. At many times I felt defeated trying to juggle a full-time job, a personal life and a doctorate but you were always compassionate and gave me the chance to disconnect and regroup when I needed to. Thank you for helping me stay on course and making this dream a reality.

A special thanks to my co-advisor's Professor Sherif Karam, Professor Amr Amin, and Dr. Soleiman Hisaindee. The expertise that you provided me in your fields has broadened my learning and understanding, making this dissertation well-rounded and impactful.

This opportunity would not have arisen without the continued support of my department heads, Professor Mohamed Al-Azab and Professor Abbas Khalil. Maintaining a work-study balance is challenging and you were always there to help me overcome the hurdles.

Dedication

I dedicate this work to all women in science-past, present and future. May we continue to inspire and support each other.

Table of Contents

List of Tables

List of Figures

List of Abbreviations

AA	Acrylic Acid
AGS	Human Gastric Cancer Stem Cells
AMF	Alternating Magnetic Field
APIs	Active Pharmaceutical Ingredients
ASGPR	Asialoglycoprotein Receptor
ATP	Adenosine-triphosphate
AuNS	Gold Nanostar
AuNC	Gold Nanocluster
BDC	1,4-Benzenedicarboxylic Acid
BET	Brunauer-Emmett-Teller
BioMOF	Biological MOF (biocompatible)
BSA	Bovine Serum Albumin
BTC	1,3,5-Benzenetricarboxylic Acid
bpydbH$_2$	4,4'-(4,4'Bipyridine-2,6-Diyl) Dibenzoic Acid
CCK-8	Cell Counting Kit-8
CCM	Curcumin
CD	Cyclodextrin
Ce6	Chlorin e6
Cel	Celecoxib
CLSM	Confocal Laser Scanning Microscopy
CoPc	Cobalt Phthalocyanine
COX-2	Cyclooxygenase-2

CTAB   Cetyl Trimethylammonium Bromide

Cu^{2+} Copper Ion

CYLD   CYLD Lysine 63 Deubiquitinase Gene

Cyt *c*   Cytochrome

DCA   Dichloroacetate

4,4'-DTBA   4,4'-Dithiobisbenzoic Acid

DMF   Dimethylformamide

DMSO   Dimethyl Sulfoxide

DNA   Deoxyribonucleic Acid

DOX   Doxorubicin

DPBF   Diphenylisobenzofuran

DTT   DL-Dithiothreitol

E. coli   *Escherichia Coli*

EDX   Energy Dispersive X-Ray

EGF   Epidermal Growth Factor

EIS   Electrochemical Impedance Spectroscopy

FA   Folic Acid

FTIR   Fourier Transform Infrared

5-FU   5-Fluorouacil

GA   Gallic Acid or 3,4,5-Trihydroxybenzoic Acid

Gd   Gadolinium

GQDs   Graphene Quantum Dots

GSH   Glutathione

HA   Hyaluronic Acid

HCC	Hepatocellular Carcinoma
H$_2$pbic	2-(Pyridin-4-yl)-1H-Benzo[d]Imidazole-5-Carboxylic Acid
H. pylori	Helicobacter Pylori
ICP-AES	Inductively Coupled Plasma-Atomic Emission Spectroscopy
IBU	Ibuprofen
JCPDS	Joint Committee on Powder Diffraction Standards
KBr	Potassium Bromide
LPA	Lysophosphatidic Acid
LPOs	Toxic Lipid Peroxides
MB	Methylene Blue
MDR	Multidrug Resistance
mGS	Mouse Gastric Cancer Stem Cells
MIC	Minimum Inhibitory Concentration
MOF	Metal-Organic Framework
MRI	Magnetic Resonance Imaging
MT	Microtubule
MTT	3-(4,5-Imethylthiazol-2-yl)-2,5-Diphenyltetrazolium
MV-PAH	Polyallylamine Hydrochloride
NF	Nanoflower
NIPAM	N-Isopropyl Acrylamide
NIR	Near-Infrared
NMOF	Nano-Metal-Organic Framework
NP	Nanoparticle
Ori	Oridonin

PBS	Phosphate Buffer Solution
PDA	Polydopamine
PDAC	Pancreatic Ductal Adenocarcinoma
PDT	Photodynamic Therapy
PDTC	Pyrrolidinedithiocarbamato
PEG	Polyethylene Glycol
PEM	Polyelectrolyte Multilayer
PFP	Perfluoropentane
PS	Photosensitizer
PTT	Photothermal Therapy
PVP	Polyvinylpyrrolidone
PXRD	Powder X-Ray Diffraction
ROS	Reactive Oxidative Species
siRNA	Small Interfering RNA
SEM	Scanning Electron Microscope
S. aureus	Staphylococcus Aureus
TEA	Triethylamine
TGA	Thermogravimetric Analysis
TNBC	Triple-Negative Breast Cancer
TPP	Triphenylphosphonium
$\alpha/°$, $\beta/°$, $\gamma/°$	Interaxial Angles
ρ_{calc} g/cm^3	Calculated Density

Chapter 1: An Introduction to the Development of Bio-based Metal-Organic Frameworks (MOFs)

1.1 Introduction

The majority of biological applications focus on the use of MOFs as drug delivery systems for the transport of therapeutic agents to targeted sites in a controlled manner for cell internalization (El-Hammadi & Arias, 2021). However, little attention has been made on the utilization of their physical and chemical properties for potential anticancer and antibacterial treatment. Chemotherapeutics face certain limitations such as, poor pharmacokinetics, rapid clearance and nonspecific biodistribution (Cho et al., 2008). Efforts in designing drug delivery carriers to overcome these challenges are made by improving targeted delivery, reducing toxicity and increasing drug accumulation in targeted tissue. However, the efficacy of these vehicles depends on their hydrophobicity, size, shape and surface features (Patel et al., 2015; Senapati et al., 2018). Designing a bio-friendly material is essential for biological applications such as drug delivery. Ideally, the drug carrier should be biocompatible and biodegradable with minimum side effects. Various types of nanocarriers for biological applications have been developed such as, metal NPs (Chen et al., 2018; Du et al., 2018; Kim et al., 2009; Kooti et al., 2018), micelles (Lu et al., 2018; Zhou et al., 2018), liposomes (Miyazaki et al., 2018), dendrimers (Wu et al., 2018; Zhang et al., 2018) and hydrogels (Ghawanmeh et al., 2019; Hyun et al., 2019) Figure 1. What differentiates these nanomaterials from each other are their surface properties, porosity, hydrophobicity, etc. For example, micelles, which consist of hydrophobic and hydrophilic components, can be tuned to release a drug in a stimuli-sensitive environment (e.g., pH and enzyme). They can be functionalized more so than other

drug delivery vehicles because of their higher surface area and nano-size. A micellar system, prepared by Watanabe et al., bearing camptothecin was conjugated with polymeric micelles composed of various poly (ethylene glycol)–poly (aspartate ester) block copolymers. This system showed prolonged circulation and efficient release of the drug at the tumor site (Watanabe et al., 2006).
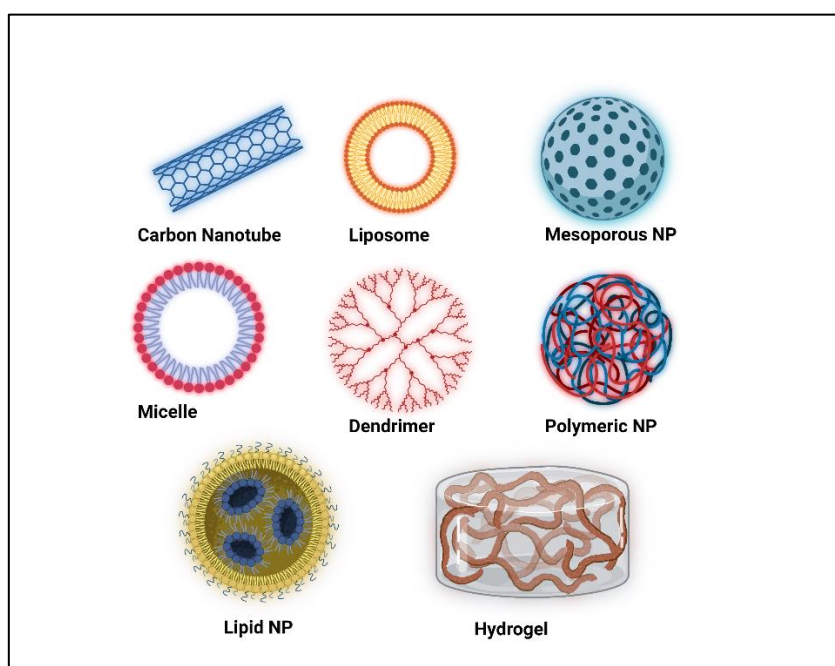
Figure 1: Nanocarriers used as controlled drug delivery vehicles.

Dendrimers have also been used as drug delivery vesicles in tumor tissue because of their modifiable peripheral groups and their ability to perform controlled and targeted drug delivery. They allow for a higher stability, increased half-life and bioavailability of drugs. Particularly, dendrimer conjugated drugs reduce systemic toxicity and increased accumulation in tumor tissue (Mignani et al., 2013; Mignani et al., 2020). Liposomes, amphiphilic molecules composed of natural or synthetic lipids, were conjugated with doxorubicin (DOX) by Ogawara et al. and investigated in colon cancer bearing mice (Ogawara et al., 2009). The polyethylene glycol-coated liposomal

DOX showed antitumor effects on DOX-resistant and non-DOX-resistant C26 cells (Ogawara et al., 2009). The success of these NP systems has led to further investigation and development of anti-cancer carriers with increased efficacy and reduced toxicity. Moreover, Nanomaterials, such as nanorods, nanoparticles and nanowires are used as stand-alone treatment against bacterial strains to help overcome the challenges faced with antibiotic resistance towards conventional pharmaceutical drugs (Blair et al., 2015). These nanomaterials can also be used as drug cargos for the enhanced targeted delivery and antibiotic accumulation in bacteria (Naskar & Kim, 2019).

Compared to other nanomaterials, metal-organic frameworks (MOFs), a class of crystalline materials, exhibit several advantages such as ultrahigh porosity and a surface area that can exceed 6,000 $m^2 \, g^{-1}$ (Zhou et al., 2012). These MOFs consist of metal ions or clusters coordinated to organic bridging ligands (Li et al., 1999) allowing for the fine tuning and flexible design of pore size, surface area and functionality with different building blocks (Yaghi et al., 2003). The high crystallinity of MOFs provides defined networks and clear structural information, which is important in determining the interactions with guest molecules. Applications of MOFs include gas adsorption (Jhung et al., 2007), storage of clean gas fuels (Latroche et al., 2006; Qin et al., 2014), catalysis (Sun et al., 2009; Tonigold et al., 2009), separation science (Britt et al., 2009; Chen et al., 2006; Hu et al., 2010), and drug delivery (Hartlieb et al., 2017). MOFs used for biomedical applications need to be biocompatible with little to no toxicity. This research explores the design and fine tuning of copper-based MOFs and their effect against various cancers and bacterial strains.

1.2 Research Problem

The list of bioMOFs used as drug delivery carriers are endless and have proven to drastically enhance drug targeting and accumulation. However, a focus on the use of MOF materials as a stand-alone treatment is needed. More recently, researchers are looking into the physical and chemical properties of MOFs and their ability to inhibit tumor growth and bacterial inhibition through various mechanisms such as oxidative stress. In particular, copper-based MOFs have shown promising results but an effort is needed to further investigate the viability against various cancer cell lines to prove the success of treatment without the need for encapsulation of additional drug molecules. Also, the design of a MOF that includes a combined therapeutic effect from both the inorganic and organic components is needed.

Recent advances in the post-synthesis modification of MOFs have shown improved stability, thermal behavior, porosity, catalytic behavior, and adsorption capacity. Cu-BTC (HKUST-1), being a microporous MOF (pore size ~ 1nm), can face challenges with hosting larger guest molecules. Previously, researchers successfully attempted to increase the pore size in other MOFs by extending the linker during synthesis, however, the MOF lacked stability (DeCoste et al., 2013). Only a few MOFs are reported to have both micro- and mesopores within their structure and the current methods, leading to a hierarchical structure can be harsh and require lengthy synthetic procedures (Huang et al., 2015; Huo et al., 2013; Li et al., 2013; Qiu et al., 2008). Gallic acid (GA) is a weak acid that possesses antioxidant properties. Therefore, GA can be used as an etching agent to create a hierarchical Cu-BTC structure while simultaneously being encapsulated within the structure for further investigation in drug delivery applications. Furthermore, most MOFs display poor stability in

biological media such as, PBS (phosphate buffer solution). The goal is to improve the stability while controlling the leaching out of copper ions from our copper-based MOFs.

Research Approach

1) In Chapter 2 Cu-BTC is used as a model bioMOF for its high porosity, biocompatibility and biodegradable features. To enhance the biological effects of copper-based MOFs, GA was used as the organic linker to synthesize Cu-GA MOF. The antioxidant properties of GA could possibly cause a synergistic cancer killing effect along with Cu^{2+}. Furthermore, the lipophilic properties of Cu-GA could increase the cellular uptake compared to free GA in cancer and bacterial cells. Both pristine Cu-BTC and pristine Cu-GA were studied for their anti-cancer and anti-bacterial effects (Chapters 5 and 6). An attempt was made to combine both GA and BTC for a mixed linker Cu-BTC-GA MOF, however, characterization proved that GA was not present in the structure.

2) Chapter 3 discusses the post-synthesis etching and encapsulation of Cu-BTC using GA. In this work, GA was shown to create a hierarchical structure on Cu-BTC. Gallic acid, a weak acid was used an etching agent to create a micro- and meso- porous structure of Cu-BTC to host larger molecular entities. In addition, the encapsulation of GA was successful all while maintaining the overall crystal structure of the MOF. The formation of surface and bulk porosity in Cu-BTC results in a material that could be a potential candidate in future drug delivery applications.

3) Chapter 4 focuses on improving the stability of the copper-based MOFs presented in this dissertation. The copper release of Cu-BTC was first studied

in PBS and RPMI (Roswell Park Memorial Institute) biological media. It was serendipitously discovered that the copper release in RMPI was sustained and controlled due to the presence of phosphate and amino acids in the media, which ultimately led to the formation of $Cu_3(PO_4)_2$ nanoflowers (NFs).

4) Presented in Chapter 5, Cu-BTC and Cu-GA were both examined for their effect on gastric and colon cancer cells as stand-alone treatments. Although, gastric cancer being the second most common cause of cancer and colon cancer being the third worldwide, few efforts have been made in utilizing MOFs for the treatment of these deadly diseases. Research efforts to detect, diagnose and treat these deadly cancers early on, before metastasizing in patients, is crucial. Cu-BTC has been studied for its Fenton-like properties by inducing cell apoptosis and causing oxidative stress in certain cancers. Also, the lipophilic and antioxidant properties of Cu-GA could allow for a higher uptake in cancer cells and an overall synergistic effect.

5) In Chapter 6, the antibacterial effects of Cu-BTC and Cu-GA were tested on *E. coli* (gram negative) and *Lactobacillus* (gram-positive). Both Cu^{2+} and GA have the ability to disrupt bacterial cellular membrane through oxidative damage and ROS accumulation within the cell. When compared to the controls (Cu^{2+} and GA), Cu-BTC and Cu-GA were specific to certain bacterial strains and observed an overall sustained release of its constituents all while inhibiting bacterial growth. Cu-BTC and Cu-GA were further examined for their effect on bacterial DNA and their ability to cause morphological damage.

1.3 Literature Review

This review, not only focuses on the synthesis and application of MOFs as nanocarriers and theragnostic agents, it is also followed by a survey of the most recently developed MOFs for the treatment of breast (Afzalinia & Mirzaee, 2020; Alijani et al., 2020; Alves et al., 2021; Chen et al., 2017; Deng et al., 2020; Haddad et al., 2020; Kim et al., 2019; Laha et al., 2019; Li et al., 2021; Liang et al., 2021; Nejadshafiee et al., 2019; Pooresmaeil et al., 2021; Sun et al., 2019; Sun et al., 2021; Sun et al., 2020; Tian et al., 2021; Tian et al., 2017; Wang et al., 2019; Wang et al., 2019; Wang et al., 2021; Zhang et al., 2020; Zhang et al., 2020; Zhang et al., 2018; Zhou et al., 2019), lung (Afzalinia & Mirzaee, 2020; Wang et al., 2021; Wei et al., 2020), oral (Tan et al., 2020; Xiang et al., 2020), hepatic (Chen et al., 2019; Chen et al., 2018; Hu et al., 2020; Leng et al., 2018; Li et al., 2020; Sun et al., 2019; Xiao et al., 2020), pancreatic (Ke et al., 2011; Sharma et al., 2019), colon (Duan et al., 2020; Li et al., 2019; Li et al., 2020; Lu et al., 2019; Lv et al., 2020), bladder (Wu et al., 2021), ovarian (Chen et al., 2020; Chen et al., 2019; He et al., 2014; Li et al., 2020; Sun et al., 2015; Xiang et al., 2021; Yan et al., 2020; Zhang et al., 2015; Zhao et al., 2020), cervical (Li et al., 2020; Yang et al., 2020; Zheng et al., 2015), brain (Mu et al., 2020) and blood cancers (Xi et al., 2019). In addition, the review covers the use of copper-based MOFs as antibacterial agents and the mechanism towards a newly improved treatment overcoming challenges faced with antibiotic resistance.

MOFs are a class of crystalline materials with ultrahigh porosity and surface area that can exceed 6,000 m^2 g^{-1} (Zhou et al., 2012). MOFs can be constructed in the form of 1D, 2D and 3D structures for a wide range of applications (Jeremias, 2015). Their synthesis takes place by self-assembly of a metal ion cluster and an organic

linker forming highly thermal and mechanical stable compounds, which can be useful in photothermal therapy (PTT) (Czaja et al., 2009). Depending on the structure of the MOF as well as its desired application, there are various approaches to MOF synthesis such as solvothermal, hydrothermal, vapor diffusion, microwave synthesis, ultrasonic, mechanochemical and electrosynthesis. Moreover, MOFs can also be post-synthetically modified, introducing functional groups to allow for additional functionality while maintaining the MOFs integral network (Wang & Cohen, 2009).

Due to the above-mentioned unique characteristics of MOFs, they are further investigated for biomedical applications, especially in the areas of imaging, bio-sensing, bio-catalysis, drug delivery and cancer treatment (Giménez-Marqués et al., 2016; Rojas et al., 2017; Yang & Yang, 2020). MOFs used for biomedical applications need to be biocompatible with little to no toxicity. There are a few factors to consider when selecting a metal to be used for biomedical applications including the kinetics of degradation, biodistribution, accumulation in tissues and organs and daily dosage requirements. These characteristics are often studied for the metal ions and the organic linkers on an individual basis as well as after their augmentation in the form of a MOF structure.

1.3.1 Biocompatibility of Metal Ions and Linkers

The most fitting metals with acceptable toxicities include Ca, Cu, Fe, Ti, Zn or Mg with a lethal dose (LD_{50}) ranging from 0.025 g/kg to 30g/kg. Daily dosage and chemical formulation of the metal needs to be taken into consideration when using MOFs for biomedical applications (Alnaqbi et al., 2021; Horcajada et al., 2012). Exogenous linkers, polycarboxylic and imidazolate, have been proven to have low toxicity due to their high polarity and clearance under physiological conditions

(Horcajada et al., 2012). These linkers can also be functionalized to improve their pharmacokinetics and to allow for an improved delivery system of bioactive molecules.

The use of functional groups has not only enhanced host-guest interactions but also the adsorption and delivery of the bioactive molecules due to changes in the MOF flexibility (Devic et al., 2010; Horcajada et al., 2011). Alternatively, endogenous linkers with less toxic effects are also ideal for biomedical applications. Amino acids are chiral and can be used to synthesize homochiral MOFs for applications including separation of chiral structures (Zhang et al., 2017). A functionalized Zr-fumarate MOF was reported to outperform UiO-66 for nanoscale drug delivery (Taddei et al., 2019). Figure 2 shows various MOF structures for drug delivery formulations, including Zr-fumarate.
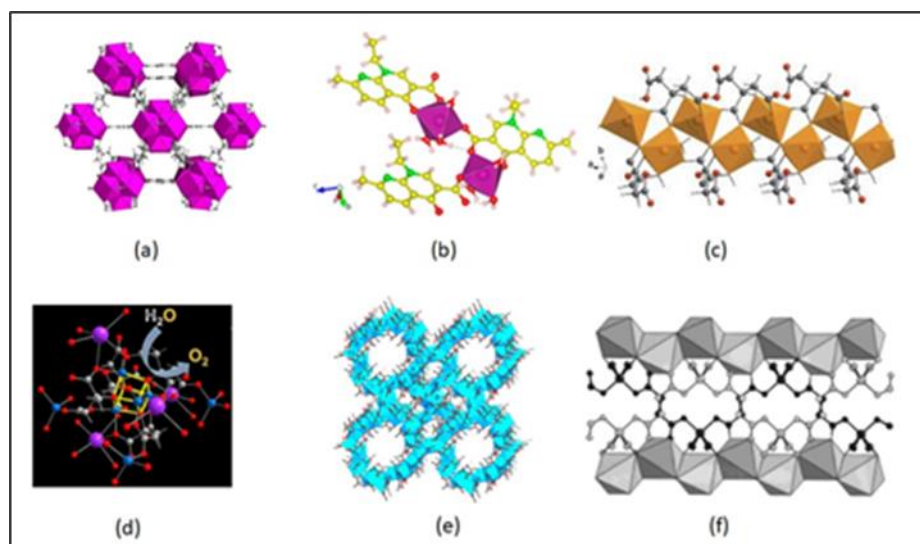
Figure 2: MOF structures for drug delivery formulations. a) Zr-fumarate. b) Zn-nalidixate. c) [Fe(H$_2$cit) (H$_2$O)]$_n$ (NICS-2). d) Co$_4$O$_4$ cubane. e) MOF-1201. f) K$_2$Co(C$_4$H$_4$O$_4$)$_2$. (Taddei et al., André et al., 2019; 2019; Birsa Čelič et al., 2013; Jiang et al., 2017; Yang et al., 2017; Livage et al., 2001).

Active pharmaceutical ingredients (APIs) are ideal linkers as they possess reduced adverse effects once the MOF components are degraded (Rojas et al., 2017). Using an API in the MOF structure can also lead to improved dosage and/or solubility (Al Neyadi et al., 2021). Miller et al. built a MOF using non-toxic iron and the therapeutically active linker, nicotinic acid. This bioactive MOF displayed a high drug uptake (71 wt%) and a fast release of the drug in phosphate buffer solution (Miller et al., 2010). Zinc and bismuth were also used as coordination networks where an iron overload drug, deferiprone, was used as a chelating ligand (Burrows et al., 2013; Burrows et al., 2015). Olsalazine, a prodrug of the anti-inflammatory 5-aminosalicyclic acid, has the same coordinating functionalities as 4,4′-dioxidobiphenyl-3,3′-dicarboxylate but slightly longer (Chen et al., 2012; Xiao et al., 2011). Other APIs have been used as MOF linkers including the antibiotic nalidixic acid and the anti-inflammatory, anti-oxidative and anti-cancer drug, curcumin (CCM) (André et al., 2019; Su et al., 2015). Medi-MOF-1 was initially synthesized solvothermally using the less toxic zinc as a metal node and curcumin as a functional natural linker (Su et al., 2015). The MOF was loaded with ibuprofen (IBU) and used as a co-delivery cargo for the treatment of pancreatic cancer cells (BxPC-3) (Su et al., 2015). Other biocompatible linkers include: citric acid (Birsa Čelič et al., 2013; Jiang et al., 2017), lactic acid (Yang et al., 2017), succinic acid (Jung et al., 2018; Livage et al., 2001; Zhang et al., 2017), L-malic acid (Nagaraja et al., 2012; Senthil Raja et al., 2013; Yutkin et al., 2013; Zavakhina et al., 2014; Zhang et al., 2008), and peptides (Katsoulidis et al., 2019; Kirchon et al., 2018).

1.3.2 Synthesis of BioMOFs

In a typical MOF synthesis, the precursor solutions are usually mixed together to allow for nucleation and crystal growth. Mixing of MOF precursors takes place in

a suitable solvent at room temperature, while the formation of MOF takes place under various temperatures and pressure (Della Rocca et al., 2011). Methods such as solvothermal (Bian et al., 2018),sonochemical (Lee et al., 2013), electrochemical, reverse-phase, microemulsion have been used to synthesize BioMOFs, as illustrated in Figure 3. The key to obtain formulations that are stable and reproducible is to control the particle size of NPs as this dictates the properties of the NP's such as, reactivity, external surface, packing, etc. (Manna et al., 2003; Mokari et al., 2007; Peng et al., 2000; Sun et al., 2000). When synthesizing NP's for specific administration routes, the goal is to produce nanosized, homogenous, monodispersed and stable particles that fit for the targeted route (Horcajada et al., 2012).
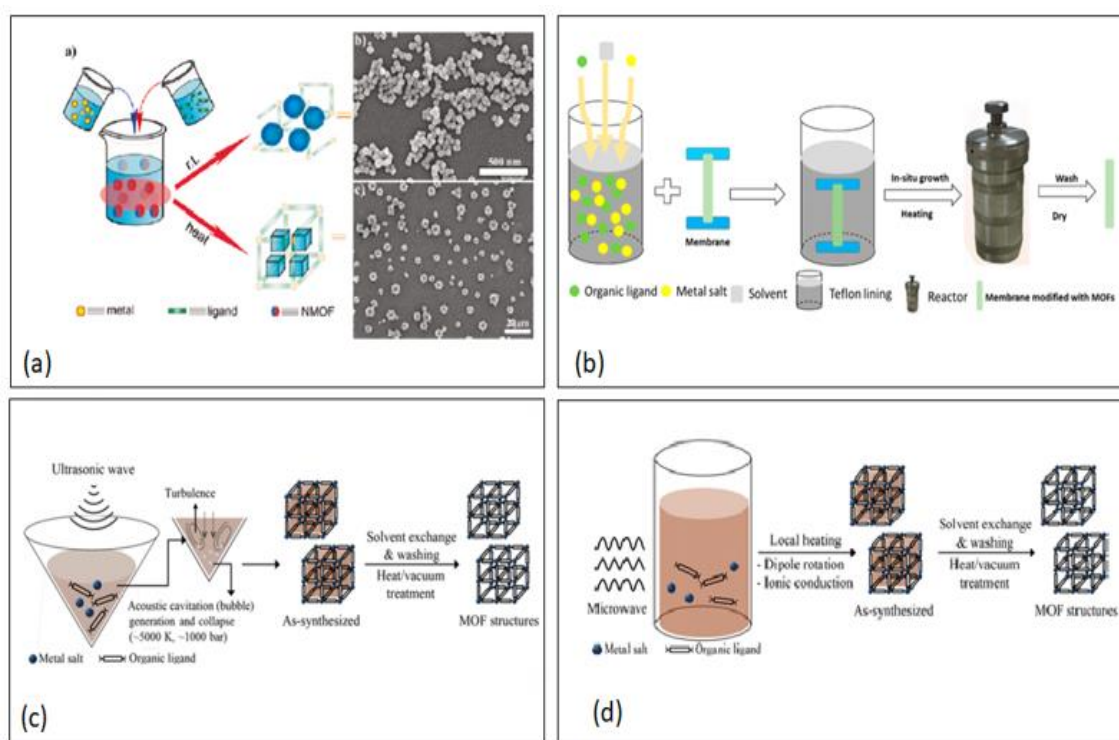
Figure 3: MOF synthesis. a) Low temperature synthesis. b) Solvothermal/hydrothermal. c) Sonochemical. d) Microwave-assisted solvothermal synthesis. (Della Rocca et al., 2011; Bian et al., 2018; Lee et al., 2013; Lee et al., 2013).

Solvothermal/Hydrothermal

Conventional synthesis of MOFs takes place in a solvent at temperatures ranging from room temperature to around 250°C (Stock & Biswas, 2012). Solvothermal and hydrothermal methods allow for a higher yield and smaller, more homogenous crystals than non-thermal methods (He et al., 2021). Various parameters can affect the nucleation and growth of the MOF particles such as, temperature, reaction time, stoichiometry, etc. Zinc imidazolate (ZIF-8) is an example of how reducing temperature and reaction time can produce nanocrystals with the size ~85 nm with enhanced thermal, hydrothermal and solvothermal stabilities (Pan et al., 2011). Horcajada et al. fine-tuned porous hybrid solids: MIL-88A and MIL-88B_4CH$_3$ to improve their structures and porosities for better drug interactions and high loadings and to serve as nanocarriers for delivery and imaging applications. They determined that non-toxic porous iron(III)-based MOFs with engineered cores and surfaces were efficient drug nanocarriers for the delivery of anti-tumor and retroviral biomolecules (Horcajada et al., 2010).

Sonochemical

Recent MOF synthesis has been geared to a 'greener' approach. Using a synthetic method can minimize the use of organic solvents, decrease reaction temperature/pressure and reduce reaction time. Sonochemistry, electrochemistry and ball milling are a few examples of green synthesis. The interaction of high-energy ultrasound with the liquid sample, leads to extremely high temperatures and pressures contributing to a rapid heating and cooling rate and ultimately fine crystal growth (He et al., 2021; Stock & Biswas, 2012). Li et al. synthesized HKUST-1 crystals under ultrasonic irradiation at ambient temperatures for 5-60 min (Li et al., 2009). They

observed improved pore volumes and no significant differences in porosity when compared with the traditional solvothermal synthesis of HKUST-1. This work proves that environment-friendly and efficient alternative methods to MOF synthesis are promising.

Electrochemical

Electrochemical synthesis allows for the possibility of preparing a higher solids content when compared to batch reactions (Stock & Biswas, 2012). Bio-based MOF, [$Zn_3(BTC)_2$] (BTC = benzenetricarboxylate) was prepared using electrochemistry and sonochemistry and then loaded with IBU (Lestari et al., 2018). The electrochemical method produced larger average particle size (ca. 18.43 ± 8.10 µm) compared to the sonochemical method (average particle size ca. 87.63 ± 22.86 nm). The study also showed that the longer the reaction time took place under ultrasonic irradiation, the larger the MOF particle size (Lestari et al., 2018).

Microwave-Assisted

Microwave-assisted synthesis involves the interaction between electromagnetic waves and moving electric charges in the MOF solid sample Compared to conventional heating, microwave-assisted synthesis is faster and produces smaller crystals. (Stock & Biswas, 2012). This rapid method is environment-friendly and produces a high-yield of sample with good monodispersity and controlled size (He et al., 2021). Horcajada et al. synthesized an iron terephthalate MOF, MIL-53 (Fe), at 220°C for 30 min under microwave irradiation at 600 W yielding a flexible framework with pore size of 8.6 Å and particle size of 350nm (Horcajada et al., 2010). The iron (III)-based MOF was successfully loaded with pharmaceutical drugs

including, busulfan, azidothymidine triphosphate, ibuprofen, caffeine, urea and benzophenone 4.

Vapor Diffusion

Vapor diffusion is a method that requires a small amount of reactants yielding good crystals with control over reaction parameters (Rajkumar et al., 2019). Cyclodextrin MOF (CD-MOF) is prepared using edible ingredients including, γ-cyclodextrin, potassium chloride, and ethanol under vapor diffusion synthesis (Smaldone et al., 2010). This porous "edible" MOF has been successfully used for various applications including drug delivery (Jia et al., 2019; Li et al., 2017).

Reverse-Phase microemulsions

This method allows for the control of the MOF particle size by tuning the dimensions of the micelles of cationic cetyl trimethylammonium bromide (CTAB) surfactant. Surfactant-assisted synthesis of two novel gadolinium (Gd) nanoMOFs (NMOFs) at elevated temperatures were noted and demonstrated to have potential as magnetic resonance imaging (MRI) and optical contrast agents (Taylor et al., 2008). Also, Mn containing NMOFs with controllable morphologies were synthesized at room temperature using surfactant-assisted procedure at 120°C with microwave heating. The cell-targeting molecules on the MOF improved their delivery to cancer cells to allow for target-specific MRI imaging (Taylor et al., 2008).

1.3.3 Surface Modification of BioMOFs

Surface modification of BioMOFs is a strategy that can solve challenges such as, targeted delivery, opsonization by blood proteins, biodistribution, and transcytosis of drug molecules (Horcajada et al., 2012) as illustrated in Figure 4. It can improve the

MOFs water dispersity and reduce plasma protein binding to help avoiding the reticuloendothelial system and allow for targeted cell delivery of drugs (Li & Huang, 2008). Figure 4 shows the ability to modify the surface (internal and external) of the MOF structure in order to accommodate the differences in the hydrophobicity/hydrophilicity of the drug and MOF crystal (Abánades Lázaro et al., 2018).
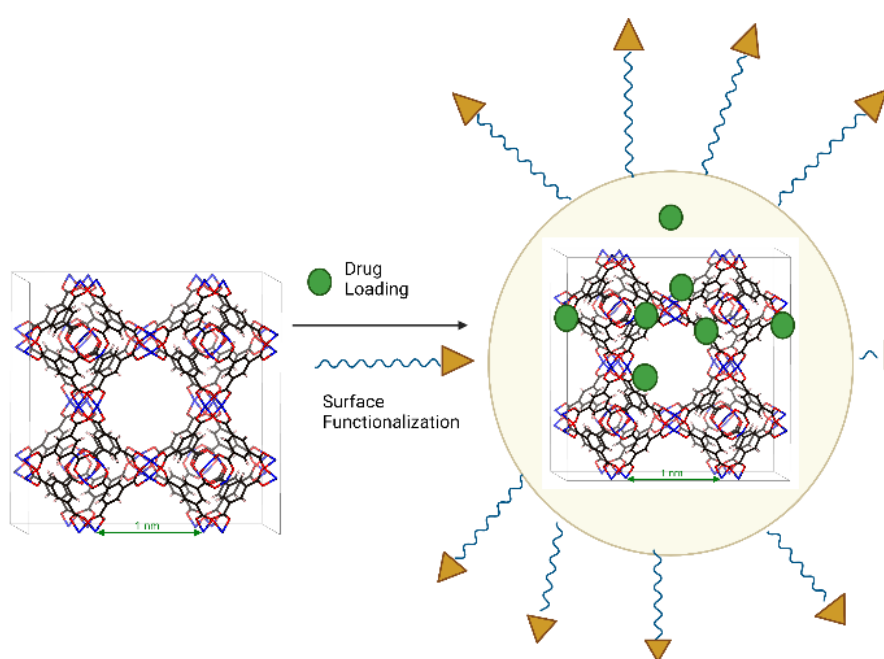
Figure 4: Surface modification of MOF nanostructures.

Certain coating materials such as polyethylene glycol (PEG), can 'protect' the NMOF from early degradation, allowing for a more targeted and increased accumulation of the biomolecule. MIL-100 (Fe) was functionalized with acryl-PEG (480 Da, 2 kDa, and 5 kDa) and acryl-Hyaluronic acid (HA)-PEG moieties using a green, biocompatible and simple GraftFast method. This method produced homogenous coatings and improved its shielding effect. The modified PEG-coated MIL-100 (Fe) produced a lower immune response while maintaining the drug loading

and release. Also, the circulation time was prolonged due to reduced macrophage phagocytosis (Giménez-Marqués et al., 2018). PEG acts as a brush like shell on the NMOF that would sterically protect it from macrophage uptake (Horcajada et al., 2012).

Chowdhuri et al. synthesized a carboxymethyl chitosan-modified magnetic NMOF (IRMOF-3) composed of Zn^{2+} ions and 2-amino terephthalic acid with a target molecule, folic acid (FA), on its surface. The results displayed that the carboxymethyl chitosan increased the drug loading efficiency and improved the performance of the pH-responsive drug release. The anti-cancer drug, DOX was incorporated into the NMOF with a loading capacity of 1.63 g g^{-1}. The release of the drug was investigated in PBS with an intercellular cancer cell environment (pH 5.5) at 37°C. After 24h at pH 7.4, about 26.72% of DOX was released, whereas at pH 5.5, 55.1% was released (Chowdhuri et al., 2016).

1.3.4 BioMOFs for Drug Delivery and Imaging Applications

A drug-MOF conjugate would combine the properties of both, the biomolecule and MOF carrier, and enhance the efficacy of the drug. The MOF would create a stabilized microenvironment for the drug while improving its activity against harsh conditions, allowing for the separation and recovery of the drug upon internal/external stimuli. The formation of a drug-MOF conjugate could be synthesized using various methods Figure 5.
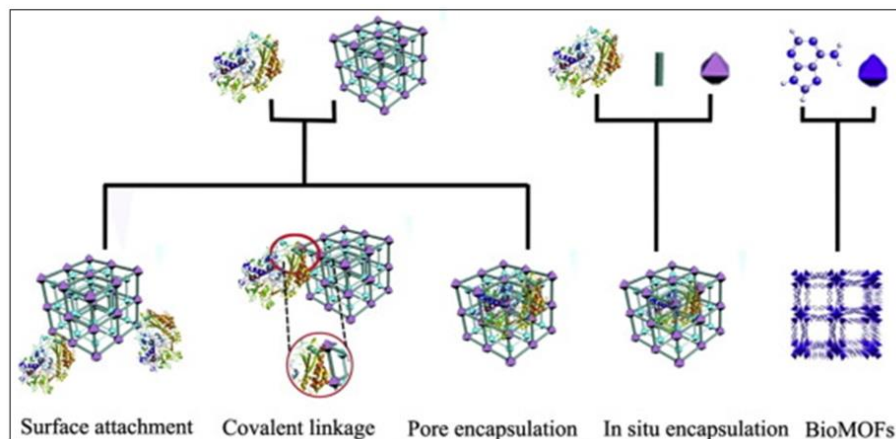
Figure 5: Various strategies for drug loading into MOF nanostructures. (An et al., 2019)

In general, biomolecules are incorporated through different methods (An et al., 2019):

1. Biomolecules can be absorbed into the pores of MOFs

2. Biomolecules can be attached on the external surface of MOF crystals

3. Biomolecules can be in situ encapsulated into MOF crystals as 'crystal defect'

4. Biomolecules can be directly used as ligands to synthesize MOFs.

In 2004 and 2005, Férey et al., developed mesoporous rigid chromium carboxylate MOFs (MIL-100 (Cr) and MIL-101 (Cr)) that were then loaded with the model drug, IBU (Férey et al., 2005; Férey et al., 2004). The MOF structures possessed cage sizes around 25 to 34 Å and windows 5 to 16 Å. The Brunauer-Emmett-Teller (BET) surface areas (2100 to 4400 m^2 g^{-1}) allowed for a successful loading of IBU that was 4 times higher than silica materials and 9 times higher than zeolites (He & Shi, 2011; Horcajada et al., 2006). Although, mesoporous silica MCM-41 has a larger pore size and more impressive pore volume than MIL-101, the higher drug loading capacity in MIL-101 is an evidence that the surface area plays an important role in

drug encapsulation along with the drug/metal interaction (Horcajada et al., 2006). The same group later encapsulated MIL-53 (Fe and Cr) with IBU and determined that the smaller the pore volume, the less drug loading occurred (Horcajada et al., 2008). The release of IBU from MIL-100, MIL-101 and MIL-53, happened through diffusion and drug-matrix interaction. The MOFs released the drug cargo after 3, 6, or 21 days, respectively when immersed in simulated body fluid (pH 7.4 @ 37°C) (Horcajada et al., 2012).

Rojas et al. conducted an experimental and computational study on the physiochemical parameters that were driving the drug adsorption and desorption kinetics of aspirin and IBU using MIL-100(Fe), UiO-66(Zr) and MIL-127(Fe) (Rojas et al., 2018). Given that aspirin is hydrophilic and IBU is hydrophobic, the drug uptake was dependent on the cargo/matrix interaction and the accessibility of the drug in the framework. The release kinetics was dependent on: i) the structure of the MOF, a slower release with a narrower pore or ii) the hydrophobicity/hydrophilicity of the carrier (with UiO-66, aspirin displayed a faster release and slower release with IBU) (Rojas et al., 2018).

MOFs are promising chemotherapeutic drug delivery carriers. More recently, researchers have combined porous MOFs with organic polymers to prevent a burst release of drug molecules (Souza et al., 2020). Souza and colleagues synthesized a nanocomposite MOF, HKUST-1, embedded in a polymeric matrix (polyurethane) for the encapsulation and release of 5-fluorouracil (5-FU) (5-FU@HKUST-1/polyurethane). They used synchrotron microspectroscopy to track the release kinetics of 5-FU and discovered that HKUST-1 created hydrophilic channels within the hydrophobic polyurethane matrix to prevent a burst release effect. The MOFs role

was to release the cancer agent while the polymer matrix protected the moisture sensitive MOF structure from water degradation, as shown in Figure 6 (Souza et al., 2020).
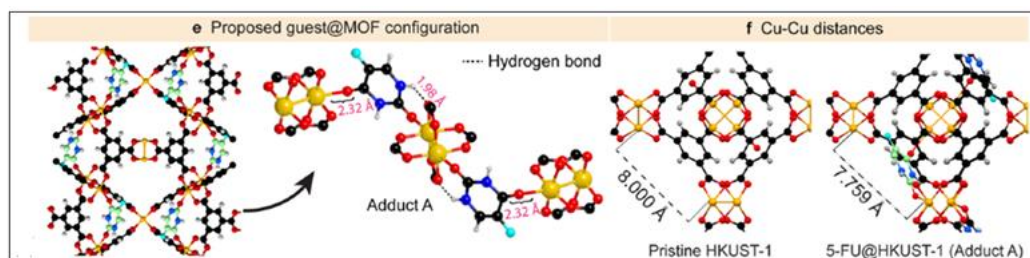
Figure 6: Incorporation of drugs through MOF nanostructures. f-fluorouracil@HKUST-1. (Souza et al., 2020).

MOFs can also carry out multiple roles in therapeutic and diagnostic applications such as, drug delivery carriers and MRI contrast agents, simultaneously. MRI is a non-invasive imaging technique that provides 3D anatomical images based on the detection of nuclear spin reorientations. A contrasting agent, Gd, is usually given to patients intravenously to allow for faster proton alignment within the magnetic field, for a brighter image (Bioengineering). The Gd chelates a T_1-weighted or positive signal enhancement and can help distinguish between diseases and non-diseased tissue (Della Rocca et al., 2011). MRI contrast agents exist as T_1- (positive contrast), shortening the longitudinal relaxation time of water protons and T_2- (negative contrast), which can reduce the transverse relaxation time of water protons (Chowdhury, 2017). MOFs can be utilized as a T_1- or T_2- contrast or combined for the use of drug delivery and as an MRI contrasting agent (Chowdhury, 2017).

MOF-based magnetic composites can also be used for targeted drug delivery as demonstrated by Ke et al. in 2011 (Ke et al., 2011). The group synthesized the nanocomposites by encapsulating Fe_3O_4 nanorods in HKUST-1. The material

displayed magnetic properties and high porosity, that was able to adsorb around 16 wt% of Nimesulide and release the drug for up to 11 days in physiological saline solution at 37°C (Ke et al., 2011).

1.3.5 Stimuli-Responsive BioMOFs

BioMOFs can be designed to respond to intrinsic triggers (pH, ATP, redox, etc.) and/or external triggers (temperature, ions, pressure, light) to offer an enhanced permeability and active targeting of the drug molecule, as illustrated in Figure 7 (Cai et al., 2019). The drug delivery system, once activated by these triggers, will release the drug molecule in a controlled manner, making them ideal for cancer treatments.

pH-Responsive BioMOFs

pH-responsive MOFs are of particular interest in cancer treatment as the coordination bonds are extremely sensitive to external pH changes (Angelos et al., 2009). MOFs can be designed to release cargo at tumor sites (pH ~ 6.5−6.9) for a targeted delivery and increased cellular uptake. ZIF-8, commonly used for the pH-responsive drug release, was encapsulated with DOX/Bovine serum albumin (BSA) NPs by Liang et al. (Liang et al., 2018). The MOF carrier was designed for the protection of the drug as it is stable at pH7.4 and can decompose under acidic conditions and to also introduce positive charges on the outer surface for an increased cellular uptake (Liang et al., 2018; Ren et al., 2014; Zheng et al., 2016; Zhuang et al., 2014). The BSA/DOX@ZIF nanocomposite demonstrated a higher efficiency than the free drug and showed an improved biocompatibility when compared to pure ZIF NPs (Liang et al., 2018).

The polyacrylic acid@ZIF-8 (PAA@ZIF-8) NPs were synthesized using a simple synthetic strategy for the ultrahigh DOX loading capacity of 1.9 g g^{-1} NPs (Ren et al., 2014). This high drug loading capacity could be due to the electrostatic interaction between the positively charged drug molecule and the negatively charged –COOH groups located on the PAA@ZIF-8 structure. The coordination of Zn^{2+} and DOX also plays a role in the uptake of the drug molecule (Ren et al., 2014). The DOX-loaded NPs were efficiently taken by MCF-7 cells and displayed a faster release of DOX in a mild acidic buffer solution (pH 5.5) when compared to a neutral PBS (pH 7.4). The nanocarriers showed low toxicity to normal healthy cells, making them a promising anti-cancer treatment and potential use in biological applications (Ren et al., 2014).
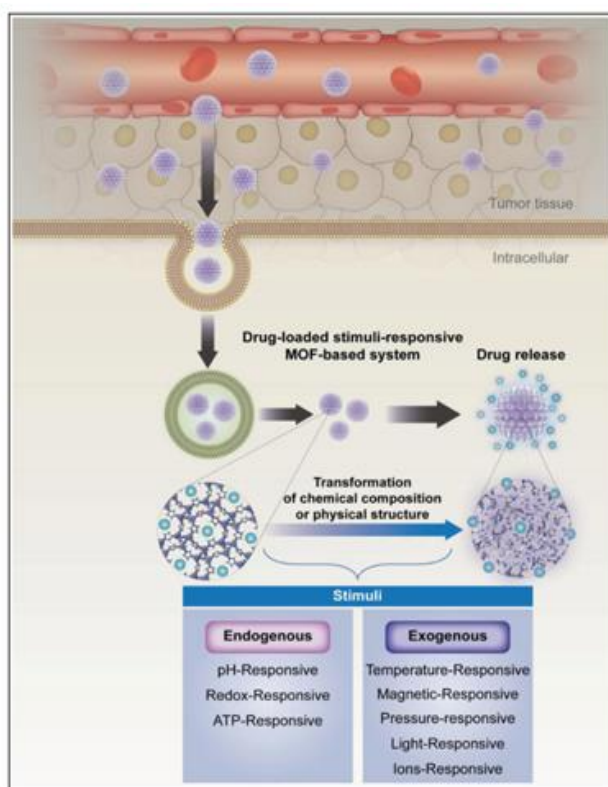
Figure 7: MOFs based stimuli-responsive system for drug delivery. (Cai et al., 2019)

Ion-Responsive BioMOFs

A drug@MOF composite consists of strong electrostatic interactions between the ionic drug and ionic MOF structure. This interaction allows for the release of the drug compound through diffusion, making it an ion-responsive mode of drug delivery. An et al. synthesized a porous anionic MOF, bio-MOF-1, using adenine as the building block for the storage and release of procainamide, a cationic antiarrythmic drug (An et al., 2009). With a short half-life and a dosing of every 3-4 hours, procainamide HCl, is an ideal drug for controlled release studies. After the drug was introduced in the MOF pores, through a cation exchange process over 15 days, the loading capacity was determined to reach up to 0.22 g g^{-1}. The ionic interaction between the drug and the MOF triggered a release of the drug from the carrier when placed in PBS (pH 7.4). This was studied against a control (nanopure water) to prove that the drug released was mediated by the buffer cations (An et al., 2009).

Later on, the Hu group prepared a positively charged carrier, MOF-74-Fe (III) through the oxidation of the neutral MOF (Hu et al., 2014). The cationic MOF was loaded with IBU anions and displayed a loading capacity of 0.19 g g^{-1}. Two different release rates were observed due to the presence of coordinated or free IBU anions. The drug release occurred by diffusion and triggered by the anionic phosphate buffer solution. Therefore, the drug release can be controlled by regulating the carrier size and encapsulating them into other stimuli-responsive matrices Figure 8 (a) (Hu et al., 2014).

In 2016, Yang and colleagues, constructed a cationic nanocarrier, ZJU-101, by post-modification of MOF-867. Methyl groups were added to the pyridyl groups of MOF-867 (zirconium with 2,2′-bipyridine-5,5′-dicarboxylate) and loaded with the

anionic drug, diclofenac sodium (Yang et al., 2016). Diclofenac sodium forms anions in solution, making it ideal for loading in cationic MOF pores. The loading of the drug was carried out in ethanol solution and determined to have a loading capacity of 0.546 g g^{-1}. The drug demonstrated a more efficient release in PBS of pH 5.4 compared to PBS of pH 7.4. This displays a drug delivery system that is pH-responsive and a drug release controlled by the anionic PBS and drug anions, as shown in Figure 8 (b) (Yang et al., 2016).
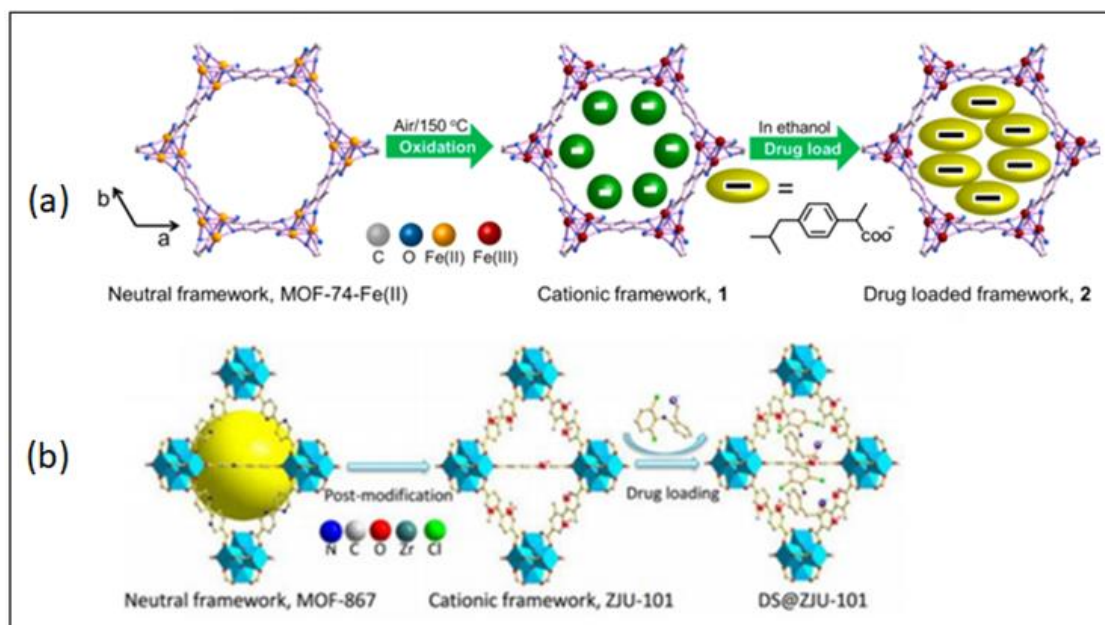
Figure 8: Examples of ion-responsive chemically-modified bioMOF nanostructures. a) Oxidative procedure of MOF-74-Fe(II). b) Ionic-modified MOF-867. (Yang, et al., 2016; Hu et al., 2014).

Magnetically-Responsive BioMOFs

Magnetic-responsive drug delivery systems work under the influence of a magnetic field and can be used for magnetic targeting, MRI, magnetic separation and magnetic hyperthermia (Hergt et al., 2006). In 2019, Chen et al. constructed a magnetic composite for the simultaneous treatment using magnetic hyperthermia and

chemotherapy (Chen et al., 2019). ZIF-90 was grown on polydopamine (PDA) coated Fe_3O_4 NPs to give Fe_3O_4@PDA@ZIF-90 core-shell particles with an average size of 200nm. ZIF-90 was encapsulated with DOX with a loading efficiency of 80% (160 µg mg^{-1}) due to the porosity and MOF/drug interaction. The Fe_3O_4 cores allowed for the localized temperature to reach hyperthermia conditions under an alternating magnetic field while eradicating tumor cells with an enhanced efficiency. This synergistic effect is a promising form of cancer treatment compared to magnetic hyperthermia alone, as shown in Figure 9 (a) (Chen et al., 2019).

Recently, Mukerjee et al. designed a NP composite for theragnostic applications by doping $NaGdF_4$ with Yb^{3+} and Er^{3+} NPs as imaging agents and MIL-53(Fe) as a drug carrier with FA conjugated on the surface for targeted drug delivery (Mukherjee et al., 2020). The nanocomposite was loaded with the anticancer drug, DOX, displaying a drug loading efficiency of 16% and drug encapsulation efficiency of 65%. Not only did the $NaGdF_4$:Yb/Er@MIL-53(Fe)/FA system suppress tumor cell growth and enhanced cancer cellular uptake, it also showed colloidal stability and enhanced magnetic and fluorescence properties, making it an ideal candidate for both relaxation times, T_1 and T_2 MRI contrasting agents, as shown in Figure 9 (b) (Mukherjee et al., 2020).

Temperature-Responsive BioMOFs

The ability of temperature-responsive MOFs to transform upon thermal stimuli while maintaining its crystalline structural integrity is of particular interest when it comes to designing drug delivery nanocarriers.
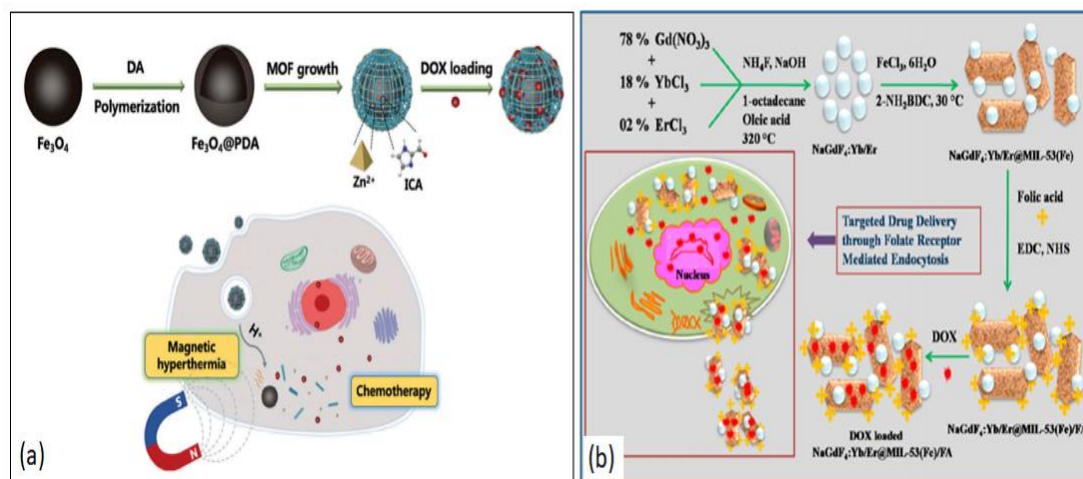
Figure 9: Examples of magnetically-responsive chemically-modified bioMOF nanostructures. a) Fe3O4@PDA@ZIF-90 core-shell NPs. b) DOX-loaded NaGdF4:Yb/Er@MIL-53(Fe)/FA. (Chen et al., 2019; Mukherjee et al., 2020).

A temperature would induce a change in the thermoresponsive material allowing for the release of the drug cargo. Procainamide has recently been studied for the control release from UiO-66 in a temperature and pH sensitive environment (Nagata et al., 2020). The MOF was surrounded with *N*-isopropyl acrylamide (NIPAM) and acrylic acid (AA) by post-synthetic modification to give UiO-66-P(NIPAM-AA). PNIPAM is known for its thermoresponsive properties and its solubility in water at cloud point, making it useful in drug delivery systems (Roy et al., 2013). UiO-66-P(NIPAM-AA) experienced an on/off release when exposed to variations in pH and temperature. At pH 6.86 or low temperatures (less than 25°C) the polymer composite turned into a coil conformation, allowing procainamide to be instantly released from the MOF pores. With a pH 4.01 or high temperatures (more than 40°C), the polymer displayed a globular conformation and the release of the drug was suppressed. Therefore, drug release can be controlled by applying an external stimulus (eg. temperature or pH) even after the initial release of the drug from the MOF carrier (Nagata et al., 2020).

Redox-Responsive BioMOFs

Redox concentrations vary between normal human tissue and cancerous tissue with tumors having a higher concentration due to the presence of reducing agents such as, glutathione (GSH) (Li et al., 2012; Meng et al., 2009). Redox-responsive MOFs can be functionalized to target the receptor site that is responsible for the cleavage of the disulfide group in the presence of GSH. Lei and co-workers developed an intrinsic redox-responsive MOF carrier, MOF-M(DTBA) (M = Fe, Al or Zr) by using iron, aluminum, or zirconium as metal nodes and 4,4′-dithiobisbenzoic acid (4,4′-DTBA) as the organic ligand (Lei et al., 2018). DTBA is a GSH-sensitive organic ligand, which contains a disulfide bond, cleavable by GSH. In this study, the researchers loaded the drug carrier with the natural polyphenol anticancer drug, CCM producing, CCM@MOF-M(DTBA). The redox-responsiveness of the synthesized NP was exposed to various concentrations of DL-dithiothreitol (DTT). The results showed that with an increase of DTT in PBS, the release of CCM from the drug delivery system was much faster Figure 10 (a). It is clear that the cleavage of the disulfide bond led to a more efficient release of the drug molecule (Lei et al., 2018). Ferroptosis is cell death dependent on iron and the accumulation of toxic lipid peroxides (LPOs), usually in tumor tissue. Once GSH is consumed by cells, glutathione peroxide 4 (GPX4) activity is inhibited and the level of lipid oxidation in cells increases accordingly, which leads to ferroptosis (Gao et al., 2019; Gaschler et al., 2018; Hangauer et al., 2017; Liu et al., 2019; Seibt et al., 2019). The ability to produce LPOs can lead researchers into developing effective targeted cancer treatment.
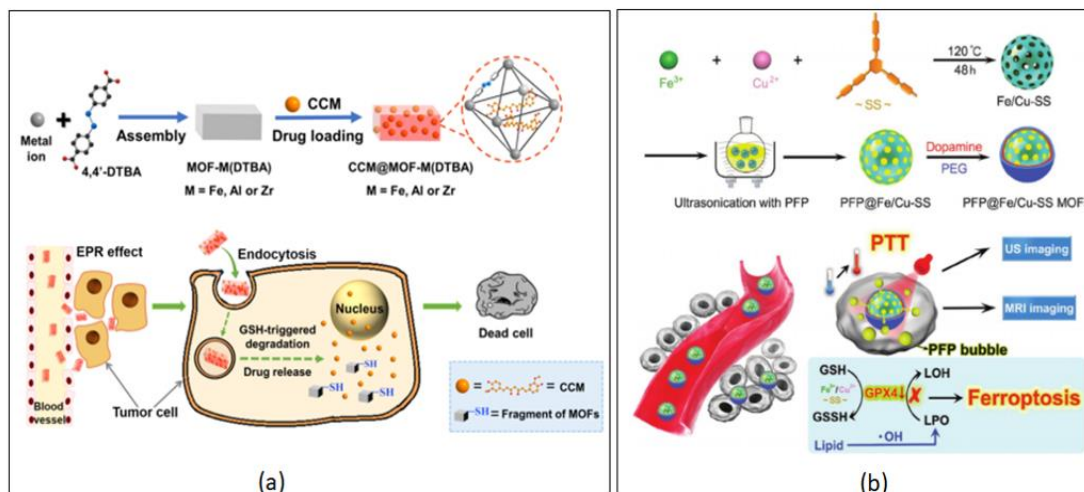
Figure 10: Examples of redox-responsive chemically-modified bioMOF nanostructures. a) CCM@MOF-M(DTBA). b) PFP@Fe/Cu-SS MOFs. (Lei et al., 2018; He et al., 2020).

Recently, a group synthesized a hybrid PFP@Fe/Cu-SS MOF by coordinating the disulfide-modified, phloroglucinol with Fe^{3+} and Cu^{2+} metals (He et al., 2020). The porous MOF was loaded with perfluoropentane (PFP) and the nanocarrier was functionalized with PDA and PEG for improved stability and biocompatibility. The system proved to increase LPO concentration in tumor sites through redox reactions generating $\cdot$OH while inhibiting the activity of GPX4. This prevented the conversion of toxic LPO to nontoxic hydroxyl compounds in the presence of GSH Figure 10 (b). The inclusion of the copper(II) metal also allows for the PFP@Fe/Cu-SS NP to be used as an MRI contrasting agent (He et al., 2020).

ATP-Responsive BioMOFs

Adenosine triphosphate (ATP) provides energy for all living cells by hydrolyzing phosphoanhydride bonds. Tumor cells contain a higher level of ATP compared to normal cells, allowing for the use of ATP-responsive drug delivery systems. A ZIF-90/protein NP was synthesized using ZIF-90 as a platform for the

cytosolic protein delivery and CRISPR/Cas9 genome editing. With ATP present as stimuli, the NPs were degraded to release the protein and this was due to the ATP and zinc metal bond of ZIF-90 (Yang, Tang, et al., 2019). The RNase A-NBC (RNase A modified with 4-nitrophenyl 4-(4,4,5,5-tetramethyl-1,3,2-dioxaborolan-2-yl) benzyl carbonate) protein, having cytotoxic effects against cancer cells, showed enhanced toxicity against HeLa cells when compared to the free protein Figure 11. The cell viability was reduced to 15%, suggesting that ATP can promote protein release from ZIF-90/RNase A-NBC (Yang, Tang, et al., 2019). Photodynamic therapy (PDT) is non-invasive and has been successfully used in treatment and diagnostics. Light-responsive MOFs can be designed to deliver biomolecules by irradiation of specific wavelengths of light where the photosensitizers (PSs) in target cells would absorb the light energy and produce ROS upon activation and killing the target cells (Lucky et al., 2015). Recently, ZIF-8 NPs were co-encapsulated with chlorin e6 (Ce6, a potent PS) and cytochrome *c* (Cyt *c*, a protein that induces apoptosis) by Ding et al. (Ding et al., 2020). The NP was then functionalized with a HA shell to produce Ce6/Cyt *c*@ZIF-8/HA for targeted cancer cell activity.
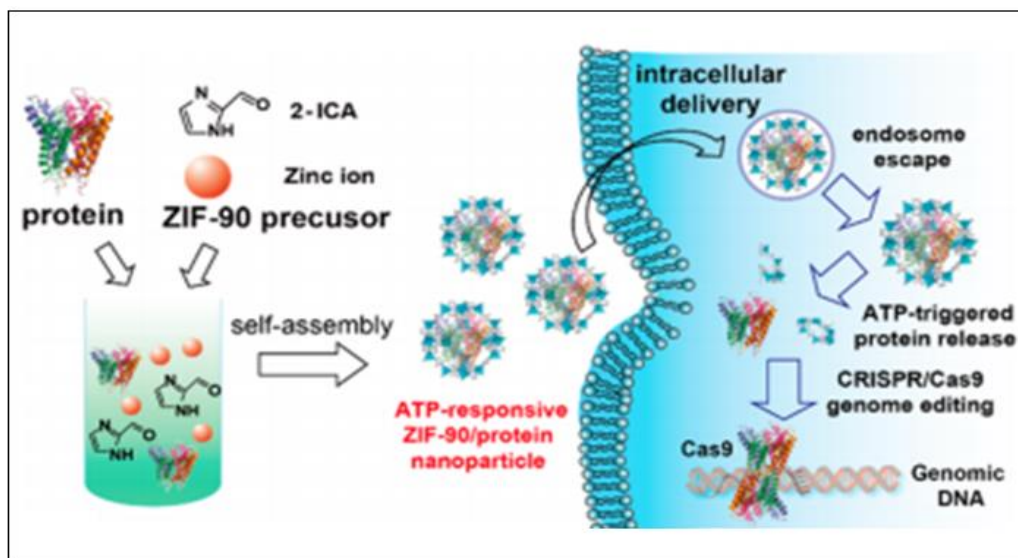
Figure 11: Example of ATP-responsive chemically-modified bioMOF nanostructure: ZIF-90/protein NPs. (Yang et al., 2019).

Light-Responsive BioMOFs

1,3-Diphenylisobenzofuran (DPBF), an ROS probe, was used to determine the ROS (reactive oxidative species) generation of Ce6. Along with a pH-responsive release behavior of the nanocarrier, light irradiation caused Ce6 to produce ROS for a PDT effect. Furthermore, Cyt *c*, in the presence H_2O_2, will generate ROS while further inducing cell apoptosis Figure 12. The co-encapsulation of therapeutic protein in the porous MOF structure allowed for a synergistic mode of cancer therapy that could lead to further developments in drug delivery design (Ding et al., 2020).
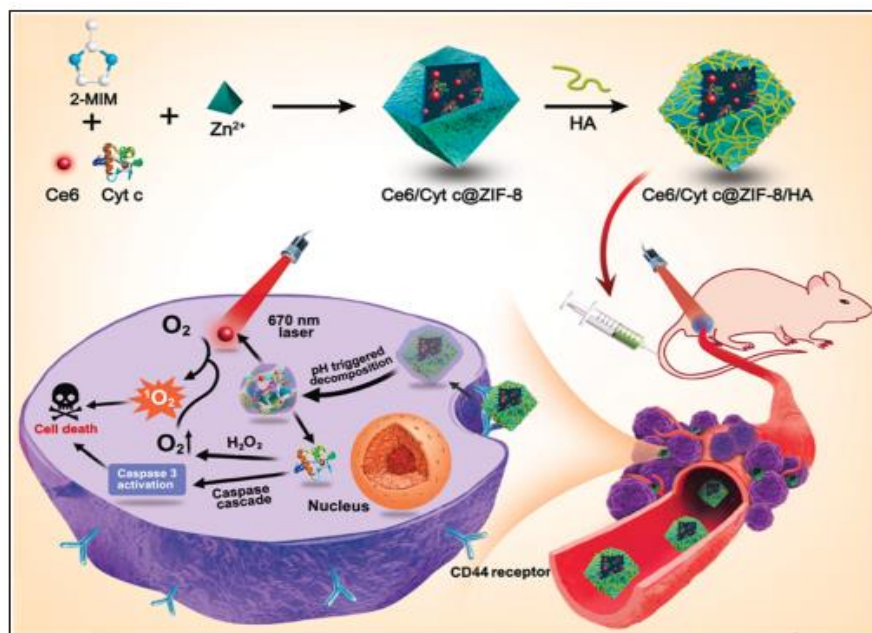
Figure 12: Examples of Light-responsive chemically-modified bioMOF nanostructures: Ce6/Cyt c@ZIF-8/HA NPs. (Ding et al., 2020).

1.3.6 BioMOFs for Cancer Treatment

MOFs have alleviated most of the limitations observed from traditional nanocarriers by providing an enhanced targeted delivery and higher accumulation of drug molecules. Especially, MOFs can be tuned to respond to endogenous and external stimuli, which can be beneficial in cancer treatment and diagnosis. Their porosity and high surface area, allows for a more efficient loading of biomolecules while providing a low toxic carrier. Various cancer treatments and/or diagnosis using MOFs include: radiotherapy, MRI imaging, carbon monoxide therapy, magnetic hyperthermia treatment and PDT depending on the targeted tumor cells.

Breast Cancer

Breast cancer, according to the World Cancer Research Fund, is the most prevalent cancer in women and the second most common overall, ranking the highest

in Belgium, Luxembourg and the Netherlands (World Cancer Research Fund). Methods of treatment include: radiotherapy, hormone therapy, chemotherapeutics and/or surgery, each having their disadvantages and toxic side effects. Breast cancer chemotherapeutics such as, Tamoxifen, can cause cancer endometrial carcinoma and other unwanted side effects (Dhull et al., 2013). Using MOFs as anti-cancer drug delivery vehicles would reduce toxic side effects while increasing drug accumulation in breast cancer cells compared to the free drug.

Zhang et al. engineered a triple-negative breast cancer (TNBC) targeted peptide (ZD2) using a single gold nanostar (AuNS) coated within MIL-101-NH$_2$(Fe) producing a well-defined core-shell AuNS@MOF-ZD2 nanocomposite (Zhang et al., 2018). These nanocomposites were utilized for MRI and photothermal therapy (PTT) specifically towards TNBC. The AuNS@MOF-ZD2 nanoprobes targeted TNBC cells (MDA-MB-231) but not any other subtypes of breast cancer cells (MDA-MB-435, MDA-MB-468, and MCF-7), making them promising tools for theragnostics of breast cancers of a certain molecular classification (Zhang et al., 2018). Laha and co-workers also developed a system to target TNBC both in vitro and in vivo by encapsulating CCM in FA conjugated IRMOF-3 (IRMOF-3@CCM@FA) (Laha et al., 2019). As previously mentioned in this review, folate receptors are overexpressed in tumor cells, allowing for the targeted delivery of drug molecules when FA is conjugated on the MOF surface. The IRMOF-3@CCM@FA system was successful in reducing tumor size in mice and induced apoptosis by upregulating the pro-apoptotic protein Bax and downregulating the anti-apoptotic Bcl-2 while upregulating JNK and p53 in human TNBC cells (Laha et al., 2019).

Microtubules (MT) play an important role in fundamental cellular activities such as, cell motility, cell division and intracellular trafficking. Evidence shows that a minor disruption in the dynamics of MTs can arrest cell cycle progression at mitosis and eventually lead to cell death. Current treatment includes Paclitaxel and Vinca alkaloids, which are designed to disrupt microtubule dynamics without changing MT mass for solid tumors and leukemias (Chen et al., 2017). Although, these drugs have been proven to be successful, tumor drug resistance can be caused by the overexpression of the multidrug resistance (MDR) protein, P-glycoprotein (Pgp, MRP4, ABCB1) and the class III β-tubulin (TUBB3) (Kodaira et al., 2010; Mozzetti et al., 2005). Breast cancer, in particular, has an overexpression of TUBB3, which can increase the dynamic instability of MTs, reducing the effect of taxane drugs (Lebok et al., 2016; Yeh et al., 2003). The goal, to overcome this treatment obstacle, is to downregulate the expression of Pgp while disrupting the MT dynamics for the inhibition of drug-resistant tumor cells. Chen and co-workers developed a selenium/ruthenium NP modified MIL-101(Fe) for the delivery of small interfering RNAs (siRNAs) to inhibit MDR genes while disrupting MT dynamics in MCF-7/T (taxol-resistance) cells. RNA interference can be useful for gene-targeted therapy because of its ability to suppress specific sequences in genes. Previous work has shown that the simultaneous delivery of nucleic acid drugs and chemotherapeutics reversed MDR in tumor tissue (Li et al., 2014; Zheng et al., 2015). Selenium was chosen for its ability in reducing the incidence of cancers while having low toxicity (Abdulah et al., 2005; Hatfield et al., 2014; Sinha & El-Bayoumy, 2004; Wang et al., 2007). In addition, ruthenium was added to the MOF NP for its anti-metastatic activity as an attempt for enhanced effect and efficiency (Bergamo et al., 2012; Levina et al., 2009). MIL-101(Fe) was modified with cysteine owing to the strong linkage between Se/Ru

and the MOF structure forming NPs (Se@MIL-101 and Ru@MIL-101). Small interfering RNA (siRNA) loaded MOFs provided enhanced protection against MDR and nuclease degradation while increasing cellular uptake in MCF-7/T cells Figure 13 (a). Furthermore, in vivo studies confirmed the chemotherapeutic efficiency of Se@MIL-101-(P+V)siRNA NPs by causing significant shrinkage of tumor size, nuclei fragmentation and chromosome condensation, and induced apoptosis (Chen et al., 2017).

More recently, researchers designed a mitochondria-targeted MOF that tested to increase the efficacy of the anti-cancer drug, dichloroacetate (DCA) when compared to the free drug (Haddad et al., 2020). Given that the mitochondria play an important role in oncogenesis, targeting it with a triphenylphosphonium (TPP) conjugated MOF would localize the drug delivery system. Zirconium-based MOF, UiO-66, was conjugated with TPP and loaded with DCA, which inhibits pyruvate dehydrogenase kinase (PDK), shifting cancer cell metabolism from aerobic glycolysis to oxidative phosphorylation (Bonnet et al., 2007). To confirm the targeted delivery to the site of action, Haddad et al. modified the particles with a fluorescent pyrene group, fTPP@(DCA5-UiO-66), for imaging and tracking Figure 13 (b). It was reported that the required dose of the DCA5-TPP5-UiO-66 drug delivery system was reduced to less than 1% when compared to the free drug (10%) (Haddad et al., 2020).

PDT involves three key components: 1) light (laser), 2) tissue oxygen and 3) the photosensitizer (PS) (Huang et al., 2013). When the PS is illuminated using the appropriate wavelength, it is able to transfer the absorbed photon energy to oxygen molecules, generating ROS leading to cell death and tissue destruction (Huang et al., 2011; Huang et al., 2012). Gold nanoclusters (AuNCs), as inorganic PSs, have been

used in PDT, but due to their short circulation in the bloodstream their application is limited. To overcome this hurdle, Zhang et al. developed a stimuli-responsive ZIF-8 encapsulated with AuNCs and loaded with the anti-tumor drug, DOX to obtain AuNCs@MOF-DOX nanoprobes for breast cancer treatment (Zhang et al., 2020).
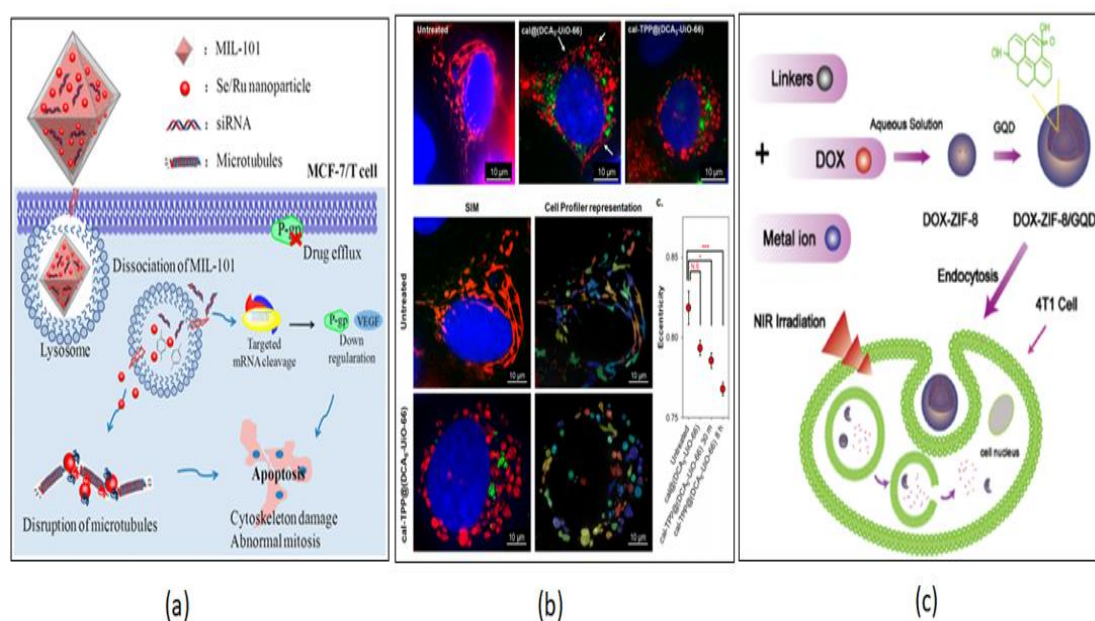
Figure 13: Applications of chemically-modified bioMOF nanostructures for breast cancer treatment. a) MIL-101. b) UiO-66. c) PDT/ZIF-8/Graphene Quantum Dots. (Chen et al., 2017; Haddad et al., 2020; Tian et al., 2017).

The structure of ZIF-8 degraded when exposed to a microenvironment with pH 5.5, releasing about 77.1% of DOX. The simultaneous treatment of DOX and PDT, displayed almost complete tumor inhibition and only partial inhibition when treated individually (Zhang et al., 2020). PDT using photo absorbers located in tumors can also be used to convert near-infrared (NIR) energy into heat, causing irreversible cellular damage leading to tumor eradication (Shen et al., 2015). Tian et al. functionalized ZIF-8 with graphene quantum dots (GQDs) and encapsulated the carrier with the anti-cancer drug, DOX, using a one-pot synthesis method (Tian et al., 2017).

GQDs exhibit good NIR absorbance, high photothermal conversion efficiency, excellent thermal conductivity, and low toxicity (Biswal et al., 2013; Wang et al., 2013; Yang et al., 2015). The ZIF-8/GQD multifunctional NPs were able to generate heat caused by NIR irradiation while also displaying a pH-responsive release of DOX under acidic conditions in breast cancer cells, 4T1 cells. The system exhibited a synergistic effect in cancer therapy and is a promising tool for future drug delivery design, as shown in Figure 13 (c) (Tian et al., 2017).

Lung Cancer

According to the World Health Organization, lung cancer was the most common cause of cancer death worldwide in 2020 with around 1.8 million deaths (Organization, 2021). Risk factors include environmental, lifestyle, and occupational exposures with cigarette smoking being the lead cause of the deadly cancer (Barta et al., 2019). About 16% of cases are detected before malignancy occurs with most detected during malignant stages (Barash et al., 2009). Therefore, the development of a more complex nanocarrier with better diagnostic and therapeutic efficacy is needed. Recently, Wang et al. modified a Fe-MOF system with a cationic polymer made from methyl viologen and polyallylamine hydrochloride (MV-PAH) for the treatment of A549 lung cancer cells (Wang et al., 2021). Methyl viologen, a bipyridyl herbicide, can have genotoxic and cytotoxic effect due to its ability to generate ROS (Wang et al., 2021). With the pH-responsiveness of the Fe-MOF system, the encapsulation of DOX and polyelectrolyte multilayer (PEM) coating, the group was able to successfully synthesize DOX@Fe-MOF@PEM NPs. The uptake of the NPs by A549 cells was successful and explained by the effective encapsulation of DOX due to the pH-sensitivity of the PEM coating. The amount of ROS generation in the cancer cells was

30-fold more than that of the control group and 8.29-fold more than that of the free drug alone. The DOX@Fe-MOF@PEM system induced higher apoptosis (62.9%) in A549 cells when compared with the Fe-MOF (3.34%), the free drug (22.39%), and DOX@Fe-MOF (39.79%) alone. These results prove the heightened synergistic effect of the drug, Fe-MOF, and PEM (Wang et al., 2021).

Liver Cancer

Hepatocellular carcinoma (HCC) and pancreatic ductal adenocarcinoma (PDAC) are the most deadly forms of cancer with the shortest life expectancy after diagnosis (Siegel et al., 2012). HCC is the most common primary cancer of the liver and the fastest rising cause of cancer related deaths in the US and second leading cause of cancer deaths in East Asia and Sub-Saharan Africa (Juaid et al., 2021; Rawla et al., 2018). Both cancers are mostly inoperable and the primary treatment is chemotherapy or palliative procedures (Chong et al., 2013; Siegel et al., 2012; Warsame & Grothey, 2012). There have been limitations with targeted therapy and the only FDA approved drug, Sorafenib, is for the treatment of advanced HCC cases. Sorafenib, a protein kinase inhibitor, blocks vascular endothelial growth factor and platelet-derived growth factor receptors (Keating & Santoro, 2009; Wilhelm et al., 2008). The epidermal growth factor (EGF) receptor kinase inhibitor, Erlotininib, is also used in conjunction with Gemcitabine to modestly improve the life expectancy in a sub-group of patients (Urtasun et al., 2015). To overcome the hurdles associated with traditional chemotherapeutics, researchers are focused on developing combined cancer treatments to downregulate MDR, increase drug efficacy and reduce toxic effects.

Leng et al. encapsulated the ent-kaurene diterpenoid compound, Oridonin (Ori), in MIL-53(Fe) for the delivery in human liver cancer cells, HepG2 (Leng et al.,

2018). Although, possessing strong anti-cancer activity, Ori is moderately hydrophobic, chemically instable and has a short half-life (Wang et al., 2017; Wang et al., 2016). Using the flexible, mesoporous and biocompatible MIL-53(Fe) would help alleviating the challenges of delivering the free drug on its own. The drug loading capacity was determined to be 56.25 wt% using a solvent diffusion method and left for 2/3/4 days at room temperature. The drug release was carried out in PBS pH 5.5 (91.75%) and pH 7.2 (82.23%) on the seventh day. Ori@MIL-53(Fe) showed inhibition of HepG2 cells at 28–57 µg/mL (equivalent to 15–30 µg/mL of free Ori), as shown in Figure 14 (a).

For an enhanced targeted delivery and improved pharmacokinetics, Chen and co-workers synthesized a Gd-porphyrin NMOF with the conjugation of FA to produce FA-NPMOF (Chen et al., 2018). FA is used as a targeting ligand for specific drug delivery in tumor tissue while porphyrin MOFs work as PSs for their use in PDT. The addition of Gd to the nanostructure will provide the combination of imaging and therapy owing to Gd^{3+} ions having long electronic relaxation times. The study was conducted using HCC cells in $kras^{G12V}$ zebrafish with DOX as the model drug for drug delivery. According to the MRI study, the T_1-weighted signals were enhanced when FA-NPMOF dosage increased with no malformations observed. The tumor targeting effect of FA-NPMOF NPs on HCC-bearing $kras^{G12V}$ zebrafish was determined by treating the cells with 200 µg/mL for 96 hours and observing the fluorescence signal. A gradual increase in fluorescence occurred during the first 48 hours suggesting that the NPs were specially delivered to HCC for that time period. There was also a noticeable shrinkage in tumor size with a tumor volume of around 23 mm^3 in the FA-NPMOF/PDT group vs. 48 mm^3 in the FANPMOF group, concluding the significance of using PDT in cancer treatments (Chen et al., 2018).

More recently, MIL-100(Fe) was synthesized by solvothermal method and tested on two types of hepatocytes (HL-7702 and HepG2) to determine the biocompatibility and safety of the MOF structure (Chen et al., 2019). MTT assays on various concentration of MIL-100(Fe) on HL-7702 cells (normal human liver cells) revealed a concentration less than 80 µg/mL was nontoxic with a cell viability greater than 85%. When the concentration was increased to 160 µg/mL, LDH was released indicating that the cell membrane was compromised and therefore, toxic to HL-7702 cells. With human liver cancer cells, Hep-G2, the cell viability was greater than 91% when treated with various concentrations of MIL-100(Fe), revealing a high tolerance up to 160 µg/mL. The study proved the use of MIL-100(Fe) as potential drug carriers in HCC treatment (Chen et al., 2019). Sun and co-workers loaded a Gd(III) MOF carrier, $[Gd(BCB)(DMF)](H_2O)_2$, with an anticancer drug (5-FU) and evaluated its activity on both cell lines (HL-7702 and Hep-G2) (Sun et al., 2019). The 5-FU loaded carrier had a drug uptake of 36.4% and stimuli dependent release in an acidic pH cancer microenvironment. Furthermore, the drug loaded carrier showed anticancer activity against HCC (Chen et al., 2019).
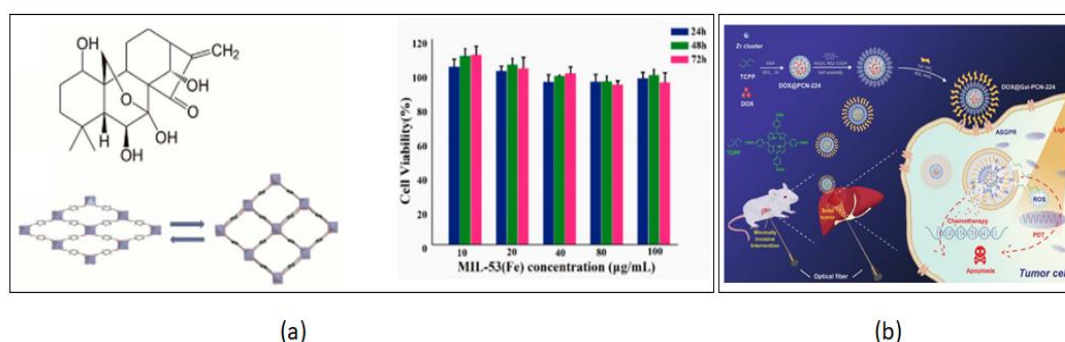
Figure 14: Applications of chemically-modified bioMOF nanostructures for hepatic cancer Treatment. a) MIL-53(Fe). b) DOX@Gal-PCN-224. (Leng et al., 2018; Hu et al., 2020).

In 2020, Hu and co-workers synthesized a photosensitive porphyrinic galactose modified MOF encapsulated with the anti-cancer drug, DOX (DOX@Gal-PCN-224) for the synergistic interventional PDT and chemotherapy using HCC cells and tumor tissue (Hu et al., 2020). Galactose can target asialoglycoprotein receptor (ASGPR), which is expressed on the surface of liver cancer cells, enhancing the cellular uptake of the NP (Wang et al., 2016). The Dox loading efficiency was determined to be around 14% while release studies revealed a 16% release of the drug in PBS (pH = 7.4) compared to an impressive 65% in a more acidic environment (pH = 5.6). Targeted cellular uptake was determined using confocal laser scanning microscopy (CLSM) and flow cytometry analysis. HepG2 and Huh7 cells exhibited significant fluorescence indicating active targeting using DOX@Gal-PCN-224 toward ASGPR+ cells. In vivo studies proved the DOX@Gal-PCN-224-RhB tumor targeting ability owing to the higher fluorescence intensity in tumor tissue compared to other organs. As for the combined chemotherapy and PDT effect on tumor growth inhibition, there was a noticeable increase (>40%) with the group treated using combination therapy, demonstrating a the potential treatment for hepatocellular carcinoma, as shown in Figure 14 (b) (Hu et al., 2020).

Colon Cancer

MOFs have also been used as cytosensors to detect colon (CT26) cancer cells (Duan et al., 2020). Researchers created a nanohybrid by combining a Cr-based MOF (Cr-MOF) with cobalt phthalocyanine (CoPc) nanoparticles. The idea of combining MOFs with metal nanoparticles can enhance the electrochemical features of the MOF and can be used in bio-sensing (Al-Sagur et al., 2019; Liang et al., 2018). The early detection of colon cancer is paramount when treating patients as it is the third most

prevalent cancer and has contributed to a high number of cancer-related deaths (Clarke et al., 2013). The Cr-MOF@CoPC cytosensor developed by Duan et al., demonstrated a higher sensing sensitivity towards CT26 cells when compared to the Cr-MOF and CoPc alone (Duan et al., 2020). The low limit of detection in CT26 cells was 36 cells mL^{-1} and 8 cells mL^{-1} for electrochemical impedance spectroscopy (EIS) and differential pulse voltammetry, respectively. These values were compared with the detection limit in human normal L929 cells, which showed no significant EIS signals, proving the selectivity of the MOF towards colorectal (CT26) cells.

A biocompatible porous In(III)-based MOF, $[In(Hpbic)(pbic)](DMF)_3$, was prepared using solvothermal synthesis with 2-(pyridin-4-yl)-1H-benzo[d]imidazole-5-carboxylic acid (H_2pbic) as the organic linker for the treatment of SW60 colon cancer cells (Li et al., 2019). The nontoxic MOF was loaded with 36.2% of 5-FU and displayed a 73% cumulative release up to 192 h. Cell Counting Kit-8 (CCK-8) assay revealed that the MOF system successfully reduced cell viability and proliferation in SW60 cells. Furthermore, the encapsulated MOF increased intracellular ROS levels with 65.17% and 95.80% of apoptosis at 1x IC_{50} and 3 x IC_{50}, respectively. Tumor volume was also inhibited in SW60 colon cancer treated mice when treated with the 5-FU@$[In(Hpbic)(pbic)](DMF)_3$ system (Li et al., 2019). More recently, Lv and coworkers synthesized an Er(III) MOF, $[Er_3(bpydb)_3(HCOO)(OH)(H_2O))]\cdot 6H_2O_n$, using a rigid tripodal nitrogen-containing heterotopic ligand 4,4′-(4,4′-bipyridine-2,6-diyl) dibenzoic acid (bpydbH_2) for the inhibition on Caco-2 colon cancer cells (Lv et al., 2020). The Er(III) based MOF showed a significant decrease in cell viability, while the metal ion and ligand had no effect on the Caco-2 cancer cells.

Endogenous H_2S is found to be overexpressed in colon and ovarian cancers resulting from the catalysis of cysteine related enzymes (Chen et al., 2019; Dong et al., 2019; Liu et al., 2019; Szabo et al., 2013; Wu et al., 2018). When exposed to endogenous H_2S, HKUST-1 NPs produce NIR-activatable copper sulfide for the synergistic PTT and CDT (chemodynamic therapy) of colon cancer (Li et al., 2020). Researchers treated CT26 colon cancer cells with the Cu-based MOF as a stand-alone treatment. Not only can HKUST-1 be converted to photoactive copper sulfide for PTT, the MOF NP also exhibits a conversion of H_2O_2 in cancer cells into a more toxic $\cdot$OH for CDT (Li et al., 2020) (Wang et al., 2019; Wang et al., 2019). CT26 colon cancer cells exhibited a gradual reduction in cell viability with increasing concentrations of HKUST-1.

Pancreatic Cancer

Pancreatic cancer is the seventh leading cause of cancer related deaths worldwide and the fourth in developed countries (Rawla et al., 2019). It remains one of the most lethal malignant neoplasms with over 400,000 new cases globally and a 5-year survival rate at only 9%. $Cu_3(BTC)_2$ (HKUST-1) was incorporated with Fe_3O_4 nanorods to produce magnetic MOF nanocomposites for the targeted drug delivery of Nimesulide in pancreatic cancer cells (Ke et al., 2011). Nimesulide, a selective cyclooxygenase-2 (COX-2) inhibitor, exhibits chemopreventive activity by blocking COX-2, thereby decrease the concentration of prostaglandins inside tumor tissue. It has been shown to protect against *N*-nitrosobis(2-oxopropyl) amine-induced pancreatic tumors in hamsters and the post-initiation development of squamous cell carcinomas in 4-nitroquinoline-1-oxide-induced rat tongue carcinogenesis (Furukawa et al., 2003; Kawamori et al., 2002; Nakatsugi et al., 2000). The Nimesulide carrier

system demonstrated magnetic properties while showing a drug uptake of up to 0.2g g^{-1}. The system is a promising anti-cancer treatment as the drug displayed a sustained release for up to 11 days (Ke et al., 2011).

More recently, GA, an anti-oxidant and anti-cancer agent was used for the synthesis of a copper-gallic acid MOF (Cu-GA NMOF) and post-synthetically loaded with the PS, methylene blue (MB), for PDT using Panc-1 cells (Sharma et al., 2019). The copper bioactive MOF framework was determined to have a BET specific surface area of 172 m^2 g^{-1} and an average pore diameter of 2.2 nm. The loading efficiency of MB in the Cu-GA NMOF reached 2 wt% owing to the hydrogen bonding between the nitrogen or sulfur groups on MB and the H^+ of GA. There was a higher drug release of GA and MB (69% and 94%) when placed in PBS (pH 7, pH 4) making it ideal for the drug delivery in tumor tissue. The hydrophilic nature of GA will reduce its uptake into tumor tissue, whereas the Cu-GA NMOF exhibits lipophilicity giving it the ability to interact with the cell membrane of tumor cells more readily than the free GA. According to the MTT (3-(4,5-dimethylthiazol-2-yl)-2,5-diphenyltetrazolium) assay using PANC-1 cells, Cu-GA induced cytotoxicity (IC_{50} = 50 µg/mL) more efficiently than the free GA (IC_{50} = 25 µg/mL). The MB-loaded Cu-GA NMOFs induced a significant tumor growth inhibition in rats, proving its synergistic PDT and chemotherapeutic effects in pancreatic cancer cells (Sharma et al., 2019).

Bladder Cancer

Bladder cancer occurs on the bladder mucosa when the cells DNA begins to mutate. The different types of bladder cancer include urothelial carcinoma, squamous cell carcinoma, and adenocarcinoma. These types are differentiated by the type of cells that are affected. Risk factors include smoking, age, sex, chemical exposure, chronic

bladder inflammation and family history (Clinic, 2020b). CYLD (CYLD Lysine 63 Deubiquitinase) is a gene that plays a negative regulatory role in bladder cancer and the loss of CYLD expression can be observed in different types of human cancer (Massoumi, 2011; Wu et al., 2021). MiR-181b (microRNA 181b), a RNA gene, has been shown to regulate the expression of CYLD, leading to the apoptosis of certain cancer cells (Yang et al., 2020). Wu et al. prepared a MOF based on Zn(II) via the rigid V-shaped ligand 2,6-di(2′,5′-dicarboxylphenyl)pyridine (H_4L) with $Zn(NO_3)_2 \cdot 6H_2O$ giving the complex, $[Zn_3(L)(OH)_2(H_2O)_4](DMF)_5$ (Wu et al., 2021). The MOF complex was observed for the detection of miR-130 and CYLD and their roles in the progression and downregulation of bladder cancer. The group exhibited a decrease in miR-130 and an increase in CYLD gene expression when treated with $[Zn_3(L)(OH)_2(H_2O)_4](DMF)_5$. These results indicate that the MOF compound can induce programmed cell death by regulating the miR-130 and CYLD genes in bladder cancer.

Ovarian and Cervical Cancer

Ovarian cancer is the 8th most commonly occurring cancer in women and the deadliest among gynecological patients due to the asymptomatic nature of the disease (Coleman et al., 2013; World Cancer Research Fund). Patient prognosis has not improved much compared to other cancers due to the resistance of epithelial ovarian cancer to platinum based chemotherapy (Vaughan et al., 2011). Ovarian cancer patients are usually diagnosed with stage III and stage IV because of late detection and poor screening tests (Koshiyama et al., 2017; Mathieu et al., 2018). Current advanced ovarian cancer treatment involves a combination of surgical cytoreduction and chemotherapy (Wright et al., 2016). The goal is to overcome drug resistance while

using new imaging techniques and contrasting agents for early diagnosis and targeted delivery towards ovarian cancer cells (van-Dam et al., 2011). Silencing genes via siRNA, has been used in combating resistant cancers and can reverse cisplatin (Cis) resistance in ovarian cancer (Fire et al., 1998; Meng et al., 2010; Xiong & Lavasanifar, 2011; Yellepeddi et al., 2012). He et al. encapsulated a UiO NMOF with siRNA and the anticancer drug, Cis, for the co-delivery in human ovarian cancer cells, SK-OV-3 (He et al., 2014). The nanocarrier protects the siRNA from nuclease degradation allowing for an increased cellular uptake while promoting release from endosomes for the silencing of MDR genes in OC cells. UiO-Cis exhibited a 12.3 wt% drug loading capacity determined by inductively coupled plasma mass spectrometry (ICP-MS). Dynamic light scattering measurements increased after the loading of siRNA confirming its presence in the drug delivery system. There was a much higher siRNA/UiO-Cis cellular uptake compared to the free siRNA solution confirmed by confocal laser scanning microscopy with red fluorescence in the cytoplasm of SK-OV-3 cells. The nanosystem was successful in the knockdown and reversal of three MDR-relevant genes (survivin, Bcl-2 and P-gp) with IC_{50} decreasing by more than 11-fold by co-delivering pooled siRNAs and cisplatin in a NMOF carrier (He et al., 2014).

Sun et al. reported a dinuclear gold(I) pyrrolidinedithiocarbamato (PDTC) complex with a bidentate carbene ligand for the cytotoxic activity towards Cis-resistant ovarian cancer cells, A2780cis (Sun et al., 2015). PDTC, a dithiocarbamate, has been proven to exhibit cytotoxic and antiangiogenic activities (Pfeilschifter et al., 2010). Furthermore, metal-based dithiocarbamato complexes have been proven to have anticancer potencies comparable to Cis (Keter et al., 2014). Zn-MOF (zinc (II), adenine, and a BTC linker was used as a carrier for the uptake and release of dinuclear gold(I) pyrrolidinedithiocarbamato complex. The Zn-MOF complex was successful in

killing A2780cis cancer cells with a decreased cell survival by 50% when the co-incubation period was greater than 24h. The antimigratory activity of the Zn-MOF complex was exhibited using a transwell antimigratory assay where the Zn-MOF complex effectively inhibited A2870cis OC cells (Sun et al., 2015).

Lysophosphatidic acid (LPA), a bioactive phospholipid, causes the proliferation of cancer cells with elevated levels in plasma, suggesting that it plays an important role in the pathophysiology of cancer cells (Mills & Moolenaar, 2003; Xu et al., 1998). LPA has also been shown to alter receptor expression in ovarian carcinogenesis and metastasis when compared to other epithelial tumors; therefore, early detection of LPA levels in plasma could aid in early diagnosis and treatment of the disease (Ren et al., 2006; Sutphen et al., 2004; Umezu-Goto et al., 2004). Zhang et al. constructed a three mixed-crystal isostructural MZMOFs with variable Eu:Tb stoichiometry for the detection of LPA, the biomarker for OC (Zhang et al., 2015). Lanthanide-MOFs exhibit luminescent properties associated with those of lanthanide cations, which can be tuned by host-guest chemistry for the chemical sensing of LPA (Cui et al., 2014). MZMOF-3 ($Eu_{0.6059}Tb_{0.3941}$-ZMOF) was successful in the detection of LPA in the presence of other major compounds in the blood plasma making it a promising biochemical sensing tool, as illustrated in (Zhang et al., 2015).

Recently, Chen et al. loaded a nucleic acid functionalized UiO-68 with DOX for the unlocking and release of the anticancer drug towards OVCAR-3 ovarian cancer cells (Chen et al., 2019). The nucleic acid includes a base sequence that is complementary to the miRNA-221, a specific biomarker for ovarian cancer cells, inducing the 'un-locking' of the MOF carrier for targeted delivery of DOX (Dahiya et al., 2008). The research revealed the enhanced release of DOX from the carrier with

increased concentrations of miRNA-221, proving its unlocking capabilities in target tissue when exposed to exonuclease III. Upon treatment with the DOX-loaded miRNA-221-responsive NMOFs, OVCAR-3 cells exhibited a 50% decrease in cell viability, displaying cytotoxicity towards OCCAR-3 ovarian cancer cells (Chen et al., 2019).

More recently, a Cu(II) metal-organic framework (MOF), $[(Cu(L)_2(H_2O)_2](DMF)_4)_n$ (L = 3-(1H-pyrazol-4-yl)pyridine) was studied for its inhibitory effect on Hey ovarian cancer cells (Li et al., 2020). MTT assay, CCK-8 proved the anti-cancer activity of the MOF system with an IC_{50} value 2.81 ± 0.17 μg/mL. The system induced cell apoptosis in Hey cells by increasing ROS accumulation. The treatment was dose-dependent, meaning that the level of ROS accumulation increased significantly with increased concentrations of the Cu-MOF.

Cervical cancer is the fourth most common gynecologic cause of cancer with about 99% of cases linked with high-risk human papillomaviruses. Early diagnosis and treatment can lead to very successful eradication of the cancer (Organization). Zheng and co-workers synthesized a CCM loaded nanoscale ZIF-8 (CCM@NZIF-8) NP to evaluate the antitumor effect on xenograft tumors of U14 cervical cancer (Zheng et al., 2015). The CCM@NZIF-8 NPs exhibited a drug encapsulation efficiency of 88.2% and a tumor inhibitory rate of 85% making it an ideal, biocompatible drug delivery carrier. The NPs were also proven to be highly stable when placed in methanol solution, PBS, and fetal calf serum solutions as the hydrodynamic parameters did not change significantly. TGA was also used to measure the stability of the NP, resulting in the structure breaking down at 547°C. Furthermore, CCM@NZIF-8 had a higher

inhibition rate and enhanced cytotoxicity in HeLa cells when compared to the free CCM due to the effective endocytosis by the cells, as shown in (Zheng et al., 2015).

Oral Cancer

Traditional single cancer therapy has limitations and harmful side effects, owing to the need of multimodal systems for a more effective therapy (Fan et al., 2017). Xiang et al. synthesized magnetic MOF NPs with porous carbon ($Fe_3O_4@C$) for the combined cancer therapy and magnetic-triggered hyperthermia in human oral squamous cell carcinoma cell line, CAL27 and CAL27 tumor-bearing mice (Xiang et al., 2020). The NPs were further coated with PVP and encapsulated with DOX to give $Fe_3O_4@C$-PVP@DOX nanocomposites. About 70% of DOX was adsorbed and loaded in the porous MOF NP with only 4% being released after 6 h at pH 7.4, indicating the effectiveness of the drug loading. The DOX release increased when an alternating magnetic field (AMF) was added, proving that the NPs are magnetically triggered. Furthermore, the NPs were incubated with CAL27 cells followed by magnetic hyperthermia (MHT) at 43°C where more DOX was released, indicating the AMF-triggered heat leads to the accumulation of the drug towards cancer cells (Xiang et al., 2020).

Tan and researchers developed a hybrid nanocomposite (DOX/Cel/MOFs@Gel) by integrating IRMOF-3 with a thermosensitive hydrogel, poly(D,L-lactide-coglycolide)-poly(ethylene glycol)-poly(D,L-lactide-coglycolide) triblock copolymers (PLGA-PEG-PLGA) where DOX and celecoxib (Cel) were coloaded for a localized treatment in KB and SCC-9 oral cancer cells (Tan et al., 2020). The group compared the nanocomposite along with the free drug, DOX/MOFs, and DOX/Cel/MOFs. DOX exhibited more than 80% release in an acidic environment (pH

~6.5) with a sustained release due to the protective layer from the IRMOF-3. The introduction of the thermosensitive hydrogel decreased the burst release of Cel from the nanocomposite and about 66% of the drug experienced a cumulative release after 11 days in the acidic medium, which could be due to the hydrophobic nature of the gel (Tan et al., 2020). The cytotoxicity studies on KB and SCC-9 oral cancer cells revealed that DOX/Cel/MOFs had the highest amount of cell death. The thermosensitive gel added an extra layer for the drug to be able to break through, leading to a weakened cell killing effect. However, the DOX/Cel/MOFs@Gel nanocomposite exhibited the most tumor ablation in nude mice bearing SCC-9 xenografts. This could be due to the steady drug release and the combined effect of the DOX and Cel, indicating a localized treatment for oral cancer patients.

Brain Cancer

Brain cancer is one of the most aggressive cancers due to late diagnosis and the inability of drug delivery systems being able to pass through the blood-brain barrier (BBB). NPs have tremendously improved early and accurate diagnosis while providing enhanced sensitivity and targeted drug delivery (Biswas et al., 2019; Meyers et al., 2015). Researchers studied the effect of a planar MOF-based composite on U87MG brain cancer cells and U87MG tumor-bearing nude mice (Mu et al., 2020). They seeded Au NPs on Zr-based porphyrinic MOF nanosheets and loaded them with $_L$-Arg for PDT and gas therapy (Mu et al., 2020). The Au NPs were added for their ability to catalyze glucose into H_2O_2 and gluconic acid in the presence of O_2 (Luo et al., 2010; Xu et al., 2019). This generated H_2O_2 can metabolize $_L$-Arg to $_L$-citrulline, leading to NO generation (Fan et al., 2017; Keshet & Erez, 2018; Stuehr, 2004). NO could inhibit cancer growth by causing DNA damage, nitrosylation of certain

enzymes, or mitochondrial ablation (Chandrawati et al., 2017; Fan et al., 2018; Wang et al., 2015). A hydrogen peroxide assay kit was used to measure H_2O_2 generation and the results indicated that the levels of H_2O_2 decreased due to the consumption by L-Arg. Griess assay revealed that NO generation was proportional to L-Arg loading and that the designed MOF composite (GMOF-LA) could produce NO in the presence of converted H_2O_2, leading to an enhanced tumor suppression by means of a biocatalytic cascade (Mu et al., 2020). Cellular uptake of the MOF composite in U87MG human glioblastoma cells increased gradually with a maximum internalization reaching 12 h. Furthermore, the GMOF nanosheets showed little to no toxicity against U87MG cells when compared to the combination treatment system (GMOF-LA + laser). The cell viability decreased to 18.6% when the MOF composite was used in conjunction with PDT and NO-mediated gas therapy (GMOF-LA). Finally, in-vivo studies revealed the accumulation of GMOF-LA nanosheets in U87MG tumor-bearing mice reaching a maximum value of $4.45 \pm 0.70\% \text{ID g}^{-1}$, owing to the enhanced permeability and retention effect (Mu et al., 2020). This multifunctional MOF composite can pave the way for future developments using nanoreactor-mediated therapy.

Blood Cancer

Leukemia, a cancer of blood tissue, occurs when bone marrow overproduces white blood cells, causing an abnormal amount white blood cells leading to overall malfunction. Risk factors include genetics, smoking, history of cancer treatment, chemical exposure and family history (Clinic, 2021). Traditional drug delivery systems used for treating leukemia revealed some challenges such as stability, drug leakage, and toxicity (Draz et al., 2014; Elsabahy & Wooley, 2012; Reynolds et al., 2012; Williford et al., 2014).

A porous MOF was synthesized by reacting 3-phenylpyridine polycarboxylic (H_3L) ligands with $Ni(NO_3)_2 \cdot 6H_2O$ giving, $(Me_2NH_2)[Ni_3(L)_2(\mu_3\text{-}OH)(H_2O)] \cdot 2DMF$ (Xi et al., 2019). DCFH-DA detection kit assay was used to determine ROS production of the MOF compound in HL-60 promyelocytic leukemia cells. Results revealed ROS accumulation in a dose-dependent manner, with 58.70% and 90.02% at 1 x IC_{50} and 3 x IC_{50}, respectively. The compound was further tested on HL-60 cells using the MTT assay. Results showed significant reduction in cell colonies and cell viability with IC_{50} of 2.13 ± 0.07 µg/mL, suggesting the MOFs anti-cancer effect without the addition or encapsulation of other drug compounds.

1.3.7 Copper-based MOFs as Antibacterial Agents

Copper has been studied for its antimicrobial effects since 1962 and increasing since (Rosenberg et al., 2019). Studies have shown its efficacy against *Staphylococcus aureus (S. aureus), Clostridium difficile, Bacillus subtilis, Escherichia coli (E. coli), Pseudomonas aeruginosa and Legionella pneumophilia* (Carson et al., 2007; Gant et al., 2007; Harrison et al., 2008; Ibrahim et al., 2008; Ren et al., 2009; Ruparelia et al., 2008; Santo et al., 2008; Stout & Yu, 2003; Weaver et al., 2008; Wheeldon et al., 2008). Cu^{2+} ions have been identified to induce damage by binding to lipopolysaccharides or peptidoglycans or carboxylic groups of bacteria causing a disruption in the bacterial envelope (Casey et al., 2010; Fang et al., 2009; Langley & Beveridge, 1999; Santo et al., 2012). Cu^{2+} ions cause membrane depolarization by binding to negatively charged domains and reducing the potential. This process could eventually lead to membrane leakiness or complete membrane rupture (Mitra et al., 2020). Bacterial damage can also be caused by Cu NPs that have been internalized or bound by bacteria. ROS generated by Cu NPs can lead to oxidative stress and

eventually lead to deoxyribonucleic acid (DNA) damage and lipid peroxidation in bacterial membranes (Chatterjee et al., 2014; Lemire et al., 2013; Slavin et al., 2017). Rodríguez et al. examined HKUST-1 for its antibacterial activity (Rodríguez et al., 2014). The group immobilized the MOF material onto cellulosic fibers and observed complete elimination of *E. coli* growth. They determined that HKUST-1 was responsible for the antibacterial activity against *E. coli* and not due its individual components (Rodríguez et al., 2014).

Chapter 2: Synthesis and Characterization of Copper-based MOFs

2.1 Introduction

Copper, a trace element, plays an important role in the growth and development of the human body (Wang et al., 2021). Recent advances made with copper-based biomaterials has encouraged researchers to further expand their use in biological applications to overcome challenges such as, antibiotic resistance (Blair et al., 2015; Cox et al., 2019), bone fracture healing (Ren et al., 2015), cardiovascular diseases (Jin et al., 2018), and conventional chemotherapeutics (Dicken et al., 2005). In particular, copper-based MOFs offer a high degree of tunability, porosity and thermal stability. Cu-BTC, synthesized by Chui Stephen et al. in 1999, consists of Cu^{2+} ions bridged by 1,3,5-benzenetricarboxylic acid (BTC) organic linker molecules (Chui Stephen et al., 1999). The dimeric metal unit is connected to four carboxylate groups from the linker molecule forming the paddlewheel unit also known as the secondary building unit (SBU). Herein, we synthesize Cu-BTC according to the method published by Rowsell and Yaghi in 2006 (Rowsell & Yaghi, 2006) for further modifications (Chapters 3 & 4) and use in biological applications (Chapters 5 & 6).

The second MOF candidate in this work includes Cu-GA. GA, a phenolic compound, is a scavenger of ROS and can also act as a pro-oxidant by generating ROS, ultimately causing oxidative stress (Babich et al., 2011). However, a free GA compound is hydrophilic in nature, so having it a part of a MOF structure, would improve its stability and solubility in biological media (Sharma et al., 2019). We synthesized Cu-GA using a novel method and further investigated its effect on cancer and bacterial cells. Lastly, an approach was made to combine both GA and BTC in a

mixed linker Cu-BTC-GA MOF. Tables 1 and 2 list all experimental conditions that were explored for the synthesis of Cu-BTC and Cu-GA.

2.2 Materials and Methods

The synthesis of Cu-BTC and Cu-GA structures were explored through various preparations as explained in the literature. In both reactions, a base was used to deprotonate the -COOH groups of both linkers. Despite the fact that triethylamine (TEA) has been widely used to deprotonate BTC during the synthesis of Cu-BTC, our optimized conditions showed that the presence of TEA can be replaced by using DMF in a mixed solvent of DMF: H2O: EtOH. Similarly, A stronger base (KOH) was used to deprotonate the GA linker in a mixed solvent of DMF: H2O: EtOH.

Based on the chemical structure of the GA and BTC linkers, both have the affinity to Cu^{2+} ions forming 2D-3D structures. This has been established, as mentioned above, through the formation of pristine Cu-BTC and Cu-GA MOF nanostructures. Accordingly, we attempted to explore the formation of a mixed-linker MOF structure through the utilization of the binding potential of both linkers and study the contribution of each linker for the formation of a BTC and GA mixed linker MOF structure. This study was carried out by varying the proportion of the BTC and GA linkers while maintaining the stoichiometry of reaction between Cu^{2+} ions and the -COOH functional groups. Three formulations were investigated by varying the molar ratio of the BTC:GA (1:1, 3:1 and 1:3). The detailed characterization of the structures are explained in the following sections. Due to relevance of the results, a description of the 1:1 and 3:1 formulations will be explained followed by that of the 1:3 formulation.

Table 1: Experimental approaches for the preparation of Cu-BTC MOF nanostructures.

Sample Code	Metal source	Linker	Base	Conditions	Time	Reactor System	Notes
Sample 1	Copper nitrate 2.38 mmol	BTC 4.31 mmol	DMF in solvent	Dissolve metal in 12 mL DMF:H$_2$O:EtOH (1:1:1). Same for BTC. Combine. Stir x 15 min. Heat @ 85°C x 24h. Pour mother liquor out. Wash 2x with DMF. Exchange with DCM 3x for 2 days and then heat x 5h @200°C	24h	Glass bottle	Targeted Surface area was not achieved
Sample 2	Copper nitrate 2.38 mmol	BTC 4.31 mmol	DMF in solvent and Triethyl amine	Dissolve metal in 12 mL DMF:H$_2$O:EtOH (1:1:1). Same for BTC. Combine. Add 0.5mL of triethylamine. Stir x 15 min. Heat @ 85°C x 24h. Pour mother liquor out. Wash 2x with DMF. Exchange with DCM 3x for 2 days and then heat x 5h @200°C.	24h	Glass bottle	XRD did not appear crystalline
Sample 3	Copper nitrate 2.38 mmol	BTC 4.31 mmol	DMF in solvent	Dissolve metal in 12 mL DMF:H$_2$O:EtOH (1:1:1). Same for BTC. Combine. Stir x 23h at room temperature	23h	Beaker	very little product was formed. Discontinued before XRD
Sample 4	Copper nitrate 2.38 mmol	BTC 4.31 mmol	DMF in solvent and Triethyl amine	Dissolve metal in 12 mL DMF:H$_2$O:EtOH (1:1:1). Same for BTC. Combine. Add 0.5mL of triethylamine. Stir x 23h at room temperature	23h	Beaker	very little product was formed. Discontinued before XRD

Table 1: Experimental approaches for the preparation of Cu-BTC MOF nanostructures. (continued)

Sample Code	Metal source	Linker	Base	Conditions	Time	Reactor System	Notes
Sample 5	Copper nitrate 8.62 mmol	BTC 4.76 mmol	DMF in solvent	Dissolve metal in 24 mL DMF:H_2O:EtOH (1:1:1). Same for BTC. Combine. Stir x 15 min. Heat @ 85°C x 24h. Pour mother liquor out. Wash 2x with DMF. Exchange with meOH 3x for 2 days and then heat x 5h @200°C	24h	Glass bottle	Modification: solvent used in exchange Target surface area was not achieved
Sample 6	Copper nitrate 8.62 mmol	BTC 4.76 mmol	DMF in solvent	Dissolve metal in 24 mL DMF:H_2O:EtOH (1:1:1). Same for BTC. Combine. Stir x 15 min. Heat @ 85°C x 24h. Pour mother liquor out. Wash 2x with DMF. Exchange with DCM 3x for 3 days (Filter vacuum each time) and then heat under vacuum @ 170°C. A RBF and vacuum line were used here (before vacuum oven arrived)	24h	Glass bottle	Target surface area was not achieved

Table 1: Experimental approaches for the preparation of Cu-BTC MOF nanostructures. (continued)

Sample Code	Metal source	Linker	Base	Conditions	Time	Reactor System	Notes
Cu-BTC	Copper nitrate 8.62 mmol	BTC 4.76 mmol	DMF in solvent	Dissolve metal in 24 mL DMF:H_2O:EtOH (1:1:1). Same for BTC. Combine. Stir x 15 min. Heat @ 85°C x 24h. Pour mother liquor out. Wash 2x with DMF. Exchange with DCM 3x for 3 days (Filter vacuum each time) and then heat in vacuum oven @ 140°C x 24h.	24h	Sealed tube	Highest surface area achieved here. This was the method used for further synthesis of Cu-BTC

Table 2: Experimental approaches for the preparation of Cu-GA MOF nanostructures.

Sample Code	Metal Source	Linker	Base	Conditions	Time	Reactor System	Notes
Sample A	Copper nitrate 2mmol	GA 1mmol	KOH 2mmol	150°C	24h	RBF	XRD did not appear crystalline
Sample B	Copper nitrate 2mmol	GA 1mmol	TEA 2mmol	50°C x 1h under stirring first with TEA and GA soln then add metal and stir x 48h. 150°C for synthesis	24h	RBF	XRD did not appear crystalline
Sample C	Copper nitrate 2mmol	GA 1mmol	KOH 2mmol	150°C	24h	RBF	XRD did not appear crystalline
Sample D	Copper nitrate 2mmol	GA 1mmol	KOH 2mmol	85°C in oven and then dry sample under reflux	24h	Sealed tube	XRD did not appear crystalline
Sample E	Copper nitrate 2mmol	GA 1mmol	DMF	Solvothermal synthesis @110°C x 24h and exchanged with DCM x 1week	24h	Sealed tube	XRD did not appear crystalline

Table 2: Experimental approaches for the preparation of Cu-GA MOF nanostructures. (continued)

Sample Code	Metal Source	Linker	Base	Conditions	Time	Reactor System	Notes
Sample F	Copper nitrate 2mmol	GA 1mmol	5M KOH	GA dissolved in water and then Cu added to GA soln. 5M KOH was added til pH reached 9. Heat x 12h @120°C in Autoclave. Wash with water	12h	Autoclave reactor	XRD did not appear crystalline
Sample G	Copper nitrate 2mmol	GA 1mmol	DMF	Cu dissolved in DMF:H$_2$O:EtOH (1:1:1). and GA dissolved in DMF and added to Cu soln. Heat x 24h @110°C in sealed tube. Wash with DMF. Exchange with DCM x 1 week	24h	Sealed tube	XRD did not appear crystalline
Sample H	Copper nitrate 2mmol	GA 1mmol	5M KOH	GA dissolved in water and then Cu added to GA soln. 1000μL of 5M KOH added. Heat x 12h @120°C in Autoclave. Wash with water. Exchange with DCM x 1 week	12h	Autoclave reactor	XRD did not appear crystalline
Sample I	Copper nitrate 2mmol	GA 1mmol	5M KOH	GA dissolved in DMF:H$_2$O:EtOH (1:1:1). and then Cu added to GA soln. 700μL of 5M KOH added. Heat x 12h @120°C in Autoclave. Wash with water. Exchange with DCM x 1 week	12h	Autoclave reactor	XRD did not appear crystalline
Sample J	Copper nitrate 2mmol	GA 1mmol	DMF	GA dissolved in 11 mL of DMF and then Cu added to GA soln. Heat x 12h @120°C in Autoclave. Wash with DMF. Exchange with DCM x 1 week	12h	Autoclave reactor	XRD did not appear crystalline

Table 2: Experimental approaches for the preparation of Cu-GA MOF nanostructures. (continued)

Sample Code	Metal Source	Linker	Base	Conditions	Time	Reactor System	Notes
Sample K	Copper nitrate 2mmol	GA 1mmol	DMF	Cu dissolved in DMF:H$_2$O:EtOH (1:1:1). and GA dissolved in DMF and added to Cu soln. Heat x 24h @120°C in sealed tube. Wash with DMF. Exchange with DCM x 1 week	24h	Sealed tube	XRD did not appear crystalline
Sample L	Copper nitrate 2mmol	GA 1mmol	5M KOH	GA dissolved in water and then Cu added to GA soln. 1000µL of 5M KOH added. Heat x 12h @120°C in Autoclave. Wash with water. Exchange with DCM x 1 week	24h	Autoclave reactor	XRD did not appear crystalline
Sample M	Copper nitrate 2mmol	GA 1mmol	5M KOH	GA dissolved in DMF:H$_2$O:EtOH (1:1:1). and then Cu added to GA soln. 700µL of 5M KOH added. Heat x 12h @120°C in Autoclave. Wash with water. Exchange with DCM x 1 week	24h	Autoclave reactor	XRD did not appear crystalline
Cu-GA	Copper nitrate 2mmol	GA 1mmol	5M KOH	GA dissolved in DMF:H$_2$O:EtOH (1:1:1). and then Cu added to GA soln. 5M KOH added til pH~7. Heat x 12h @120°C in Autoclave. Wash with methanol and Exchange with DCM 3x for 3 days	24h	Autoclave reactor	XRD very close to patter in the literature. This was the method used for further synthesis of Cu-GA.

Table 2: Experimental approaches for the preparation of Cu-GA MOF nanostructures. (continued)

Sample Code	Metal Source	Linker	Base	Conditions	Time	Reactor System	Notes
Cu-GA (base change)	Copper nitrate 2mmol	GA 1mmol	5M NaOH	GA dissolved in DMF:H$_2$O:EtOH (1:1:1). and then Cu added to GA soln. 5M KOH added til pH~7. Heat x 12h @120°C in Autoclave. Wash with methanol and Exchange with DCM 3x for 3 days	24h	Autoclave reactor	Base was changed to determine if crystallinity can be improved. However, it did not.
Cu-GA (solvent change)	Copper nitrate 2mmol	GA 1mmol	5M KOH	GA dissolved in DMF:H$_2$O:EtOH (1:1:1). and then Cu added to GA soln. 5M KOH added til pH~7. Heat x 12h @120°C in Autoclave. Wash with methanol and Exchange with DCM 3x for 3 days	24h	Autoclave reactor	solvent was changed to determine if crystallinity can be improved. However, it did not.
Cu-GA (salt change)	Copper Chloride 2mmol	GA 1mmol	5M KOH	GA dissolved in DMF:H$_2$O:EtOH (1:1:1). and then Cu added to GA soln. 5M KOH added til pH~7. Heat x 12h @120°C in Autoclave. Wash with methanoland Exchange with DCM 3x for 3 days	24h	Autoclave reactor	Copper salt was changed to determine if crystallinity can be improved. However, it did not.
Cu-GA (temp. change)	Copper nitrate 2mmol	GA 1mmol	5M KOH	GA dissolved in DMF:H$_2$O:EtOH (1:1:1). and then Cu added to GA soln. 5M KOH added til pH~7. Heat x 24h @85°C in Autoclave. Wash with methanol and Exchange with DCM 3x for 3 days	24h	Autoclave reactor	temperature was changed to determine if crystallinity can be improved. However, it did not.

Table 2: Experimental approaches for the preparation of Cu-GA MOF nanostructures. (continued)

Sample Code	Metal Source	Linker	Base	Conditions	Time	Reactor System	Notes
Cu-GA (time change)	Copper nitrate 2mmol	GA 1mmol	5M KOH	GA dissolved in DMF:H_2O:EtOH (1:1:1). and then Cu added to GA soln. 5M KOH added til pH~7. Heat x 24h @120°C in Autoclave. Wash with methanol and Exchange with DCM 3x for 3 days	24h	Autoclave reactor	Synthesis time was changed to determine if crystallinity can be improved. However, it did not.

Cu-BTC (HKUST-1) was prepared from the synthesis procedure carried out by Rowsell and Yaghi (Rowsell & Yaghi, 2006) as follows: 1,3,5-benzenetricarboxylic acid (BTC) (1.0 g, 4.76 mmol, Aldrich) and copper(II) nitrate hemipentahydrate (1.72 g, 8.62 mmol, Aldrich) were each dissolved in 24 mL of solvent consisting of equal parts N,N-dimethylformamide (DMF) (Fisher), ethanol (Fisher) and deionized water. Once dissolved, the copper solution was added to the linker solution and stirred for 15 minutes. The entire mixture was added to a 150 mL sealed tube and placed in an 85 °C oven for 24h to yield small octahedral crystals. After decanting the hot mother liquor and rinsing with DMF, the product was immersed in dichloromethane (DCM) (Fisher) and filtered, washed and replaced with fresh DCM daily for 3 days. The remaining solvent was evacuated completely from the pores under vacuum at 140°C for 24h, yielding the porous material.

Cu-GA MOF was synthesized by dissolving gallic acid monohydrate (0.376 g, 2 mmol, Riedel-de Haën) in 5 mL of solvent consisting of equal parts N,N-dimethylformamide (Fisher), ethanol (Fisher) and deionized water. Simultaneously, copper(II) nitrate hemipentahydrate (0.232 g, 1 mmol, Aldrich) was also dissolved in 5 mL of the same solvent mixture. Once the two solutions were completely dissolved,

the copper solution was then added dropwise to the gallic acid solution while stirring. 5M KOH was added to the Cu-GA mixture dropwise until the pH reached ~ 6.5. The reaction mixture was put in a sealed Teflon lined autoclave reactor and placed in the oven for 12h at 120°C. The sample was then washed with methanol 3 times daily for 2 days and then with DCM 3 times for 1 day for the evacuation of the original solvent from the pores. Finally, to activate the sample, the dried powder was placed under vacuum at 130°C for 24h.

Cu-BTC-GA (1:1 mixed linker) was prepared by dissolving GA (0.282 g, 1.5 mmol) in 5 mL of solvent consisting of equal parts DMF, ethanol and deionized water. Triethylamine (TEA) (0.152 g, 1.5 mmol, Aldrich) was added to the GA solution and stirred for 15 min. Simultaneously, BTC (0.105g, 0.5 mmol) was dissolved in 5 mL of solvent consisting of equal parts DMF, ethanol and deionized water. TEA (0.152 g, 1.5 mmol) was also to the BTC solution and stirred for 15 min. Both linker solutions are combined and kept under stirring. Copper(II) nitrate hemipentahydrate (0.349 g, 1.5 mmol) was dissolved in 5 mL of the same solvent mixture and then added to the combined linker solution. The reaction mixture is added to a sealed Teflon lined autoclave reactor and placed in the oven for 24h at 85°C. The sample was then washed with methanol 3 times daily for 2 days and then with DCM 3 times for 1 day to evacuate original solvent from the pores. The product is dried first in the oven for about 9h at 120°C and then finally, to activate the sample, the dried powder was placed under vacuum at 120°C for 24h.

Cu-BTC-GA (3:1 mixed linker) was prepared by dissolving GA (0.094 g, 0.5 mmol) in 5 mL of solvent consisting of equal parts DMF, ethanol and deionized water. TEA (0.051 g, 0.5 mmol) was added to the GA solution and stirred for 15 min. Simultaneously, BTC (0.105 g, 0.5 mmol) was dissolved in 5 mL of solvent consisting

of equal parts DMF, ethanol and deionized water. TEA (0.152 g, 1.5 mmol) was also to the BTC solution and stirred for 15 min. Both linker solutions are combined and kept under stirring. Copper(II) nitrate hemipentahydrate (0.233 g, 1 mmol) was dissolved in 5 mL of the same solvent mixture and then added to the combined linker solution. The reaction mixture is added to a sealed Teflon lined autoclave reactor and placed in the oven for 24h at 85°C. The sample was then washed with methanol 3 times daily for 2 days and then with DCM 3 times for 1 day to evacuate original solvent from the pores. The product is dried first in the oven for about 9h at 120°C and then finally, to activate the sample, the dried powder was placed under vacuum at 120°C for 24h.

Cu-BTC-GA (1:3 mixed linker) was prepared by dissolving GA (0.564 g, 3 mmol) in 10 mL of solvent consisting of equal parts DMF, ethanol and deionized water. TEA (0.304 g, 3 mmol) was added to the GA solution and stirred for 15 min. Simultaneously, BTC (0.070 g, 0.33 mmol) was dissolved in 5 mL of solvent consisting of equal parts DMF, ethanol and deionized water. TEA (0.101 g, 1 mmol) was also to the BTC solution and stirred for 15 min. Both linker solutions are combined and kept under stirring. Copper (II) nitrate hemipentahydrate (0.465 g, 2 mmol) was dissolved in 5 mL of the same solvent mixture and then added to the combined linker solution. The reaction mixture is added to a sealed Teflon lined autoclave reactor and placed in the oven for 24h at 85°C. The sample was then washed with methanol 3 times daily for 2 days and then with DCM 3 times for 1 day to evacuate original solvent from the pores. The product is dried first in the oven for about 9h at 120°C and then finally, to activate the sample, the dried powder was placed under vacuum at 120°C for 24h.

Characterization of MOF samples. The morphology and particle size of the MOF samples were obtained using a JEOL JSM–6010LA scanning electron microscope (SEM). Powder x-ray diffraction (XRD) data was recorded on a

Shimadzu-6100 powder XRD diffractometer with Cu-K$_\alpha$ radiation, λ = 1.542 Å. Diffraction data were collected in the 2θ angle range of 20–70 degrees on a Bruker D8 Advance Diffractometer. Thermogravimetric analysis (TGA) was performed to determine the thermostability of the material. A Shimadzu DTG60 thermogravimetric analyzer with a temperature ramp of 10°C/min in N_2 was used. BET and Langmuir surface areas and total pore volumes of the samples were determined from N_2 adsorption isotherms at 77 K on a Quantachrome Autosorb-1 volumetric gas sorption instrument. The MOF materials were first degassed at 140°C for 3 hours to completely eradicate all solvents and moisture from the pores. Fourier transform infrared (FTIR) spectra (4000–400 cm^{-1}) were obtained from KBr pellets using a Bruker Vector 22 instrument. To confirm the structure and the presence of organic linkers (BTC and GA) in the MOF network, 0.5 mL of dimethyl sulfoxide-d$_6$ (DMSO) (Sigma-Aldrich) was added to 3 mg of MOF material and digested with 40%HCl/60%D_2O (Sigma-Aldrich). The sample was then sonicated until the powder was completely dissolved. ^{1}H NMR spectra were recorded, using Varian-400 MHz (USA), at 25°C in DMSO-d_6 using solvent peaks 2.50 ppm as internal references. The assignment of chemical shifts was relative to a known standard compound.

2.3 Results and Discussion

Pristine Cu-BTC and Cu-GA MOFs

X-ray diffraction (XRD): A detailed characterization of the as-prepared and activated Cu-BTC and Cu-GA metal-organic frameworks are shown in Figure 15. The powder XRD pattern for Cu-BTC shown in Figure 15a is consistent with previously published work (Biemmi et al., 2009; Chowdhury et al., 2009; Schlichte et al., 2004; Tranchemontagne et al., 2008). The material exhibited high crystallinity with intensive peaks appearing in the 2θ range of 5° to 15°, where the most intense peaks were

observed at 2θ values of 5.97,6.88, 9.67, 11.80 and 13.58°. The presence of high intensity XRD peaks within this range is characteristic of microporous MOF materials due to the small pores and cavities of MOF nanostructures. All peaks were indexed to their standard *hkl* values as compared with the previously published work. Figure 15 (b) is the XRD pattern of the as-prepared Cu-GA MOF, which indicates a highly crystalline material with the most intense peak at 10.3°. Despite the presence of a single high intensity peak within the 2θ range of 5° to 15°, Cu-GA has been previously known to exhibit a typical MOF structure (Azhar et al., 2020; Sharma et al., 2019). The broadness of the peaks at 2θ > 25° may indicate the nm-size of the as-prepared Cu-GA, as will be shown in the SEM of these samples.

Single-crystal X-ray diffraction (SC-XRD): The crystal structure of the as-prepared Cu-BTC is cubic with space group Fm-3m, and lattice parameters a = 26.32 Å, and a = 90°. The empirical formula of the structure is $C_{1.5}HCu_{0.25}O_{1.25}$. A detailed description of the crystallographic data of the as-prepared Cu-BTC is given in Table 3. The Cu^{2+} ions are coordinated to the organic ligand BTC in the ratio (Cu:BTC = 1:1). The Cu^{2+} ions adopt a square pyramidal coordination environment, as shown in Figure 16. The BTC linker molecule consists of three carboxylic acid group attached to the benzene ring.
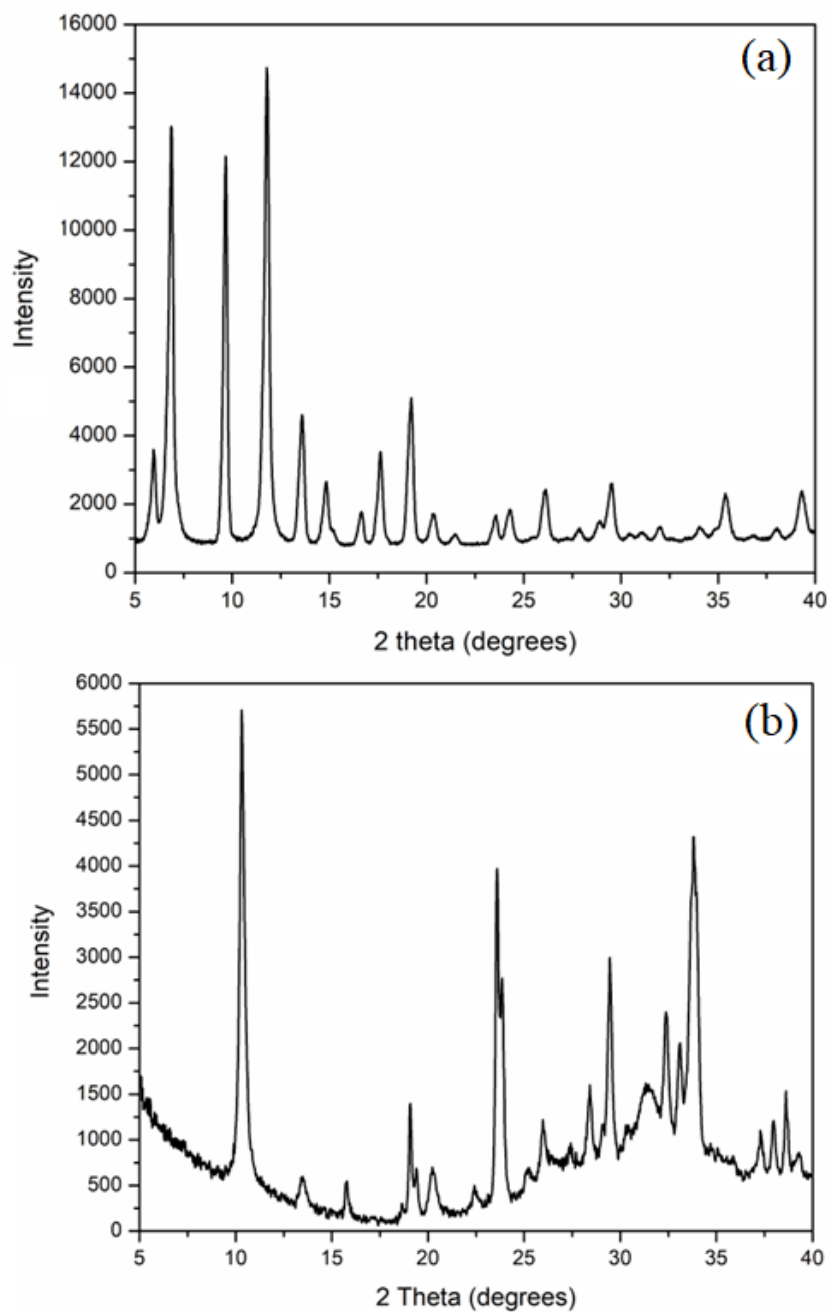
Figure 15: XRD patterns of the as-prepared a) Cu-BTC and b) Cu-GA MOF.

Table 3: Crystal Structure information for the as-synthesized Cu-BTC.

Identification code	exp_327_autoSE-1J
Empirical formula	$C_{1.5}HCu_{0.25}O_{1.25}$
Formula weight	54.91
Temperature/K	297(2)
Crystal system	Cubic
Space group	Fm-3m
a/Å, b/Å, c/Å	26.3223(3)
α/°, β/°, γ/°	90
Volume/Å^3	18237.7(6)
Z	192
ρ_{calc}g/cm^3	0.960
μ/mm^{-1}	1.982
F(000)	5232.0
Crystal size/mm^3	$? \times ? \times ?$
Radiation	CuKα (λ = 1.54184)
2Θ range for data collection/°	6.716 to 154.266
Index ranges	$-33 \leq h \leq 25, -19 \leq k \leq 33, -25 \leq l \leq 21$
Reflections collected	7835
Independent reflections	965 [$R_{int} = 0.0332$, $R_{sigma} = 0.0137$]
Data/restraints/parameters	965/0/38
Goodness-of-fit on F^2	1.343
Final R indexes [I>=2σ (I)]	$R_1 = 0.0966$, $wR_2 = 0.3140$
Final R indexes [all data]	$R_1 = 0.0989$, $wR_2 = 0.3164$
Largest diff. peak/hole / e Å^{-3}	1.39/-0.48
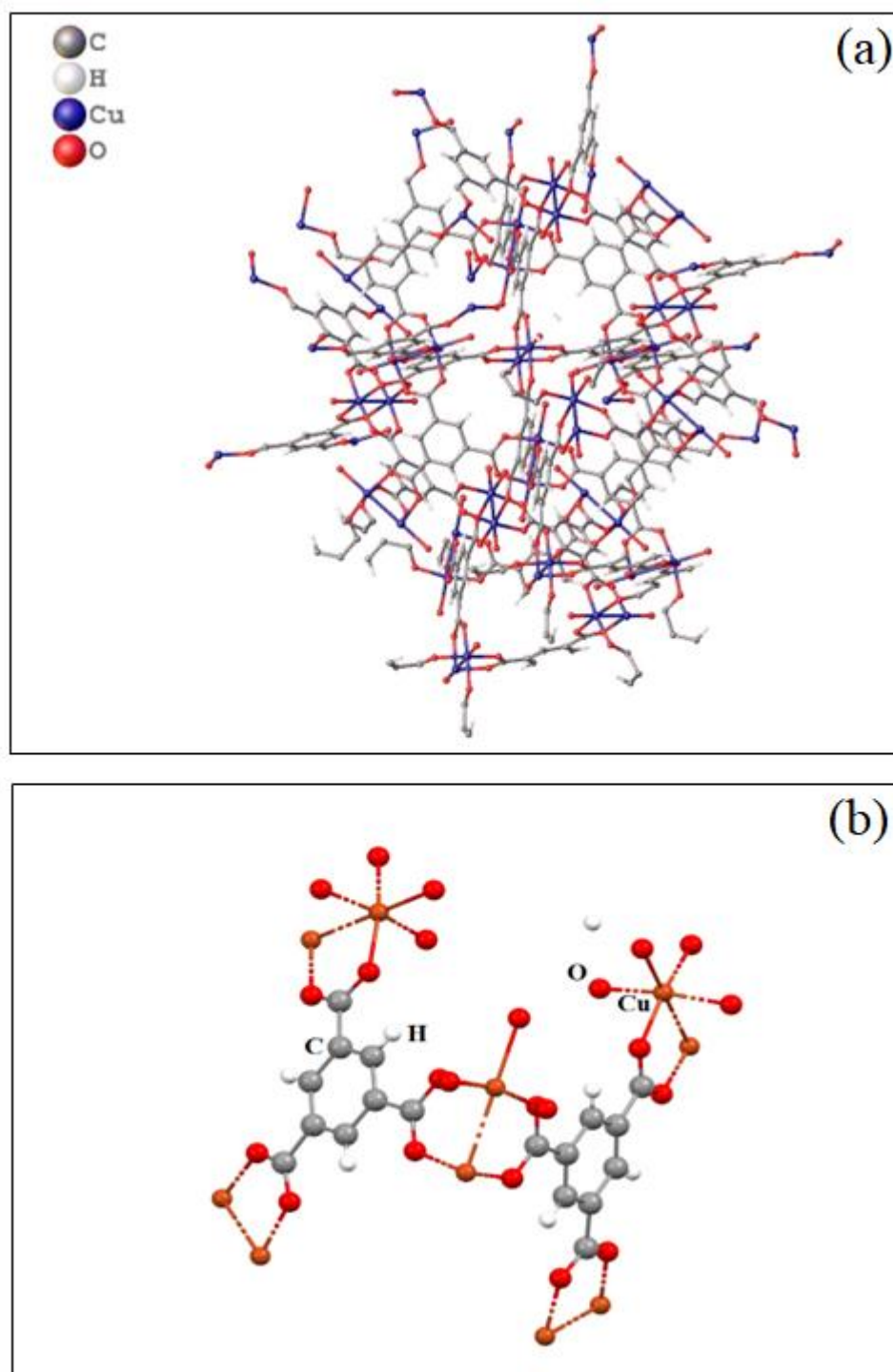
Figure 16: Crystal structure of Cu-BTC. a) 3D structure b) Paddlewheel unit (secondary building unit).

Four carboxylic groups of the ligand are coordinated to the metal dimer, forming a paddlewheel secondary building unit. The BTC linker molecules participate in the stacking of the Cu-BTC coordinated network through a combination of H-bonding and $\pi-\pi$ stacking of the BTC ligand.

Due to the relatively weak crystallinity of the as-prepared Cu-GA, it was difficult to retrieve a single crystal for further single-crystal XRD analysis. This was also confirmed by the absence of the crystallographic data in the literature. Alternatively, a simulated crystallographic arrangement of the Cu-GA MOF structure was proposed by Azhar et al (Azhar et al., 2020), as shown in Figure 17. Each GA linker molecule has one -COOH and three -OH functional groups. The Cu^{2+} clusters are bonded to all GA functional groups, while the GA linker molecules are stacked through H-bonding and $\pi-\pi$ interactions.

Fourier Transfer-Infrared Spectroscopy (FT-IR): The FT-IR spectra of Cu-BTC and Cu-GA are shown in Figure 18. The chemical structures of BTC and GA linkers were also shown in their respective FT-IR spectra. The Cu-BTC FT-IR spectrum shown in Figure 18 (a) exhibits vibrational bands at 1639, 1445 and 1378 cm^{-1} representing the vibrations of the -COOH groups from the BTC linker. The broad band at 3500 cm^{-1} can indicate the presence of physically-adsorbed water and/or -OH groups in the material. The low intensity of this band indicates the complete deprotonation of the BTC carboxylic acid groups, and is thus attributed to the physically adsorbed water molecules. The linkage between Cu^{2+} ions and the BTC carboxylate anions were shown as bands representing the Cu-O group at 752.2 and 515.5 cm^{-1}. The results are in good agreement with other reported data indicating that the Cu-MOF was properly synthesized (Li & Yang, 2008). Figure 18 (b) shows the FT-IR spectrum of the Cu-GA, where bands representing the Cu-COO- bond are

observed at 740.7 and 485.8 cm^{-1}. In addition, the highly hydroxylated GA structure

was also reflected in the high intensity band at 3236.9 cm^{-1} and 1384 cm^{-1}. Other bands

representing the GA linker are also indicated on the spectrum. These results are also

in agreement with the reported FT-IR spectra of Cu-GA (Azhar et al., 2020). The FT-

IR spectra of both Cu-BTC and Cu-GA confirm the formation of Cu-coordinated

structures with both linkers.
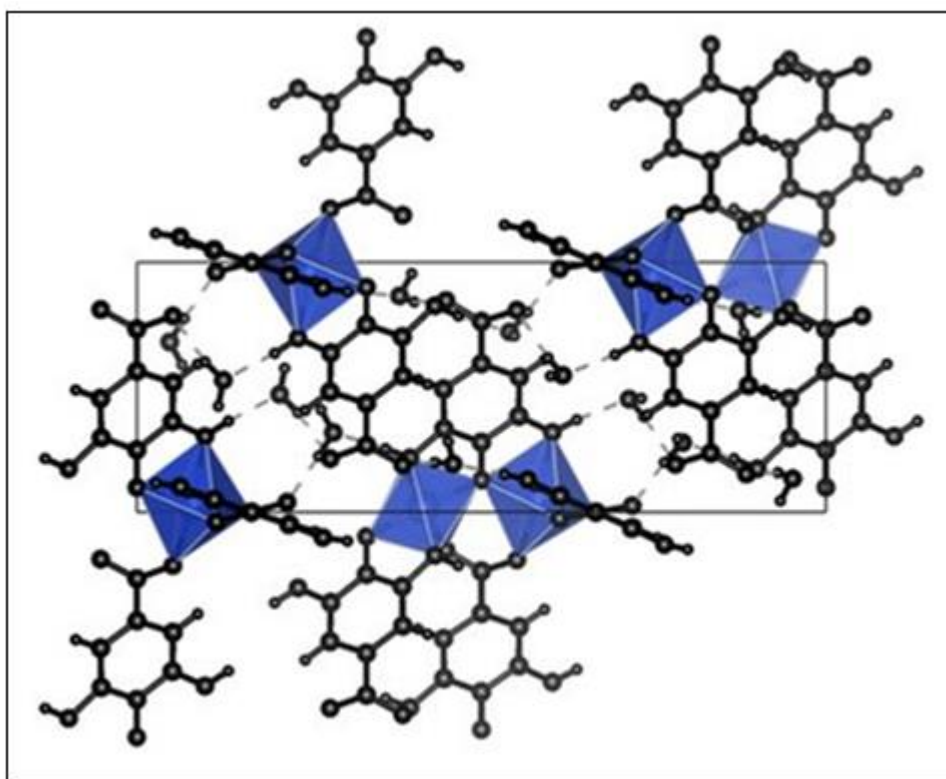
Figure 17: A simulated crystal structure of Cu-GA showing the overall 3D structure
of the MOF. (Azhar et al., 2020).
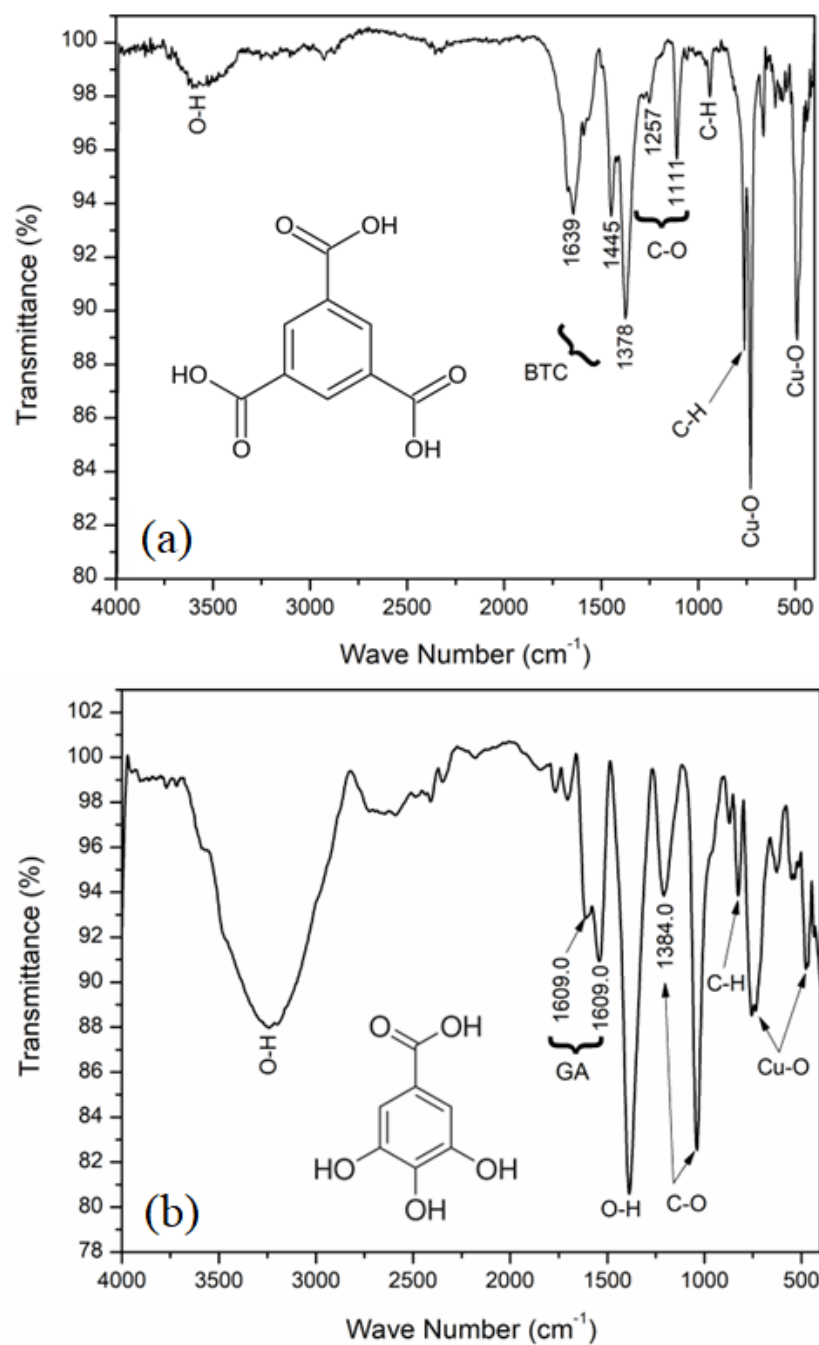
Figure 18: FT-IR spectra of a) Cu-BTC and b) Cu-GA.

Raman Spectroscopy (RS): Figure 19 represents the Raman spectra of Cu-BTC and Cu-GA MOFs. The Raman spectrum of the Cu-BTC in Figure 19 (a) reveals the presence of high intensity sharp peaks at 1007.9 and 1616.6 cm^{-1}, which are attributed to the aromatic C=C group of the GA linker (Nivetha et al., 2020).In addition, doublet peaks at Raman shifts of 748.2, 829 cm^{-1}, and at 1463.3, 1544.4 cm^{-1} are attributed to

the C-H and C=O functional groups, respectively (Nivetha et al., 2020). A low-medium intensity peak was also observed at 501.3 cm^{-1}, which is related to the Cu-O linkage (Nivetha et al., 2020). On the other hand, the Raman spectrum of the as-prepared Cu-GA in Figure 19 (b) shows the presence of bands at 1321.7 and 1391.9 cm^{-1}, 1497.5 and 1593.0 cm^{-1} and 1648.3 and 1675.6 cm^{-1}, which are related to the presence of C-OH, C=O, and C=C functional groups, respectively (Huguenin et al., 2015). Moreover, a peak at 1176.1 cm^{-1} was observed and is attributed to the C-H group (Huguenin et al., 2015). The highest intensity peak at 1321.7 cm^{-1} is correlated to the highly hydroxylated GA structure (Huguenin et al., 2015). It should be mentioned that the presence of a Raman shift due to the absorption of the Cu-O linkage was not observed. In comparison with that observed in the Raman spectrum of the Cu-BTC, this could be related to the presence of a lower proportion of Cu-COO- linkages in the Cu-GA compared to Cu-BTC.

Thermogravimetric Analysis (TGA): The elemental composition of Cu-BTC and Cu-GA was verified by TGA analysis, which records the change in the weight of the sample with increasing temperature under inert atmosphere, as shown in Figure 20. An accurate investigation of the weight loss events was also carried out via the differential TG (DTG). Figure 20 (a) illustrates the presence of multiple weight loss events as a result of the thermal degradation of the Cu-BTC structure. Two main events occurred at 67.3 and 336.1°C, attributing to the evaporation of physically attached water molecules and the thermal degradation of the BTC linker and the consequent evaporation of the organic degradation products (Kar & Srivastava, 2018). The extent of water vapor removal accounts for a weight loss of 13.2%, while the thermal breakdown of the BTC linker accounts for a weight loss of 33.7%. Lower extent weight loss events were also observed throughout the diagram, which can be attributed to the

removal of volatile organic residues. The overall weight loss of the Cu-BTC was estimated to be 66.8%. Inorganic CuO residue was formed in the process and is represented by the plateau continuing after 500°C (Kar & Srivastava, 2018). On the other hand, the TGA-DTG thermograms of the as-prepared Cu-GA in Figure 20 (b) features two major weight loss events at 225.7 and 309.9°C. These are attributed to the dihydroxylation of the GA linker and the breakdown of the GA remaining aromatic structure, respectively (Dorniani et al., 2012).In addition, two minor events can be seen at 67.5 and 195.4°C, which are related to the evaporation of the physically and chemically attached water molecules, respectively (Dorniani et al., 2012). A slowed-down thermal degradation of the Cu-GA structure was observed after 400°C without reaching a plateau, which could be attributed to the successive formation of the inorganic CuO residue.
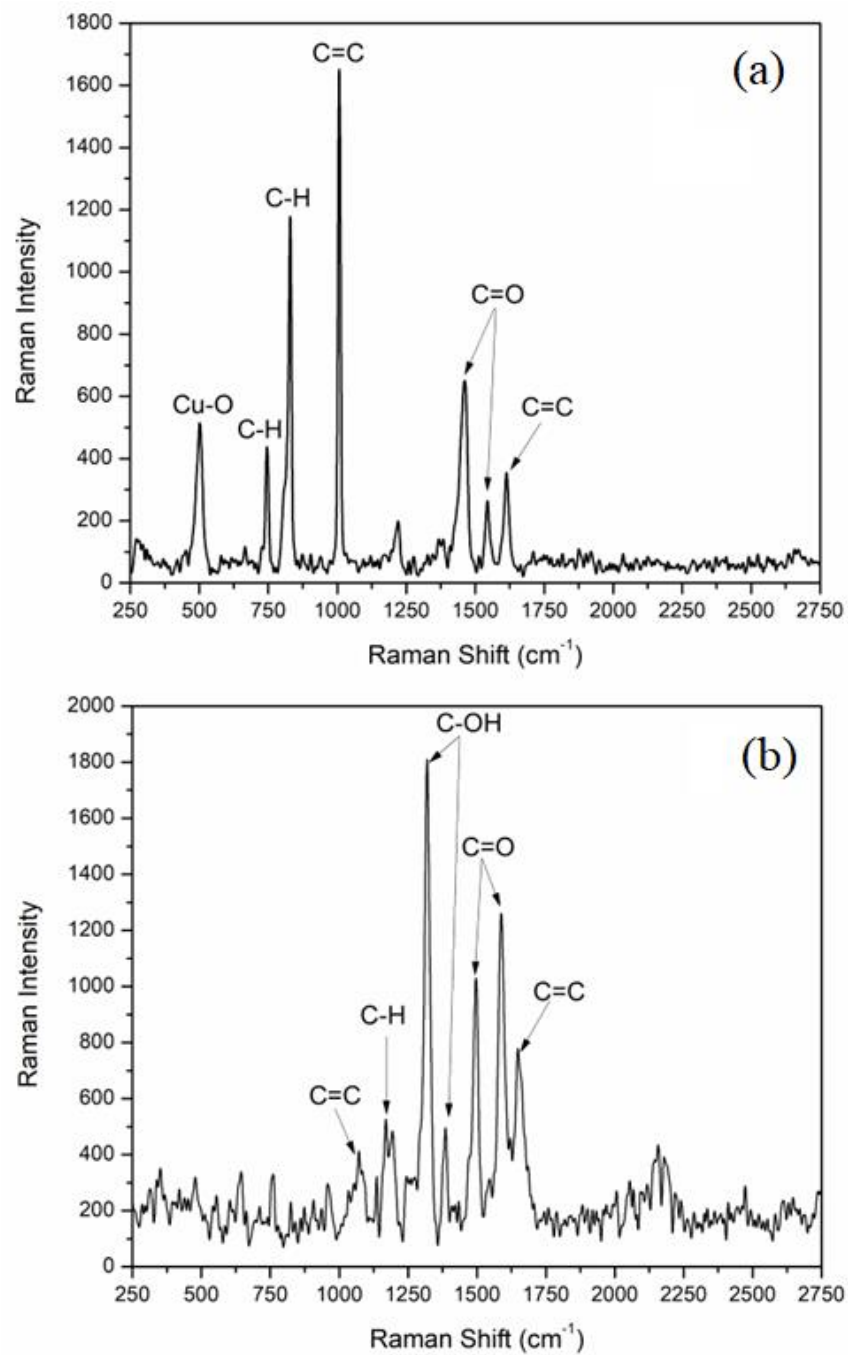
Figure 19: Raman spectra of a) Cu-BTC and b) Cu-GA.
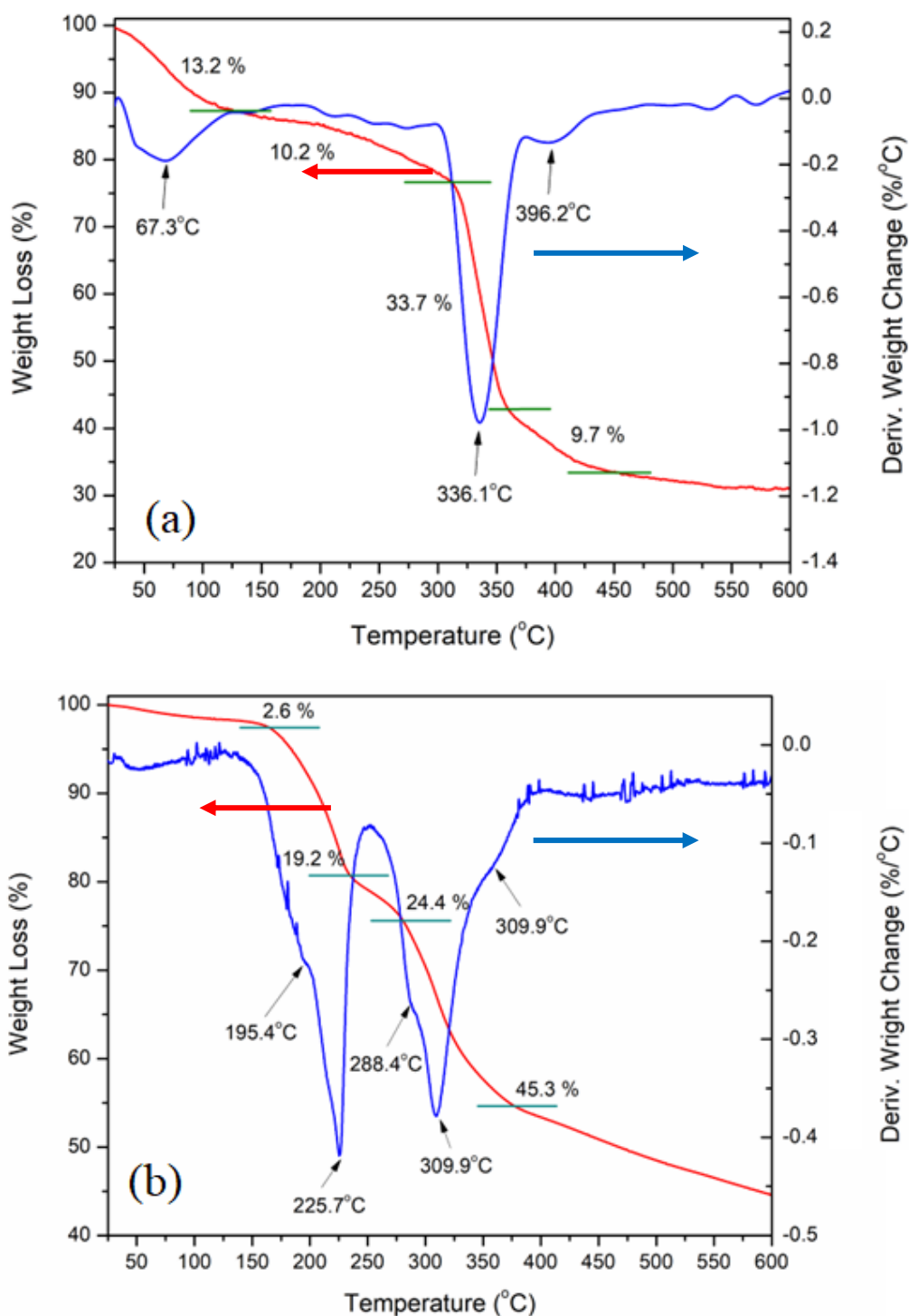
Figure 20: TGA and DTG thermograms of a) Cu-BTC and b) Cu-GA.

[1]H Nuclear Magnetic Resonance Spectroscopy (^{1}H NMR): Figure 21 shows the ^{1}H NMR spectra of the as-prepared Cu-BTC and Cu-GA MOF structures, along with a comparison to the ^{1}H NMR spectra of pure BTC and GA linkers. The pure BTC

linker was shown as a singlet at 8.63 ppm, while BTC in the Cu-BTC was observed at 8.55 ppm, Figure 21 (a). This peak is attributed to the phenyl proton of the BTC molecule. Pure GA was observed at 6.9 ppm, while GA in the Cu-GA MOF was observed at 6.86 ppm, as shown in Figure 21 (b). The presence of the peak is attributed to the phenyl proton of the GA linker. The slight shifts could be due to the presence of both linkers in the form of coordinated linkages with the Cu^{2+} ions in both structures. These findings confirm the presence of both linkers in the structure of the as-prepared Cu-BTC and Cu-GA MOFs.
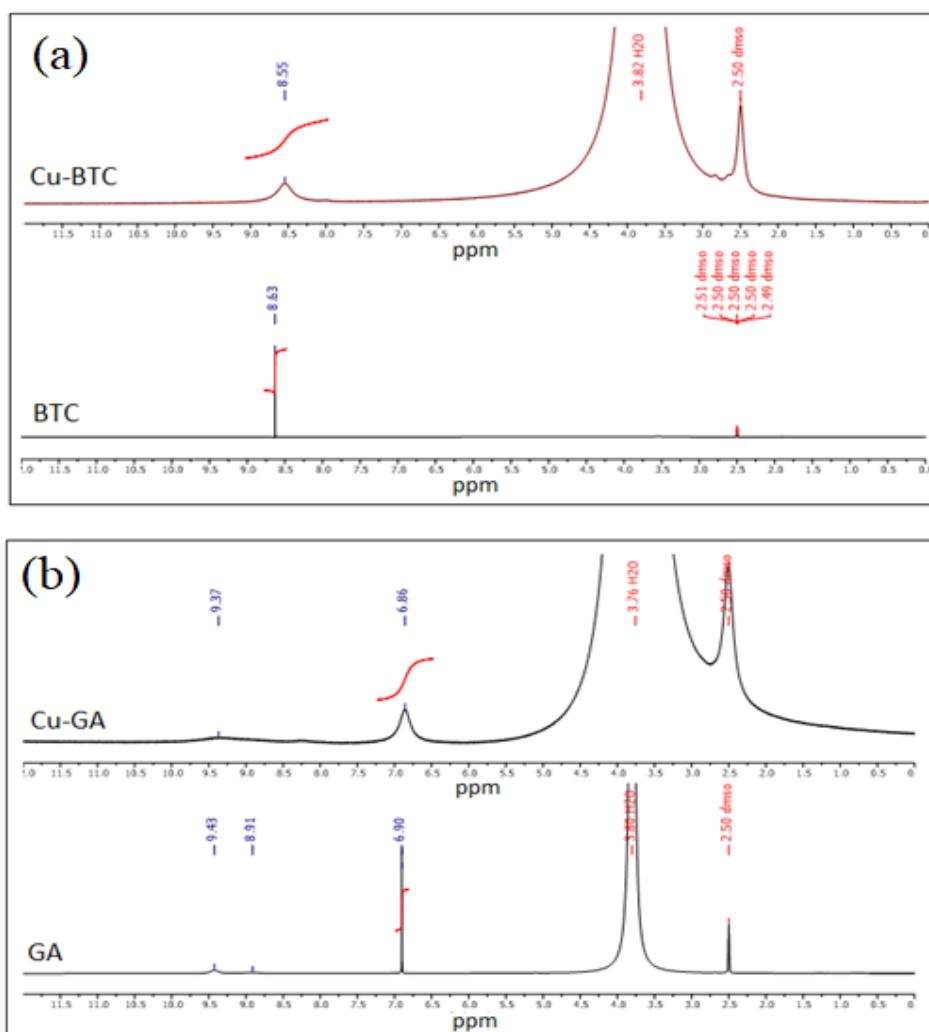
Figure 21: ¹H-NMR spectra of a) Cu-BTC and b) Cu-GA. Each MOF was prepared in 0.5 mL of DMSO + 40% HCl + 60% D_2O. All spectra were referenced to a DMSO signal at 2.50 ppm.

Scanning Electron Microscopy-Energy Dispersive X-ray Spectroscopy (SEM-EDX): The high crystallinity of the as-prepared and activated Cu-BTC was further observed in the SEM micrographs of the powder, as shown in Figure 22 (a). Cu-BTC exhibits a defect-free octahedral crystal structure with sharply identified edges and an overall unified morphology and size distribution. Elemental analysis of the powder was further examined for its elemental composition, as shown in the EDX pattern in Figure 22 (b). The presence of C, O, and Cu with weight percentages of 16.23, 19.33, and 35.86, respectively was evident. On the other hand, Cu-GA appears as highly

agglomerated 2D flakes with an average size of 1 μm and thickness of < 1 μm, as shown in Figure 23 (a). The nm-scale features of the Cu-GA explains the broadness of the XRD peaks of Cu-GA that was observed in Figure 15 (b). The EDX analysis of Cu-GA nanosized crystallites confirm the presence of C, O, and Cu with weight percentages of 23.39, 27.13, and 45.69, respectively, as shown in Figure 23 (b). The higher proportion of the Cu^{2+} in Cu-BTC compared to Cu-GA is related to the higher extent of bond formation between the Cu^{2+} ions and the three -COOH groups of BTC versus one -COOH group along every GA linker unit.
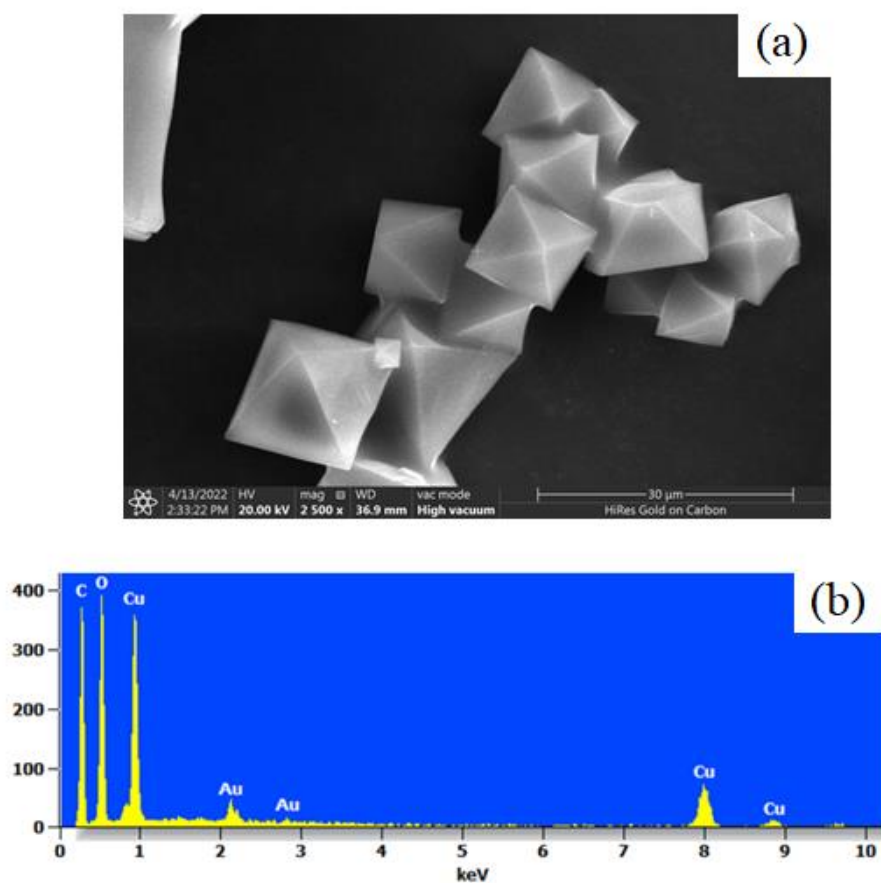
Figure 22: a) SEM micrograph and b) EDX spectrum of Cu-BTC.
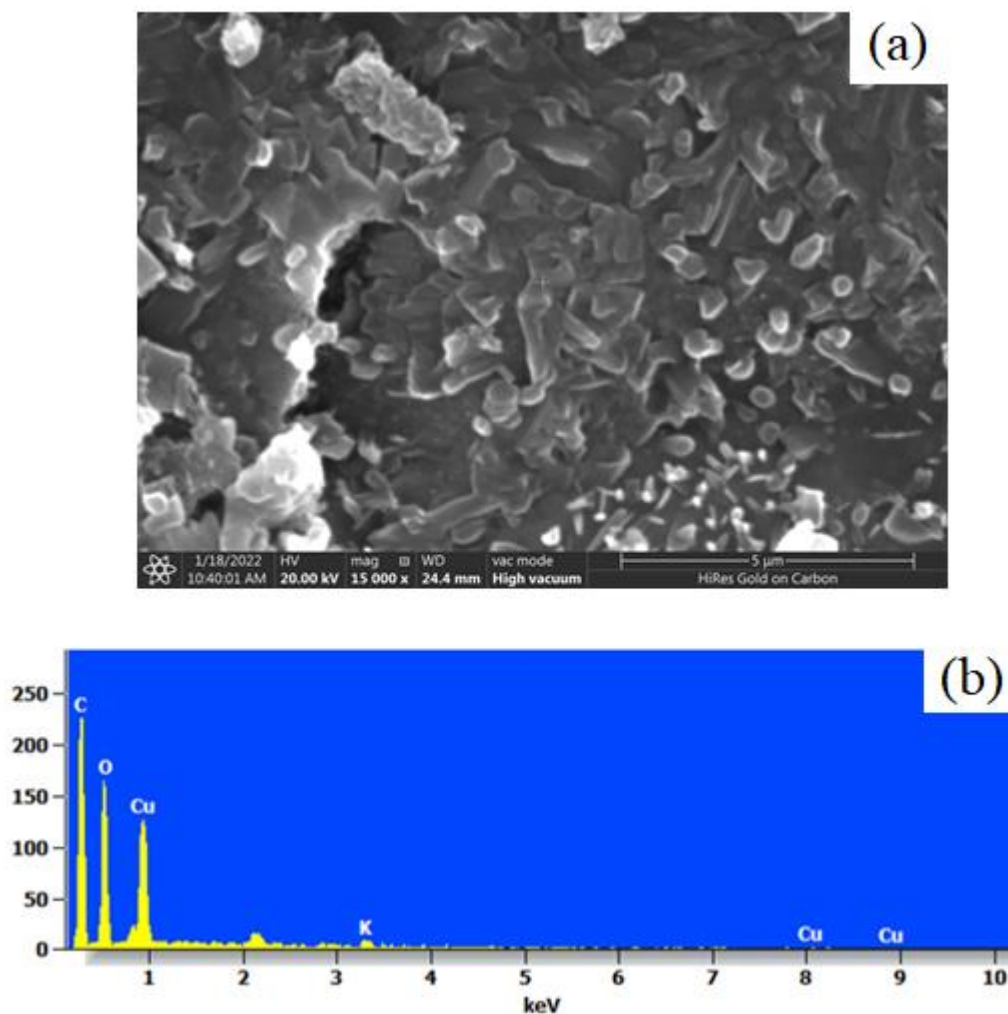
Figure 23: a) SEM micrograph and b) EDX spectrum of Cu-GA.

N_2-adsorption: Figure 24 displays the N_2-adsorption hysteresis and pore size distribution of the as-prepared and activated Cu-BTC. Gas adsorption was carried out to determine the MOFs pore size and surface area. The N_2 adsorption-desorption is type II, indicating the microporous nature of the Cu-BTC structure, as shown in Figure 24 (a). The Langmuir surface area and the Brunauer-Emmett-Teller (BET) surface areas are 1,507 $m^2 g^{-1}$ and 1,268.9 $m^2 g^{-1}$, respectively. The pore volume was 0.54 $cm^3 g^{-1}$ and the pore size and width distribution obtained by Horvath-Kawazoe is about 57.86 Å and 7.6 Å, respectively, as shown in Figure 24 (b). The observed surface area

of the activated Cu-BTC MOF structure is in accordance to the literature, and confirms

its high porosity.
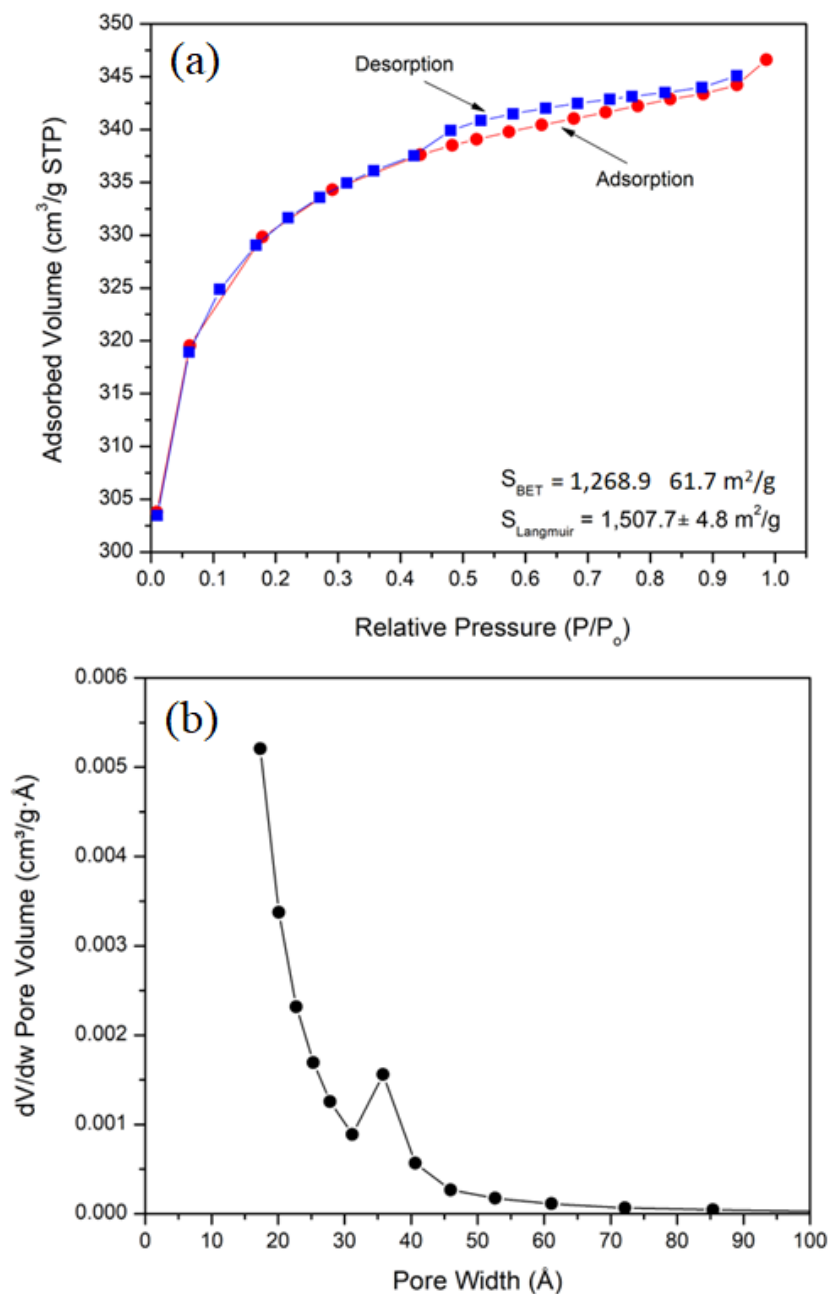
Figure 24: a) N_2-adsorption hysteresis and b) pore size distribution of Cu-BTC.

Due to the highly agglomerated morphology of the Cu-GA flaky particulates,

the MOF displayed weak adsorption of N_2, with a type III isotherm and an average

pore size of 200 Å, as shown in Figure 25. Accordingly, the measured BET and Langmuir surface area values were of 1.41 and $4.23 m^2/g$, respectively.
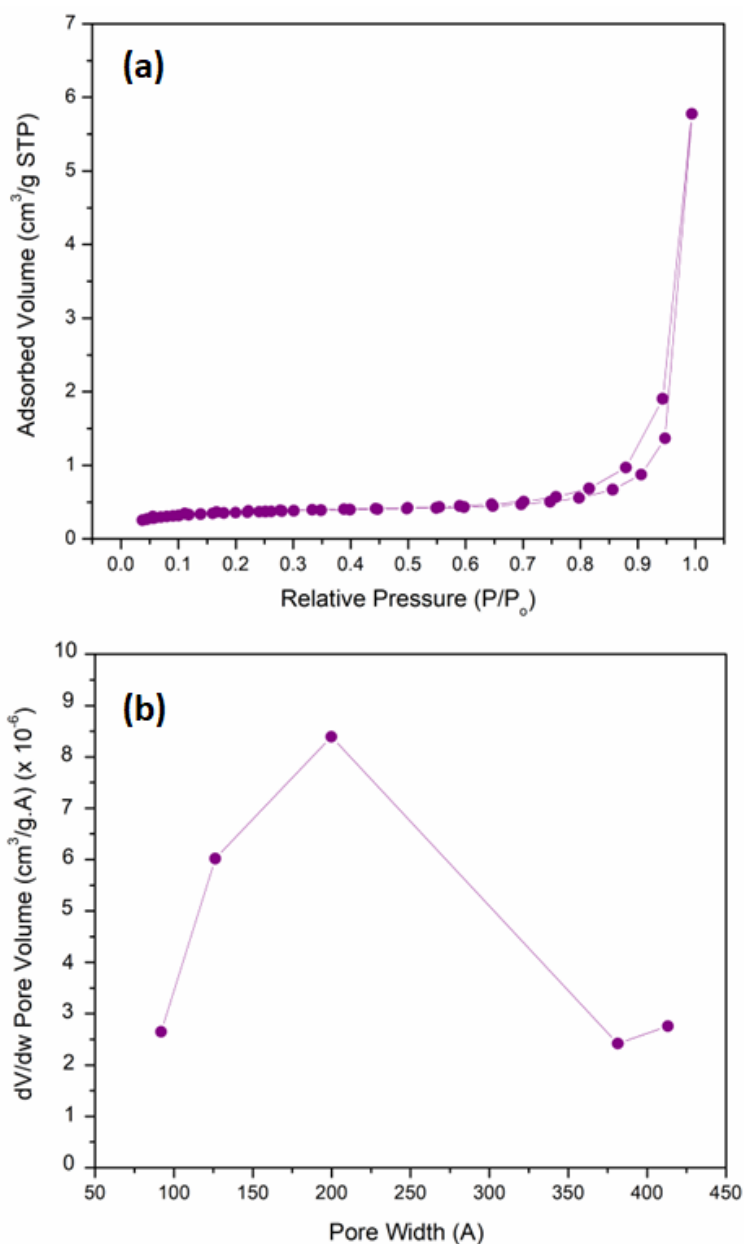
Figure 25: a) N_2-adsorption hysteresis and b) pore size distribution of Cu-GA.

Cu-BTC/GA mixed linker (1:1) and (3:1)

XRD: Figure 26 shows the XRD patterns of the Cu-BTC/GA 1:1 and 3:1 formulations in comparison to Cu-BTC and Cu-GA pristine MOFs. Both Cu-BTC/GA 1:1 and 3:1 formulations reveal the presence of intense peaks at 2θ values below 10°.

Compared with the most intense XRD peaks of pristine MOFs at 9.69, 6.89, and 5.99°
for Cu-BTC and at 10.41° for Cu-GA, the Cu-BTC/GA 1:1 formulation showed an
intense peak at 10.35 and broad low intensity peak at 8.62 with a sharp shoulder at
7.55°. On the other hand, the Cu-BTC/GA 3:1 formulation showed a broad and intense
peak at 9.22° and a sharp medium-intensity shoulder at 7.91°, while the broadness of
the peak at 9.22 shows the possibility of a peak at 9.93°, as indicated on the spectra. A
close similarity of the Cu-BTC/GA 1:1 and 3:1 peaks with those of pristine Cu-BTC
and Cu-GA were observed. The structure and position of the three peaks present in
Cu-BTC/GA 1:1 and 3:1 were previously observed in the work of Yang et al. (Yang
et al., 2015) referring to the presence of Cu-BTC structure. Considering the sole
intense peak of the pristine Cu-GA, the presence of a mixed-MOF structure was
considered a possibility. Therefore, a further investigation of the detailed structure of
the produced Cu-BTC/GA 1:1 and 3:1 was carried out by ^{1}H NMR analysis.
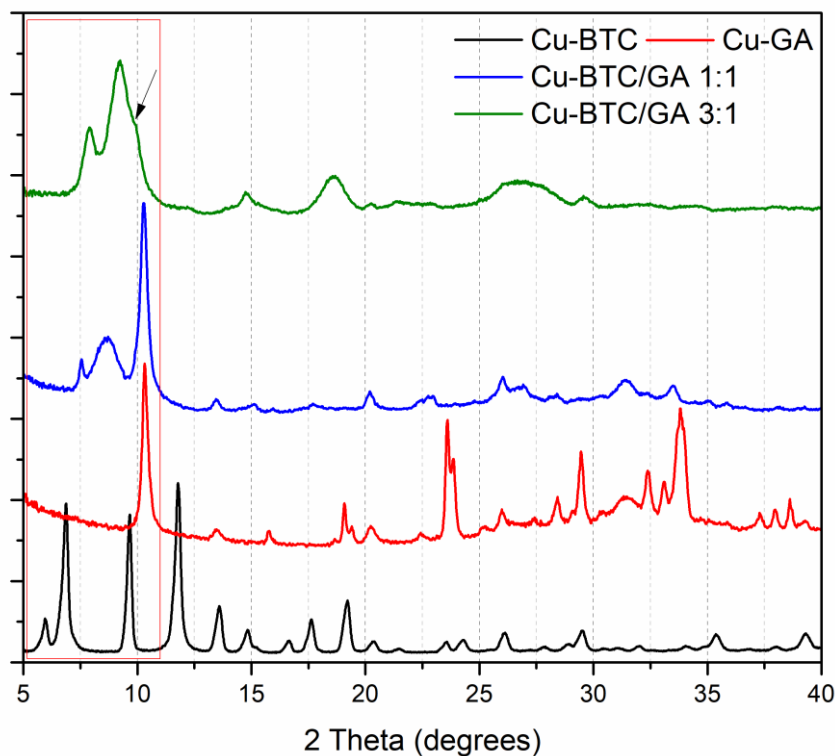
Figure 26: XRD patterns of Cu-BTC/GA 1:1 and 3:1 compared to pristine Cu-BTC and Cu-GA.

^{1}H NMR: The ^{1}H NMR spectra of the Cu-BTC/GA 1:1 and 3:1 formulations are shown in Figure 27. The presence of BTC in the structure of both Cu-BTC/GA 1:1 (Figure 27 (a)) and 3:1 (Figure 27 (b)) was confirmed at 8.6 ppm. However, the presence of a peak at 6.9 ppm, which is characteristic to GA linker, as previously shown in Figure 21 (b), was not present. These findings indicate the absence of GA in the structure of both Cu-BTC/GA 1:1 and 3:1 formulations, and the sole formation of a Cu-BTC hierarchical structure. Accordingly, no contribution of GA to the formation of the produced MOF structures was found. These results indicate the preferential interaction of the BTC linker with the Cu^{2+} ion, with the influence of [BTC] in the initial reaction mixtures, 1:1 and 3:1 were 50% and 75%, respectively. The presence of a higher BTC molecule enforced its sole interaction between the Cu^{2+} ions. It should be mentioned that the pK_a values of the BTC linker are: 3.12, 3.89 and 4.7 which

correspond to the three -COOH groups along the BTC structure. On the other hand, the pK_a values of the GA linker are 4, corresponding to the -COOH group in the GA structure, and 8.7, 11.4 and >13 attributing to the phenolic -OH groups. The relative strength of the BTC-(COOH)$_3$ groups and their higher affinity towards the interaction with the Cu^{2+} ions compared to GA-(COOH) can be presumed. Considering the stoichiometry of the reactions involved, it can be stated that a *non-stoichiometric Cu-BTC* was formed.

SEM: The unique high crystallinity of the pristine Cu-BTC MOF exhibited in the SEM micrograph in Figure 28 (a), was not observed in the SEM micrographs of the Cu-BTC/GA 1:1 and 3:1 samples in Figure 28 (c) and 28 (d), respectively. Moreover, the highly agglomerated 2D flakes of pristine Cu-GA, shown in Figure 28 (b), were also not seen in the proposed 1:1 and 3:1 formulations. Instead, both Cu-BTC/GA 1:1 and 3:1 revealed the presence of crystalline material with elongated 2D morphology. This morphology was previously cited in the work of David et al. (Shooto & Dikio, 2015) as a result of the interaction between Cu^{2+} ions and 1,2,4,5-Tetrabenzenecarboxylic acid (H$_4$TBCA). Therefore, we hypothesize that the Cu-BTC with the same elongated 2D morphology is attributed to the formation of a non-stoichiometric Cu-BTC and is related to the presence of a lower [BTC] than required for the formation of the stoichiometric Cu-BTC with the known octahedral morphology.

FT-IR: The FT-IR spectra of the Cu-BTC/GA 1:1 and 3:1 are shown in Figure 29 with pristine Cu-BTC and Cu-GA for comparison. The spectra can be divided in 5 parts. Part I shows a sharp band at 726 cm^{-1}, which is attributed to the Cu-O absorption in the pristine Cu-BTC spectrum. This band was shifted to 736 and 730 cm^{-1} in the spectra of the Cu-BTC/GA 1:1 and 3:1, respectively.
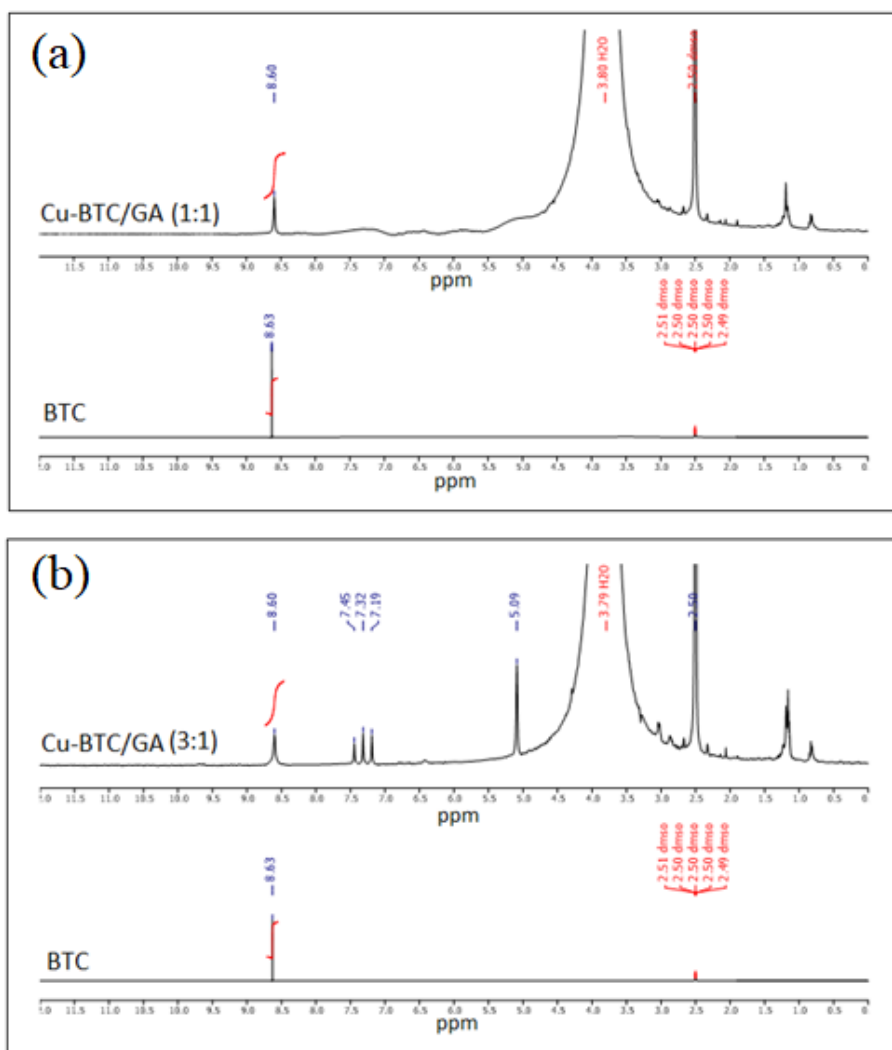
Figure 27: ^{1}H-NMR spectra of a) Cu-BTC/GA 1:1 and b) Cu-BTC/GA 3:1. Each sample was prepared in 0.5 ml of DMSO + 40% HCl + 60% D$_2$O. The ^{1}H spectra of standard BTC and GA linkers are also shown in both graphs. All spectra were referenced to a DMSO signal at 2.50 ppm.
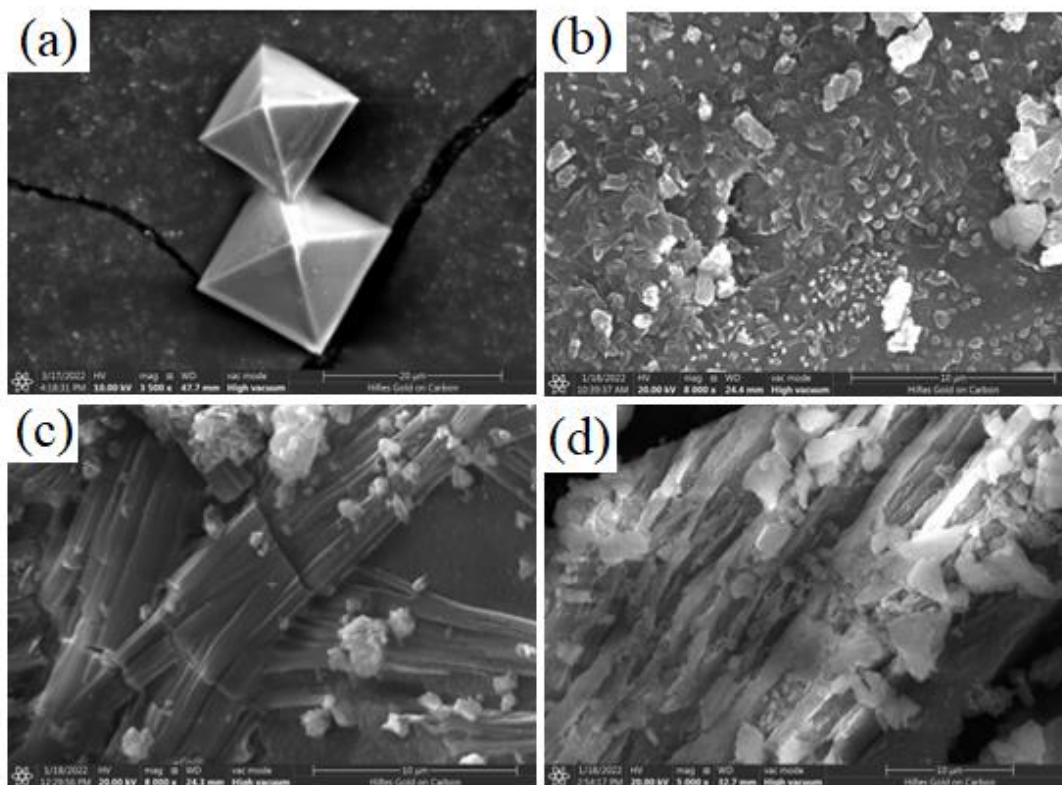
Figure 28: SEM micrographs of a) pristine Cu-BTC b) pristine Cu-GA c) Cu-BTC/GA 1:1 and d) Cu-BTC/GA 3:1.

Part II shows a medium intensity band at 1106.6 cm^{-1} in the spectrum of pristine Cu-BTC, which correlates to the C-O functional group. This band was shifted to 1040 and 1069 cm^{-1} in the spectra of the Cu-BTC/GA 1:1 and 3:1, respectively. Parts III and IV show bands at 1378 and 1645 cm^{-1}, which are characteristic to the BTC-COOH, namely the C=O and C-O functional groups, respectively, of the pristine Cu-BTC. These bands were shifted to 1389, 1695 cm^{-1} and 1377 and 1689 cm^{-1} in the spectra of the mixed formulations. In part V, the low intensity broad band at 3547 cm^{-1}, which is characteristic to the absorption of the -OH group in the pristine BTC, was observed at 3468 and 3480 cm^{-1} in the spectra of the Cu-BTC/GA 1:1 and 3:1, respectively. A careful study of these bands with those in the spectrum of Cu-GA, indicates the sole formation of Cu-BTC structures, while the shift in the Cu-BTC bands

could be attributed to the formation of the non-stoichiometric 2D Cu-BTC structures in both Cu-BTC/GA 1:1 and 3:1 formulations.
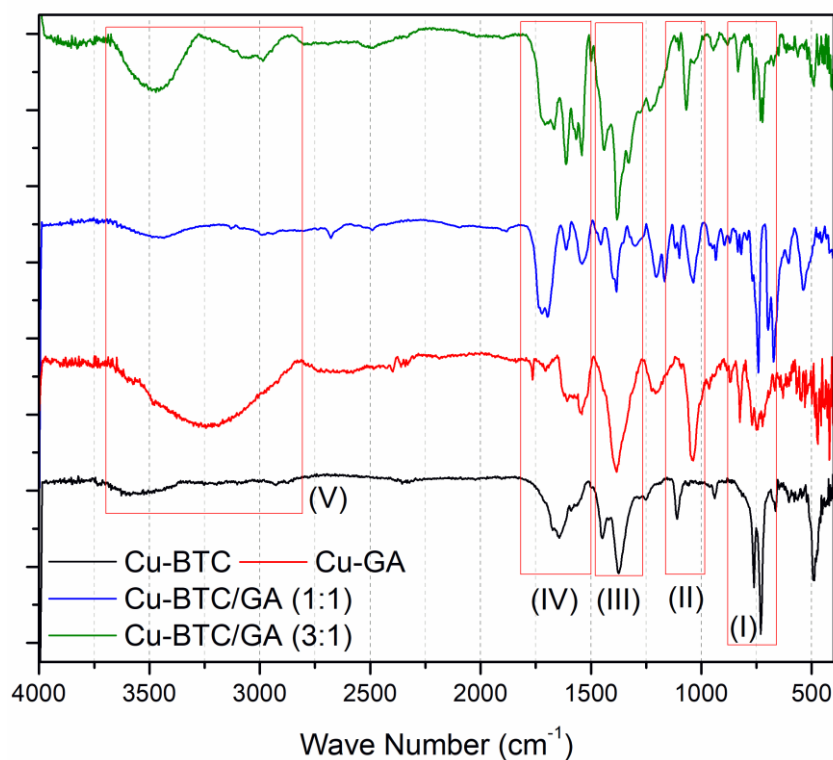
Figure 29: FT-IR spectra of Cu-BTC/GA 1:1 and 3:1 compared to pristine Cu-BTC and Cu-GA.

TGA: The thermal characteristics of the Cu-BTC/GA 1:1 and 3:1 are compared with those of pristine Cu-BTC and Cu-GA, as shown in Figures 30 and 31. Compared with overall weight loss values of 76.2 and 55.4% for pristine Cu-BTC and Cu-GA, respectively, Cu-BTC/GA 1:1 and 3:1 formulations showed weight loss values of 65.8 and 68.5%, as shown in Figure 30 (b). The detailed thermal events are represented in Figure 31 as related to their respective thermograms in Figure 30 (a). A detailed analysis of the thermal events of the Cu-BTC/GA 1:1 and 3:1 formulations as well as the pristine Cu-BTC and Cu-GA MOFs are shown in Table 4.
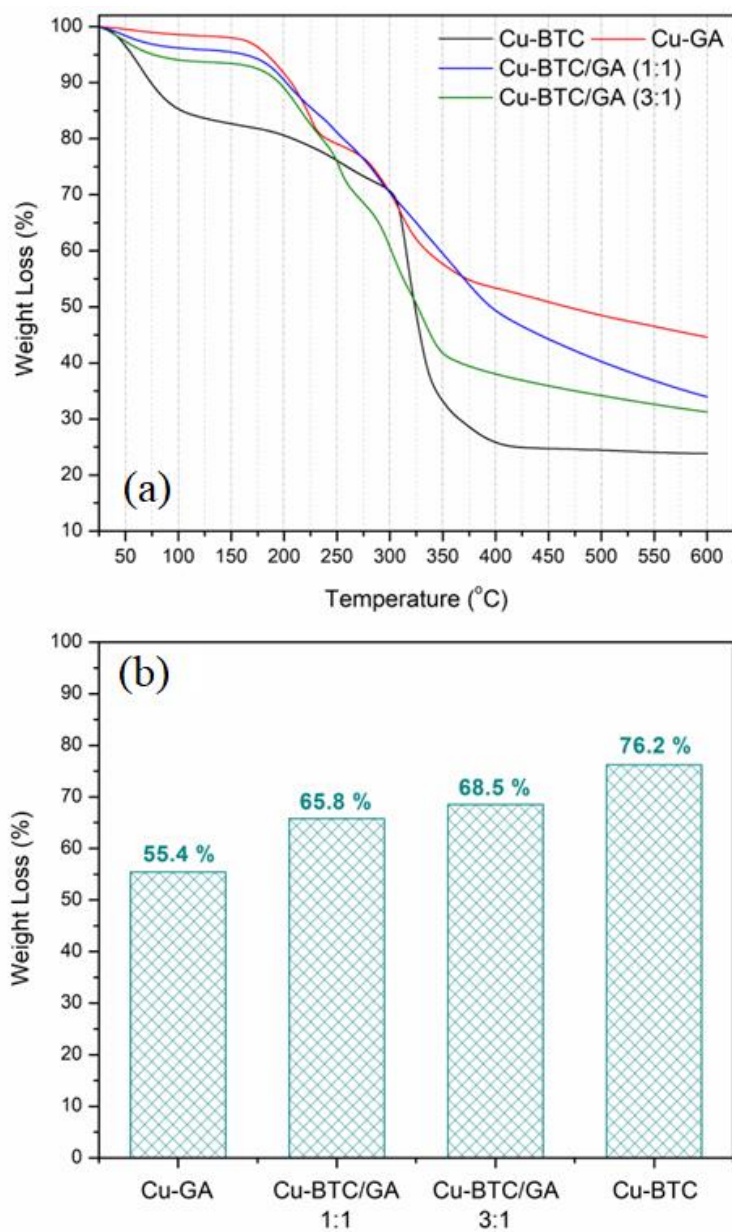
Figure 30: a) TGA thermograms of Cu-BTC/GA 1:1 and 3:1 as well as pristine Cu-BTC and Cu-GA and b) A summary of their overall weight loss values.
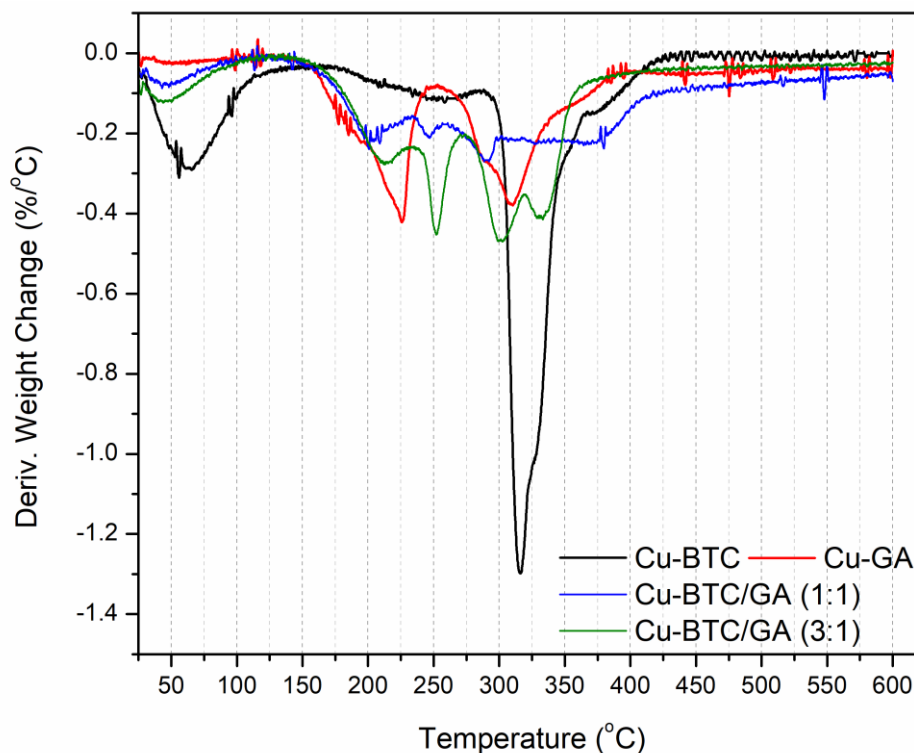
Figure 31: DTG analysis of the TGA thermograms of Cu-BTC/GA 1:1 and 3:1 compared to pristine Cu-BTC and Cu-GA.

Table 4: Thermal events depicted from the TGA thermograms of the Cu-BTC/GA 1:1 and 3:1, Cu-BTC and Cu-GA MOFs.

Cu-BTC (°C)	Cu-GA (°C)	Cu-BTC/GA 1:1 (°C)	Cu-BTC/GA 3:1 (°C)
67.3	226.3	46.3	45.7
336.1	309.8	202.1	213.2
		246.2	252.1
		289.9	301.9
		365.9	331.8

Thermal events were observed for each of the pristine MOF structures at 67.3 and 309.9°C for Cu-BTC and 226.3 and 309.8°C for Cu-GA. As previously explained, these events are related to the evaporation of physically and chemically attached water molecules and the breakdown BTC and GA molecules. Cu-BTC/GA 1:1 and 3:1 formulations showed multiple thermal events at variable temperatures, as shown in

Table 4. These thermal events could be attributed to the presence of the 2D non-stoichiometric Cu-BTC structures with variable extents of coordination between the Cu^{2+} ions and the BTC linker molecules, hence the previous findings are confirmed.

Cu-BTC/GA mixed linker (1:3)

XRD: Figure 32 shows XRD pattern of the Cu-BTC/GA 1:3 formulation compared with patterns of pristine Cu-BTC and Cu-GA. A close resemblance with the pattern of GA was observed, where the main XRD peak at 2θ value of 10.3° was observed. Other low intensity peaks were also displayed, matching closely to those of pure Cu-GA. None of the peaks observed in the XRD pattern of the Cu-BTC/GA 1:3 formulation match those in the XRD pattern of the pristine Cu-BTC. These results indicate the preferential interaction between the Cu^{2+} ions and the GA linker molecules, which are present in a higher concentration (75%) in the formulation. No signs for a possible interaction between the Cu^{2+} ions and the BTC molecules were found. The broadness of the XRD peaks of the Cu-BTC/GA 1:3 pattern could be related to the low crystallinity of the formed Cu-GA-like structure, as will be demonstrated in the next sections.
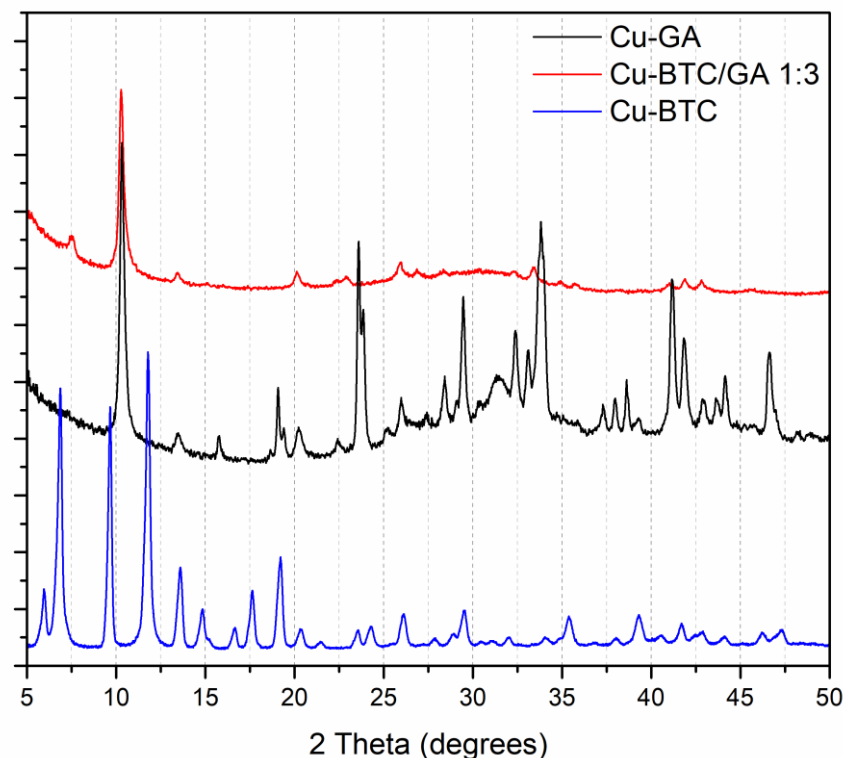
Figure 32: XRD patterns of Cu-BTC/GA 1:3 and pristine Cu-BTC and Cu-GA MOFs.

SEM: The morphology of the Cu-GA-like structure formed as a result of the interaction between the Cu^{2+} ions and the dominating GA in the BTC:GA (1:3) formulation, is shown in Figure 33. Agglomerates of 2D flaky crystallites can be seen in the SEM micrograph of the Cu-BTC/GA 1:3 formulation. These results confirm the formation of Cu-GA-like structure and the absence of signs of other morphologies that could be related to the interaction between Cu^{2+} ions and the BTC linker.

FT-IR: Figure 34 reveals the IR spectrum of the Cu-BTC/GA 1:3 in comparison with those of the pristine Cu-BTC and Cu-GA structures. A close match between the bands of the Cu-BTC/GA 1:3 and their respective counterparts in the spectrum of the Cu-GA was observed, as outlined in part I of the spectrum. On the other hand, a resolution of the broad band at 3247 cm^{-1}, which is attributed to the -OH absorption in the Cu-GA was observed in the spectrum of the Cu-BTC/GA 1:3

formulation. Two lower intensity bands were observed at 3443.5 and 3106.2 cm^{-1}, which could be contributed to the absorption of the GA phenolic -OH groups and the presence of physically adsorbed water molecules, respectively. These results, therefore confirm the formation of Cu-GA-like structure as a result of the reaction between Cu^{2+} ions and the GA-dominant Cu-BTC/GA 1:3 formulation.
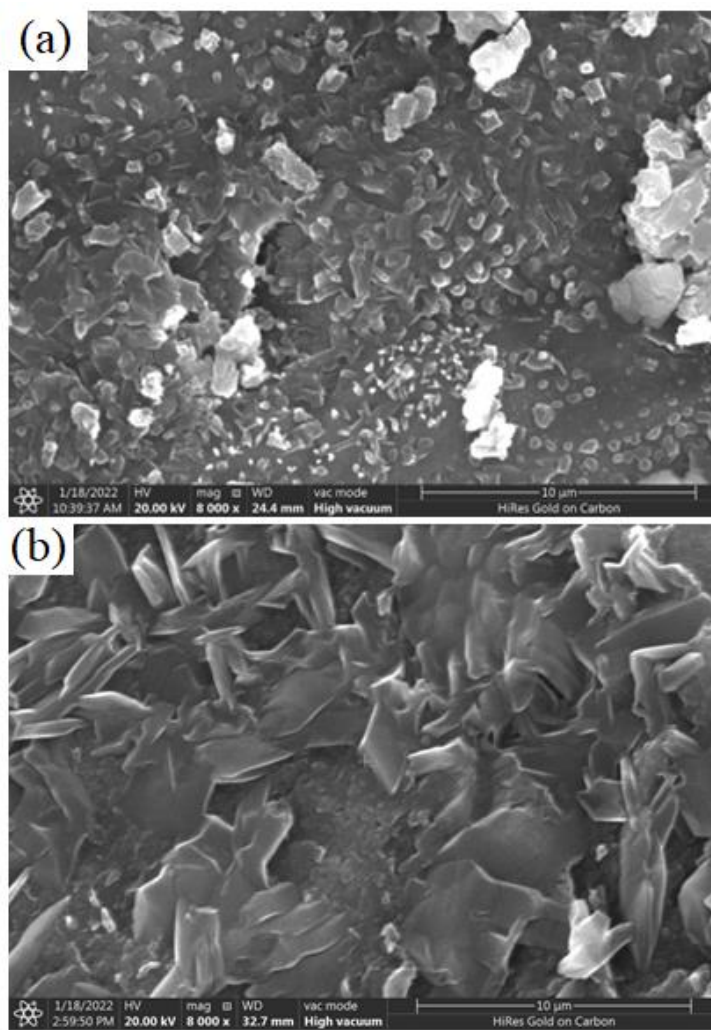
Figure 33: SEM micrographs of a) pristine Cu-GA and b) Cu-BTC/GA 1:3.
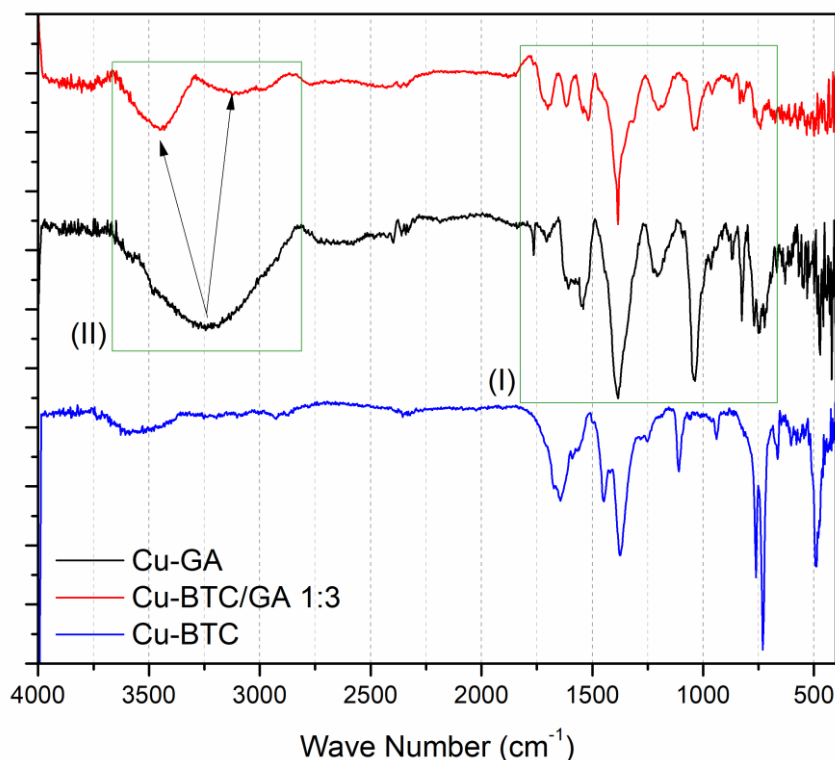
Figure 34: FT-IR spectra of Cu-BTC/GA 1:3, pristine Cu-BTC and Cu-GA.

TGA: The as-prepared Cu-BTC/GA 1:3 formulation showed an overall thermal history similar to that of the Cu-GA MOF as shown in the TGA thermograms of these samples in Figure 35 (a). The overall weight loss of the Cu-GA-like structure was found to be 59.6%, which is comparable to that of the Cu-GA which amounted for 55.3%. This slight difference is attributed to the lower proportion of GA in the Cu-BTC/GA 1:3 formulation than that of pristine Cu-GA. A detailed description of the slight differences between the thermograms of the Cu-BTC/GA 1:3 formulation and Cu-GA is shown in Figure 35 (b). In part I of the diagram, an initial event was observed at 40.1°C in the thermogram of Cu-GA but was not present in the thermogram of the Cu-GA-like sample. This difference could be attributed to the lower extent of physically-adsorbed water molecules evaporation. In part II of the diagram, the 2 events at 225.1 and 191.4°C in the thermogram of Cu-GA were unified in a single event at 217.9°C in the thermogram of the Cu-GA-like sample. On the other hand, the

two thermal events at 285.4 and 309.9°C in the thermogram of the pristine Cu-GA were shifted to 264.9 and 315.1°C in the thermogram of the Cu-GA-like sample. These slight variations could be attributed to the difference in the proportion of GA in the Cu-GA-like structure and the morphology of its crystallites.
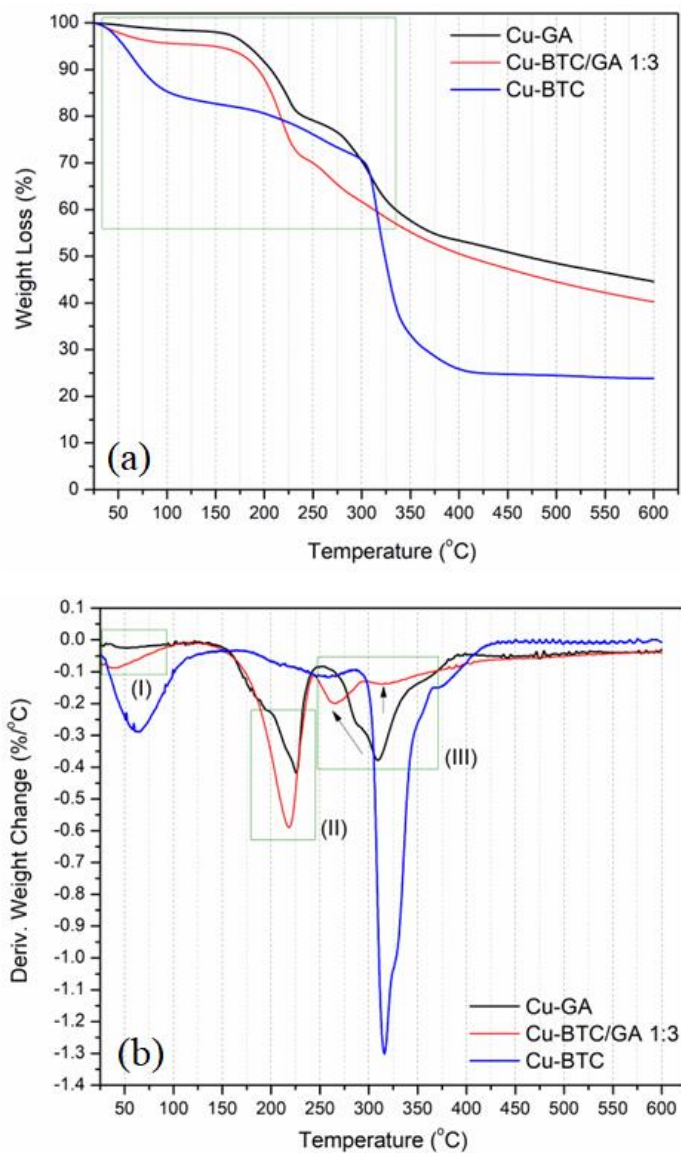
Figure 35: a) TGA thermograms and b) DTG analysis of Cu-BTC/GA 1:3, pristine Cu-BTC and Cu-GA.

2.4 Conclusion

The synthesis of two copper-based MOFs were successfully carried out with Cu^{2+} as the metal node along with a) 1,3,5-benzene tricarboxylic acid and b) gallic acid for the organic ligands. Both Cu-based MOFs were characterized using PXRD, SEM-

EDX, FT-IR spectroscopy, Raman Spectroscopy, TGA-DTG, SXRD (Cu-BTC only), ^{1}H NMR digestion and N_2 sorption. A mixed-linker MOF that contains both BTC and GA was attempted, however, the presence of both linkers was not achievable in this work. It was observed that BTC has a higher affinity to the interaction with Cu^{2+} ions, especially when its proportion was 50 and 75% where BTC dominated the Cu-BTC/GA composition. This can be attributed to the relatively higher acidic strength of the BTC as compared with that of GA considering the differences between their pK_a values. On the other hand, increasing the proportion of GA to 75% was reflected on the formation of Cu-GA-like crystallites where no signs of an interaction between the minor linker (BTC; 25%) with Cu^{2+} ions were found.

Chapter 3: Post-synthesis Modification and Encapsulation of Cu-BTC with Gallic Acid

3.1 Introduction

Cu-BTC is a microporous structure owing to its very high surface area. This feature allows for the incorporation of small guest molecules and can be challenging when introducing larger molecular entities (Cavka et al., 2008). Therefore, the ability to create mesopores with a larger pore volume is advantageous all while maintaining the overall integrity of the structure. This can be achieved by etching or hollowing out the MOF, leading to a hierarchical structure, containing both micro- and mesopores. Most recently, Ai et al. fabricated a hierarchical porous UiO-66-NH$_2$ MOF using benzoic acid as the modulator, shown in Figure 36 (Ai et al., 2022).
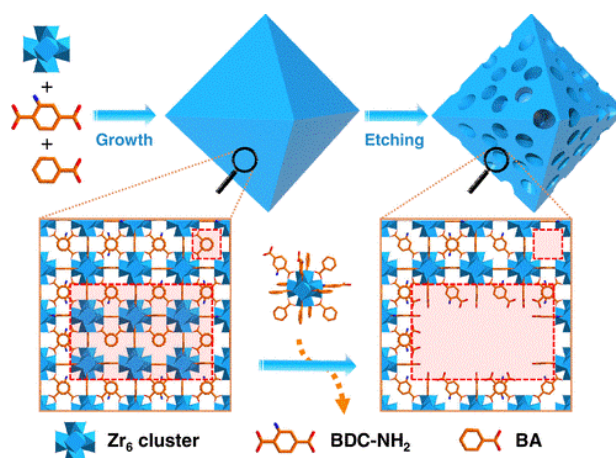
Figure 36: Synthesis of hierarchical UiO-66 MOF with benzoic acid as the modulator. (Ai et al., 2022).

Having both micro- and mesopores within a MOF structure will allow combined advantages such as high surface area and the facilitation of mass transfer process (Bueken et al., 2017; Koo et al., 2017; Küsgens et al., 2010; Lian et al., 2016; Lohe et al., 2009). Hierarchical MOF structures have also been shown to improve

catalytic processes and to host larger guest molecules (Ai et al.; Li et al., 2016; Shi et al., 2020), which is crucial for most biological applications. In this research, we use GA, a weak acid, as the etching agent, creating a hierarchical Cu-BTC structure while simultaneously encapsulating GA. This work is carried out to create an enhanced surface and bulk porosity of Cu-BTC for the intended use in future drug delivery applications. Having gallic acid encapsulated within the newly constructed pores can allow for a synergistic anti-cancer and anti-bacterial treatment. Cu-BTC was treated under mild conditions with varying concentrations of aqueous gallic acid solutions and harsher parameters with gallic acid in DMF. The effect of varying the treatment conditions; low temperature and hydrothermal, as well as the concentration of the on the structure and morphology of the produced Cu-BTC structures will be explained in detail. Finally, single x-ray diffraction (SXRD) crystallography results confirm that the overall structural integrity of the MOF was not compromised during the etching process.

3.2 Materials and Methods

Cu-BTC etching with Gallic Acid (aqueous): 50 mg of Cu-BTC was suspended in 15 mL of GA aqueous solution with various concentrations (5 mg/L, 10 mg/L, 20 mg/L, 40 mg/L, 50 mg/L, 120 mg/L, and 200 mg/L). The entire mixture was placed at room temperature in a shaker (Benchmark Incu-Shaker 10L) for 30 min at 300 rpm. The sample was then centrifuged and washed with water. The powder was left to completely dry at room temperature before continuing with characterization of the product.

Cu-BTC etching with gallic acid (0.01M, 0.05M and 0.1M): Samples were prepared by dissolving the appropriate amount of gallic acid in 5 mL of DMF and adding 200 mg of HKUST-1 (previously prepared) to the gallic acid solution. The

entire mixture was added to a sealed Teflon lined autoclave reactor and placed in the oven for 12h at 120°C. The sample solvent was washed and replaced with fresh hot DMF until the solvent appeared to be clear (~4 washes). DMF was exchanged with DCM 3 times daily for 2 days and then the sample was filtered. The final product was completely evacuated from all solvents under vacuum at 130°C for 24h. Characterization and copper leaching were carried out following the same methodology in Chapter 2.

3.3 Results and Discussion

Cu-BTC low temperature treatment with Gallic Acid

SEM-EDX: Variations in the Cu-BTC morphology after treatment with GA can be seen in Figure 37. A gradual increase in the surface roughness of the Cu-BTC was observed with increasing the concentration of GA. Moreover, a breakdown of the Cu-BTC crystal surface was evident at high concentration of GA, as shown in Figure 37 (g). A higher magnification was carried out to further study the surface morphological changes, as shown in Figure 38. A consistent increase in the roughness of Cu-BTC crystal surfaces was observed with increasing [GA], evident up to 50 mg/L. Upon increasing the concentration of GA to 120 and 200 mg/L, a deeper modification of the surface was observed. The surface roughness developed a surface porosity with extended bulk porosity, as shown in Figure 38 (f). In addition, surface cracks were also observed. The elemental composition of the GA-treated Cu-BTC samples is illustrated in the EDX graphs (Figure 39). All EDX spectra exhibit the presence of Cu-BTC elements (C, O, and Cu) with minimal variation in their concentrations. These results indicate that the observed variation in the morphology of the Cu-BTC crystals are more concentrated on their surfaces.
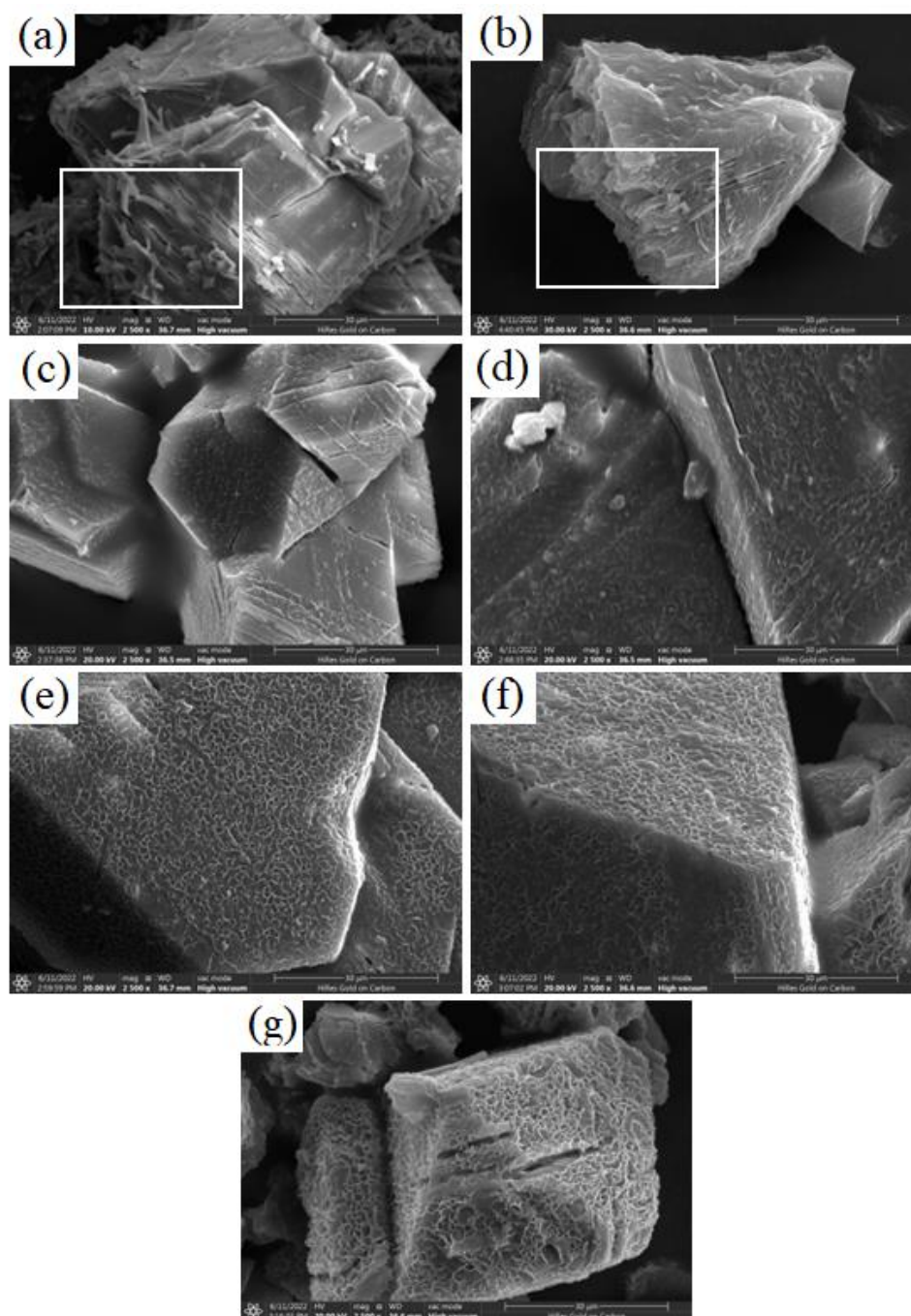
Figure 37: SEM micrographs of Cu-BTC particulates treated with a) 5 b) 10 c) 20 d) 40 e) 50 f) 120 and g) 200 mg/L GA aqueous solutions at room temperature for 30 minutes.

XRD: The generation of mesopores in the hierarchical structure of Cu-BTC does not significantly affect its inherent micropores. The XRD patterns of the GA-treated Cu-BTC samples are shown in Figure 40. The development of surface roughness and porosity of the GA-treated Cu-BTC powder samples were not reflected

on their phase composition and crystallinity. All samples showed a consistent resemblance of their phase purity and degree of crystallinity to the XRD pattern of the pristine Cu-BTC. Three additional peaks were observed in the XRD patterns of the Cu-BTC treated with 5 and 10 mg/L GA. These peaks were observed at 2θ values of 12.03°, 9.08° and 7.78°, and are attributed to the presence of 2D Cu-BTC crystallites, as highlighted in their respective SEM micrographs in Figure 37 (a, b). These results suggest that the hierarchical Cu-BTC@GA synthesized by this method can simultaneously own hierarchical pores and overall stability.

FT-IR: Figure 41 shows the FTIR spectra of the GA-treated Cu-BTC powder samples. Compared with that of pristine Cu-BTC, all samples showed a close similarity in terms of bands location and intensity. These results imply the structural stability of the GA-treated Cu-BTC, despite the increased concentration of GA in the reaction media. No bands were observed that may indicate the presence of GA or Cu-GA in the treated Cu-BTC samples. In addition, the increased broadness and intensity of the GA-treated Cu-BTC samples could be attributed to the presence of physically-adsorbed water molecules despite the complete dryness of the GA-treated samples. The developed surface roughness and porosity contribute to the availability of surfaces for the adsorption of water molecules. The latter takes place on the newly formed surfaces as well as into the opened channels to the bulk, especially with samples that were treated in a high concentration of GA.
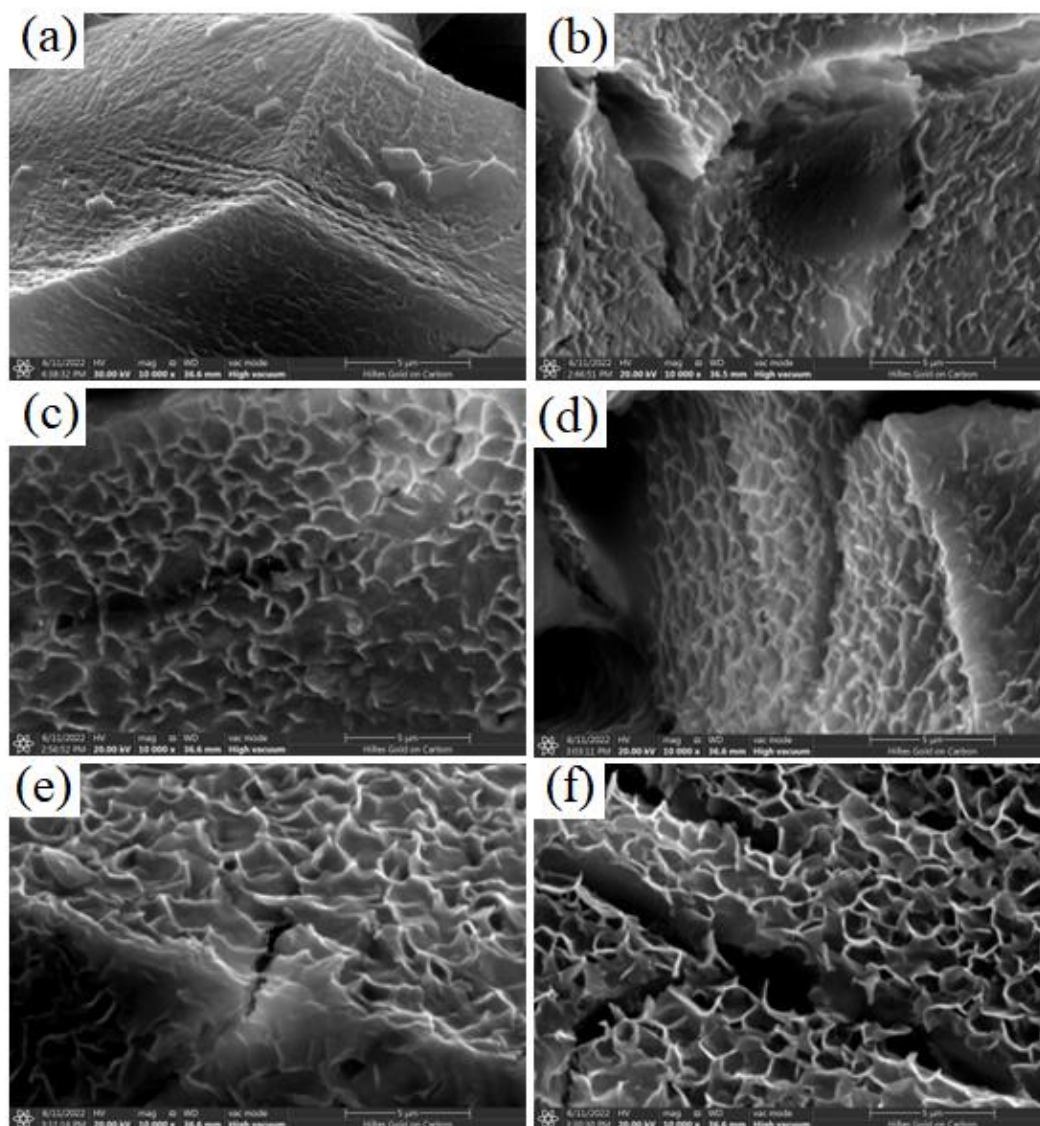
Figure 38: High magnification SEM micrographs of Cu-BTC particulates treated with a) 10 b) 20 c) 40 d) 50 e) 120 and f) 200 mg/L GA aqueous solutions at room temperature for 30 minutes.
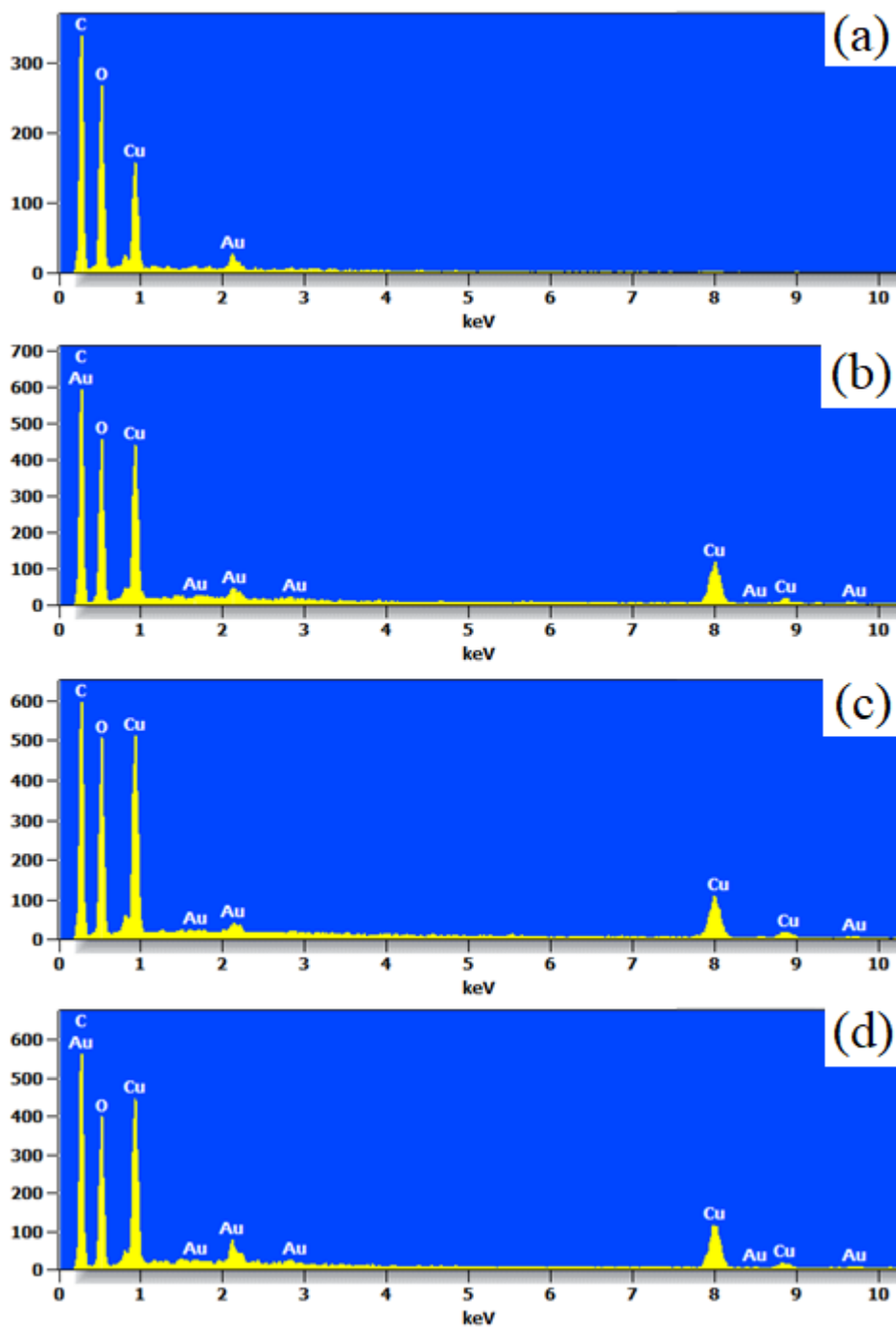
Figure 39: EDX spectra of Cu-BTC particulates treated with a) 10 b) 40 c) 120 and d) 200 mg/L of GA aqueous solutions at room temperature for 30 minutes.
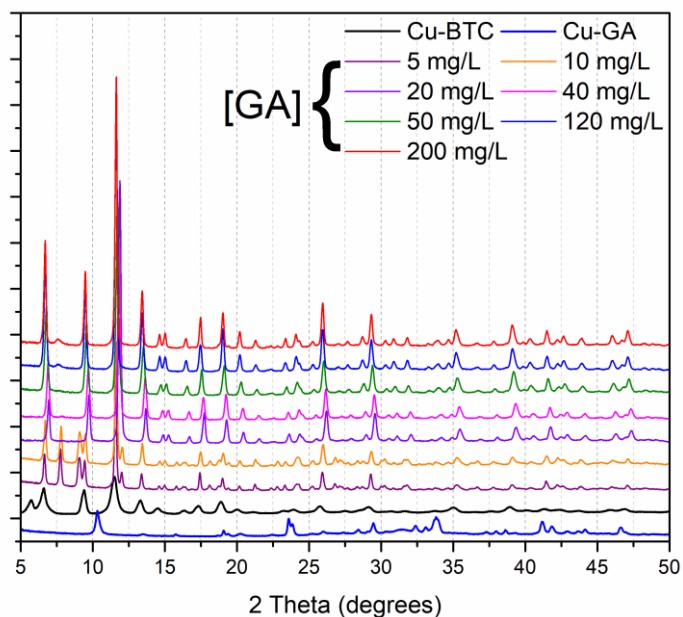
Figure 40: XRD patterns of Cu-BTC particulates treated with 5, 10, 20, 40, 50, 120, and 200 mg/L of GA aqueous solutions at room temperature for 30 minutes. XRD patterns of pristine Cu-BTC and Cu-GA are included for comparison.
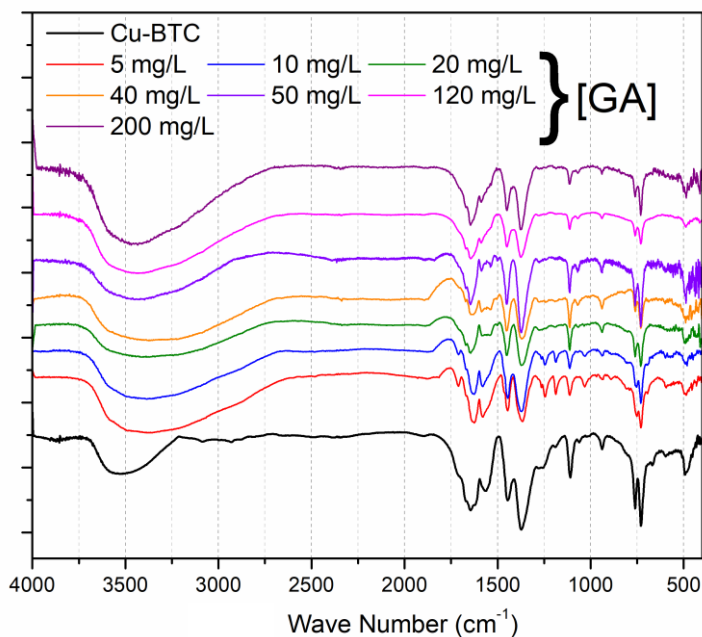
Figure 41: FT-IR patterns of Cu-BTC particulates treated with 5, 10, 20, 40, 50, 120, and 200 mg/L of GA aqueous solutions at room temperature for 30 minutes. FT-IR spectrum of pristine Cu-BTC is included for comparison.

Raman Spectroscopy: The development of Raman spectra in Figure 42 indicates the continued presence of GA in the structure of the etched Cu-BTC under

aqueous conditions. Compared with the Raman spectra of pure Cu-GA, Raman peaks highlighted in Figure 42 within the range of 1250-1650 ppm shows a consistent increase in their intensities with increasing the concentration of GA initially used during the etching process. These findings further confirm the potential encapsulation of GA onto and within the surface porosity created on the Cu-BTC.
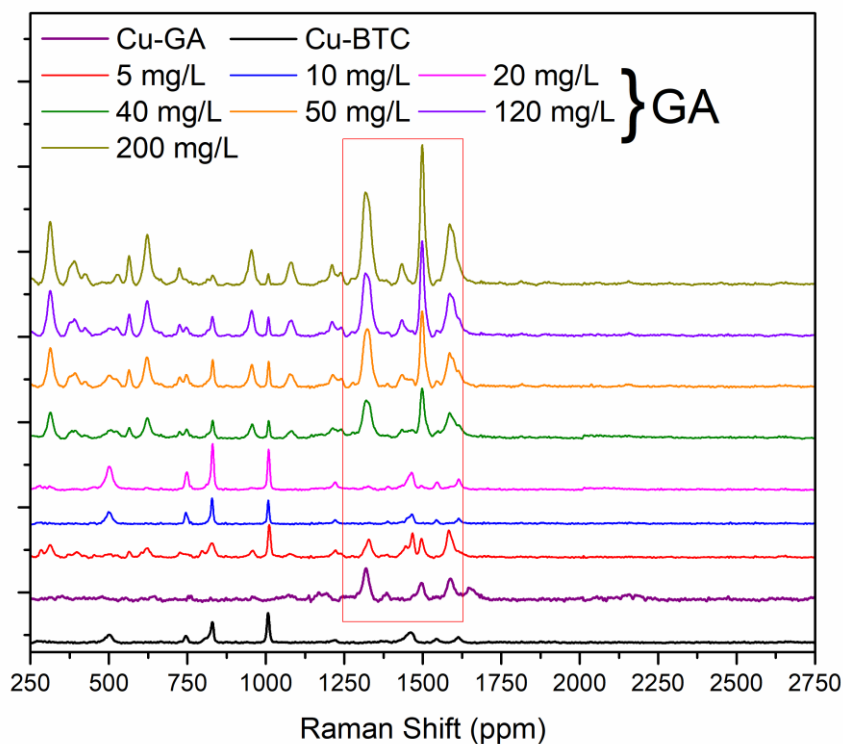
Figure 42: Raman Spectra of Cu-BTC particulates treated with 5, 10, 20, 40, 50, 120, and 200 mg/L of GA aqueous solutions at room temperature for 30 minutes. Raman spectra of pristine Cu-BTC and Cu-GA are included for comparison.

TGA: All GA-treated Cu-BTC samples showed a consistent thermal history with an overall similarity to that of pristine Cu-BTC, as shown in the TGA thermograms of these samples in Figure 43. All samples showed the presence of two major thermal events at temperature ranges of 50-110°C and 300-355°C, which are attributed to the evaporation of physically adsorbed water molecules and the breakdown of the BTC linker molecules. A closer investigation of the extent of weight

loss of these events is seen in Figure 43 (b). All samples displayed an increased weight loss for the first thermal event, which is related to the evaporation of the physically adsorbed water molecules. These results are in accordance with the FTIR findings (Figure 41) and confirm the increase of water absorption on the newly developed surface roughness and porosity.

Cu-BTC etching and encapsulation with GA

SEM-EDX: The variation in the morphology of the hydrothermally treated Cu-BTC in the presence of variable concentrations of GA is shown in Figure 44. Compared with the smooth geometry of the Cu-BTC octahedron crystals that were observed in the micrographs of pristine Cu-BTC, all samples showed a developed surface degradation accompanied by the formation of surface mesopores. The extent of surface modification was observed to increase with increasing the concentration of GA in the reaction medium. A closer look at the GA-treated samples at higher magnification is shown in Figure 45. A remarkable increase in the surface porosity of the Cu-BTC crystals was observed. Moreover, this etching was also extended to the bulk of the crystals causing a breakdown of the Cu-BTC hierarchical octahedron crystalline structure to highly porous smaller crystallites, as shown in Figure 45 (c). The surface of the 0.1M GA-treated Cu-BTC was
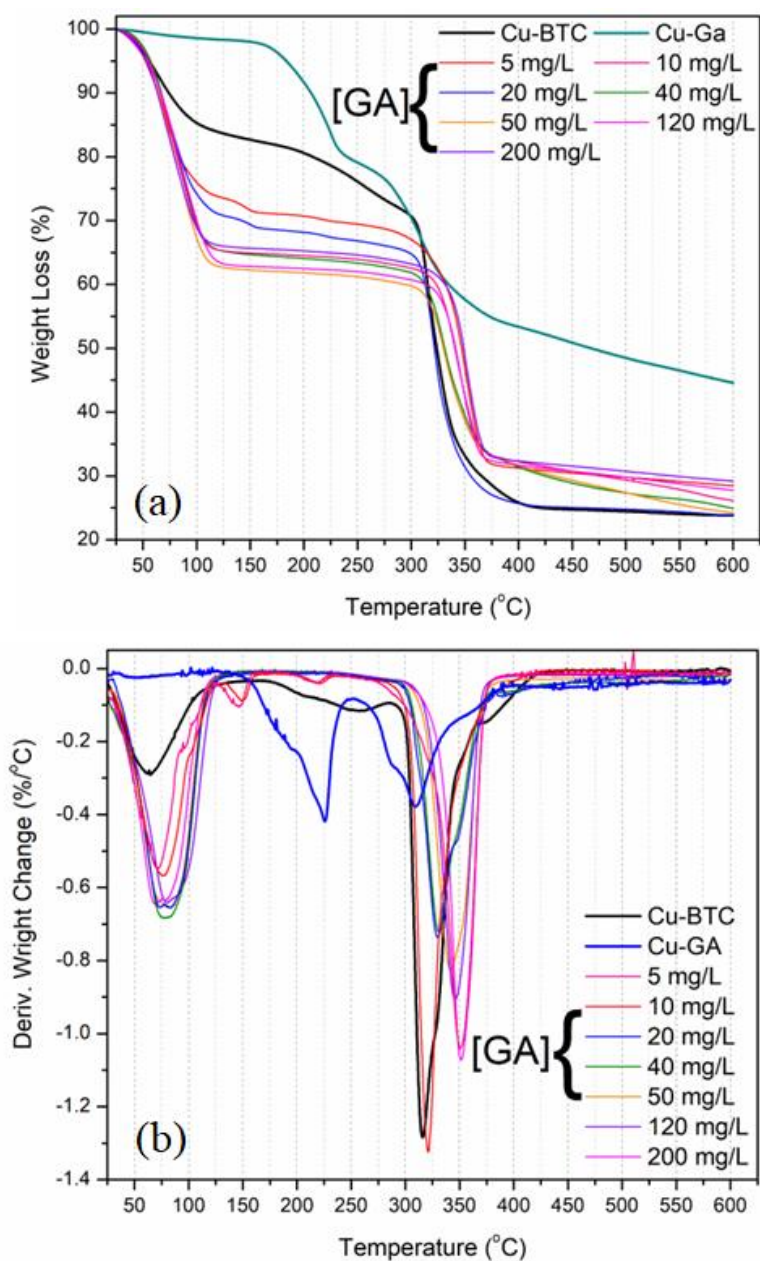
Figure 43: a) TGA thermograms and b) DTG analysis of Cu-BTC particulates treated with 5, 10, 20, 40, 50, 120, and 200 mg/L of GA aqueous solutions at room temperature for 30 minutes. TGA and DTG thermograms of pristine Cu-BTC is included for comparison.
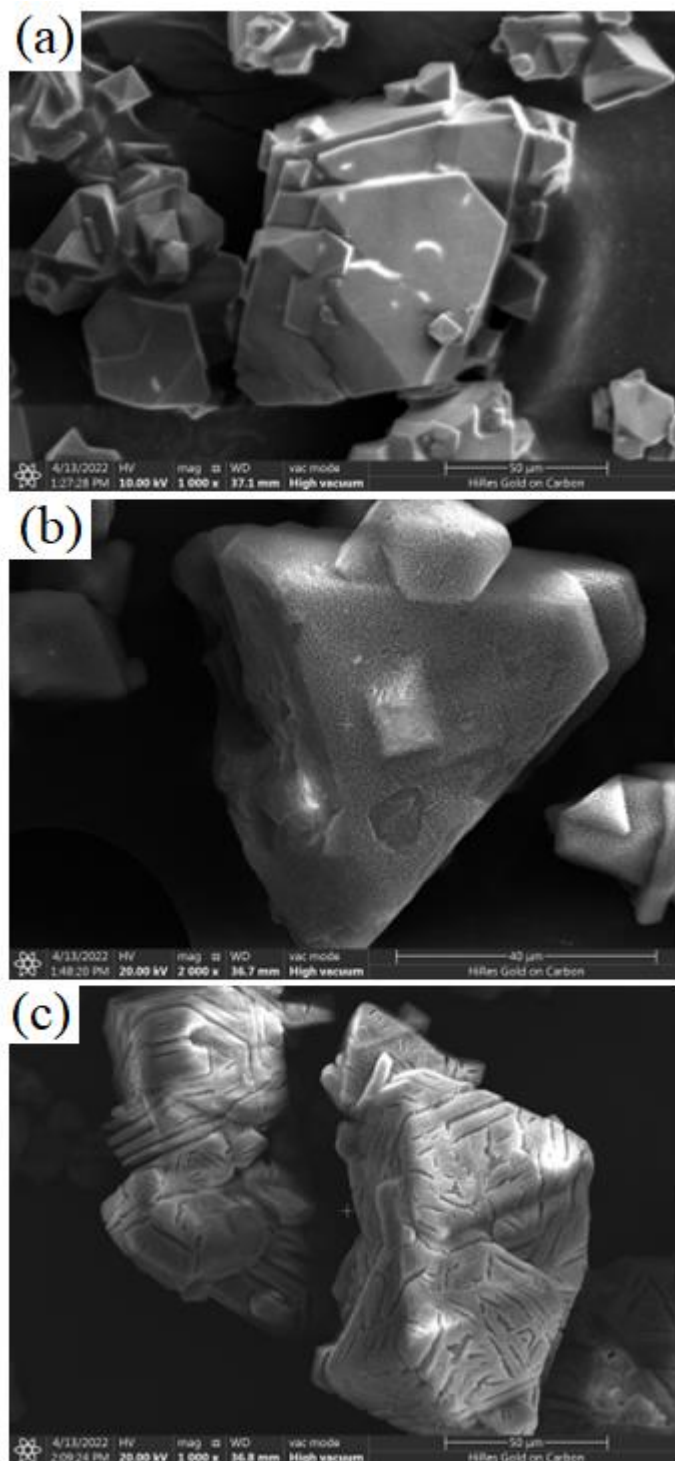
Figure 44: SEM micrographs of Cu-BTC MOF particulates hydrothermally treated with a) 0.01 b) 0.05 and c) 0.1 M GA in DMF.
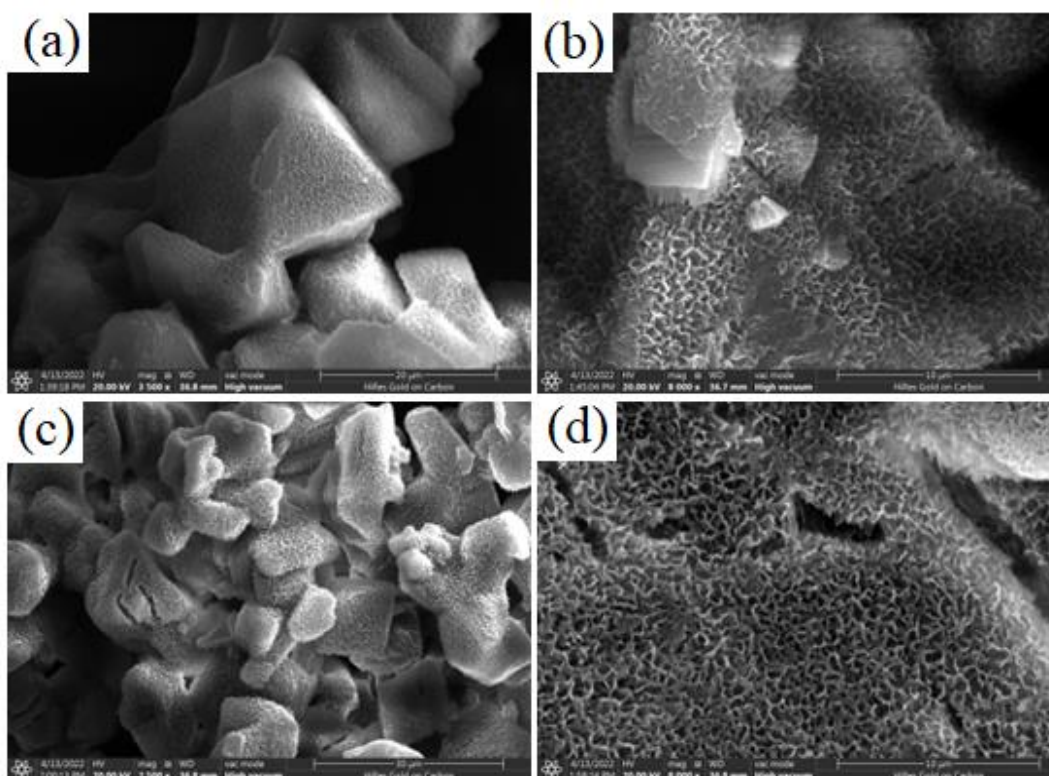
Figure 45: High magnification SEM micrographs of Cu-BTC MOF particulates hydrothermally treated with a, b) 0.05 and c, d) 0.1 M GA in DMF.

Also shown to develop a homogeneously distributed porosity, as shown in Figure 45 (d). These results indicate an etching process, where the GA weak acid molecules started to attack the Cu-BTC crystallites leading to the development of a hierarchical structure. These findings were previously observed using phosphoric acid etchant for Cu-BTC (Doan et al., 2019) and MIL-101(Fe) (Koo et al., 2017), UiO-66 by sulfuric acid (Shi et al., 2020) and UiO-66 (NH_2) by formic acid (Ai et al., 2022). In these studies, weak acids or dilute strong acid, were used to create surface and bulk porosity of the corresponding MOF structures for the purpose of introducing mesopores to extend the readily porous MOF structures for gas-sorption, water treatment, and drug delivery applications. The effect of increasing the concentration of GA on the elemental composition of the produced etched Cu-BTC is shown in the

EDX diagrams of the etched samples in Figure 46. A comparison between the elemental composition of the etched samples is also shown in Figure 47. A gradual decrease in the concentration of Cu in the etched sample was observed with increasing the concentration of GA in the medium. Compared with the C:O:Cu elemental proportions in the non-treated Cu-BTC, the decrease in the concentration of Cu^{2+} ions with etching could be related to the leaching out of these ions from the Cu-BTC structure as a result of GA etching. However, the increase in the concentration of C and O in the etched samples with increasing the concentration of GA indicates the increased organic content in the etched samples. The maintained morphology of the Cu-BTC after etching may also indicate a selective leaching of the Cu^{2+} ions from the Cu-BTC structure as a result of the interaction with the attacking GA molecules. An additional possibility is the replacement of the BTC units with GA molecules or the encapsulation of the GA within the open porosity created as a result of etching of the Cu-BTC structure. A detailed analysis of these possibilities is presented in the following sections.

XRD: The variation in the phase composition and crystallinity of the etched Cu-BTC samples as a result of hydrothermal treatment with variable concentrations of GA is shown in the XRD patterns of these samples in Figure 48. Compared with the XRD pattern of the pristine non-treated Cu-BTC all patterns showed a consistent degree of crystallinity and constancy in their phase composition. No signs were observed for phase transformation or formation of other Cu-based coordination compounds. Relating these results to the SEM micrographs of the etched samples in Figure 43 indicate that the hierarchical crystal structure of Cu-BTC was created. Furthermore, the highly deformed and highly porous morphologies that were observed in the SEM micrographs of the Cu-BTC treated with 0.1M GA (Figure 44 (c)) did not

reflect a change in the phase composition and crystallinity of the etched samples. These findings may indicate that the observed deformed morphologies in Figures 45 (c) still maintain the known crystallographic structure of the crystallites, which is reflected on a maintained degree of crystallinity and constancy in the phase composition of these samples.
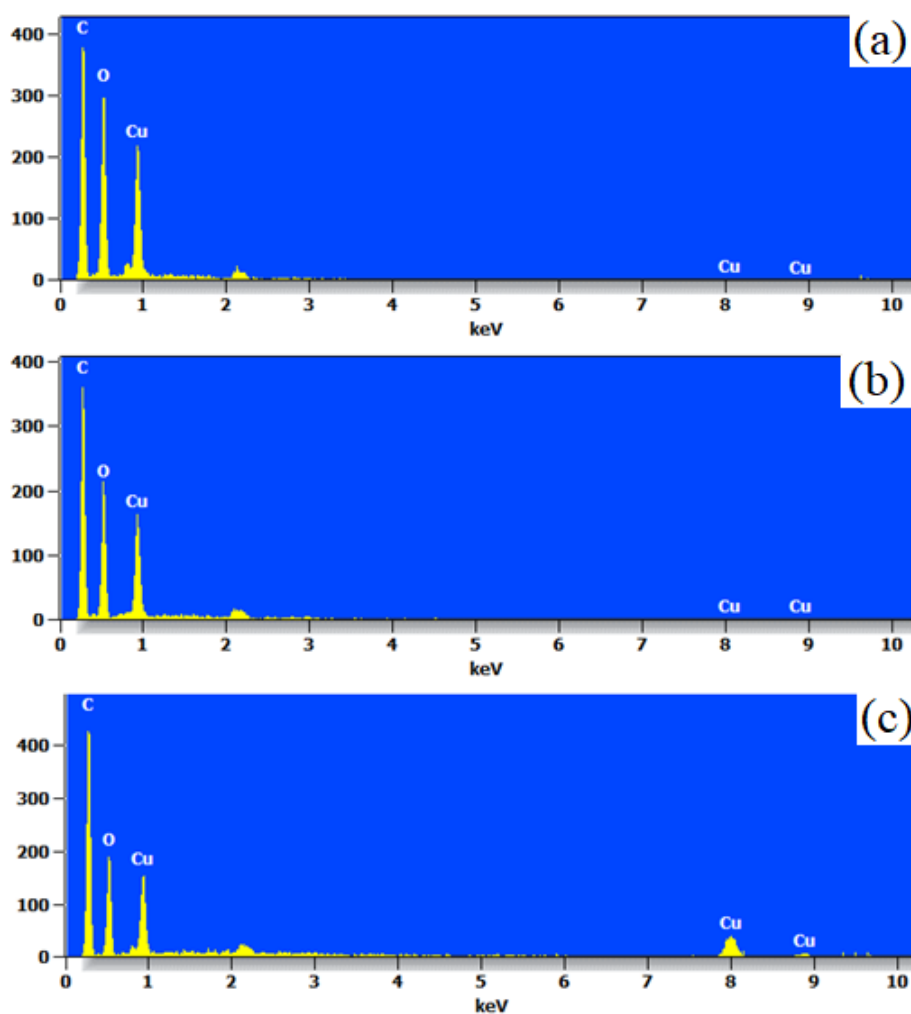
Figure 46: EDX spectra of Cu-BTC MOF particulates hydrothermally treated with a) 0.01 b) 0.05 and c) 0.1 M GA in DMF.
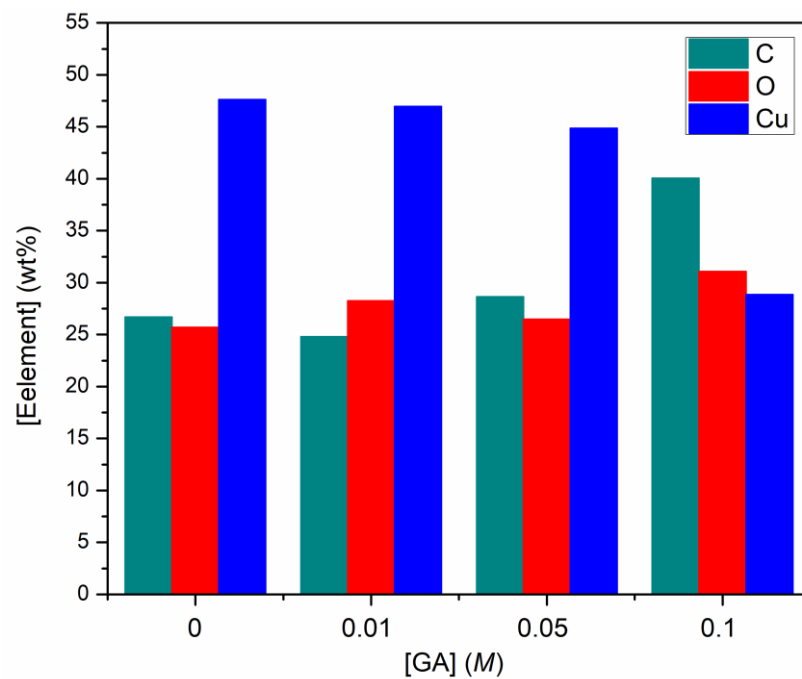
Figure 47: Variation of the elemental composition of pristine Cu-BTC MOF and Cu-BTC particulates hydrothermally treated with 0.01, 0.05 and 0.1 M GA in DMF.
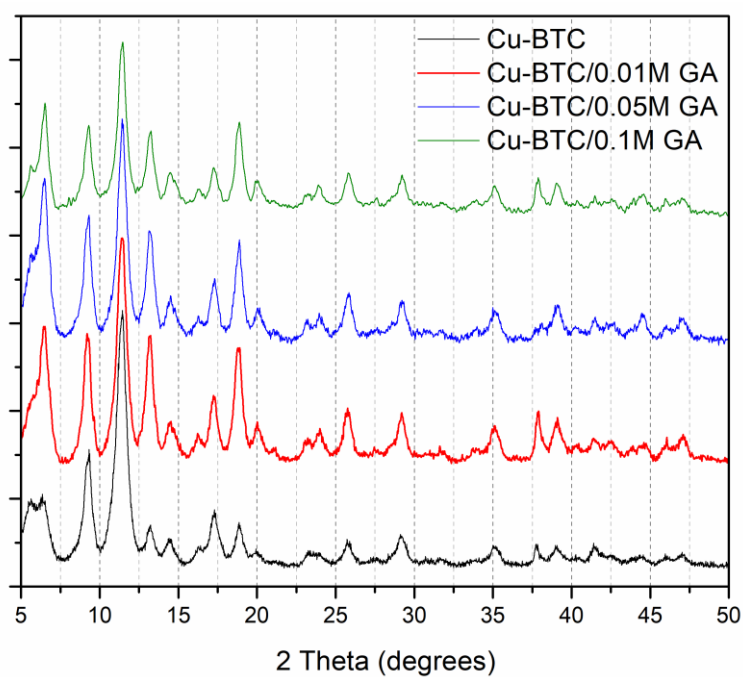
Figure 48: XRD patterns of Cu-BTC MOF particulates hydrothermally treated with 0.01, 0.05 and 0.1 M GA in DMF.

SC-XRD: All Cu-BTC etched samples were subjected to a detailed analysis of their crystallographic features using single-crystal XRD technique. Tables 5-7 summarize the crystallographic data of the three samples. All etched samples exhibited a cubic crystal system with no variation in the lattice parameters nor the lattice volume. However, a change in the space group of the Cu-BTC (Fm-3m) was observed in the crystal structure of the sample to Pa-3 as a result of etching in 0.1M GA but the overall Cubic crystal system was maintained. This could be attributed to the deformation of the Cu-BTC crystal structure, as depicted from its morphology in Figure 45 (c). The simulated crystal structures of the etched samples are shown in Figures 49-51. All structures showed the coordination of Cu^{2+} oxy clusters with the -COOH functional groups along the BTC linker. There was no evidence that GA is a part of the crystal structure. Therefore, the increase organic content in the etched samples could be related to the encapsulation of GA within the created porosity of the etched Cu-BTC crystallites. This assumption will be investigated in more detail using Raman spectroscopy, N2 sorption, and ^{1}H NMR digestion.
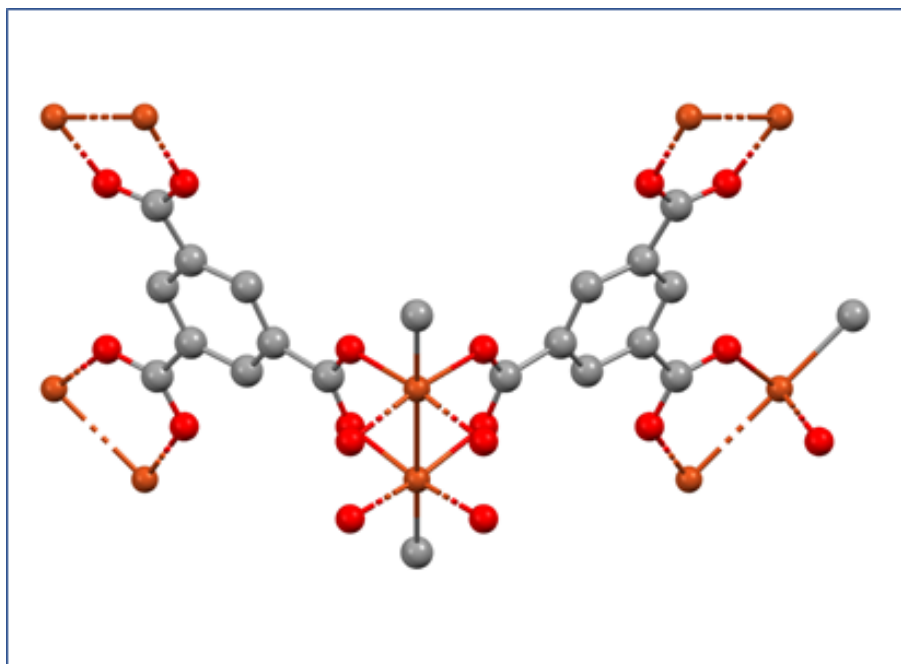
Figure 49: Crystal structure of Cu-BTC@GA 0.01M.
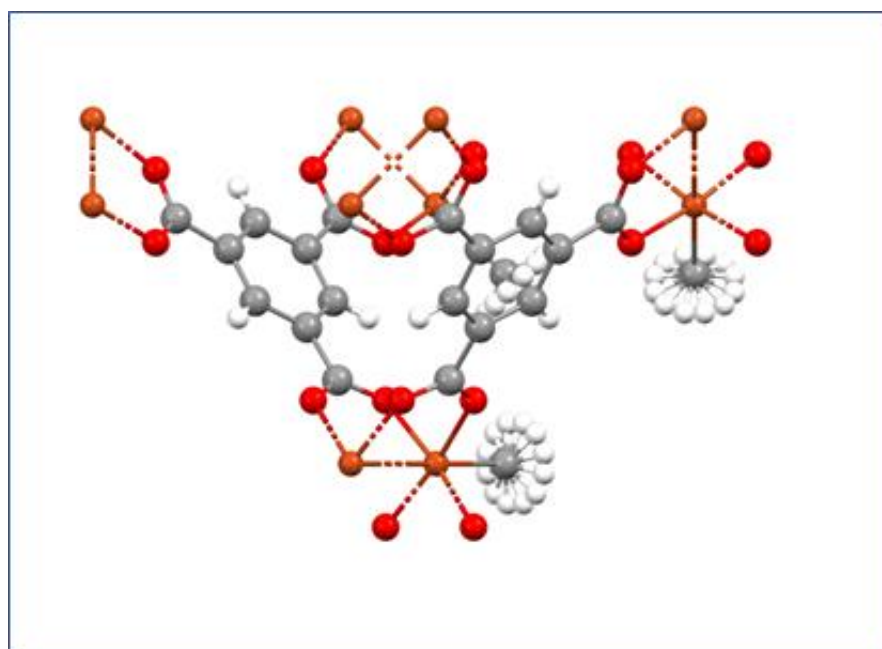
Figure 50: Crystal structure of Cu-BTC@GA 0.05M.
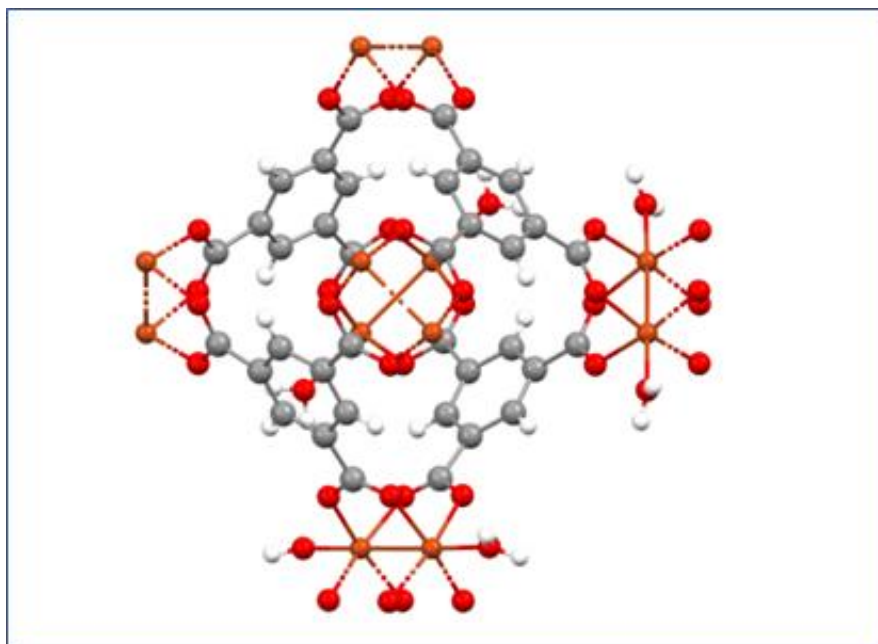
Figure 51: Crystal structure of Cu-BTC@GA 0.1M.

Table 5: Crystal data for Cu-BTC@GA 0.01M.

Identification code	exp_326_auto 0.01M
Empirical formula	$C_{1.875}H_{1.375}Cu_{0.25}O_{0.875}$
Formula weight	53.79225
Temperature/K	297(2)
Crystal system	cubic
Space group	Fm-3m
a/Å	26.3148(3)
b/Å	26.3148(3)
c/Å	26.3148(3)
α/°	90
β/°	90
γ/°	90
Volume/Å^3	18222.2(6)
Z	12
ρ_{calc}g/cm^3	180.697
μ/mm^{-1}	364.745
F(000)	990720.0
Crystal size/mm^3	? × ? × ?
Radiation	CuKα (λ = 1.54184)
2Θ range for data collection/°	6.718 to 153.514
Index ranges	-19 ≤ h ≤ 22, -31 ≤ k ≤ 21, -30 ≤ l ≤ 25
Reflections collected	8012

Table 5: Crystal data for Cu-BTC@GA 0.01M. (continued)

Independent reflections	983 [R_{int} = 0.0206, R_{sigma} = 0.0149]
Data/restraints/parameters	983/0/18
Goodness-of-fit on F^2	5.825
Final R indexes [I>=2σ (I)]	R_1 = 0.1559, wR_2 = 0.5420
Final R indexes [all data]	R_1 = 0.1624, wR_2 = 0.5598
Largest diff. peak/hole / e $Å^{-3}$	2.06/-2.33

Table 6: Crystal data for Cu-BTC@GA 0.05M.

Identification code	exp_328 0.05M
Empirical formula	$C_{1.75}H_{1.25}Cu_{0.25}O$
Formula weight	54.16475
Temperature/K	297(2)
Crystal system	Cubic
Space group	Fm-3m
a/Å	26.3252(3)
b/Å	26.3252(3)
c/Å	26.3252(3)
α/°	90
β/°	90
γ/°	90
Volume/$Å^3$	18243.8(6)
Z	192
$\rho_{calc}g/cm^3$	0.947
μ/mm^{-1}	1.926
F(000)	5184.0
Crystal size/mm^3	? × ? × ?
Radiation	CuKα (λ = 1.54184)
2Θ range for data collection/°	6.716 to 138.396
Index ranges	-22 ≤ h ≤ 31, -26 ≤ k ≤ 24, -30 ≤ l ≤ 26
Reflections collected	7890
Independent reflections	905 [R_{int} = 0.0496, R_{sigma} = 0.0166]
Data/restraints/parameters	905/0/38
Goodness-of-fit on F^2	1.353
Final R indexes [I>=2σ (I)]	R_1 = 0.1006, wR_2 = 0.3192
Final R indexes [all data]	R_1 = 0.1027, wR_2 = 0.3226
Largest diff. peak/hole / e $Å^{-3}$	1.36/-0.66

Table 7: Crystal data for Cu-BTC@GA 0.1M.

Identification code	exp_329 0.1
Empirical formula	$C_{1.5}H_1Cu_{0.25}O_{1.25}$
Formula weight	54.90975
Temperature/K	297.00(10)
Crystal system	Cubic
Space group	Pa-3
a/Å	26.3148(6)
b/Å	26.3148(6)
c/Å	26.3148(6)
α/°	90
β/°	90
γ/°	90
Volume/Å^3	18222.1(7)
Z	24
ρ_{calc}g/cm^3	0.948
μ/mm^{-1}	1.928
F(000)	5106.4
Crystal size/mm^3	N/A × N/A × N/A
Radiation	Cu Kα (λ = 1.54184)
2Θ range for data collection/°	5.82 to 154.64
Index ranges	-20 ≤ h ≤ 24, -31 ≤ k ≤ 30, -31 ≤ l ≤ 25
Reflections collected	26119
Independent reflections	5840 [R_{int} = 0.1371, R_{sigma} = 0.0636]
Data/restraints/parameters	5840/0/220
Goodness-of-fit on F^2	1.817
Final R indexes [I>=2σ (I)]	R_1 = 0.2356, wR_2 = 0.5874
Final R indexes [all data]	R_1 = 0.3335, wR_2 = 0.6485
Largest diff. peak/hole / e Å^{-3}	3.47/-1.17

N$_2$-adsorption and Pore size distribution: The effect of etching Cu-BTC with

GA under hydrothermal conditions resulted in the degree and type of porosity of the

etched crystals, as depicted from their N$_2$-adsorption isotherms in Figure 52. A

pronounced decrease in the volume of adsorbed N$_2$ gas was observed by increasing the

concentration of GA. Moreover, a typical type II isotherm of the as-prepared Cu-BTC

was converted to type IV isotherms upon etching with GA, as shown in Figure 52 (a).

Moreover, the etching process resulted in the creation of mesoporosity within the

highly porous crystals, as shown in Figure 53. An average pore size of 150 Å was observed in all etched samples with an increased volume of adsorbed gas with increasing the concentration of GA used for etching. These results further confirm the previous findings where highly mesoporous architecture is created by etching on the surface and throughout the bulk of the Cu-BTC crystals.

BET and Langmuir surface areas: The variation in the BET and Langmuir surface area of the GA-etched Cu-BTC particulates is shown in Figure 54. Compared with a BET and Langmuir surface area of 1,268.9 and 1,507.7 m^2/g for pristine Cu-BTC, all GA-etched Cu-BTC particulates showed a gradual decrease in their surface area with increasing the concentration of GA in DMF. The development of surface porosity was initially believed to result in an increase in the surface area of the etched Cu-BTC particulates. However, the decrease in the surface area of all etched samples indicate the occupation of the freshly created porosity with other molecules, such as solvent and/or GA molecules. It should be mentioned that all etched samples were thoroughly dried under vacuum to remove any remaining solvent molecules. Therefore, the gradual decrease in the surface area is directly proportional to the increased concentration of the GA etchant. Accordingly, it is presumed that GA molecules could be entrapped within the freshly created surface and bulk pores.
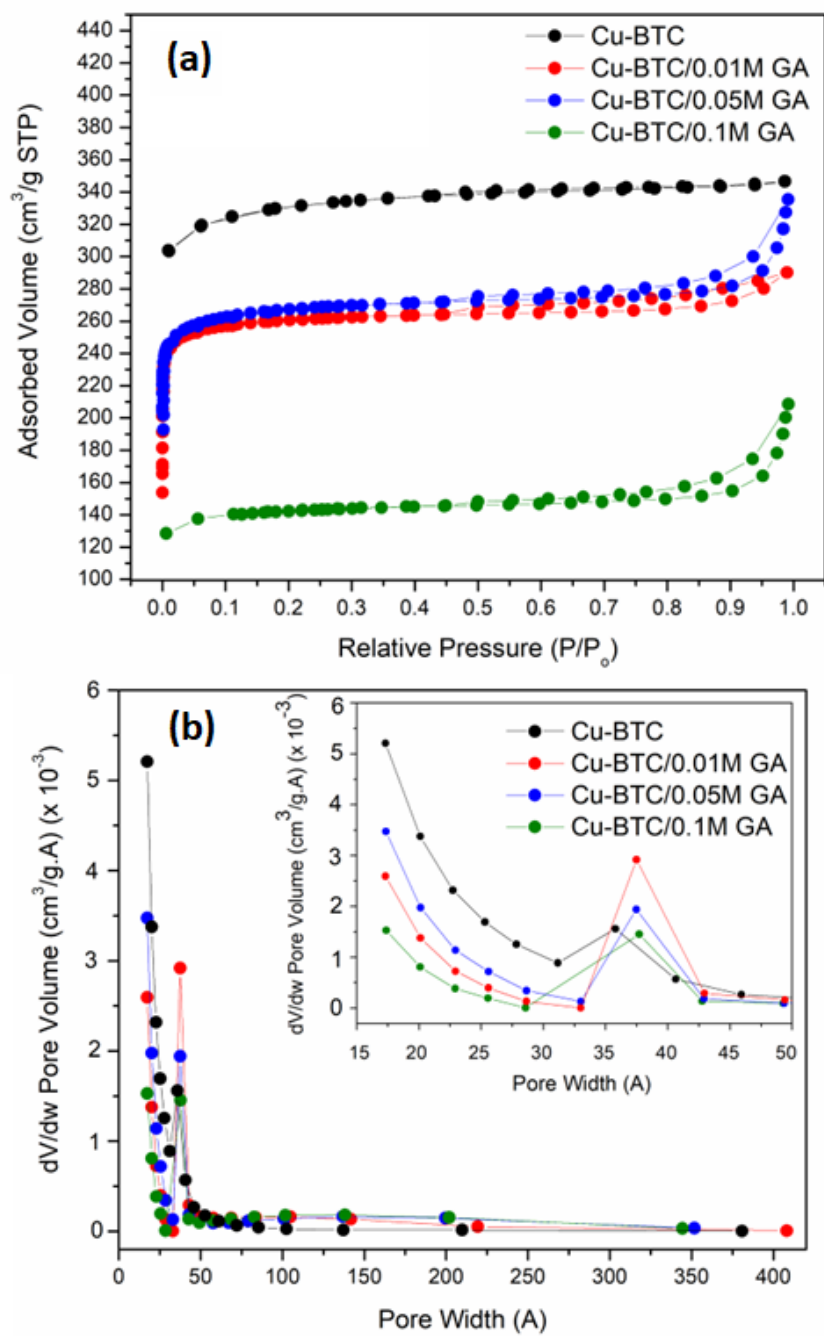
Figure 52: a) N$_2$-adsorption hysteresis and b) pore size distribution of Cu-BTC etched with GA in DMF under hydrothermal conditions.
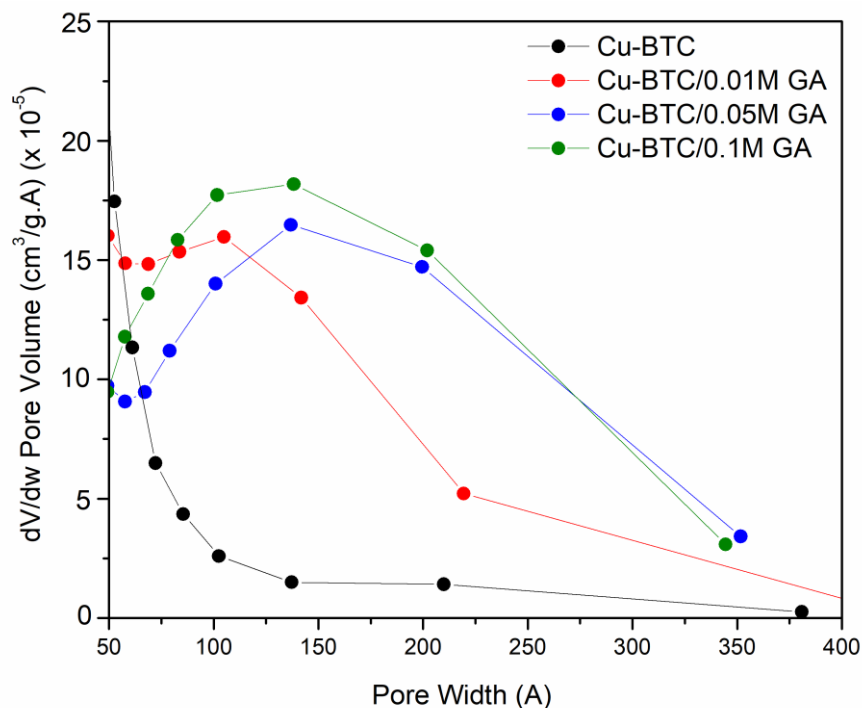
Figure 53: Pore size distribution of Cu-BTC etched with GA in DMF under hydrothermal conditions showing the developed mesoporosity.
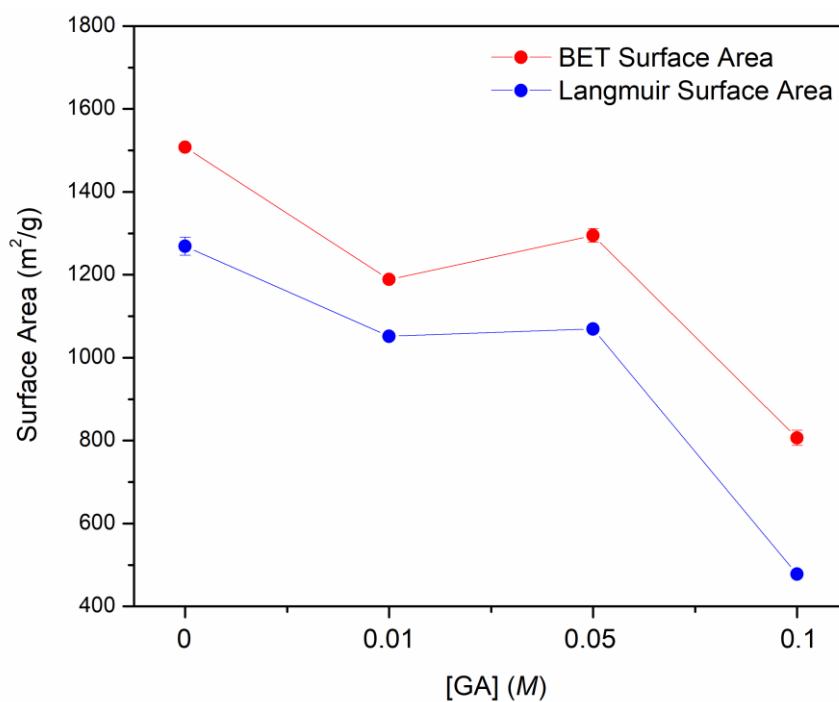
Figure 54: Variation of the BET and Langmuir surface area of pristine Cu-BTC etched with GA in DMF.

FT-IR: The FTIR spectra of the GA-etched Cu-BTC structures are shown in

Figure 55. All spectra showed a similar pattern that closely resembles the FTIR

spectrum of pure Cu-BTC in terms of band location and intensity. However, a closer look at parts I and II that are highlighted in Figure 55 indicate the presence of GA residues in the etched Cu-BTC samples. The band at 1034.7 cm^{-1}, which is characteristic to the absorption of the C-O functional group in GA has a counterpart band at 1110.2 cm^{-1} in the FTIR spectrum of pristine Cu-BTC. A decrease in the intensity of the latter band was observed with the increase in the concentration of GA in the etching medium. Concurrently, an increase in the band at 1063.1 cm^{-1} was observed, which could be considered a shifted band of the GA that was found at 1034.7 cm^{-1}. Moreover, a gradual decrease in the location of the broad band that is characteristic to the -OH absorption was also observed, as shown in part II in Figure 55. This band was shown at 3527.7 cm^{-1} and 3244.6 cm^{-1} in the FTIR spectra of pristine Cu-BTC and Cu-GA, respectively. Upon etching with 0.01, 0.05 and 0.1 GA, the bands shifted to 3471.3, 3427.3 and 2295.7 cm^{-1}, respectively. These findings confirm the presence of GA in the structure of post-etching. Furthermore, the absence of Cu-GA peaks in the XRD patterns of the etched samples indicate that Cu-GA was not a possible product of the etching process. We can assume that GA is physically entrapped within the pores of the etched Cu-BTC.
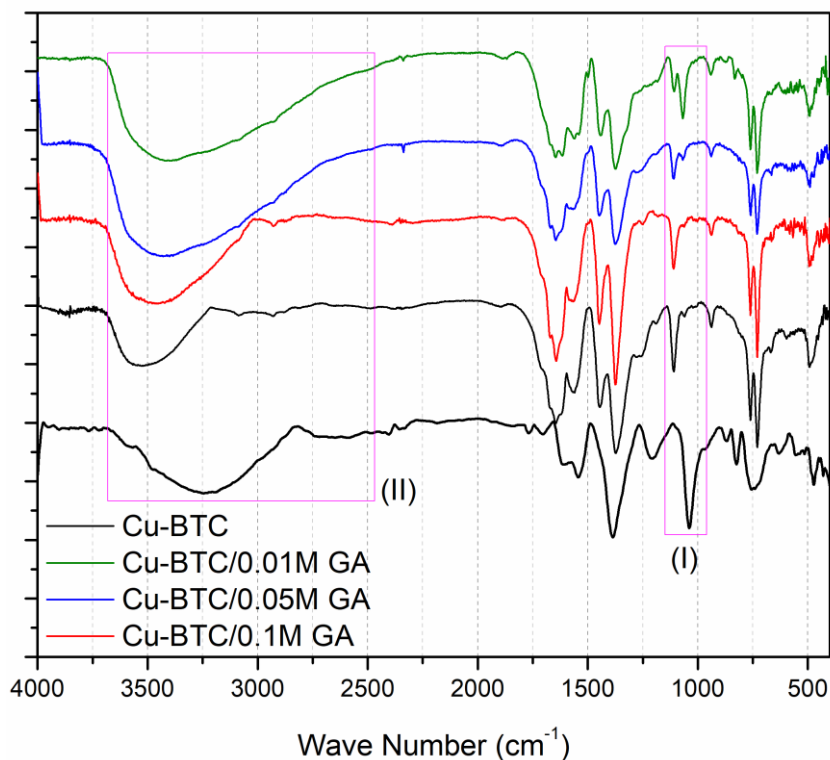
Figure 55: FT-IR spectra of Cu-BTC@GA etched samples compared to pure Cu-BTC.

TGA: Figure 56 (a) shows the TGA thermograms of the etched Cu-BTC samples as a function of the concentration of GA in the medium. All etched samples exhibit a similar weight loss pattern to that of pristine Cu-BTC. Two major events were observed within the ranges of 62.3-84.5°C and 311.7-340.5°C, as shown in Figure 55 (b). These events are attributed to the removal of the weakly adsorbed water molecules and the breakdown of the BTC linker molecules, respectively. A gradual decrease in the overall weight loss of the etched Cu-BTC samples was observed, as shown in Figure 57. This is related to overall decreased organic content of the etched Cu-BTC samples as a result of being etched. However, the dramatic extent of etching, as depicted from the SEM micrographs of the etched samples indicate a higher extent of organic materials removal, hence a higher weight loss was expected. Therefore, it could be also assumed that the removal of the BTC linker units from the BTC

hierarchical structure is accompanied by the entrapment of GA units in the remaining porous structures.

¹H-NMR: It has been established that ^{1}H NMR digestion is one of the most successful tools to provide additional evidence of the presence of organic species in the MOF structures. This technique has, therefore, been selected to investigate the structure of the etched Cu-BTC samples. Figure 58 shows the ^{1}H NMR spectra of the etched samples as a function of the initial [GA] in the reaction media. The ^{1}H NMR spectra of pristine BTC and GA linker molecules are also included for comparison. A peak at 8.56-8.58 ppm was observed in the spectra of the etched samples, which account for the presence of the BTC linker molecules (8.63 ppm). On the other hand, a peak denoting the structure of the GA linker molecule is known to appear at 6.9 ppm. Upon etching of the Cu-BTC structures, this peak started to appear at 6.85 ppm in the spectrum of the Cu-BTC sample that was etched by 0.05 M GA. With increasing the concentration of GA etchant to 0.1M, a pronounced increase in the intensity of this peak was exhibited, while its location was maintained at 6.88 ppm. These strings of evidences clearly indicate the presence of GA molecules entrapped within the porous structure of the GA-etched Cu-BTC hierarchical and highly porous structure. The highly hydroxylated GA molecule is, therefore, expected to be entrapped within the pores of the highly porous Cu-BTC units through the formation of H-bonding with the surrounding BTC linker units, and as part of the Cu-BTC 3D structure.
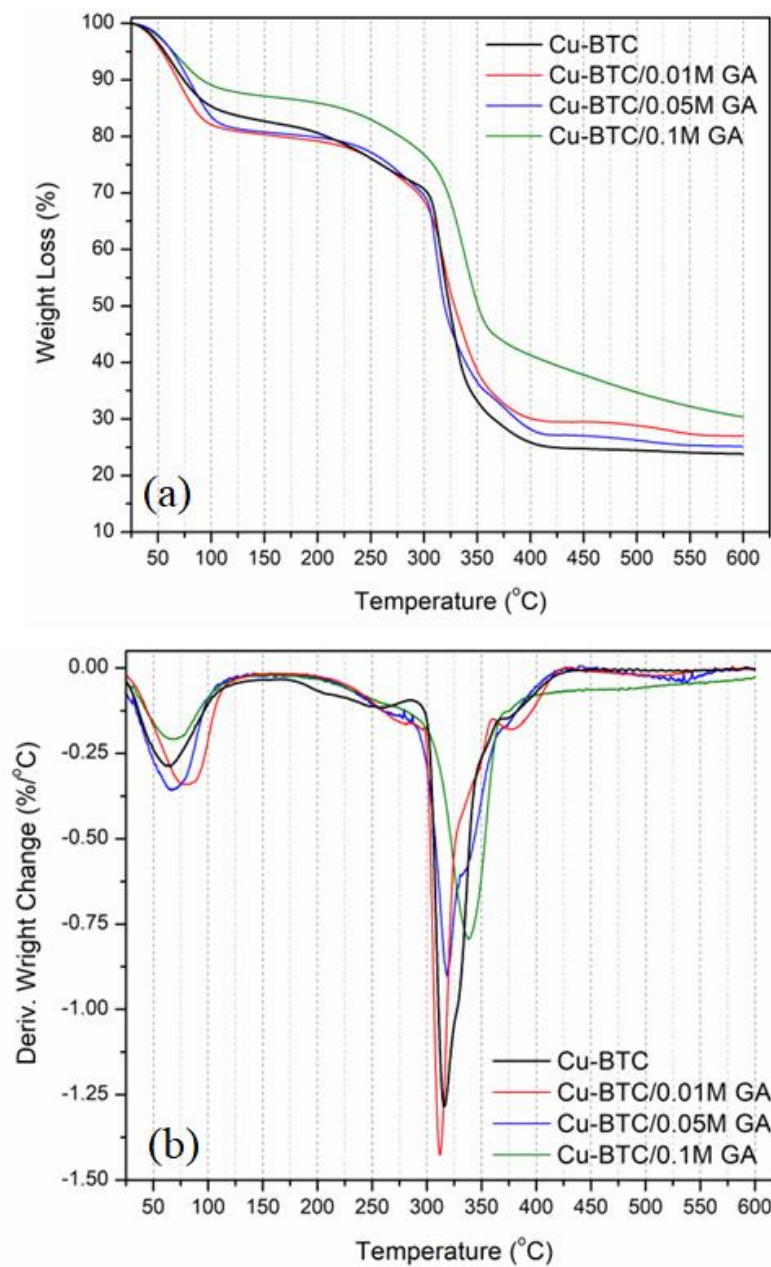
Figure 56: a) TGA thermograms and b) DTG analysis of Cu-BTC@GA etched samples compared to Cu-BTC.
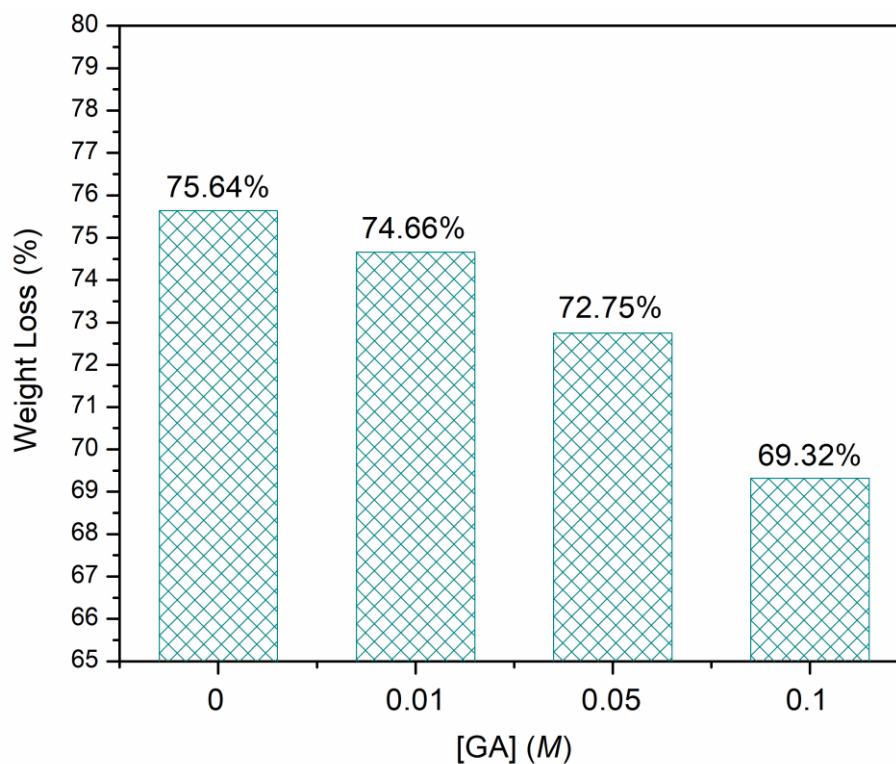
Figure 57: Variation of the overall weight loss of pristine Cu-BTC and that of Cu-BTC@GA etched samples.
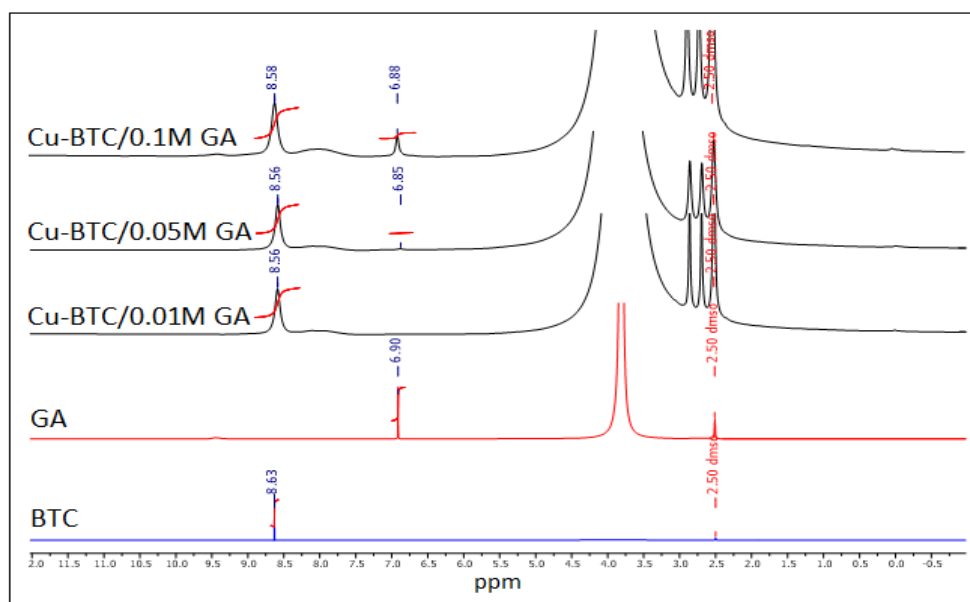
Figure 58: ^{1}H-NMR spectra of Cu-BTC@GA etched samples. Each sample was prepared in 0.5 ml of DMSO + 40% HCl + 60% D_2O. ^{1}H spectra of standard BTC and GA linkers are provided for comparison. All spectra were referenced to a DMSO signal at 2.50 ppm.

Raman Spectroscopy: Figure 59 displays the Raman spectra of all etched Cu-BTC samples, compared with Cu-BTC and Cu-GA MOF structures. All etched spectra resemble the spectrum of pure Cu-BTC. However, peaks in the three highlighted areas of the spectra strongly indicate the presence of GA after the etching process. In area I, a peak at 1322.5 cm^{-1}, is attributed to the absorption of the C-OH bond of the Cu-GA in the Raman spectra of the etched samples with increasing intensities correlated to the increasing [GA]. Similarly, two peaks at 1503.0 and 1588.7 cm^{-1}, which are attributed to the absorption of the C=O functional group of GA, were also observed in the spectra of the etched samples. Their intensities seem to increase with increasing GA treatment concentrations. These findings provide strong evidence for the presence of GA in the structure of the etched Cu-BTC samples. The possibility of the interaction between GA and the Cu^{2+} ions that are linked to the BTC linker units in the Cu-BTC structure and the consequent formation of Cu-GA has been excluded since no evidence for the presence of Cu-GA was found. It is, therefore, confidently proven that GA molecules have caused a surface and bulk etching of the Cu-BTC molecules and have been encapsulated within the created highly porous structure of the Cu-BTC. These findings are in accordance with the previously observed results and provide a novel modality for the creation of a hierarchical Cu-BTC MOF structure.
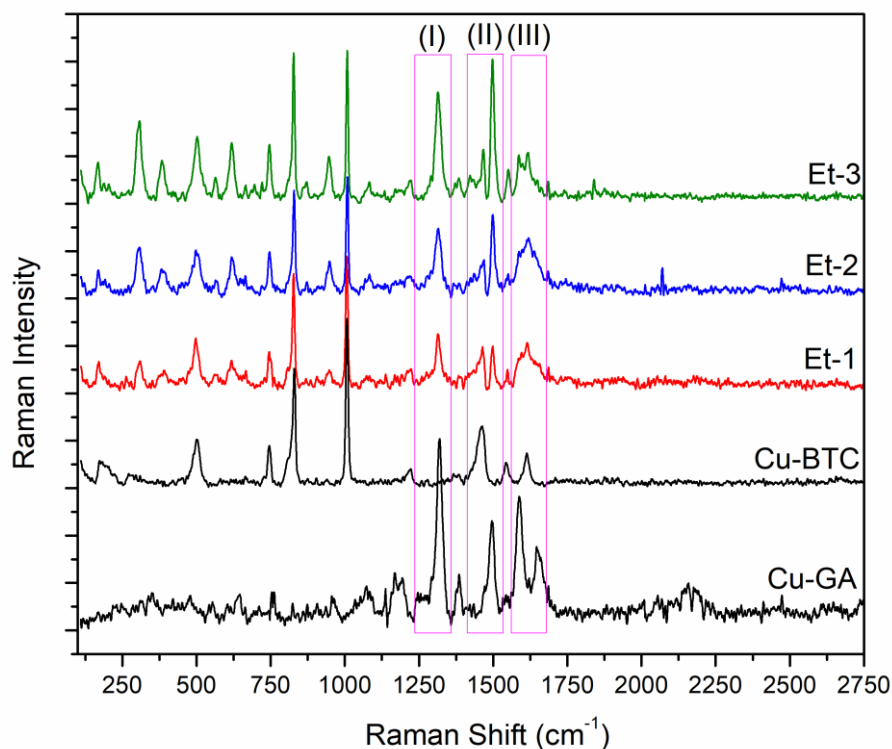
Figure 59: Raman spectra of Cu-BTC@GA etched samples compared to Cu-BTC and Cu-GA.

3.4 Conclusion

The ability to fine tune the porosity and create a hierarchical structure of Cu-BTC using gallic acid has been proven in this work. Simultaneously, the encapsulation of gallic acid within the structure was also a success. This research overcomes the challenges faced with the drug loading of larger molecular entities within microporous MOFs and enhances its mass transfer all while maintaining the MOFs overall crystalline structure. The degree of etching or hollowing out of the MOF can be controlled by varying the concentration of gallic acid. In addition, the higher the concentration of gallic used, the more loading into the MOF structure. The modified Cu-BTC@GA NPs can further be studied for possible enhanced anti-cancer and anti-bacterial synergistic properties. In addition, the removal of GA from the pores to obtain

a completely empty and hollowed out hierarchical Cu-BTC structure can be attempted

for drug delivery applications.

Chapter 4: Development of a Hierarchical Cu-BTC@Cu$_3$(PO$_4$)$_2$ MOF Core-Shell Nanoflower for Improved Stability and Enhanced Biological Activity

4.1 Introduction

Nanoflowers (NFs) are hybrid organic-inorganic nanostructures that are driven by biomolecules for their assembly into micro- and nano-superstructures (Altinkaynak et al., 2016; Ge et al., 2012; Lee et al., 2015; Yao et al., 2011). These nanoflowers are usually synthesized using amino acids as the organic component and metal phosphates or metal ions as the inorganic material (Ge et al., 2012; Li et al., 2016; Wang et al., 2014; Zhang et al., 2016; Zhang et al., 2015). The flower-like structures occur under mild conditions and possess high surface-to-volume ratios (Wu et al., 2016). Lee et al. explain the formation of NFs in 3 steps: 1) primary crystals of metal phosphate are formed from the coordination of metal ions with protein through amide groups 2) metal-protein crystals nucleate into larger molecules, where petals start to form 3) protein continues to induce crystal growth to form the complete structure while keeping the scaffold intact (Lee et al., 2015). Hybrid NFs allowed for a higher catalytic activity compared to the free enzyme, owing to the localization by the NFs for ease of accessibility to the substrate (Batule et al., 2019; Li et al., 2014; Lin et al., 2014). Li et al. developed a multienzyme-inorganic nanocrystal complex using horseradish peroxidase and glucose oxidase (Li et al., 2014). The complex demonstrated high catalytic activity due to the direct substrate transport. The complex also observed well-defined spatial distribution of the enzymes, making it a promising nano-biomaterial (Li et al., 2014).

More recently, Hu et al. designed a CuCo$_2$O$_4$@CoS-Cu/Co-MOF core-shell nanoflower derived from copper/cobalt bimetallic MOFs for enhanced

electrochemical properties (Hu et al., 2021). They synthesized $CuCo_2O_4$ and CoS on Ni foam coated with Cu/Co bimetal MOF by using a two-step electrodeposition technique. According to the authors, the core-shell NF structure increased sites for redox reaction, improving the ability of charge storage and transfer of the composites (Hu et al., 2021).

In addition to enhancing enzymatic activity, protein-incorporated NFs exhibit an intrinsic peroxidase-like activity (Batule et al., 2019; Wu et al., 2016). In 2015, researchers synthesized copper NFs and studied the intrinsic peroxidase of various amino acid copper-based complexes. They determined, when exposed to H_2O_2, the 20 amino acid NFs experienced peroxidase-like activity against that was more pronounced than that of copper phosphate crystals (Wu et al., 2016). In particular, positively charged amino acids NFs exhibited the highest peroxidase-like activity. TEM images proved that the positively charged R groups induced the appearance of Cu^{1+} ions, which was noticeable in the more compacted Lys-incorporated NFs comparing to the Asn-incorporated NFs (Wu et al., 2016).

The overall goal in drug delivery or stand-alone treatments by MOF structures is to have the material breakdown over time for the release of its constituents. To mimic this effect in the human body, PBS and RPMI are used as physiological media. PBS is composed of NaCl, KCl, NaH_2PO_4, and K_2HPO_4 and is usually buffered to be at a pH of 7.4. On the other hand, a common media used for cell culture experiments for the in vitro evaluation of nanomaterials in terms of their interaction with live cells RPMI. RPMI has been found suitable for the assessment of a variety of mammalian cells, including HeLa, Jurkat, MCF-7, PC12, PBMC, astrocytes, and carcinomas. The composition of RPMI is shown in Table 8. The aim of this study is to evaluate the structural and morphological stability of Cu-BTC nanostructures in PBS and RPMI

media and the potential transformation of Cu-BTC into NFs. Creating NFs using our copper-based samples would allow for the sustained release of copper from the structure overcoming the burst release effect observed in the PBS biological media. Copper-based NFs are also known to exhibit intrinsic peroxidase like properties with high surface area to volume ratios (Wu et al., 2016). We hypothesize that the development of NF composite from our copper-based MOFs will enhance the stability and overall anticancer and antibacterial activity of the MOFs.

Table 8: The composition of RPMI Physiologic Media.

Components	Molecular Weight	Concentration (mg/L)	mM
Amino Acids			
Glycine	75.0	10.0	0.13333334
L-Arginine	174.0	200.0	1.1494253
L-Asparagine	132.0	50.0	0.37878788
L-Aspartic acid	133.0	20.0	0.15037593
L-Cystine 2HCl	313.0	65.0	0.20766774
L-Glutamic Acid	147.0	20.0	0.13605443
L-Glutamine	146.0	300.0	2.0547945
L-Histidine	155.0	15.0	0.09677419
L-Hydroxyproline	131.0	20.0	0.15267175
L-Isoleucine	131.0	50.0	0.3816794
L-Leucine	131.0	50.0	0.3816794
L-Lysine hydrochloride	183.0	40.0	0.21857923
L-Methionine	149.0	15.0	0.10067114
L-Phenylalanine	165.0	15.0	0.09090909
L-Proline	115.0	20.0	0.17391305
L-Serine	105.0	30.0	0.2857143
L-Threonine	119.0	20.0	0.16806723
L-Tryptophan	204.0	5.0	0.024509804
L-Tyrosine disodium salt dihydrate	261.0	29.0	0.11111111
L-Valine	117.0	20.0	0.17094018
Vitamins			
Biotin	244.0	0.2	8.1967213E-4

Table 8: The composition of RPMI Physiologic Media. (continued)

Components	Molecular Weight	Concentration (mg/L)	mM
Choline chloride	140.0	3.0	0.021428572
D-Calcium pantothenate	477.0	0.25	5.24109E-4
Folic Acid	441.0	1.0	0.0022675737
Niacinamide	122.0	1.0	0.008196721
Para-Aminobenzoic Acid	137.0	1.0	0.00729927
Pyridoxine hydrochloride	206.0	1.0	0.004854369
Riboflavin	376.0	0.2	5.319149E-4
Thiamine hydrochloride	337.0	1.0	0.002967359
Vitamin B12	1355.0	0.005	3.690037E-6
i-Inositol	180.0	35.0	0.19444445
Inorganic Salts			
Calcium nitrate ($Ca(NO_3)_2$ $4H_2O$)	236.0	100.0	0.42372882
Magnesium Sulfate ($MgSO_4$) (anhyd.)	120.0	48.84	0.407
Potassium Chloride (KCl)	75.0	400.0	5.3333335
Sodium Bicarbonate ($NaHCO_3$)	84.0	2000.0	23.809525
Sodium Chloride (NaCl)	58.0	6000.0	103.44827
Sodium Phosphate dibasic (Na_2HPO_4) anhydrous	142.0	800.0	5.633803
Other Components			
D-Glucose (Dextrose)	180.0	2000.0	11.111111
Glutathione (reduced)	307.0	1.0	0.0032573289
Phenol Red	376.4	5.0	0.013283741

4.2 Materials and Methods

Cu-BTC nanoparticles were investigated for their stability in PBS and RPMI physiologic media, which are readily adjusted at a pH of 7.4. In a typical experiment, 100 mg of the Cu-BTC powder sample was added to 10 mL PBS or RPMI media. All samples were placed in a shaker incubator at 110 rpm and a temperature of 37°C for up to 72 hours. solutions were collected after 1, 3, 6, 9, 12, 24, 36 and 48 hours, filtered through a 0.22 μm syringe filter in a separate vial to be analyzed for their composition in terms of $[Cu^{2+}]$ using inductively coupled plasma-atomic emission spectroscopy (ICP-AES) technique. Solid samples were dried and used for the analysis of their composition and morphology using XRD and SEM-EDX techniques, respectively.

4.3 Results and Discussion

The structural and morphological stability of Cu-BTC in two physiologic media (PBS and RPMI) were assessed. Figure 60 illustrates the effect of time on the fate of Cu-BTC particulates when soaked in both media for up to 3 days. Initially, there was increase in the concentration of Cu^{2+} ions within the first 3 hours of Cu-BTC in PBS media along with an increase in the equilibrium concentration. This burst leaching out of the Cu^{2+} ions describes its role as a drug delivery vehicle, where it is a sign of the breakdown of the Cu-BTC structure. A sustained release of the Cu^{2+} ions was observed throughout the duration of the experiment. On the other hand, a slower rate Cu^{2+} ion release was observed in RPMI media during the first 3 hours. The highest observed concentration of Cu^{2+} ions as a result of this release was 18 ppm, which is much lower than that observed in PBS media (145 ppm). The slow burst of Cu^{2+} ions from the Cu-BTC particulates in RPMI media was sustained at the same level for the entire duration of the experiment.
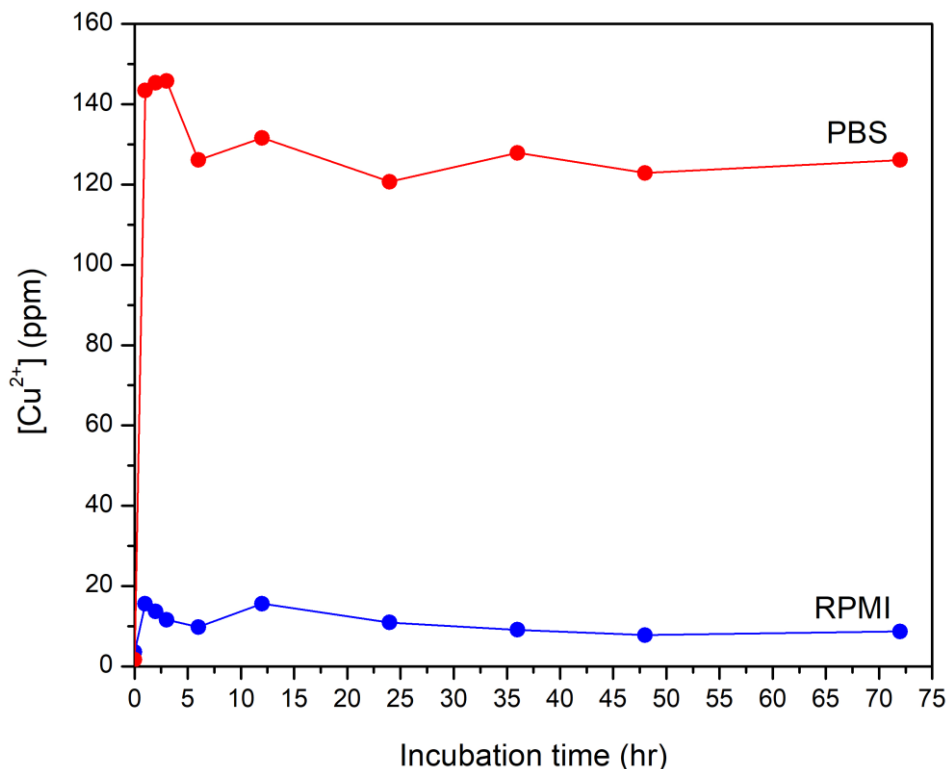
Figure 60: ICP-AES analysis of Cu²⁺ ions in PBS and RPMI media after incubation with Cu-BTC for up to 3 days.

An investigation of the structural stability of the Cu-BTC particulates after 24, 48 and 72 hours of exposure to both types of media was carried out using XRD and SEM analyses, as shown in Figures 61 and 62. The burst release of Cu^{2+} ions from the Cu-BTC particulates in PBS media was reflected in a dramatic change in the phase composition and crystallinity of the Cu-BTC structure, as shown in Figure 61 (a). The most intense peaks that characterize the structure of Cu-BTC as a MOF nanostructure at 2θ values 5-15° were diminished, leaving more intense peaks at 2θ values of 30.2, 31.2 and 35.2°. These results may indicate the destruction of the Cu-BTC structure and its conversion to Cu-coordinated BTC units. These assumptions were further proven through the examination of the SEM micrographs of the PBS-treated Cu-BTC particulates, as shown in Figure 62 (a-c). The characteristic morphology of the Cu-

BTC octahedral crystalline structures disappeared and an agglomeration of the resulting Cu-coordinated BTC crystallites was seen.

The crystallinity and phase composition of the Cu-BTC immersed in RPMI media was preserved for the entire duration of the experiment. All Cu-BTC characteristic XRD peaks were observed in the XRD patterns after 24, 48 and 72 hours. However, new peaks were observed after a 48h incubation period and further increased in intensity after 72 hours of exposure, as shown in Figure 61 (b). These peaks appeared at 2θ values of 9.3, 9.9, 10.9, 15.1, 17.1, 18.6, 21.9, 25.3, and 28.5°, and are attributed to the presence of $Cu_3(PO_4)_2$ crystalline phase with JCPDS (Joint Committee on Powder Diffraction Standards) card number 80-0992 (PramilaDevamani & Alagar, 2013). The development of this phase was also observed in the SEM micrographs of the RPMI-treated Cu-BTC particulates, as shown in Figure 62 (d-f). $Cu_3(PO_4)_2$ phase appears in its characteristic nanoflower morphology, epitaxially grown onto the Cu-BTC octahedrons. A detailed investigation of the morphology of the $Cu_3(PO_4)_2$ nanoflowers is shown in Figure 63. $Cu_3(PO_4)_2$ nanoflowers are formed from the agglomeration of $Cu_3(PO_4)_2$ nano-flakes adopting the spherical flower morphology, producing a hierarchical MOF Cu-BTC@$Cu_3(PO_4)_2$ core-shell NF. An EDX analysis of the $Cu_3(PO_4)_2$ nanoflowers at two different spots is shown in Figure 63 (c-d), in which the elemental composition of the $Cu_3(PO_4)_2$ nanoflowers where Cu, P and O elements were shown in addition to possible contamination with Na and Cl which are present in the form of soluble ions in the RPMI media. This work exhibits the mechanism Cu^{2+} ions leaching out from Cu-BTC octahedra, reacting with phosphate ions (800 ppm) in the surrounding RPMI medium, forming $Cu_3(PO_4)_2$. Once the precipitation of copper phosphate develops, metal-protein crystals nucleate into larger molecules, where petals start to form and continue to grow into a flower-like scaffold,

aided by the existing protein in the media. Figure 64 (a) shows a magnified image of the SEM micrograph in Figure 63 (a), where the process of nucleation of the $Cu_3(PO_4)_2$ nanoflowers is highlighted. Accordingly, the process of self-assembly of the precipitated leaflets and its further growth and agglomeration in the form of $Cu_3(PO_4)_2$ nanoflowers is outlined in Figure 64 (b).
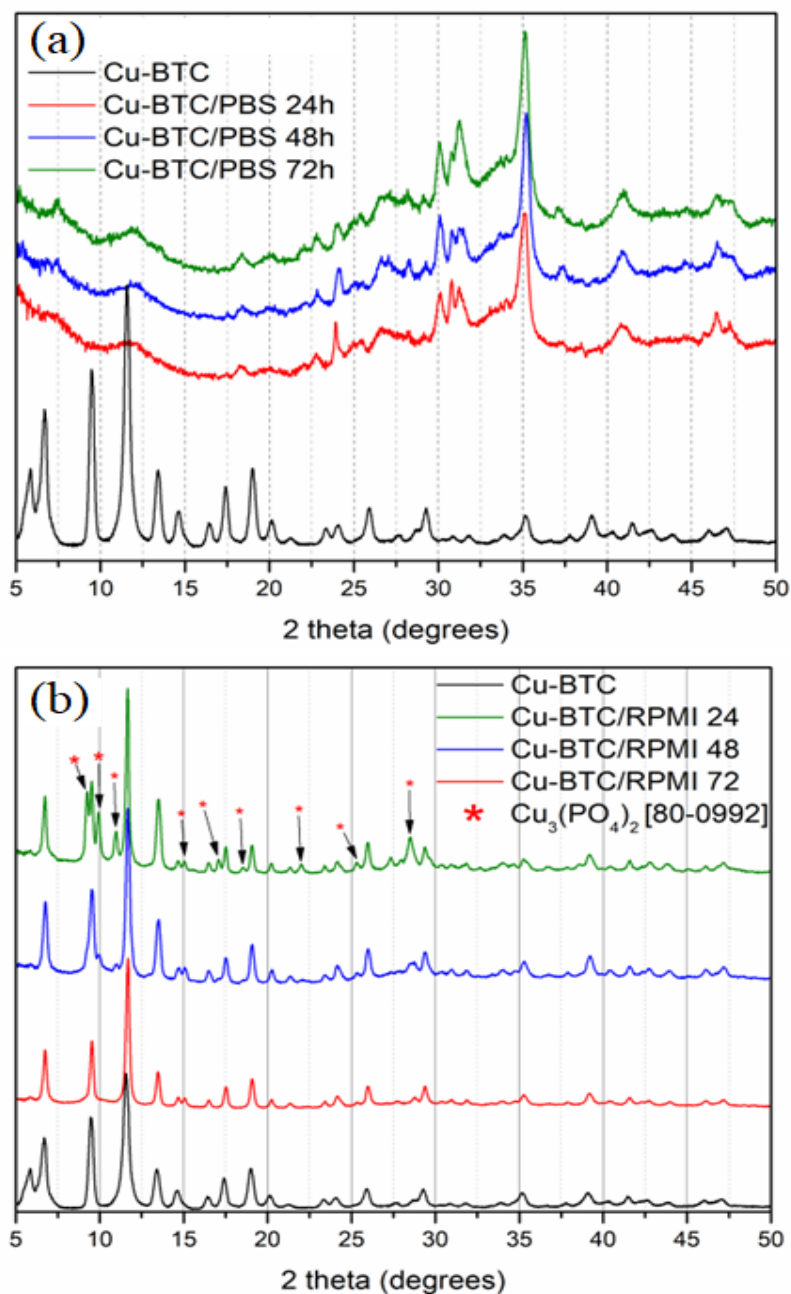
Figure 61: XRD patterns of Cu-BTC particulates incubated in a) PBS and b) RPMI media for 24, 48 and 72 hours at 37°C. XRD pattern of pristine Cu-BTC MOF is included for comparison.
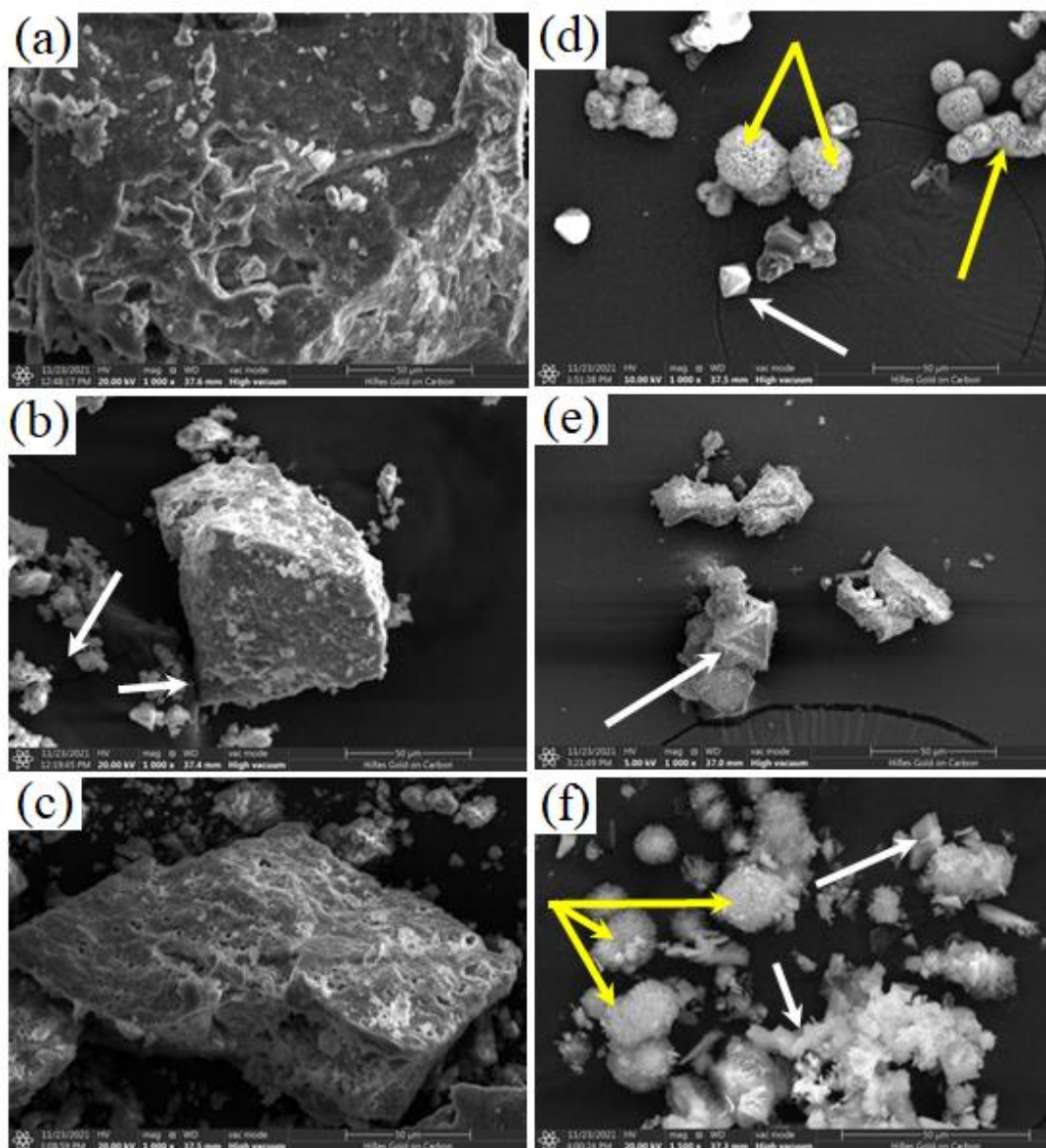
Figure 62: SEM micrographs of Cu-BTC suspended in PBS (left) and RPMI (right) physiological media at 37°C x up to 72 hours. a, d) 24 hours b, e) 48 hours and c, f) 72 hours. Cu-BTC crystals are indicated by white arrows and copper phosphate NF formation are referred to by yellow arrows.
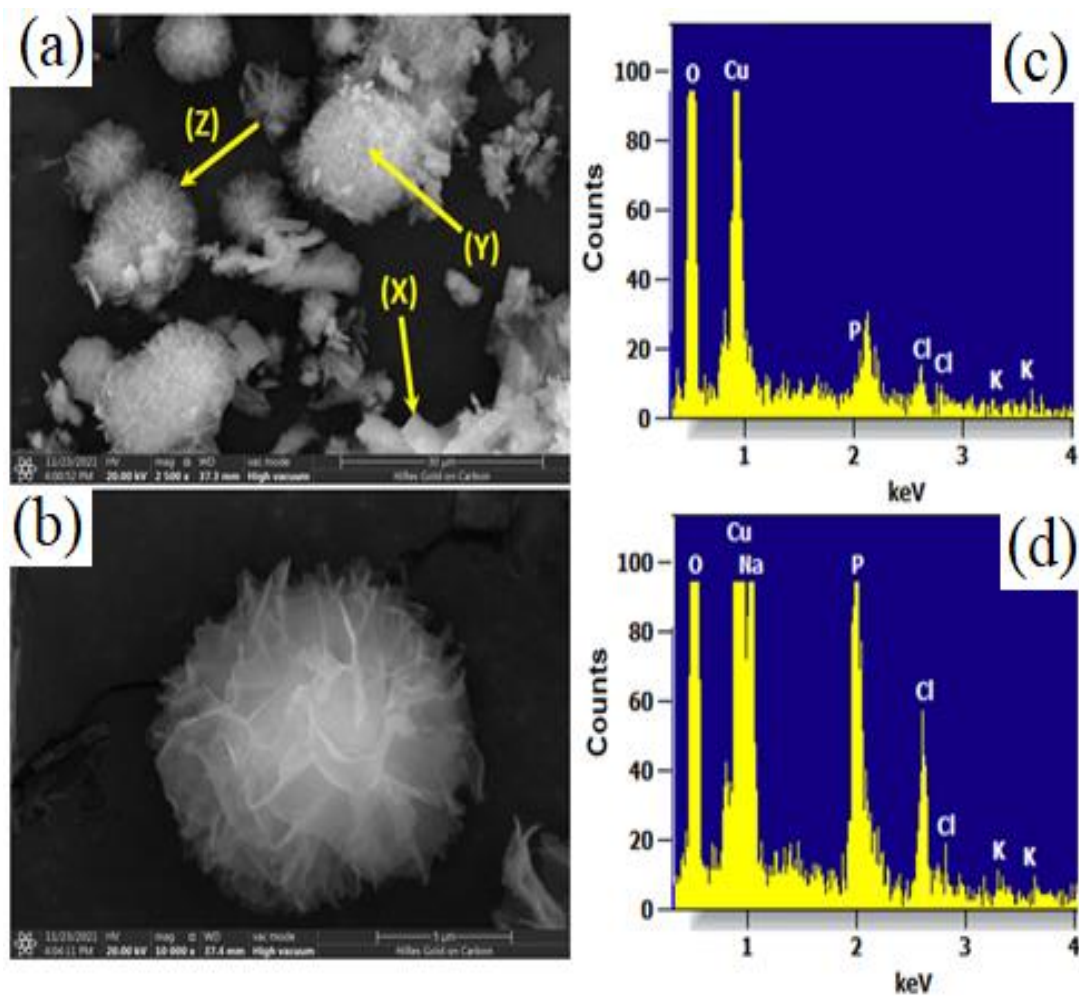
Figure 63: a) SEM micrograph of Cu-BTC@Cu$_3$(PO$_4$)$_2$ MOF core-shell NF and b) EDX selected spot analysis of points (x) in (c) and (Y) in (d). The process of nanoflowers growth is referred to by the arrow in (z).
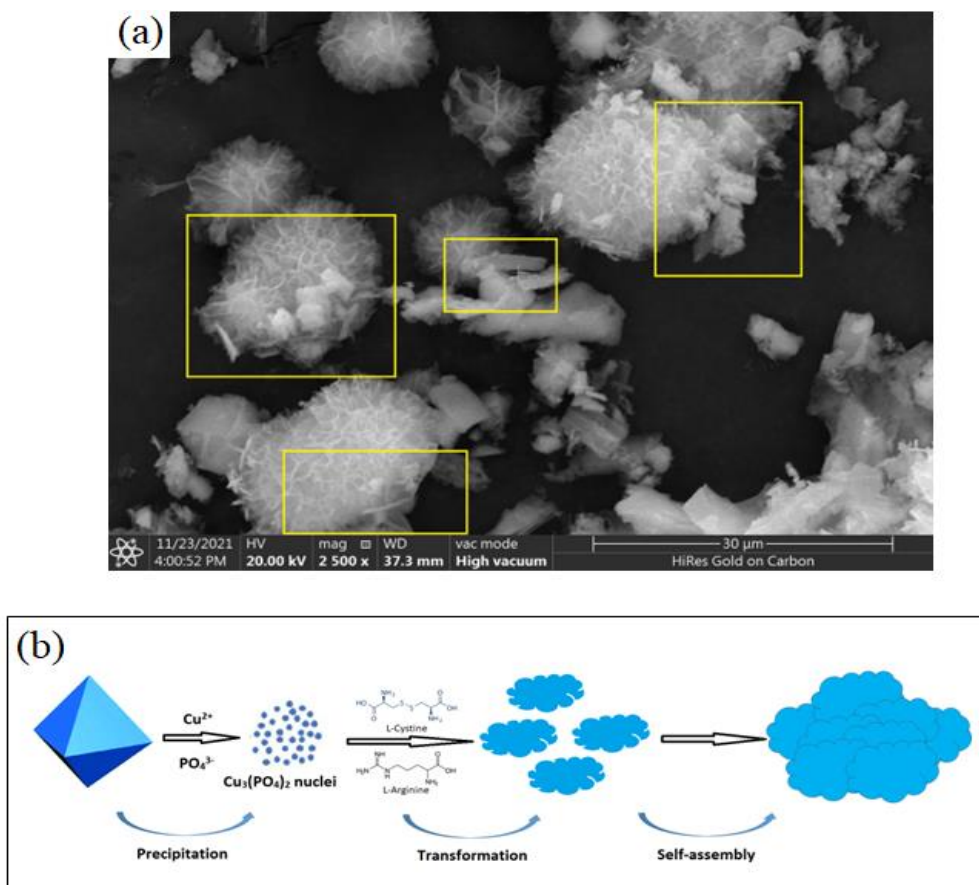
Figure 64: a) A magnified SEM micrograph showing the epitaxial growth of $Cu_3(PO_4)_2$ nanoflowers onto the surfaces of Cu-BTC MOF crystals after incubation with RPMI media for 72 hours at 37°C. and b) a schematic representation of the mechanism of hierarchical Cu-BTC@$Cu_3(PO_4)_2$ MOF core-shell NF formation.

4.4 Conclusion

A hybrid organic-inorganic NF was developed for the overall stability of the MOF structures listed in this work. The goal is to control the amount of copper leaching from the copper-based MOFs for the sustained release in biological applications. Previously, NFs were proven to enhance catalytic activity and the stability of enzymes. In particular, copper-based NFs exhibit intrinsic peroxidase-like activity, which could potentially augment the anti-cancer and ant-bacterial activity of our MOFs. These flower-shaped NPs are simply "grown" from the Cu^{2+} ions present in the MOF, in PBS, and amino acids yielding hierarchical Cu-BTC@$Cu_3(PO_4)_2$ core-shell NFs.

Chapter 5: Copper-based Metal-Organic Frameworks and Their Anti-gastric and Anti-colon Cancer Activities

5.1 Introduction

Gastric Cancer is the second most common cause of cancer death worldwide, especially among older males, and any advancement in treatment and prevention would have a global significance (World Health Organization, 2018). The incidence and mortality rates vary from region to region but the majority of new diagnoses per year occur mainly in Asian and South American countries (World Cancer Research Fund, 2016). Risk factors include genetics, smoking, diet, prior stomach surgery, race, age, and/or being infected with *Helicobacter pylori (H. pylori)* (American Institute for Cancer Research). The 5-year survival rate has increased from 15% to 31% in the United States with the latest advancements in chemotherapy (Bando et al., 2016). However, the 5-year survival rate worldwide remains at 25% due to diagnoses of the deadly cancer at later stages and due to chemotherapy resistance (Sexton et al., 2020). Researchers are continuously working on improved treatment monitoring, early diagnosis and targeted therapy to increase the survival rates for this deadly disease. Current treatment for *in situ* gastric cancers include surgery, radiation and chemotherapy, however, metastatic stages do not usually respond to these traditional forms of treatment (Comis & Carter, 1974; Cui et al., 2015; Dicken et al., 2005; Kuo et al., 2014; Proserpio et al., 2014; Takahashi et al., 2013; Uemura et al., 2001). Furthermore, colon cancer, the third most common cancer in both men and women, is the third leading cause of cancer related deaths in the world (Division of Cancer Prevention and Control, 2021; Fund, 2022). Most colorectal cancers are asymptomatic and can reach deadlier stages without early diagnosis and detection (Clinic, 2020a).

Therefore, the goal is to detect, diagnose, and kill gastric and colon cancer cells at an early stage to prevent these deadly diseases from metastasizing in patients.

Certain metals can act as a Fenton catalysts including, Cu^{2+}, Fe^{2+} and Mn^{2+}, owing to the mechanism of MOF materials in the Fenton-like reaction (Yang et al., 2019). Recently, Li et al. used Cu-BTC for the PTT of colon cancer cells (CT26) (Li, et al., 2020). The cancer cells exhibited a gradual decrease in cell viability with an increased concentration of the Cu-MOF when compared to normal mouse fibroblast cells (L929). The authors attributed this selectivity due to the high levels of H_2O_2 in the cancer cells. Additionally, GA can generate ROS, causing oxidative stress and overall apoptosis in cancer cells (Babich et al., 2011). This work examines BioMOFs, Cu-BTC and Cu-GA, for their efficacy against gastric and colon cancer cells.

5.2 Materials and Methods

Cytotoxicity assay (gastric cancer cells): The cytotoxic activity of Cu-BTC and Cu-GA was analyzed by the 3-(4,5-dimethylthiazol-2-yl)-2,5-diphenyltetrazolium bromide (MTT) method (Mosmann, 1983). Mouse gastric cancer stem cells (mGS), human gastric cancer stem cells (AGS) and normal mouse cells (L929) were seeded in quadruplicates into 96-well plates at a density of 5,000 cells per well in RPMI containing 10% FBS, 1% penicillin-streptomycin, 25mM HEPES and cultured overnight at 37°C in a humidified incubator with 5% CO_2. After 24 hours the culture media was removed with a suction and replaced with fresh media containing Cu-BTC with various concentrations (2.5, 5, 10, 25, 50, and 75 µg/mL) and with Cu-GA, the same concentrations were used against mGS cancer cells but concentrations of 5, 10, 15, 25, 50, and 100 µg/mL were chosen for AGS cancer cells. For the control, the vehicle (PBS) was used. After 24 and 48 hours of incubation, MTT solution was added

to a final concentration of 0.5 mg/mL and the plates were further incubated at 37°C for 4 hours. The culture media containing MTT was then aspirated carefully and 150 µL of DMSO was added to each well for dissolving the developed formazan crystals. The plates were kept on a shaker for 5 minutes at room temperature and the absorbance was taken at 570 nm and 690 nm using BioTek microplate reader.

Cytotoxicity assay (colon cancer cells): Colorectal carcinoma cell, HCT116 cell line, was used in this study. The HCT116 cells were cultured in McCoy's Medium (Hyclone). The medium was supplemented with 10% fetal bovine serum (Sigma Aldrich) containing 1% of 100 U/ml penicillin and 100 µg/ml streptomycin (Sigma Aldrich) at 37 °C in a humidified 5% CO2 atmosphere. Cells were sub-cultured every 3–5 days using Trypsin 0.25% (Hyclone). Cu-BTC and Cu-GA were mixed in the culture medium to prepare a stock of 1mg/ml. The stock was further diluted into working concentrations with the cell culture medium. The compound suspension was made on the day of treatment. All cells were seeded at a density of 5000 cells/well in 96-well plates in 100 µl of complete growth medium. Cells were allowed to attach for 24h before being treated with different concentrations (2.5, 5, 10, 25, 50 and 75 µg/ml, for Cu-GA) and (2.5, 5, 10, 25, 50, 75 and 100 µg/ml, for Cu-BTC) of the MOF for 24h and 48h time periods. Cells were then treated with each MOF for 24h and 48h. The formed formazan crystals were dissolved using DMSO and the absorbance of the resulting product was measured at 570 nm using GloMax Microplate Reader (Promega). Cell viability is the percent of viable cells = (Abs. of treated cells/Abs. of control cells) X 100. The experiment was carried out in triplicates

5.3 Results and Discussion

Gastric cancer inhibition by Cu-BTC

Cu-BTC was evaluated for its cytotoxic activity against mGS and AGS cell lines following a 24h and 48h incubation period. Figure 65 depicts the cell viability results after both time points. The increase in the concentration of Cu-BTC is associated with a decrease in the viability of both types of cells. At 10 µg/ml concentration, the mGS cells lost about 50% of their viability within one day and within two days at the same concentration, they lost almost 75% of their viability. In the case of AGS cells, the 10 µg/ml concentration for 1 day led to loss of a 55% drop in the viability. By 2 days, 65% of the cells lost their viability. Cu-BTC had little to no effect on the cell viability in L929 cells for up to a concentration of 25 µg/mL, as seen in Figure 65. At 25 µg/mL, the cell viability in L929 cells was 4-fold and 4.7-fold higher than AGS cells after 24 and 48 hours, respectively. Furthermore, at the same concentration, cell viability in L929 cells was almost 21-fold higher than mGS cells after a 48h incubation period, indicating that Cu-BTC was more potent against mGS and AGS cells than normal mouse L929 cells.

A microscopic examination of the mGS cells post-treatment can be seen in Figure 66. decrease of cell viability percentages is also correlated with the increase in the number of floating "dead" cells. Moreover, the close microscopic examination of the cells revealed small clumps of floating cells appearing at 10 µg/mL, becoming more apparent with increasing MOF concentration up to 75 µg/mL (Figure 66).

On the basis of previous reports, the mechanism of the Cu-based MOF is to catalyze overexpressed H_2O_2 within the tumor microenvironment to generate toxic hydroxy radicals (OH), leading to apoptosis in colon cancer cells (Li et al., 2020). Another mode of action, according to the literature, is the changes of gene expression

and actin cytoskeleton inflicted on SKOV3 cancer cells by Cu-BTC (Li et al., 2020). The MOF successfully induced programmed cell death by disrupting microtubule dynamics and disruption of F-actin on SKOV3 cancer cells. However, these results were not observed on A549, HT-29, and KB cell lines, indicating the specificity of the MOF to certain types of cancers (Chen et al., 2020). In this work, Cu-BTC displayed promising results in both gastric cancer cell lines used, mGS and AGS.

Gastric cancer inhibition by Cu-GA

Cu-GA was also evaluated for its cytotoxic activity against mGS and AGS cell lines following a 24h and 48h incubation period. Figure 67 displays the cell viability results after both time points. The effect of Cu-GA on the mGS cell line was not as dramatic as AGS cancer cells for both 24 and 48 hours. In mGS cells, there was only a noticeable inhibition of cell growth after 48h with 50 µg/mL of Cu-GA. However, after 24 hours, a 25 µg/mL and 50 µg/mL concentration led to almost a 60 and 15% decrease in cell viability with AGS cancer cells, respectively. After day two, AGS cells experienced almost total cell death at 75 µg/mL. This can also be seen in the microscopic images of AGS cells after 24h treatment with Cu-GA (Figure 68). The number of live cells diminish with increasing concentrations of the MOF. A concentration of 100 µg/mL causes almost all cells to shrink and float, as shown in the microscopic image.
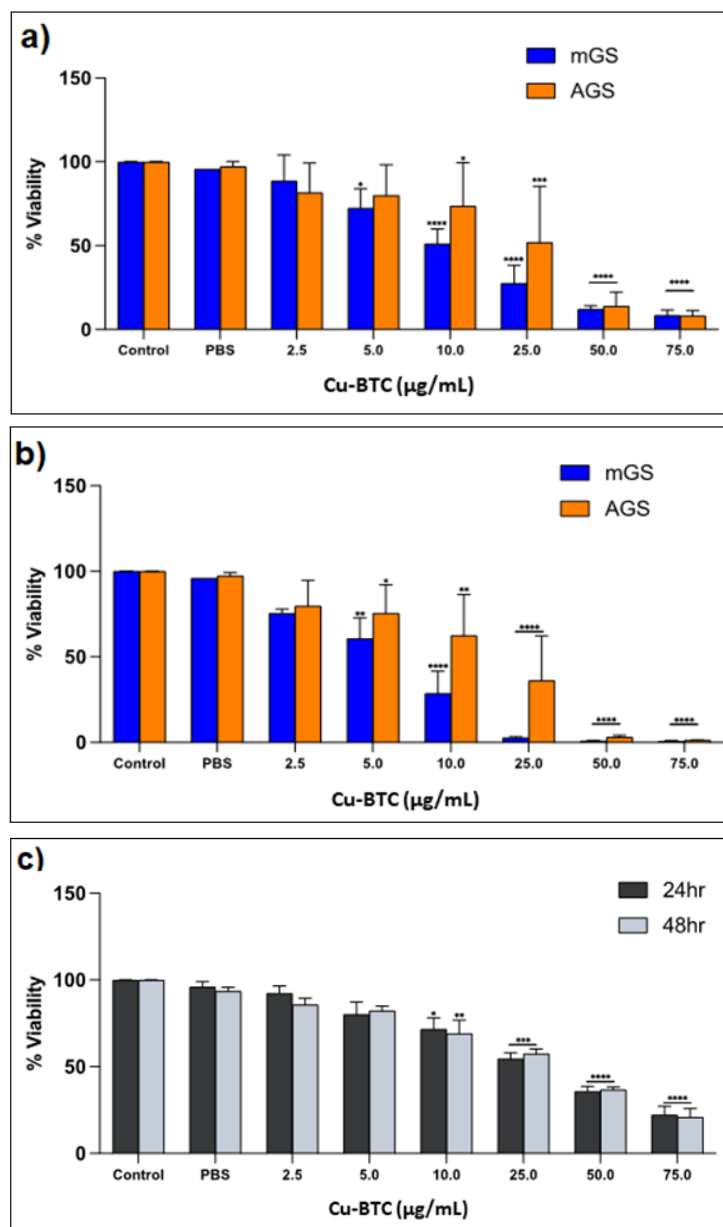
Figure 65: Cell viability assay demonstrating the effects of Cu-BTC on a) 24h incubation on mGS and AGS cancer cells b) 48h incubation on mGS and AGS cancer cells and c) 24h and 48h incubation on L929 normal fibroblasts.
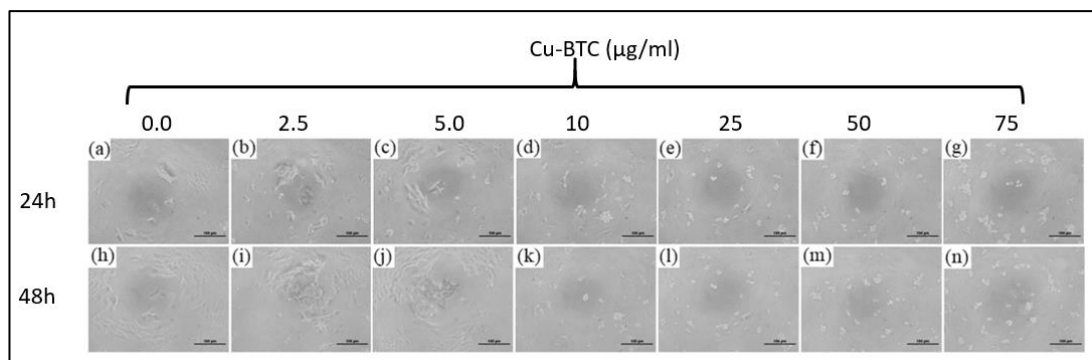
Figure 66: Microscopic images of mGS cancer cells treated with Cu-BTC after 24h (a-g) and 48 (h-n) hours in culture, treated with (a, h) 0 (control), (b, i) 2.5 µg/mL, (c, j) 5 ug/mL, (d, k) 10 ug/mL, (e, l) 25 ug/mL, (f, m) 50 ug/mL, and (g, n) 75 ug/mL at 37°C. Scale bar = 100 µm
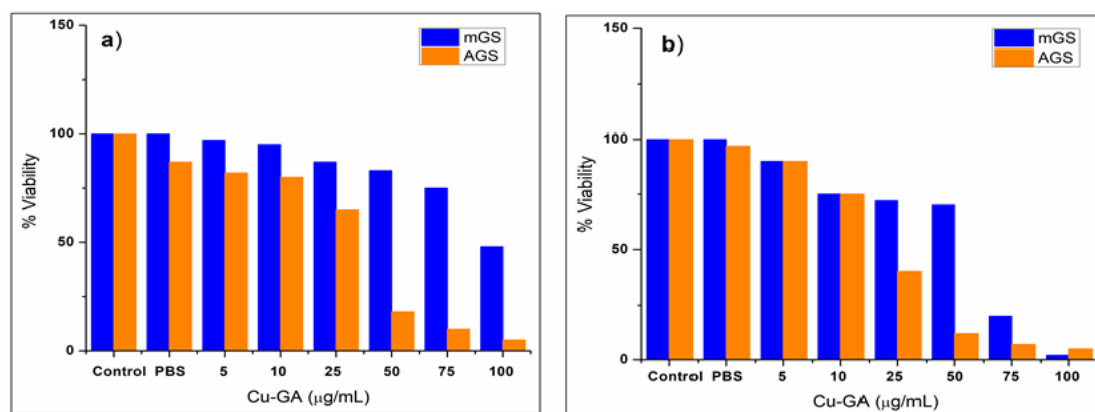
Figure 67: Cell viability assay demonstrating the effects of Cu-GA on a) 24h incubation on mGS and AGS cancer cells b) 48h incubation on mGS and AGS cancer cells
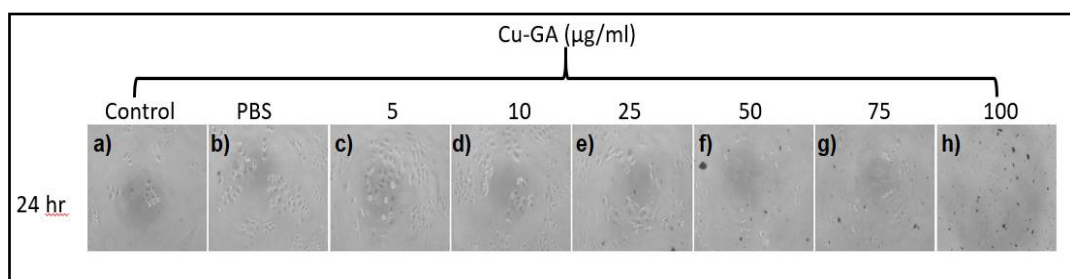
Figure 68: Microscopic images of AGS cancer cells treated with Cu-GA after 24h in culture. a) 0 (control), b) PBS, c) 5 ug/mL, d) 10 ug/mL, e) 25 ug/mL, f) 50 ug/mL, g) 75 ug/mL, and h) 100 µg/mL at 37°C. Scale bar = 100 µm.

Colon cancer inhibition by Cu-BTC

Cu-BTC barely displayed an inhibitory effect on HCT116 cells. The cells treated with the MOF powder at 24h exhibited healthy grown cells that were comparable to the control (untreated cells). After 48h, the cell viability decreased by about 20% with a concentration of 50 µg/mL and a 60% loss at 100 µg/mL, as shown in Figure 69. This was also mirrored in the microscopic images in Figure 70. The number of 'live' cells can be seen throughout all concentrations, with very minimal 'dead' for floating cells.
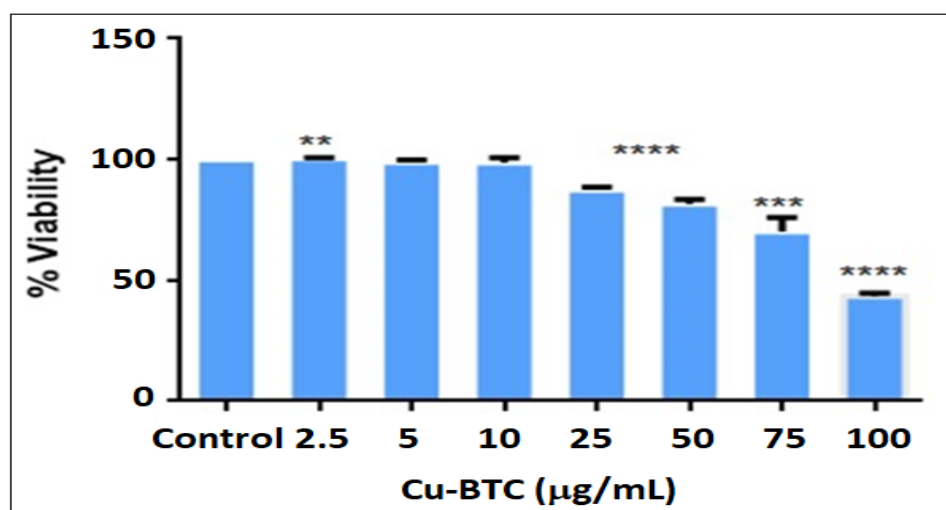
Figure 69: Cell viability assay demonstrating the effects after 48 hours of incubation with Cu-BTC on HCT116 colon cancer cells.
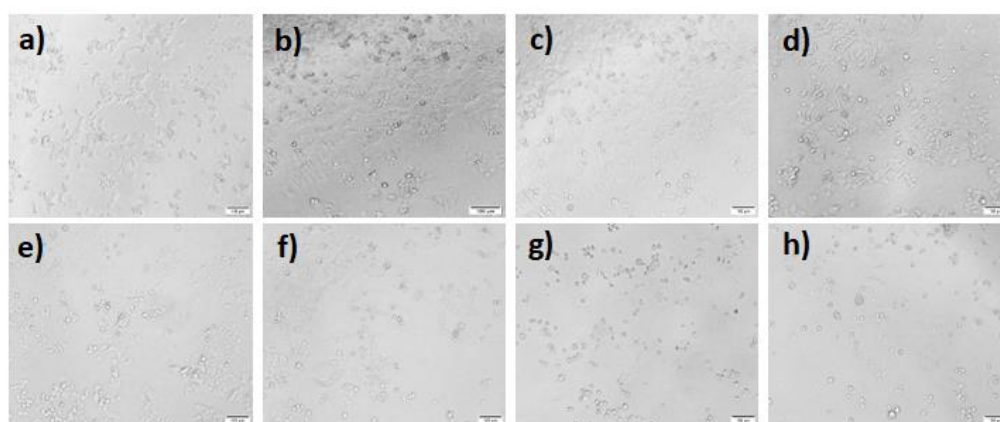
Figure 70: Microscopic images of HCT116 colon cancer cells treated with Cu-BTC after 24h in culture. a) 0 (control), b) 2.5 ug/mL, c) 5 ug/mL, d) 10 ug/mL, e) 25 ug/mL, f) 50 ug/mL, g) 75 ug/mL, and h) 100 µg/mL at 37ºC. Scale bar = 100 µm.

Colon cancer inhibition by Cu-GA: Contrary to the results exhibited by Cu-BTC, Cu-GA demonstrated impressive cytotoxic activity against HCT116 cells. After just one day of treatment with the MOF powder, cell viability decreased by about 40% with the lowest concentration used (2.5 µg/mL). Furthermore, a Cu-GA concentration of 50 µg/mL caused a 70% loss of cell viability. The results in Figure 71 show that Cu-GA could obviously decrease the viability of HCT116 cells in a dose-dependent manner compared with the control. In addition, the microscopic images of HCT116 cells treated with Cu-GA (Figure 72) illustrate obvious 'dead' or floating cells. This can be seen in the lowest concentration (2.5 µg/mL) of treatment with Cu-GA. Once reaching the highest concentration of Cu-GA (75 µg/mL), the presence of 'live' or healthy cells are almost completely diminished.

The half maximal inhibitory concentration (IC_{50}) of Cu-GA against HCT116 cells was 15 µg/mL, which is much less than the IC_{50} of Cu-BTC (99 µg/mL). This result indicates that HCT116 cells are much more sensitive to Cu-GA MOF compared to Cu-BTC.
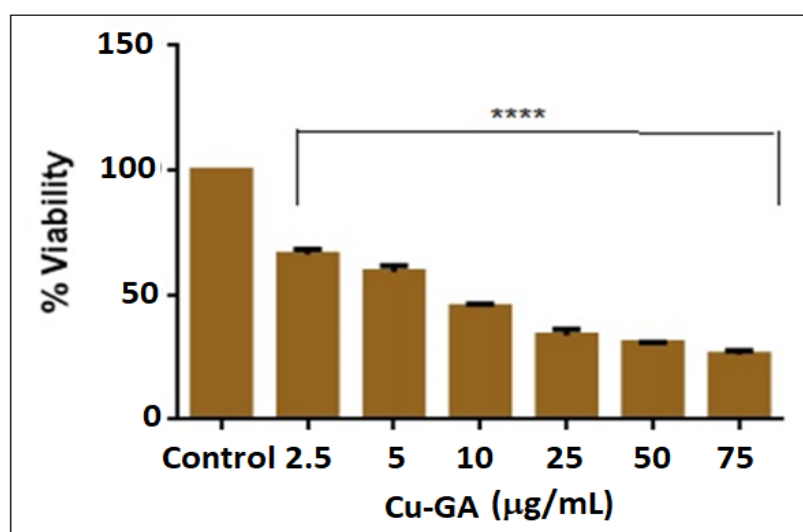
Figure 71: Cell viability assay demonstrating the effects after 24 hours of incubation with Cu-GA on HCT116 colon cancer cells.
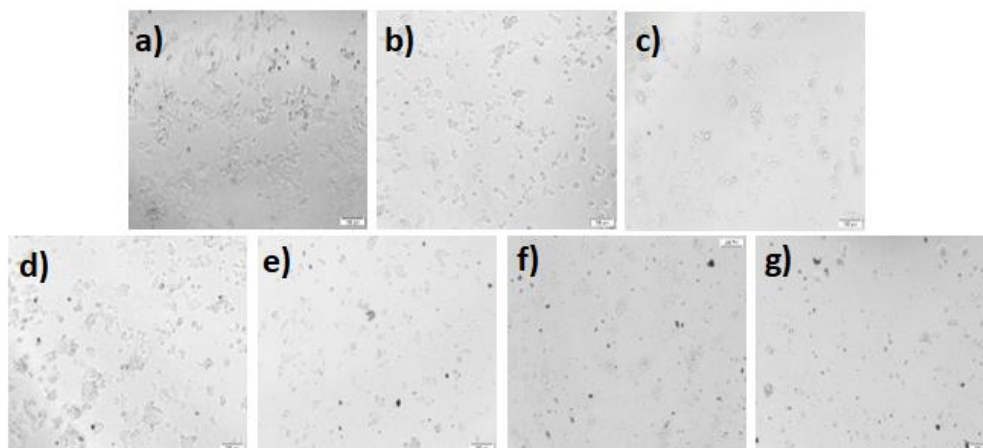
Figure 72: Microscopic images of HCT116 colon cancer cells treated with Cu-GA after 24h in culture. a) 0 (control), b) 2.5 ug/mL, c) 5 ug/mL, d) 10 ug/mL, e) 25 ug/mL, f) 50 ug/mL, and g) 75 ug/mL at 37°C. Scale bar = 100 µm.

5.4 Conclusion

The first demonstration of Cu-BTC and Cu-GA as a stand-alone treatment against gastric cancer and colorectal carcinoma cells (HCT116) is presented in this work. The cytotoxicity studies revealed that both MOFs were successful in inhibiting both gastric cancer cells but only Cu-GA showed promising effects against HCT116 colon cancer cells. Gastric cancer cells exhibited a higher sensitivity to Cu-BTC when compared to Cu-GA. Meanwhile, Cu-GA was more specific to HCT116 colon cancer cells, causing almost complete cell inhibition in a dose-dependent manner. The inhibitory activity of Cu-BTC and Cu-GA is due to the ability to induce ROS production and accumulation, leading to a decrease in cell viability.

Chapter 6: Copper-based Metal-Organic Frameworks as Anti-bacterial Agents Against E. coli and Lactobacillus

6.1 Introduction

Antibiotic resistance is a major public health threat that is rapidly emerging due to the unneeded and overuse of antibiotics in the past years (Gao & Zhang, 2021). If resistance continues without the development of effective alternatives, bacterial infections will become untreatable once again (Cox et al., 2019). Bacteria can develop resistance through various mechanisms in which traditional antibiotics can no longer be effective against (Blair et al., 2015). Copper-based MOFs can cause bacterial damage inhibit further bacterial growth without the need of antibiotic drugs. GA or 3,4,5-trihydroxybenzoic acid, is a phenolic compound that is known for its anti-inflammatory (Karimi-Khouzani et al., 2017), anticarcinogenic (Rezaei-Seresht et al., 2019), antimicrobial (Kang et al., 2008), antifungal (Li et al., 2017) and antioxidant (Inoue et al., 1994) effects. The polyphenol compound has proven to disrupt the integrity of the cell membrane and inhibit the motility of various bacteria and biofilm (Borges et al., 2012; Kang et al., 2008; Li et al., 2007; Shao et al., 2015). The antimicrobial effect is due to the disintegration of the cell membrane and the leakage of intracellular bacterial constituents (Borges et al., 2013; Nohynek et al., 2006). GA can also act as a pro-oxidant by generating ROS, and ultimately causing oxidative stress in cells (Babich et al., 2011). Wang et al, enhanced the antimicrobial activity of GA against *Escherichia coli (E. Coli)* O157:H7 by using a UV-A light for photo-irradiation (Wang et al., 2017). They discovered that the UV-A light enhanced the internalization of GA into the bacteria allowing for increased ROS accumulation and oxidative damage to cells. GA has also reported to inhibit the activity of bacterial

dihydrofolate reductase and its effect on DNA cleavage in various bacteria (Enwa, 2014). However, GA is readily metabolized after digestion and its efficacy is limited due to its poor bioavailability (Yang et al., 2020). The goal is to increase absorption, reduce the elimination rate and improve the overall bioavailability of GA. Additionally, Cu-BTC was studied for its antimicrobial activity against *E. coli* and *S. aureus* (Ouyang et al., 2021; Su et al., 2019). The study revealed that the MOF material was able to inhibit bacterial growth at high concentrations (900 mg/L for *E. coli* and 1200 mg/L for *S. aureus*). Bacterial death was due to the loss of the cytoplasm and flagella when treated with Cu-BTC and oxidative stress led to further membrane and DNA damage, as shown in Figure 73 (Ouyang et al., 2021).
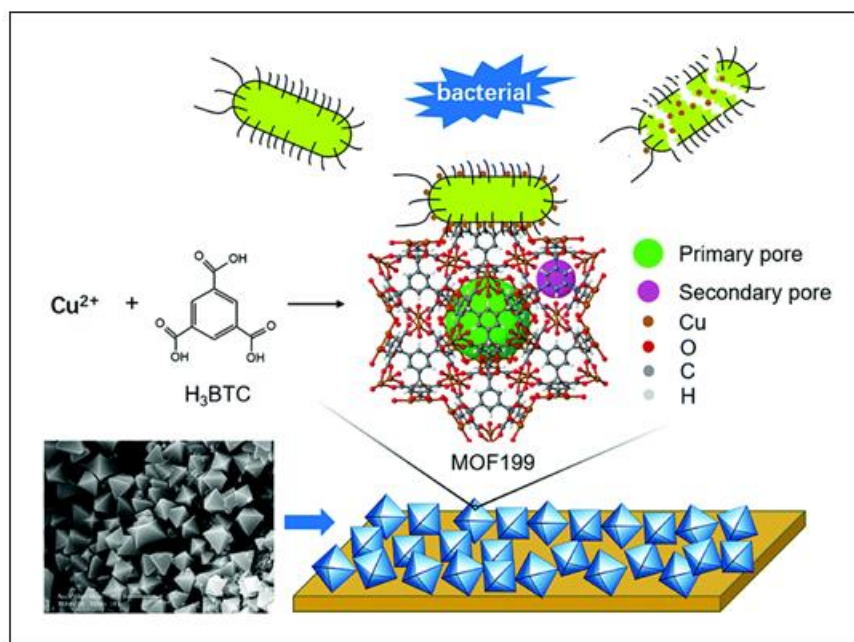
Figure 73: The fabrication of MOF-deposited woody materials and their anti-bacterial mechanism. (Ouyang et al., 2021).

Cu-BTC and Cu-GA were both tested *E. coli* (gram-negative) and *Lactobacillus* (gram-positive) for their antibacterial effects. To investigate the

sustained release of both bioMOFs we compared the zone of inhibition with two controls, Cu salt and free GA.

6.2 Materials and Methods

Zone of inhibition. The antimicrobial activity of Cu-BTC and Cu-GA was determined on *E.coli* BL21 (DE3) (gram-negative) (Strategene, USA) and *Lactobacillus* (gram-positive) cells using standard zone of inhibition or dynamic contact (ASTM E2149-13a) method with some modifications as described below (a). Fresh inoculum of *E. coli* and *Lactobacillus* cells were spread on LB agar plates to obtain a smooth microbial lawn. A 1 cm MOF disk was directly placed in the center of the plate. The antibacterial behavior of the MOF was observed after 12, 24, and 48 hours incubation at 37°, 25° and 16°C, respectively. The lower incubation temperatures, 25°C and 16°C were used to avoid the fast growth of the bacterium and provide enough time for Cu leaching from MOF to observe the antimicrobial activity of the sample for a longer time of 24 and 48 hours. A similar sized disk using copper(II) acetate and GA were used as controls. The diameter of non-growth around the MOF disk of each sample was measured per mm. The relationship between incubation time and inhibition zone was plotted on a graph.

Elucidation of the minimum inhibitory concentration (MIC). To determine the lowest concentration of Cu-BTC and Cu-GA needed for inhibiting growth of *E. coli* and *Lactobacillus* strains, MIC was measured according to microtiter broth dilution method (Moghimi et al., 2016; Xu et al., 2017). 5 µL of individual bacterial suspension, with a final concentration of 1×10^5 CFU mL^{-1}, was prepared in LB broth and added to each well in a 96 well plate. Each MOF was diluted two folds in the wells ranging concentration from 7.81 ug to 2mg. Plates were incubated at 37°C for 24h for antibacterial assessment. A negative control, without MOF powder, was also assessed

for its antibacterial activity. Absorbance of wells was measured at a wavelength of 600 nm and the MIC of both MOFs was recorded as the well that exhibited no visible growth of either bacterial strain.

Agarose gel electrophoresis for DNA disintegration. Agarose gel electrophoresis was used to analyze the destruction and disintegration of DNA for assessing cell death caused by Cu-BTC. *E. coli* was treated with Cu-BTC using various concentrations (0 – 1.5 x MIC) and incubated at 37°C for 24h. Each sample was collected, after 24h, centrifuged and their DNA was extracted using a Wizard® Genomic DNA purification kit (Promega). NanoDrop 2000 (Thermofisher) was used to quantify and qualify the DNA. 5 µl of each Cu-BTC treated sample was mixed with 1.5 µl of the loading dye and run through an agarose gel.

6.3 Results and Discussion

Zone of inhibition. To determine the antibacterial effects of Cu-BTC and Cu-GA, *E. coli* (gram negative) and *Lactobacillus* (gram-positive) were the chosen bacterial strains. A qualitative and quantitative analysis of these characteristics was carried out following a standard procedure (ASTM E2149-13a) (a). A clear zone of inhibition with an increasing diameter around the sample disks incubated with *E. coli* and *Lactobacillus* was observed after 12 hours, 24 hours and 48 hours. The larger inhibition zone with a longer exposure time is attributed to the increased extent of leaching out of the Cu^{2+} ions from both MOFs with time. At 12 hours, Cu-BTC exhibited a 2 mm and 6.5 mm zone of inhibition with *E. coli* and *Lactobacillus*, respectively (Figure 74 and 75). Cu-GA exhibited a wider zone of inhibition against in *E. coli,* with a 5.5 mm zone, but only appeared to have a 1 mm zone of inhibition with *Lactobacillus* (Figure 76 and 77). After 48 hours, Cu-BTC displayed a 4 mm zone of inhibition in *E. coli*, whereas Cu-GA observed an impressive 17 mm zone. Cu-GA

also inhibited a much larger zone than Cu-BTC in *E. coli* at 24 hours, which can be attributed to the synergistic effect of copper and GA in the MOF structure. Copper (II) acetate and pure GA were used as controls to prove the inhibiting effect of both constituents contained in the MOF structures. With *E. coli*, the metal salt displayed a 13, 17, and 23.5 mm zone of inhibition at 12, 24, and 48 hours, respectively (Figure 78 and 79). Similar results were seen in *Lactobacillus*, as shown in Figures 80 and 81.
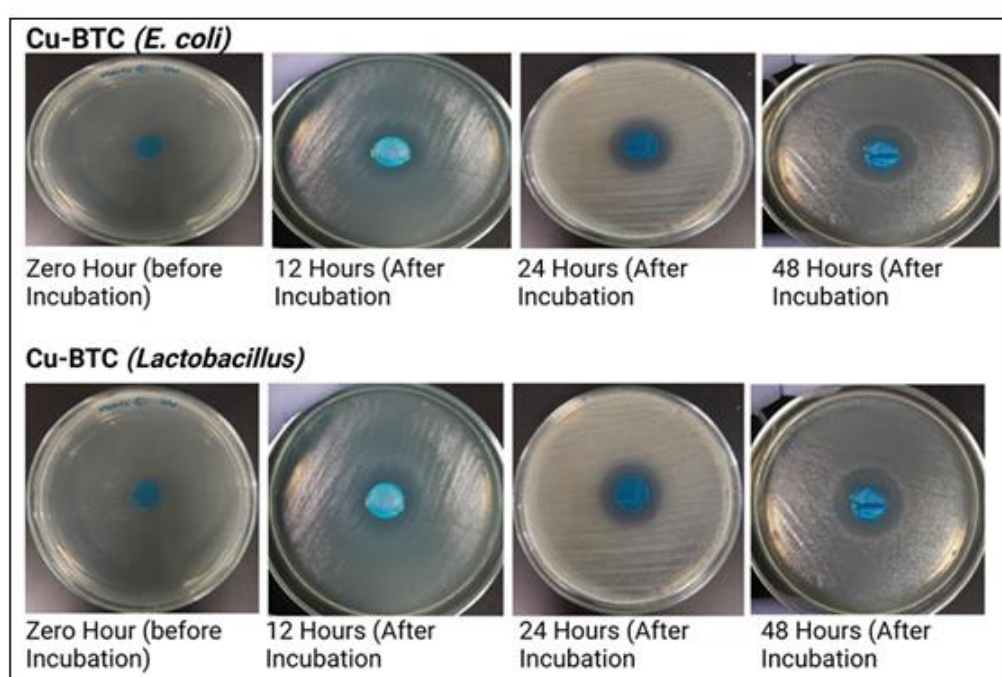
Figure 74: Antibacterial activity results Cu-BTC against *E. coli* and *Lactobacillus*.
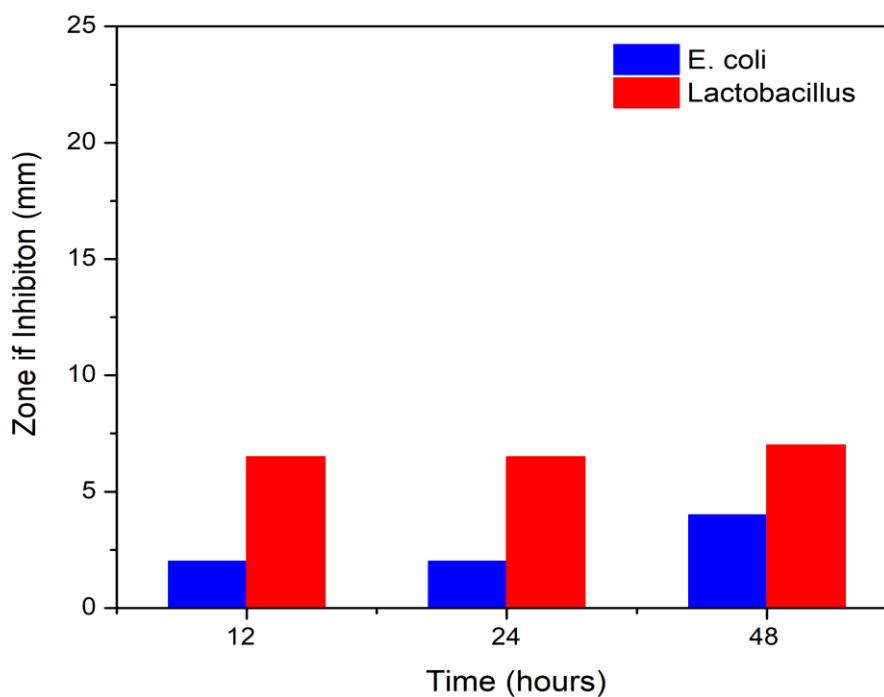
Figure 75: Diameters of zones of inhibition for Cu-BTC towards *E. coli* and *Lactobacillus*.
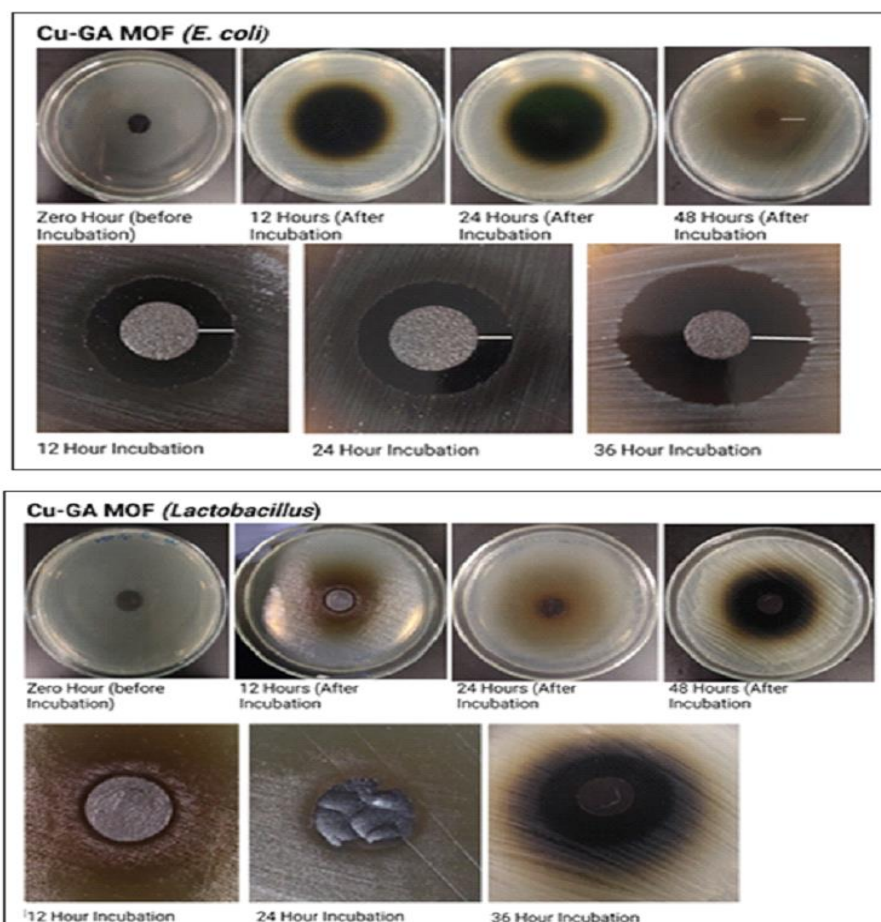
Figure 76: Antibacterial activity results Cu-GA against *E. coli* and *Lactobacillus*.
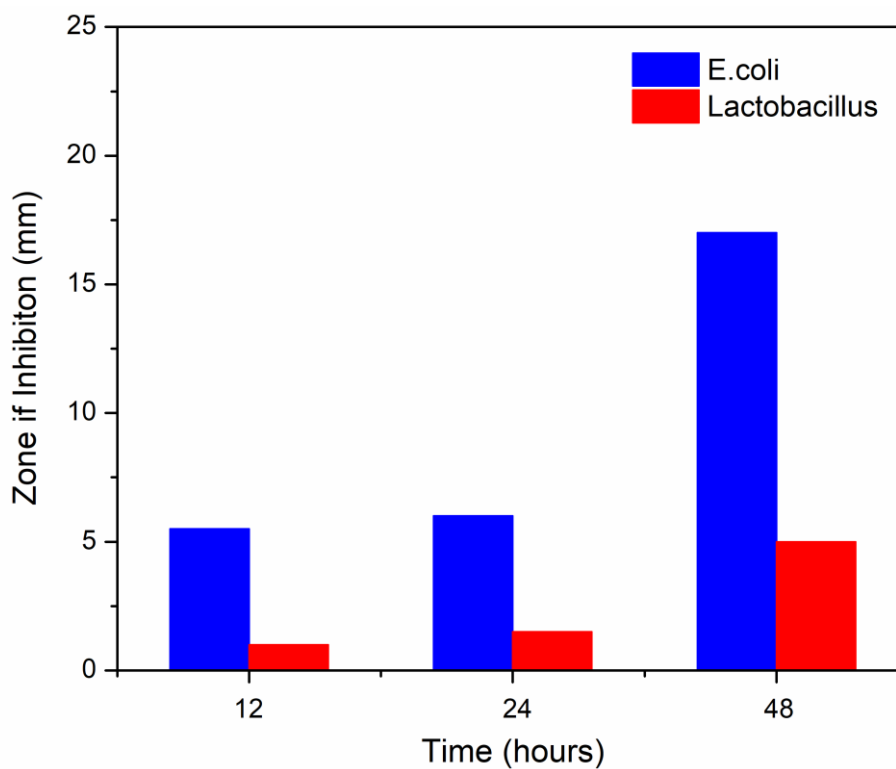
Figure 77: Diameters of zones of inhibition for Cu-GA towards *E. coli* and *Lactobacillus.*
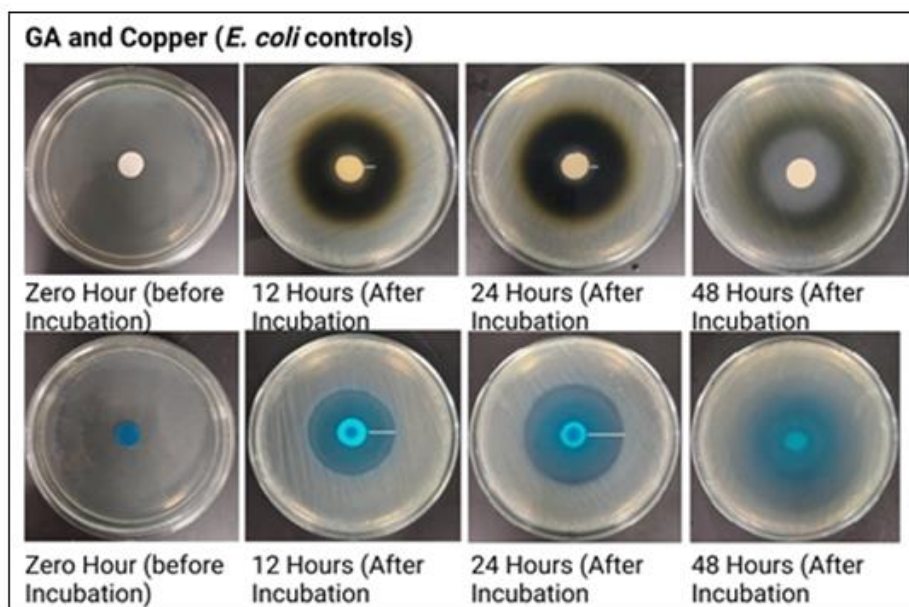
Figure 78: Antibacterial activity results of copper acetate and gallic acid controls against *E. coli*.
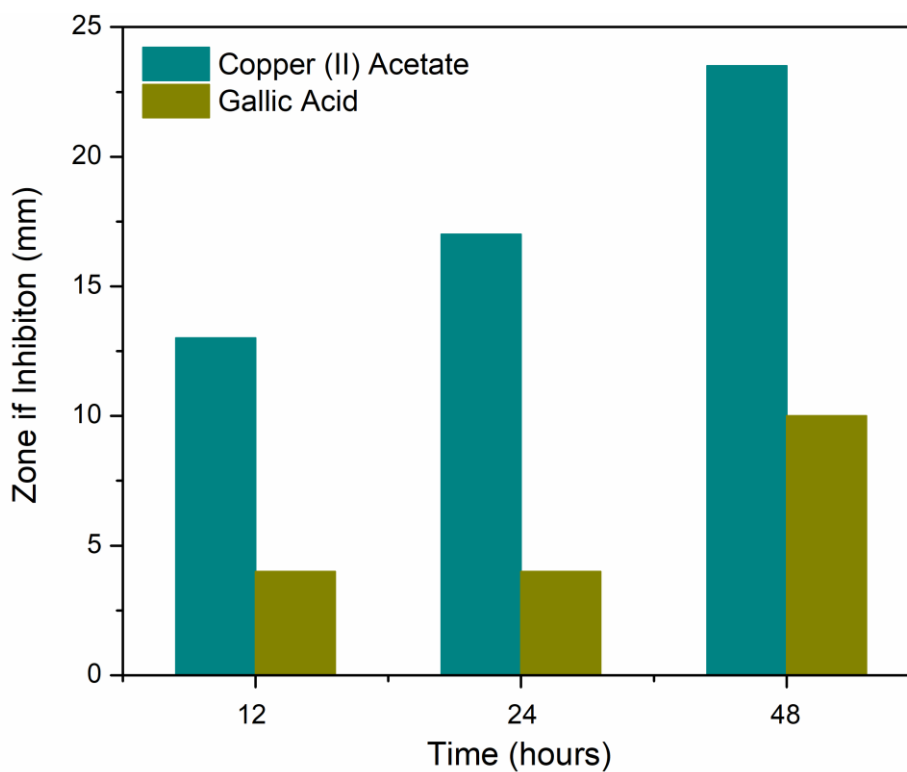
Figure 79: Diameters of zones of inhibition for copper acetate and gallic acid controls towards *E. coli.*
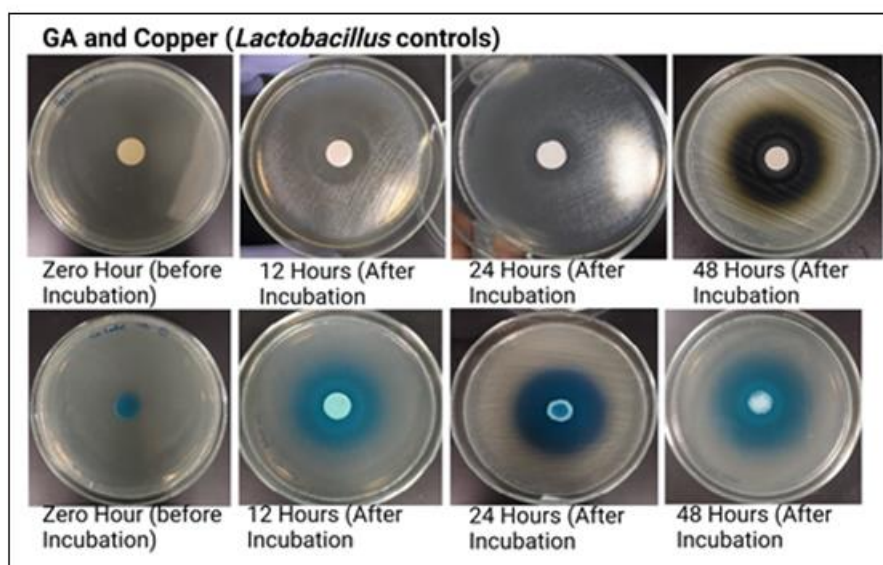
Figure 80: Antibacterial activity results of copper acetate and gallic acid controls against *Lactobacillus*.
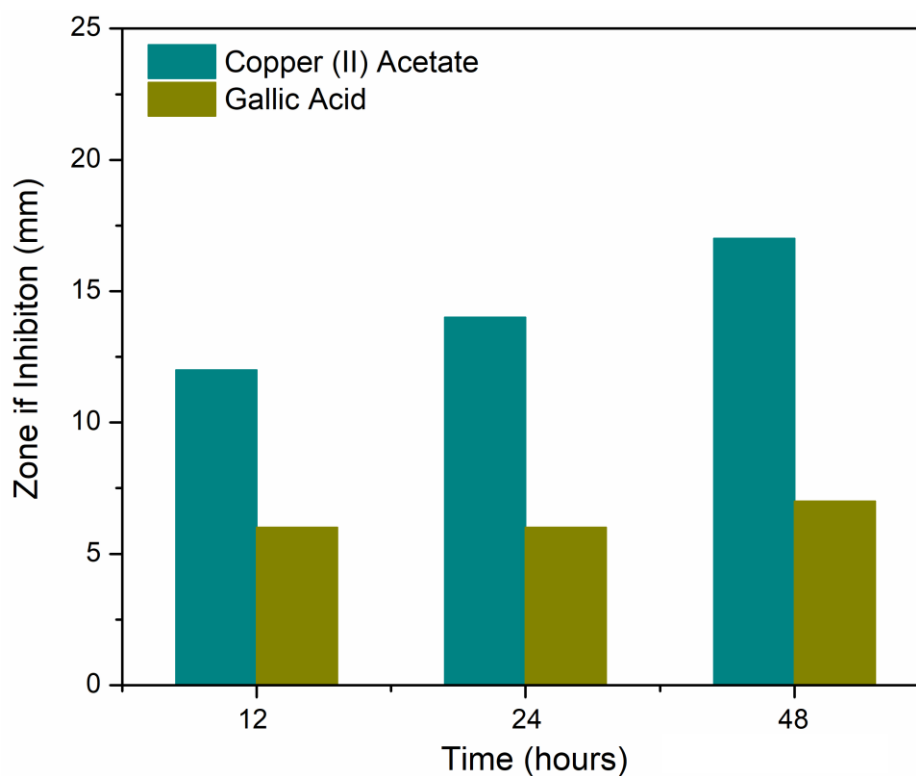
Figure 81: Diameters of zones of inhibition for copper acetate and gallic acid controls towards *Lactobacillus*.

The larger zones of inhibition for the copper control proves the burst release effect compared to both MOF samples, which gave a more sustained release of the copper ion. The antioxidant, GA, was also used as a control and successfully inhibited both strains of bacteria. With *E. coli,* GA inhibited smaller zones compared to Cu-GA proving that the addition of copper leads to a more pronounced antibacterial effect. *Lactobacillus* showed less resistance to almost all samples except for Cu-GA in comparison to *E. coli*. Being a gram-positive bacteria, *Lactobacillus* lacks an outer membrane making the bacteria more vulnerable to foreign invasion through the cell wall (Shams et al., 2020). Cu^{2+} ions have been identified to induce damage to the cell wall and cell membrane by binding to lipopolysaccharides or peptidoglycans or carboxylic groups of bacteria causing a disruption in the bacterial envelope (Casey et al., 2010; Fang et al., 2009; Langley & Beveridge, 1999; Santo et al., 2012). Cu^{2+} ions

can also cause complete membrane rupture by binding to negatively charged domains and reducing the potential (Mitra et al., 2020). For a synergistic effect, GA can further disrupt the integrity of the cell membrane and inhibit the motility of bacteria by generating ROS, causing oxidative stress in cells (Babich et al., 2011; Borges et al., 2012; Kang et al., 2008; Li et al., 2007; Shao et al., 2015).

Elucidation of the minimum inhibitory concentration (MIC). The MIC of Cu-BTC and Cu-GA at various concentrations (7.81 µg - 2000 µg) were examined against *E. coli* and *Lactobacillus*. Initially, the concentrations used for the first round, indicated a partial inhibition in both strains from 1000 µg to 2000 µg with both MOF samples. Therefore, a second experiment was conducted using 1000 µg to 2000 µg of both MOFs in order to achieve a more accurate result (Figures 82-85). Results indicate that the antibacterial activity of Cu-BTC was more pronounced against *E. coli* than *Lactobacillus* when compared to the controlled groups. With Cu-BTC, a MIC of 1500 µg and 1700 µg was notable for *E. coli* and *Lactobacillus*, respectively. Cu-GA partially inhibited microbial growth at 1800 µg and 1900 µg concentrations but exhibited complete antimicrobial activity at 2000 µg for both strains, this can be seen by the absence of growth (cloudiness) in the well. All results are shown in Table 9.
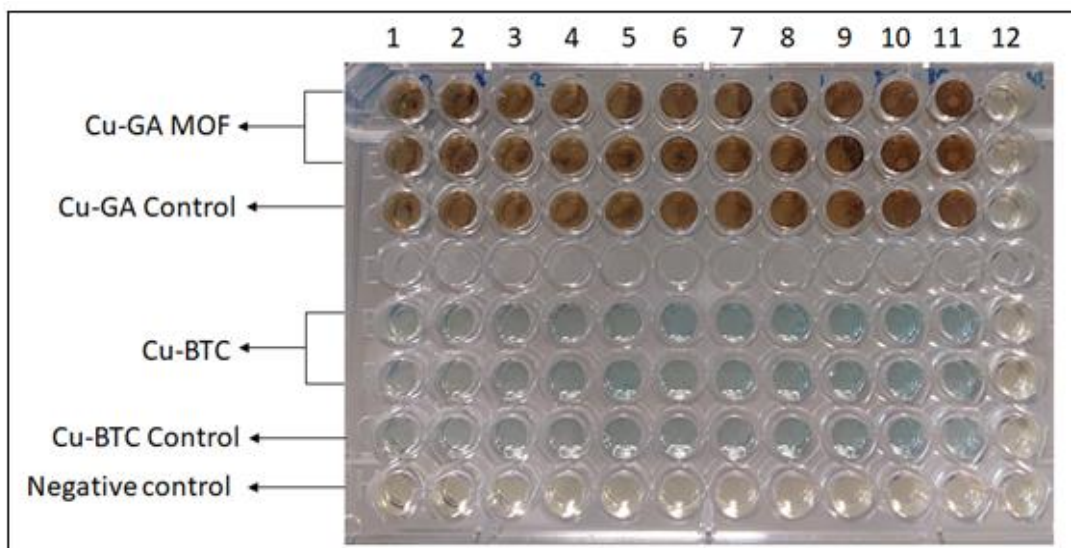
Figure 82: MIC against *E. coli* before incubation (zero hour). 1: 1000ug, 2: 1100ug, 3: 1200ug, 4: 1300ug, 5: 1400ug, 6: 1500ug, 7: 1600ug, 8: 1700ug, 9: 1800ug, 10: 1900ug, 11: 2000ug, 12: Positive control E. coli (without MOF treatment).
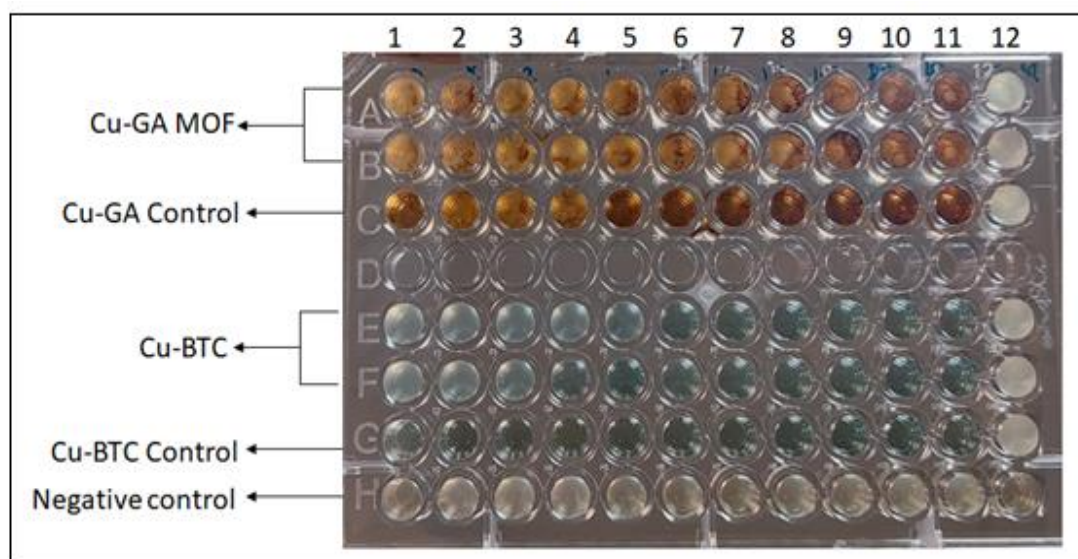
Figure 83: MIC against *E. coli* after incubation (24 hour). 1: 1000ug, 2: 1100ug, 3: 1200ug, 4: 1300ug, 5: 1400ug, 6: 1500ug, 7: 1600ug, 8: 1700ug, 9: 1800ug, 10: 1900ug, 11: 2000ug, 12: Positive control E. coli (without MOF treatment).
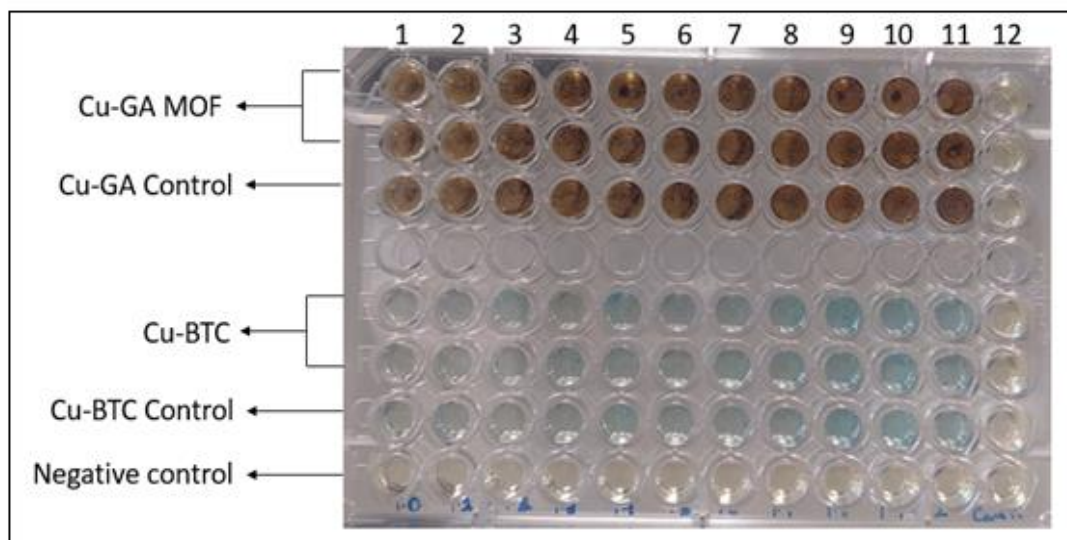
Figure 84: MIC against *Lactobacillus* before incubation (zero hour). 1: 1000ug, 2: 1100ug, 3: 1200ug, 4: 1300ug, 5: 1400ug, 6: 1500ug, 7: 1600ug, 8: 1700ug, 9: 1800ug, 10: 1900ug, 11: 2000ug, 12: Positive control Lactobacillus (without MOF treatment).
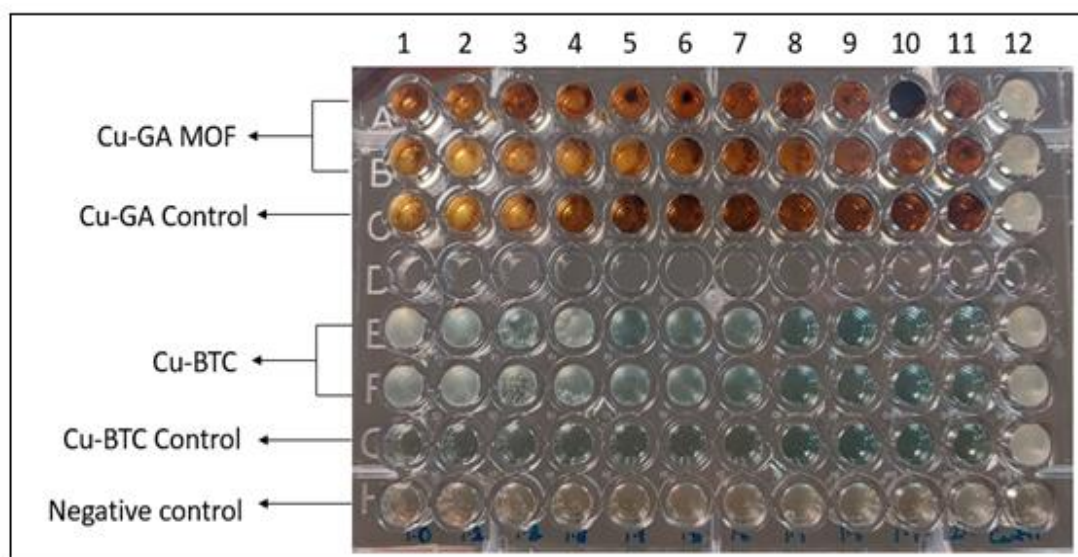
Figure 85: MIC against *Lactobacillus* after incubation (24 hour). 1: 1000ug, 2: 1100ug, 3: 1200ug, 4: 1300ug, 5: 1400ug, 6: 1500ug, 7: 1600ug, 8: 1700ug, 9: 1800ug, 10: 1900ug, 11: 2000ug, 12: Positive control Lactobacillus (without MOF treatment).

Table 9: MIC Results of Cu-BTC and Cu-GA against two bacterial strains.

							Concentration (μg)					
MIC of Cu-BTC against tested bacteria												
Strain	Control	1000	1100	1200	1300	1400	1500	1600	1700	1800	1900	2000
E. coli	+++	+++	+++	++	+	+	---	---	---	---	---	---
Lactobacillus	+++	+++	+++	+++	+++	+++	++	++	---	---	---	---
MIC of Cu-GA against tested bacteria												
Strain	Control	1000	1100	1200	1300	1400	1500	1600	1700	1800	1900	2000
E. coli	+++	+++	+++	+++	+++	+++	+++	+++	+++	++	+	---
Lactobacillus	+++	+++	+++	+++	+++	+++	+++	+++	+++	+++	++	---

--- no growth   + significant growth inhibition ++ partial growth inhibition +++ strong growth

Agarose gel electrophoresis for DNA disintegration. The influence of Cu-BTC and Cu-GA on the DNA of *E. coli* and *Lactobacillus* was studied using agarose gel electrophoresis technique. Figures 86-89 shows a brighter and clearer band of DNA for the sample that was not treated with the MOF. Once the bacterial DNA is treated with Cu-BTC, the brightness of the band decreases, indicating that the DNA morphology of *E. coli* and *Lactobacillus* was disrupted by the MOF sample. In addition, the dimness of the band increases with increasing concentrations of Cu-BTC MOF. These results indicate that not only do copper-based MOFs have an effect on bacterial cellular membrane and cellular wall, but they can also hinder their DNA structure, causing morphological damage. This disruptive effect increased with the increase in the concentration of both Cu-BTC and Cu-GA MOFs, that is, higher the concentration, the more indistinct the DNA bands.
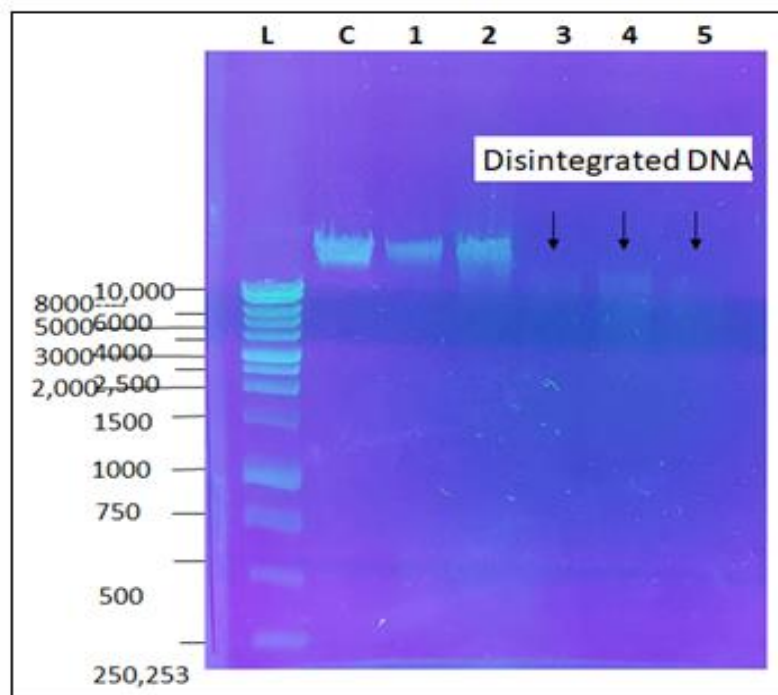
Figure 86: DNA agarose gel electrophoresis of *E. coli* treated with various concentrations of Cu-BTC. L: 1kb DNA Ladder (Promega) C: control- E. coli DNA (without MOF treatment) 1: 0.125 x MIC 2: 0.25 x MIC 3: 0.5 x MIC 4: 1 x MIC 5: 1.5 MIC.
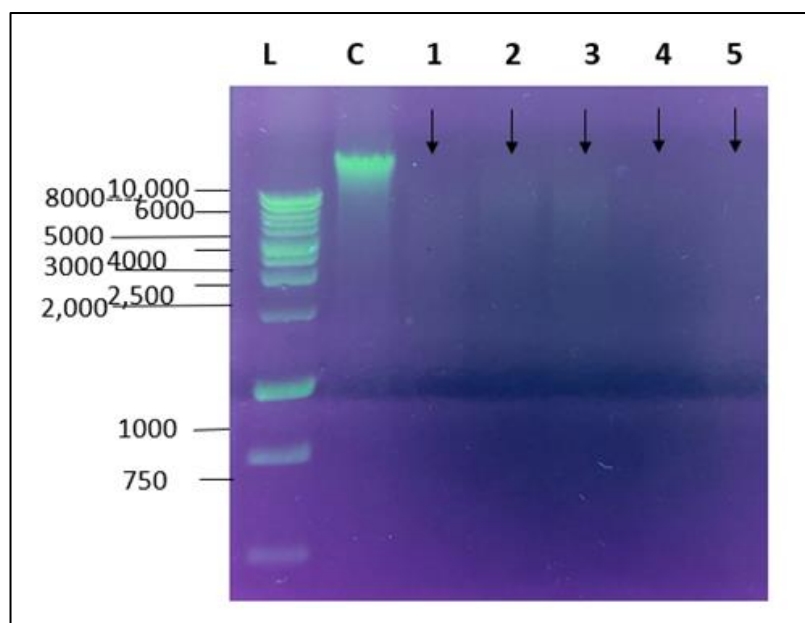
Figure 87: DNA agarose gel electrophoresis of *Lactobacillus* treated with various concentrations of Cu-BTC. L: 1kb DNA Ladder (Promega) C: control- E. coli DNA (without MOF treatment) 1: 0.125 x MIC 2: 0.25 x MIC 3: 0.5 x MIC 4: 1 x MIC 5: 1.5 MIC.
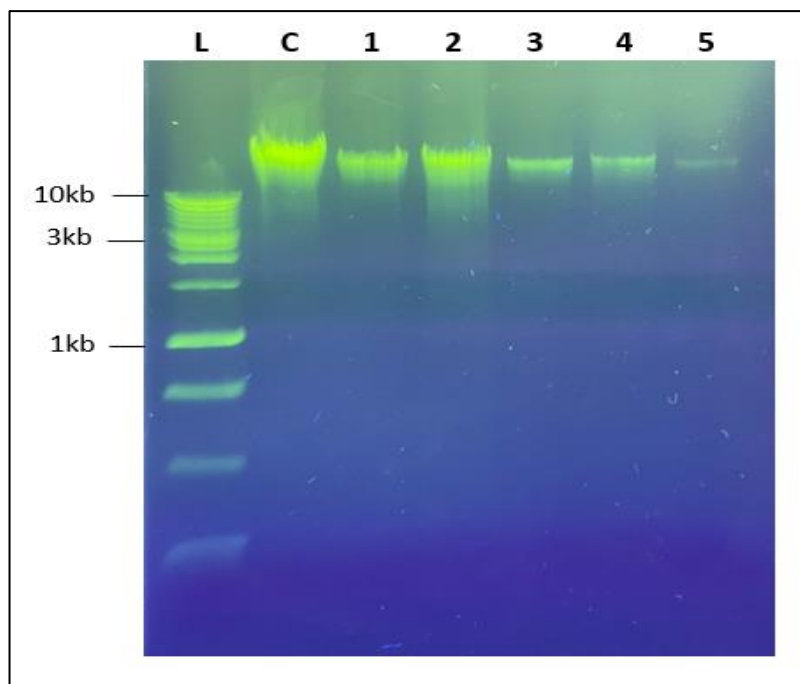
Figure 88: DNA agarose gel electrophoresis of *E. coli* treated with various concentrations of Cu-GA. L: 1kb DNA Ladder (Promega) C: control- E. coli DNA (without MOF treatment) 1: 0.125 x MIC 2: 0.25 x MIC 3: 0.5 x MIC 4: 1 x MIC 5: 1.5 MIC.
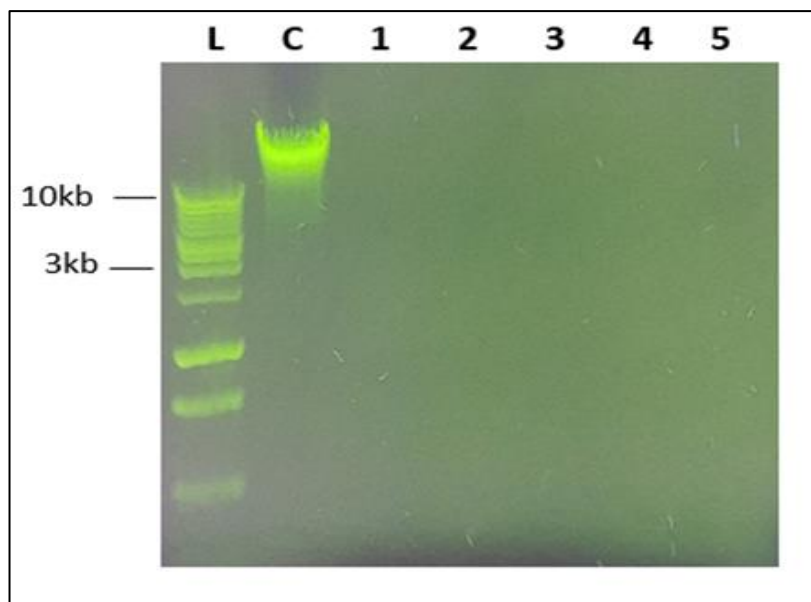
Figure 89: DNA agarose gel electrophoresis of *Lactobacillus* treated with various concentrations of Cu-GA. L: 1kb DNA Ladder (Promega) C: control- E. coli DNA (without MOF treatment) 1: 0.125 x MIC 2: 0.25 x MIC 3: 0.5 x MIC 4: 1 x MIC 5: 1.5 MIC.

6.4 Conclusion

This work demonstrates the use of Cu-BTC and Cu-GA as antibacterial agents proven by their specificity and antibacterial activity against two different types of bacterial strains. The mechanism in which bacterial death occurs is through the disruption of the cell membrane *(E. coli)* and damage of bacterial DNA. The destruction of the bacterial cell membrane makes the bacteria vulnerable to MOF treatments, ultimately degrading the DNA. *E. coli* was more sensitive to the Cu-GA MOF when compared to Cu-BTC. This could be due to the presence of GA in the structure, which possesses the ability to destroy the bacterial cellular membrane. On the other hand, *Lactobacillus* exhibited a greater sensitivity to Cu-BTC when compared to Cu-GA. Both bioMOFs were successful in inhibiting gram-positive and gram-negative bacteria, which is promising when trying to overcome challenges faced with increasing antibiotic resistance.

Chapter 7: Summary

The primary objective of the research contained within this dissertation is to develop a biocompatible and biodegradable therapeutic nanomaterial with enhanced anti-cancer and anti-bacterial properties. Copper is a trace element and plays an important role in the growth and development of the human body while demonstrating high microbicidal and chemotherapeutic effects (Mitra et al., 2020). Therefore, the synthesis of a Cu^{2+} releasing nanomaterial which can sustain its structural integrity in physiological media over an extended period of time will result in a more targeted delivery and higher accumulation in tumor tissue. This was first achieved by coordinating Cu^{2+} with the organic compound 1,3,5-benzene tricarboxylic acid producing a Cu-BTC MOF structure possessing an impressive surface area of 1,268 m^2 g^{-1}. Secondly, a Cu-GA MOF was developed based on the antioxidant and ROS scavenger properties of the organic molecule, gallic acid. Lastly, the stability and host mechanics of Cu-BTC was modified for the enhanced use in biological activities.

Characterization of both MOF materials using PXRD, FT-IR spectroscopy, TGA-DTG, SEM-EDX, SXRD (Cu-BTC only), Raman spectroscopy, and N_2 sorption is essential before measuring the materials effectiveness. Knowing that the microporous structure of Cu-BTC would be a challenge to encapsulate or host larger biological molecules lead to efforts in designing a hierarchical structure. GA was used to fine tune the MOF, creating an etched hierarchical micro- and mesoporous framework while simultaneously, encapsulating the antioxidant into the framework, all while maintaining the overall crystal structure. The extent of etching and encapsulation can be controlled with controlling the concentration of GA, as shown in Figure 90.
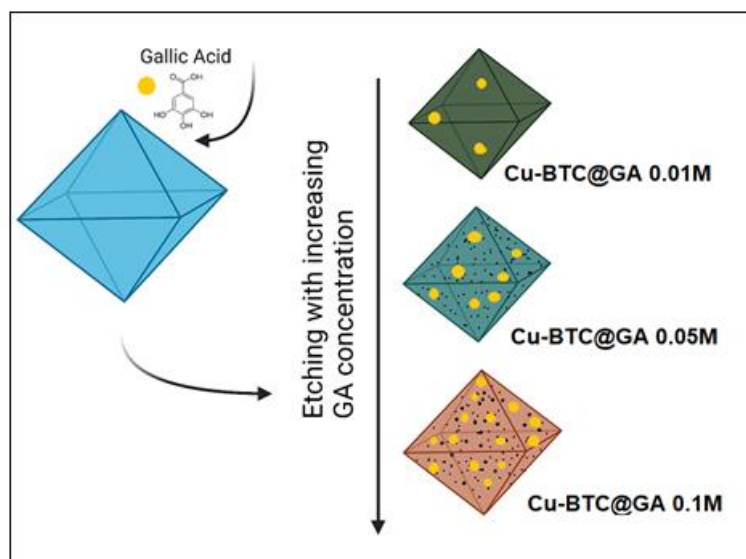
Figure 90: Post-synthesis etching and encapsulation of Cu-BTC with gallic acid.

The amount of [Cu^{2+}] leaching out of the structure is crucial for determining the stability of the MOFs. When Cu-BTC was placed in PBS for 3 days, the concentration of copper ions, in the initial stages, was much greater than in RPMI media. RPMI media allowed for the sustained release of copper ions from the MOF structure, observed by ICP-AES. SEM results revealed the formation of $Cu_3(PO_4)_2$ NFs, which were 'grown' from the presence of amino acids and phosphate in the RPMI media, as shown in Figure 91. This hierarchical Cu-BTC@$Cu_3(PO_4)_2$ core-shell NF composite enhanced the stability of the MOF, preventing the burst release of Cu^{2+} ions from the structure.

Finally, the roles of Cu-BTC and Gu-GA as anti-cancer and anti-bacterial agents was assessed through various assays. To begin with, both bioMOFs were studied for the first time against gastric cancer cells as stand-alone treatments. The MTT assay revealed that gastric cancer cells were more sensitive to Cu-BTC as a stand-alone treatment, with almost complete cell inhibition at 75 µg/µL. On the other hand, Cu-GA displayed enhanced anti-cancer effects towards HCT116 colon cancer cells when

compared to Cu-BTC. These coordination polymers can exhibit a Fenton-like activity, by generating ROS, causing oxidative stress in cancer cells and ultimately cell apoptosis (Babich et al., 2011; Liang et al., 2021). These mechanisms were further proven in the antibacterial studies conducted in this dissertation. Both MOFs successfully inhibited *E. coli* and *Lactobacillus* through disruption of bacterial cellular membrane and by damaging bacterial DNA.
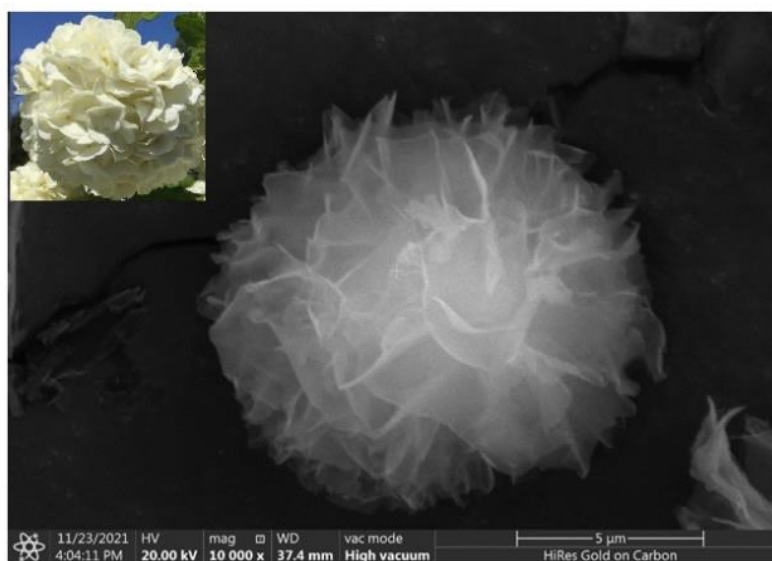
Figure 91: Copper-based nanoflower formed from Cu-BTC in RPMI media, resembling a Viburnun Opulus flower.

The research presented in this dissertation was carried out with the intention of improving the limitations and challenges faced with conventional chemotherapeutic drugs and to overcome the antibiotic resistance crisis that stems from overuse and lack of developing new antibiotics (Nathan, 2004). MOF nanomaterials possess a high surface area and small size, allowing for a larger number of assembled molecules for dynamic interfacing with cancer and bacterial cells (Gao & Zhang, 2021). This work, not only explores copper-based MOFs and their role in overcoming the hurdles listed previously, but to enhance the stability and biological functions of the bioMOFs. This

was achieved by creating two different hierarchical structures for the intent of extended copper ion release from the framework and for the encapsulation of gallic acid within the framework. These newly improved MOF structures will potentially improve the chemotherapeutic and antibacterial effects observed with Cu-BTC and Cu-GA.

7.1 Future Outlook

The suggested mechanism for which Cu-BTC and Cu-GA have been successful in inhibiting both cancer and bacterial cells requires further investigation. To determine the ROS accumulation caused by Cu^{2+} ions, a Dichloro-dihydro-fluorescein diacetate (DCFH-DA) assay can be used to measure the presence of oxidative species before and after treatment with both MOFs. The annexin V-FITC assay can be also used to detect whether both the copper-based MOFs could induce apoptosis in mGS, AGS and HCT116 cancers cell lines. Chen et al., determined that Cu-BTC caused a 25% apoptosis in SKOV4 cells. This percent was much lower than cytotoxic cells, suggesting the cytotoxicity induced by Cu-BTC was not primarily due to apoptosis (Chen et al., 2020). After showing promising *in-vitro* results against mGS, AGS and HCT116 cancer cell lines, the plan is to proceed with assessing the *in vivo* anticancer properties using mice bearing tumors from similar cell lines. This is to determine the tumor inhibition capabilities of both copper MOFS in mice while testing its safety.

The developed hierarchical Cu-BTC@ GA nanocomposite containing both micro-and mesopores needs to be further evaluated for the extent of Cu^{2+} leaching out during the etching process. This can be carried out by measuring the amount of copper ions in the remaining solvent post-synthesis. Although, having GA entrapped with the pores of the newly created hierarchical structure, an attempt needs to be made to remove all GA molecules for the complete evacuation and of Cu-BTC. This will create

a drug delivery carrier with the possibility of an enhanced surface area. Future work is aimed at using the hierarchical Cu-BTC@GA nanocomposite towards the same biological studies carried out in Chapters 3 and 4 for the possibility of enhanced properties.

Finally, we hypothesize that the newly designed Cu-BTC@$Cu_3(PO_4)_2$ core-shell NF will exhibit an enhanced stability compared to the Cu-BTC pristine MOF. One of the goals of this research is to create a biocompatible, material without the need of encapsulation with a therapeutic drug, that displays a sustained release of its constituents for anti-cancer and anti-bacterial purposes. The formation of $Cu_3(PO_4)_2$ on the Cu-BTC MOF structure will potentially lead to an enhanced intrinsic peroxidase activity and overall sustained release of copper ions. Future work is aimed at using the hierarchical Cu-BTC@$Cu_3(PO_4)_2$ core-shell NF towards the same biological studies carried out in Chapters 3 and 4 for comparison with pristine Cu-BTC.

References

Abánades-Lázaro, I., Haddad, S., Rodrigo-Muñoz, J. M., Marshall, R. J., Sastre, B., del Pozo, V., Fairen-Jimenez, D., & Forgan, R. S. (2018). Surface-Functionalization of Zr-Fumarate MOF for Selective Cytotoxicity and Immune System Compatibility in Nanoscale Drug Delivery. *ACS Applied Materials & Interfaces, 10*(37), 31146-31157. https://doi.org/10.1021/acsami.8b11652

Abdulah, R., Miyazaki, K., Nakazawa, M., & Koyama, H. (2005). Chemical forms of selenium for cancer prevention. *Journal of Trace Elements in Medicine and Biology, 19*(2), 141-150. https://doi.org/10.1016/j.jtemb.2005.09.003

Afzalinia, A., & Mirzaee, M. (2020). Ultrasensitive Fluorescent miRNA Biosensor Based on a "Sandwich" Oligonucleotide Hybridization and Fluorescence Resonance Energy Transfer Process Using an Ln(III)-MOF and Ag Nanoparticles for Early Cancer Diagnosis: Application of Central Composite Design. *ACS Applied Materials & Interfaces, 12*(14), 16076-16087. https://doi.org/10.1021/acsami.0c00891

Ai, Z., Jiao, L., Wang, J., & Jiang, H.-L. Generation of Hierarchical Pores in Metal–Organic Frameworks by Introducing Rigid Modulator. *CCS Chemistry, 0*(0), 1-10. https://doi.org/10.31635/ccschem.022.202201974

Al-Sagur, H., Shanmuga sundaram, K., Kaya, E. N., Durmuş, M., Basova, T. V., & Hassan, A. (2019). Amperometric glucose biosensing performance of a novel graphene nanoplatelets-iron phthalocyanine incorporated conducting hydrogel. *Biosensors and Bioelectronics, 139*, 111323. https://doi.org/ 10.1016/j.bios.2019.111323

Al Neyadi, S. S., Al Blooshi, A. G., Nguyen, H. L., & Alnaqbi, M. A. (2021). UiO-66-NH2 as an effective solid support for quinazoline derivatives for antibacterial agents against Gram-negative bacteria. *New Journal of Chemistry, 45*(43), 20386-20395. https://doi.org/10.1039/D1NJ03749H

Alijani, H., Noori, A., Faridi, N., Bathaie, S. Z., & Mousavi, M. F. (2020). Aptamer-functionalized Fe3O4@MOF nanocarrier for targeted drug delivery and fluorescence imaging of the triple-negative MDA-MB-231 breast cancer cells. *Journal of Solid State Chemistry, 292*, 121680. https://doi.org/10.1016/j.jssc.2020.121680

Alnaqbi, M. A., Alzamly, A., Ahmed, S. H., Bakiro, M., Kegere, J., & Nguyen, H. L. (2021). Chemistry and applications of s-block metal–organic frameworks. *Journal of Materials Chemistry A, 9*(7), 3828-3854. https://doi.org/10.1039/D0TA09678D

Altinkaynak, C., Tavlasoglu, S., ÿzdemir, N., & Ocsoy, I. (2016). A new generation approach in enzyme immobilization: Organic-inorganic hybrid nanoflowers with enhanced catalytic activity and stability. *Enzyme and Microbial Technology,* 105-112. https://doi.org/10.1016/j.enzmictec.2016.06.011

Alves, R. C., Schulte, Z. M., Luiz, M. T., Bento da Silva, P., Frem, R. C. G., Rosi, N. L., & Chorilli, M. (2021). Breast Cancer Targeting of a Drug Delivery System through Postsynthetic Modification of Curcumin@N3-bio-MOF-100 via Click Chemistry. *Inorganic Chemistry, 60*(16), 11739-11744. https://doi.org/10.1021/acs.inorgchem.1c00538

American Institute for Cancer Research, W. C. R. F. S. C. *How Diet, Nutrition, and Physical Activity Affect Stomach Cancer Risk*. Retrieved November 24, 2021 from www.wcrf.org/dietandcancer/stomach-cancer

An, H., Li, M., Gao, J., Zhang, Z., Ma, S., & Chen, Y. (2019). Incorporation of biomolecules in Metal-Organic Frameworks for advanced applications. *Coordination Chemistry Reviews, 384*, 90-106. https://doi.org/10.1016/j.ccr.2019.01.001

An, J., Geib, S. J., & Rosi, N. L. (2009). Cation-Triggered Drug Release from a Porous Zinc−Adeninate Metal−Organic Framework. *Journal of the American Chemical Society, 131*(24), 8376-8377. https://doi.org/10.1021/ja902972w

André, V., da Silva, A. R. F., Fernandes, A., Frade, R., Garcia, C., Rijo, P., Antunes, A. M. M., Rocha, J., & Duarte, M. T. (2019). Mg- and Mn-MOFs Boost the Antibiotic Activity of Nalidixic Acid. *ACS Applied Bio Materials, 2*(6), 2347-2354. https://doi.org/10.1021/acsabm.9b00046

Angelos, S., Khashab, N. M., Yang, Y.-W., Trabolsi, A., Khatib, H. A., Stoddart, J. F., & Zink, J. I. (2009). pH Clock-Operated Mechanized Nanoparticles. *Journal of the American Chemical Society, 131*(36), 12912-12914. https://doi.org/10.1021/ja9010157

ASTM E. (2013). Standard test method for determining the antimicrobial activity of antimicrobial agents under dynamic contact conditions.

Azhar, B., Angkawijaya, A. E., Santoso, S. P., Gunarto, C., Ayucitra, A., Go, A. W., Tran-Nguyen, P. L., Ismadji, S., & Ju, Y.-H. (2020). Aqueous synthesis of highly adsorptive copper–gallic acid metal–organic framework. *Scientific Reports, 10*(1), 19212. https://doi.org/10.1038/s41598-020-75927-4

Babich, H., Schuck, A. G., Weisburg, J. H., & Zuckerbraun, H. L. (2011). Research Strategies in the Study of the Pro-Oxidant Nature of Polyphenol Nutraceuticals. *Journal of Toxicology, 2011*, 467305. https://doi.org/10.1155/2011/467305

Bando, H., Doi, T., Muro, K., Yasui, H., Nishina, T., Yamaguchi, K., Takahashi, S., Nomura, S., Kuno, H., Shitara, K., Sato, A., & Ohtsu, A. (2016). A multicenter phase II study of TAS-102 monotherapy in patients with pre-treated advanced gastric cancer (EPOC1201). *European Journal of Cancer, 62*, 46-53. https://doi.org/10.1016/j.ejca.2016.04.009

Barash, O., Peled, N., Hirsch, F. R., & Haick, H. (2009). Sniffing the Unique "Odor Print" of Non-Small-Cell Lung Cancer with Gold Nanoparticles *Small, 5*(22), 2618-2624. https://doi.org/10.1002/smll.200900937

Barta, J. A., Powell, C. A., & Wisnivesky, J. P. (2019). Global Epidemiology of Lung Cancer. *Annals of global health, 85*(1), 8. https://doi.org/10.5334/aogh.2419

Batule, B. S., Park, K. S., Gautam, S., Cheon, H. J., Kim, M. I., & Park, H. G. (2019). Intrinsic peroxidase-like activity of sonochemically synthesized protein copper nanoflowers and its application for the sensitive detection of glucose. *Sensors and Actuators B: Chemical, 283*, 749-754. https://doi.org/10.1016/j.snb.2018.12.028

Bergamo, A., Gaiddon, C., Schellens, J. H. M., Beijnen, J. H., & Sava, G. (2012). Approaching tumour therapy beyond platinum drugs: Status of the art and perspectives of ruthenium drug candidates. *Journal of Inorganic Biochemistry, 106*(1), 90-99. https://doi.org/10.1016/j.jinorgbio.2011.09.030

Bian, Y., Xiong, N., & Zhu, G. (2018). Technology for the Remediation of Water Pollution: A Review on the Fabrication of Metal Organic Frameworks. *Processes, 6*(8), 122. https://doi.org/10.3390/pr6080122

Biemmi, E., Christian, S., Stock, N., & Bein, T. (2009). High-throughput screening of synthesis parameters in the formation of the metal-organic frameworks MOF-5 and HKUST-1. *Microporous and Mesoporous Materials, 117*(1), 111-117. https://doi.org/10.1016/j.micromeso.2008.06.040

Bioengineering, N. I. o. B. I. a. *Magnetic Resonance Imaging (MRI).* Retrieved December 12, 2021 from https://www.nibib.nih.gov/science-education/science-topics/magnetic-resonance-imaging-mri

Birsa-Čelič, T., Jagličič, Z., Lazar, K., & Zabukovec Logar, N. (2013). Structure and magnetic properties of a new iron(II) citrate coordination polymer. *Acta Crystallographica Section B, 69*(5), 490-495. https://doi.org/10.1107/S2052519213023713

Biswal, B. P., Shinde, D. B., Pillai, V. K., & Banerjee, R. (2013). Stabilization of graphene quantum dots (GQDs) by encapsulation inside zeolitic imidazolate framework nanocrystals for photoluminescence tuning. *Nanoscale, 5*(21), 10556-10561. https://doi.org/10.1039/C3NR03511E

Biswas, A., Shukla, A., & Maiti, P. (2019). Biomaterials for Interfacing Cell Imaging and Drug Delivery: An Overview. *Langmuir, 35*(38), 12285-12305. https://doi.org/10.1021/acs.langmuir.9b00419

Blair, J. M. A., Webber, M. A., Baylay, A. J., Ogbolu, D. O., & Piddock, L. J. V. (2015). Molecular mechanisms of antibiotic resistance. *Nature Reviews Microbiology, 13*(1), 42-51. https://doi.org/10.1038/nrmicro3380

Bonnet, S., Archer, S. L., Allalunis-Turner, J., Haromy, A., Beaulieu, C., Thompson, R., Lee, C. T., Lopaschuk, G. D., Puttagunta, L., Bonnet, S., Harry, G., Hashimoto, K., Porter, C. J., Andrade, M. A., Thebaud, B., & Michelakis, E. D. (2007). A Mitochondria-K+ Channel Axis Is Suppressed in Cancer and Its Normalization Promotes Apoptosis and Inhibits Cancer Growth. *Cancer Cell, 11*(1), 37-51. https://doi.org/10.1016/j.ccr.2006.10.020

Borges, A., Ferreira, C., Saavedra, M. J., & Simões, M. (2013). Antibacterial Activity and Mode of Action of Ferulic and Gallic Acids Against Pathogenic Bacteria. *Microbial Drug Resistance, 19*(4), 256-265. https://doi.org/10.1089/mdr.2012.0244

Borges, A., Saavedra, M. J., & Simões, M. (2012). The activity of ferulic and gallic acids in biofilm prevention and control of pathogenic bacteria. *Biofouling, 28*(7), 755-767. https://doi.org/10.1080/08927014.2012.706751

Britt, D., Furukawa, H., Wang, B., Glover, T. G., & Yaghi, O. M. (2009). Highly efficient separation of carbon dioxide by a metal-organic framework replete with open metal sites. *Proceedings of the National Academy of Sciences, 106*(49), 20637. https://doi.org/10.1073/pnas.0909718106

Bueken, B., Van Velthoven, N., Willhammar, T., Stassin, T., Stassen, I., Keen, D. A., Baron, G. V., Denayer, J. F. M., Ameloot, R., Bals, S., De Vos, D., & Bennett, T. D. (2017). Gel-based morphological design of zirconium metal–organic frameworks. *Chemical Science, 8*(5), 3939-3948. https://doi.org/10.1039/C6SC05602D

Burrows, A. D., Jurcic, M., Keenan, L. L., Lane, R. A., Mahon, M. F., Warren, M. R., Nowell, H., Paradowski, M., & Spencer, J. (2013). Incorporation by coordination and release of the iron chelator drug deferiprone from zinc-based metal–organic frameworks. *Chemical Communications, 49*(96), 11260-11262. https://doi.org/10.1039/C3CC45689G

Burrows, A. D., Jurcic, M., Mahon, M. F., Pierrat, S., Roffe, G. W., Windle, H. J., & Spencer, J. (2015). Bismuth coordination networks containing deferiprone: synthesis, characterisation, stability and antibacterial activity. *Dalton Transactions, 44*(31), 13814-13817. https://doi.org/10.1039/C5DT02458G

Cai, W., Wang, J., Chu, C., Chen, W., Wu, C., & Liu, G. (2019). Metal–Organic Framework-Based Stimuli-Responsive Systems for Drug Delivery. *Advanced Science, 6*(1), 1801526. https://doi.org/10.1002/advs.201801526

Carson Kerry, C., Bartlett Jessica, G., Tan, T.-J., & Riley Thomas, V. (2007). In Vitro Susceptibility of Methicillin-Resistant Staphylococcus aureus and Methicillin-Susceptible Staphylococcus aureus to a New Antimicrobial, Copper Silicate. *Antimicrobial Agents and Chemotherapy, 51*(12), 4505-4507. https://doi.org/10.1128/AAC.00771-07

Casey, A. L., Adams, D., Karpanen, T. J., Lambert, P. A., Cookson, B. D., Nightingale, P., Miruszenko, L., Shillam, R., Christian, P., & Elliott, T. S. J. (2010). Role of copper in reducing hospital environment contamination. *Journal of Hospital Infection, 74*(1), 72-77. https://doi.org/10.1016/j.jhin.2009.08.018

Cavka, J. H., Jakobsen, S., Olsbye, U., Guillou, N., Lamberti, C., Bordiga, S., & Lillerud, K. P. (2008). A New Zirconium Inorganic Building Brick Forming Metal Organic Frameworks with Exceptional Stability. *Journal of the American Chemical Society, 130*(42), 13850-13851. https://doi.org/10.1021/ja8057953

Chandrawati, R., Chang, J. Y. H., Reina-Torres, E., Jumeaux, C., Sherwood, J. M., Stamer, W. D., Zelikin, A. N., Overby, D. R., & Stevens, M. M. (2017). Localized and Controlled Delivery of Nitric Oxide to the Conventional Outflow Pathway via Enzyme Biocatalysis: Toward Therapy for Glaucoma. *Advanced Materials, 29*(16), 1604932. https://doi.org/10.1002/adma.201604932

Chatterjee, A. K., Chakraborty, R., & Basu, T. (2014). Mechanism of antibacterial activity of copper nanoparticles. *Nanotechnology, 25*(13), 135101. https://doi.org/10.1088/0957-4484/25/13/135101

Chen, B., Liang, C., Yang, J., Contreras, D. S., Clancy, Y. L., Lobkovsky, E. B., Yaghi, O. M., & Dai, S. (2006). A Microporous Metal–Organic Framework for Gas-Chromatographic Separation of Alkanes. *Angewandte Chemie International Edition, 45*(9), 1390-1393. https://doi.org/10.1002/anie.200502844

Chen, D., Li, B., Jiang, L., Li, Y., Yang, Y., Luo, Z., & Wang, J. (2020). Pristine Cu-MOF Induces Mitotic Catastrophe and Alterations of Gene Expression and Cytoskeleton in Ovarian Cancer Cells. *ACS Applied Bio Materials, 3*(7), 4081-4094. https://doi.org/10.1021/acsabm.0c00175

Chen, G., Leng, X., Luo, J., You, L., Qu, C., Dong, X., Huang, H., Yin, X., & Ni, J. (2019). In Vitro Toxicity Study of a Porous Iron(III) Metal–Organic Framework. *Molecules, 24*(7). https://doi.org/10.3390/molecules24071211

Chen, H.-Y., Xiao, D.-R., Yan, S.-W., He, J.-H., Yang, J., Wang, X., Yuan, R., & Wang, E.-B. (2012). Two three-dimensional pillared metal–olsalazine complexes based on infinite rod-shaped secondary building units. *Inorganica Chimica Acta, 387*, 283-288. https://doi.org/10.1016/j.ica.2012.01.035

Chen, J., Liu, J., Hu, Y., Tian, Z., & Zhu, Y. (2019). Metal-organic framework-coated magnetite nanoparticles for synergistic magnetic hyperthermia and chemotherapy with pH-triggered drug release. *Science and Technology of Advanced Materials, 20*(1), 1043-1054. https://doi.org/10.1080/14686996.2019.1682467

Chen, Q., Xu, M., Zheng, W., Xu, T., Deng, H., & Liu, J. (2017). Se/Ru-Decorated Porous Metal–Organic Framework Nanoparticles for The Delivery of Pooled siRNAs to Reversing Multidrug Resistance in Taxol-Resistant Breast Cancer Cells. *ACS Applied Materials & Interfaces, 9*(8), 6712-6724. https://doi.org/10.1021/acsami.6b12792

Chen, W.-H., Luo, G.-F., Sohn, Y. S., Nechushtai, R., & Willner, I. (2019). miRNA-Specific Unlocking of Drug-Loaded Metal–Organic Framework Nanoparticles: Targeted Cytotoxicity toward Cancer. *Small, 15*(17), 1900935. https://doi.org/10.1002/smll.201900935

Chen, W., Ni, D., Rosenkrans, Z. T., Cao, T., & Cai, W. (2019). Smart H2S-Triggered/Therapeutic System (SHTS)-Based Nanomedicine. *Advanced Science, 6*(22), 1901724. https://doi.org/10.1002/advs.201901724

Chen, W., Yang, W., Chen, P., Huang, Y., & Li, F. (2018). Disulfiram Copper Nanoparticles Prepared with a Stabilized Metal Ion Ligand Complex Method for Treating Drug-Resistant Prostate Cancers. *ACS Applied Materials & Interfaces, 10*(48), 41118-41128. https://doi.org/10.1021/acsami.8b14940

Chen, Y., Liu, W., Shang, Y., Cao, P., Cui, J., Li, Z., Yin, X., & Li, Y. (2018). Folic acid-nanoscale gadolinium-porphyrin metal-organic frameworks: fluorescence and magnetic resonance dual-modality imaging and photodynamic therapy in hepatocellular carcinoma. *International journal of nanomedicine, 14*, 57-74. https://doi.org/10.2147/IJN.S177880

Cho, K., Wang, X., Nie, S., Chen, Z., & Shin, D. M. (2008). Therapeutic Nanoparticles for Drug Delivery in Cancer. *Clinical Cancer Research, 14*(5), 1310. https://doi.org/10.1158/1078-0432.CCR-07-1441

Chong, D. Q., Tan, I. B., Choo, S.-P., & Toh, H. C. (2013). The evolving landscape of therapeutic drug development for hepatocellular carcinoma. *Contemporary Clinical Trials, 36*(2), 605-615. https://doi.org/10.1016/j.cct.2013.03.013

Chowdhuri, A. R., Singh, T., Ghosh, S. K., & Sahu, S. K. (2016). Carbon Dots Embedded Magnetic Nanoparticles @Chitosan @Metal Organic Framework as a Nanoprobe for pH Sensitive Targeted Anticancer Drug Delivery. *ACS Applied Materials & Interfaces, 8*(26), 16573-16583. https://doi.org/10.1021/acsami.6b03988

Chowdhury, M. A. (2017). Metal-Organic-Frameworks as Contrast Agents in Magnetic Resonance Imaging. *ChemBioEng Reviews, 4*(4), 225-239. https://doi.org/10.1002/cben.201600027

Chowdhury, P., Bikkina, C., Meister, D., Dreisbach, F., & Gumma, S. (2009). Comparison of adsorption isotherms on Cu-BTC metal organic frameworks synthesized from different routes. *Microporous and Mesoporous Materials, 117*(1), 406-413. https://doi.org/10.1016/j.micromeso.2008.07.029

Chui Stephen, S. Y., Lo Samuel, M. F., Charmant Jonathan, P. H., Orpen, A. G., & Williams Ian, D. (1999). A Chemically Functionalizable Nanoporous Material [Cu3(TMA)2(H2O)3]n. *Science, 283*(5405), 1148-1150. https://doi.org/10.1126/science.283.5405.1148

Clarke, S. J., Karapetis, C. S., Gibbs, P., Pavlakis, N., Desai, J., Michael, M., Tebbutt, N. C., Price, T. J., & Tabernero, J. (2013). Overview of biomarkers in metastatic colorectal cancer: Tumour, blood and patient-related factors. *Critical Reviews in Oncology/Hematology, 85*(2), 121-135. https://doi.org/10.1016/j.critrevonc.2012.06.001

Clinic, C. (2020a). Colorectal (Colon) Cancer. Retrieved November 23, 2021 from https://my.clevelandclinic.org/health/diseases/14501-colorectal-colon-cancer#symptoms-and-causes

Clinic, M. (2020b). Bladder Cancer. Retrieved Novmeber 23, 2021 from https://www.mayoclinic.org/diseases-conditions/bladder-cancer/symptoms-causes/syc-20356104

Clinic, M. (2021). Leukemia. Retrieved December 5, 2021 from https://www.mayoclinic.org/diseases-conditions/leukemia/symptoms-causes/syc-20374373

Coleman, R. L., Monk, B. J., Sood, A. K., & Herzog, T. J. (2013). Latest research and treatment of advanced-stage epithelial ovarian cancer. *Nature Reviews Clinical Oncology, 10*(4), 211-224. https://doi.org/10.1038/nrclinonc.2013.5

Comis, R. L., & Carter, S. K. (1974). A review of chemotherapy in gastric cancer. *Cancer, 34*(5), 1576-1586. https://doi.org/10.1002/1097-0142(197411)34:5<1576::AID-CNCR2820340503>3.0.CO;2-0

Cox, E., Nambiar, S., & Baden, L. (2019). Needed: Antimicrobial Development. *New England Journal of Medicine, 380*(8), 783-785. https://doi.org/10.1056/NEJMe1901525

Cui, D., Zhang, C., Liu, B., Shu, Y., Du, T., Shu, D., Wang, K., Dai, F., Liu, Y., Li, C., Pan, F., Yang, Y., Ni, J., Li, H., Brand-Saberi, B., & Guo, P. (2015). Regression of Gastric Cancer by Systemic Injection of RNA Nanoparticles Carrying both Ligand and siRNA. *Scientific Reports, 5*(1), 10726. https://doi.org/10.1038/srep10726

Cui, Y., Chen, B., & Qian, G. (2014). Lanthanide metal-organic frameworks for luminescent sensing and light-emitting applications. *Coordination Chemistry Reviews, 273-274*, 76-86. https://doi.org/10.1016/j.ccr.2013.10.023

Czaja, A. U., Trukhan, N., & Müller, U. (2009). Industrial applications of metal–organic frameworks. *Chemical Society Reviews, 38*(5), 1284-1293. https://doi.org/10.1039/B804680H

Dahiya, N., Sherman-Baust, C. A., Wang, T.-L., Davidson, B., Shih, I.-M., Zhang, Y., Wood, W., III, Becker, K. G., & Morin, P. J. (2008). MicroRNA Expression and Identification of Putative miRNA Targets in Ovarian Cancer. *PLOS ONE, 3*(6), e2436. https://doi.org/10.1371/journal.pone.0002436

DeCoste, J. B., Peterson, G. W., Jasuja, H., Glover, T. G., Huang, Y.-g., & Walton, K. S. (2013). Stability and degradation mechanisms of metal–organic frameworks containing the Zr6O4(OH)4 secondary building unit. *Journal of Materials Chemistry A, 1*(18), 5642-5650. https://doi.org/10.1039/C3TA10662D

Della Rocca, J., Liu, D., & Lin, W. (2011). Nanoscale Metal–Organic Frameworks for Biomedical Imaging and Drug Delivery. *Accounts of Chemical Research, 44*(10), 957-968. https://doi.org/10.1021/ar200028a

Deng, Z., Fang, C., Ma, X., Li, X., Zeng, Y.-J., & Peng, X. (2020). One Stone Two Birds: Zr-Fc Metal–Organic Framework Nanosheet for Synergistic Photothermal and Chemodynamic Cancer Therapy. *ACS Applied Materials & Interfaces, 12*(18), 20321-20330. https://doi.org/10.1021/acsami.0c06648

Devic, T., Horcajada, P., Serre, C., Salles, F., Maurin, G., Moulin, B., Heurtaux, D., Clet, G., Vimont, A., Grenèche, J.-M., Ouay, B. L., Moreau, F., Magnier, E., Filinchuk, Y., Marrot, J., Lavalley, J.-C., Daturi, M., & Férey, G. (2010). Functionalization in Flexible Porous Solids: Effects on the Pore Opening and the Host−Guest Interactions. *Journal of the American Chemical Society, 132*(3), 1127-1136. https://doi.org/10.1021/ja9092715

Dhull, A. K., Kaushal, V., Singh, S., & Sen, R. (2013). Tamoxifen-induced endometrial carcinoma after a lag of 14 years. *South Asian journal of cancer, 2*(1), 6-6. https://doi.org/10.4103/2278-330X.105867

Dicken, B. J., Bigam, D. L., Cass, C., Mackey, J. R., Joy, A. A., & Hamilton, S. M. (2005). Gastric adenocarcinoma: review and considerations for future directions. *Annals of surgery, 241*(1), 27-39. https://doi.org/10.1097/01.sla.0000149300.28588.23

Ding, L., Lin, X., Lin, Z., Wu, Y., Liu, X., Liu, J., Wu, M., Zhang, X., & Zeng, Y. (2020). Cancer Cell-Targeted Photosensitizer and Therapeutic Protein Co-Delivery Nanoplatform Based on a Metal–Organic Framework for Enhanced Synergistic Photodynamic and Protein Therapy. *ACS Applied Materials & Interfaces, 12*(33), 36906-36916. https://doi.org/10.1021/acsami.0c09657

Division of Cancer Prevention and Control. (2021). Colorectal Cancer Statistics. https://www.cdc.gov/cancer/colorectal/statistics/index.htm

Doan, H. V., Sartbaeva, A., Eloi, J.-C., A. Davis, S., & Ting, V. P. (2019). Defective hierarchical porous copper-based metal-organic frameworks synthesised via facile acid etching strategy. *Scientific Reports, 9*(1), 10887. https://doi.org/10.1038/s41598-019-47314-1

Dong, H., Zhou, Q., Zhang, L., & Tian, Y. (2019). Rational Design of Specific Recognition Molecules for Simultaneously Monitoring of Endogenous Polysulfide and Hydrogen Sulfide in the Mouse Brain. *Angewandte Chemie International Edition, 58*(39), 13948-13953. https://doi.org/10.1002/anie.201907210

Dorniani, D., Hussein, M. Z. B., Kura, A. U., Fakurazi, S., Shaari, A. H., & Ahmad, Z. (2012). Preparation of Fe_3O_4 magnetic nanoparticles coated with gallic acid for drug delivery. *International journal of nanomedicine, 7*, 5745-5756. https://doi.org/10.2147/IJN.S35746

Draz, M. S., Fang, B. A., Zhang, P., Hu, Z., Gu, S., Weng, K. C., Gray, J. W., & Chen, F. F. (2014). Nanoparticle-mediated systemic delivery of siRNA for treatment of cancers and viral infections. *Theranostics, 4*(9), 872-892. https://doi.org/10.7150/thno.9404

Du, Y., Xia, L., Jo, A., Davis, R. M., Bissel, P., Ehrich, M. F., & Kingston, D. G. I. (2018). Synthesis and Evaluation of Doxorubicin-Loaded Gold Nanoparticles for Tumor-Targeted Drug Delivery. *Bioconjugate Chemistry, 29*(2), 420-430. https://doi.org/10.1021/acs.bioconjchem.7b00756

Duan, F., Hu, M., Guo, C., Song, Y., Wang, M., He, L., Zhang, Z., Pettinari, R., & Zhou, L. (2020). Chromium-based metal-organic framework embedded with cobalt phthalocyanine for the sensitively impedimetric cytosensing of colorectal cancer (CT26) cells and cell imaging. *Chemical Engineering Journal, 398*, 125452. https://doi.org/10.1016/j.cej.2020.125452

El-Hammadi, M. M., & Arias, J. L. (2021). Chapter 11 - Nanomedicine for vaginal drug delivery. In P. Kesharwani, S. Taurin, & K. Greish (Eds.), *Theory and Applications of Nonparenteral Nanomedicines* (pp. 235-257). Academic Press. https://doi.org/10.1016/B978-0-12-820466-5.00011-9

Elsabahy, M., & Wooley, K. L. (2012). Design of polymeric nanoparticles for biomedical delivery applications. *Chemical Society Reviews, 41*(7), 2545-2561. https://doi.org/10.1039/C2CS15327K

Enwa, F. (2014). Mechanisms of Antimicrobial Actions of Phytochemicals against Enteric Pathogens – A Review. *Journal of Pharmaceutical, Chemical and Biological Sciences, 2*, 77-85.

Fan, W., Lu, N., Huang, P., Liu, Y., Yang, Z., Wang, S., Yu, G., Liu, Y., Hu, J., He, Q., Qu, J., Wang, T., & Chen, X. (2017). Glucose-Responsive Sequential Generation of Hydrogen Peroxide and Nitric Oxide for Synergistic Cancer Starving-Like/Gas Therapy. *Angewandte Chemie International Edition, 56*(5), 1229-1233. https://doi.org/10.1002/anie.201610682

Fan, W., Yung, B., Huang, P., & Chen, X. (2017). Nanotechnology for Multimodal Synergistic Cancer Therapy. *Chemical Reviews, 117*(22), 13566-13638. https://doi.org/10.1021/acs.chemrev.7b00258

Fan, W., Yung, B. C., & Chen, X. (2018). Stimuli-Responsive NO Release for On-Demand Gas-Sensitized Synergistic Cancer Therapy. *Angewandte Chemie International Edition, 57*(28), 8383-8394. https://doi.org/10.1002/anie.201800594

Fang, L., Cai, P., Chen, W., Liang, W., Hong, Z., & Huang, Q. (2009). Impact of cell wall structure on the behavior of bacterial cells in the binding of copper and cadmium. *Colloids and Surfaces A: Physicochemical and Engineering Aspects, 347*(1), 50-55. https://doi.org/10.1016/j.colsurfa.2008.11.041

Férey, G., Mellot-Draznieks, C., Serre, C., Millange, F., Dutour, J., Surblé, S., & Margiolaki, I. (2005). A Chromium Terephthalate-Based Solid with Unusually Large Pore Volumes and Surface Area. *Science, 309*(5743), 2040. https://doi.org/10.1126/science.1116275

Férey, G., Serre, C., Mellot-Draznieks, C., Millange, F., Surblé, S., Dutour, J., & Margiolaki, I. (2004). A Hybrid Solid with Giant Pores Prepared by a Combination of Targeted Chemistry, Simulation, and Powder Diffraction. *Angewandte Chemie International Edition, 43*(46), 6296-6301. https://doi.org/10.1002/anie.200460592

Fire, A., Xu, S., Montgomery, M. K., Kostas, S. A., Driver, S. E., & Mello, C. C. (1998). Potent and specific genetic interference by double-stranded RNA in Caenorhabditis elegans. *Nature, 391*(6669), 806-811. https://doi.org/10.1038/35888

Furukawa, F., Nishikawa, A., Lee, I. S., Kanki, K., Umemura, T., Okazaki, K., Kawamori, T., Wakabayashi, K., & Hirose, M. (2003). A cyclooxygenase-2 inhibitor, nimesulide, inhibits postinitiation phase of N-nitrosobis(2-oxopropyl)amine-induced pancreatic carcinogenesis in hamsters. *Int J Cancer, 104*(3), 269-273. https://doi.org/10.1002/ijc.10965

Gant, V. A., Wren, M. W. D., Rollins, M. S. M., Jeanes, A., Hickok, S. S., & Hall, T. J. (2007). Three novel highly charged copper-based biocides: safety and efficacy against healthcare-associated organisms. *Journal of Antimicrobial Chemotherapy, 60*(2), 294-299. https://doi.org/10.1093/jac/dkm201

Gao, M., Yi, J., Zhu, J., Minikes, A. M., Monian, P., Thompson, C. B., & Jiang, X. (2019). Role of Mitochondria in Ferroptosis. *Molecular Cell, 73*(2), 354-363.e353. https://doi.org/10.1016/j.molcel.2018.10.042

Gao, W., & Zhang, L. (2021). Nanomaterials arising amid antibiotic resistance. *Nature Reviews Microbiology, 19*(1), 5-6. https://doi.org/10.1038/s41579-020-00469-5

Gaschler, M. M., Andia, A. A., Liu, H., Csuka, J. M., Hurlocker, B., Vaiana, C. A., Heindel, D. W., Zuckerman, D. S., Bos, P. H., Reznik, E., Ye, L. F., Tyurina, Y. Y., Lin, A. J., Shchepinov, M. S., Chan, A. Y., Peguero-Pereira, E., Fomich, M. A., Daniels, J. D., Bekish, A. V., Shmanai, V. V., Kagan, V. E., Mahal, L. K., Woerpel, K. A., & Stockwell, B. R. (2018). FINO2 initiates ferroptosis through GPX4 inactivation and iron oxidation. *Nature Chemical Biology, 14*(5), 507-515. https://doi.org/10.1038/s41589-018-0031-6

Ge, J., Lei, J., & Zare, R. N. (2012). Protein–inorganic hybrid nanoflowers. *Nature Nanotechnology, 7*(7), 428-432. https://doi.org/10.1038/nnano.2012.80

Ghawanmeh, A. A., Ali, G. A. M., Algarni, H., Sarkar, S. M., & Chong, K. F. (2019). Graphene oxide-based hydrogels as a nanocarrier for anticancer drug delivery. *Nano Research, 12*(5), 973-990. https://doi.org/10.1007/s12274-019-2300-4

Giménez-Marqués, M., Bellido, E., Berthelot, T., Simón-Yarza, T., Hidalgo, T., Simón-Vázquez, R., González-Fernández, Á., Avila, J., Asensio, M. C., Gref, R., Couvreur, P., Serre, C., & Horcajada, P. (2018). GraftFast Surface Engineering to Improve MOF Nanoparticles Furtiveness. *Small, 14*(40), 1801900. https://doi.org/10.1002/smll.201801900

Giménez-Marqués, M., Hidalgo, T., Serre, C., & Horcajada, P. (2016). Nanostructured metal–organic frameworks and their bio-related applications. *Coordination Chemistry Reviews, 307*, 342-360. https://doi.org/10.1016/j.ccr.2015.08.008

Haddad, S., Abánades Lázaro, I., Fantham, M., Mishra, A., Silvestre-Albero, J., Osterrieth, J. W. M., Kaminski Schierle, G. S., Kaminski, C. F., Forgan, R. S., & Fairen-Jimenez, D. (2020). Design of a Functionalized Metal–Organic Framework System for Enhanced Targeted Delivery to Mitochondria. *Journal of the American Chemical Society, 142*(14), 6661-6674. https://doi.org/10.1021/jacs.0c00188

Hangauer, M. J., Viswanathan, V. S., Ryan, M. J., Bole, D., Eaton, J. K., Matov, A., Galeas, J., Dhruv, H. D., Berens, M. E., Schreiber, S. L., McCormick, F., & McManus, M. T. (2017). Drug-tolerant persister cancer cells are vulnerable to GPX4 inhibition. *Nature, 551*(7679), 247-250. https://doi.org/10.1038/nature24297

Harrison Joe, J., Turner Raymond, J., Joo Daniel, A., Stan Michelle, A., Chan Catherine, S., Allan Nick, D., Vrionis Helen, A., Olson Merle, E., & Ceri, H. (2008). Copper and Quaternary Ammonium Cations Exert Synergistic Bactericidal and Antibiofilm Activity against Pseudomonas aeruginosa. *Antimicrobial Agents and Chemotherapy, 52*(8), 2870-2881. https://doi.org/10.1128/AAC.00203-08

Hartlieb, K. J., Ferris, D. P., Holcroft, J. M., Kandela, I., Stern, C. L., Nassar, M. S., Botros, Y. Y., & Stoddart, J. F. (2017). Encapsulation of Ibuprofen in CD-MOF and Related Bioavailability Studies. *Molecular Pharmaceutics, 14*(5), 1831-1839. https://doi.org/10.1021/acs.molpharmaceut.7b00168

Hatfield, D. L., Tsuji, P. A., Carlson, B. A., & Gladyshev, V. N. (2014). Selenium and selenocysteine: roles in cancer, health, and development. *Trends in Biochemical Sciences, 39*(3), 112-120. https://doi.org/10.1016/j.tibs.2013.12.007

He, C., Lu, K., Liu, D., & Lin, W. (2014). Nanoscale Metal–Organic Frameworks for the Co-Delivery of Cisplatin and Pooled siRNAs to Enhance Therapeutic Efficacy in Drug-Resistant Ovarian Cancer Cells. *Journal of the American Chemical Society, 136*(14), 5181-5184. https://doi.org/10.1021/ja4098862

He, H., Du, L., Guo, H., An, Y., Lu, L., Chen, Y., Wang, Y., Zhong, H., Shen, J., Wu, J., & Shuai, X. (2020). Redox Responsive Metal Organic Framework Nanoparticles Induces Ferroptosis for Cancer Therapy. *Small, 16*(33), 2001251. https://doi.org/10.1002/smll.202001251

He, Q., & Shi, J. (2011). Mesoporous silica nanoparticle based nano drug delivery systems: synthesis, controlled drug release and delivery, pharmacokinetics and biocompatibility. *Journal of Materials Chemistry, 21*(16), 5845-5855. https://doi.org/10.1039/C0JM03851B

He, S., Wu, L., Li, X., Sun, H., Xiong, T., Liu, J., Huang, C., Xu, H., Sun, H., Chen, W., Gref, R., & Zhang, J. (2021). Metal-organic frameworks for advanced drug delivery. *Acta Pharmaceutica Sinica B, 11*(8), 2362-2395. https://doi.org/10.1016/j.apsb.2021.03.019

Hergt, R., Dutz, S., Müller, R., & Zeisberger, M. (2006). Magnetic particle hyperthermia: nanoparticle magnetism and materials development for cancer therapy. *Journal of Physics: Condensed Matter, 18*(38), S2919-S2934. https://doi.org/10.1088/0953-8984/18/38/s26

Horcajada, P., Chalati, T., Serre, C., Gillet, B., Sebrie, C., Baati, T., Eubank, J. F., Heurtaux, D., Clayette, P., Kreuz, C., Chang, J.-S., Hwang, Y. K., Marsaud, V., Bories, P.-N., Cynober, L., Gil, S., Férey, G., Couvreur, P., & Gref, R. (2010). Porous metal–organic-framework nanoscale carriers as a potential platform for drug delivery and imaging. *Nature Materials, 9*(2), 172-178. https://doi.org/10.1038/nmat2608

Horcajada, P., Gref, R., Baati, T., Allan, P. K., Maurin, G., Couvreur, P., Férey, G., Morris, R. E., & Serre, C. (2012). Metal–Organic Frameworks in Biomedicine. *Chemical Reviews, 112*(2), 1232-1268. https://doi.org/10.1021/cr200256v

Horcajada, P., Salles, F., Wuttke, S., Devic, T., Heurtaux, D., Maurin, G., Vimont, A., Daturi, M., David, O., Magnier, E., Stock, N., Filinchuk, Y., Popov, D., Riekel, C., Férey, G., & Serre, C. (2011). How Linker's Modification Controls Swelling Properties of Highly Flexible Iron(III) Dicarboxylates MIL-88. *Journal of the American Chemical Society, 133*(44), 17839-17847. https://doi.org/10.1021/ja206936e

Horcajada, P., Serre, C., Maurin, G., Ramsahye, N. A., Balas, F., Vallet-Regí, M., Sebban, M., Taulelle, F., & Férey, G. (2008). Flexible Porous Metal-Organic Frameworks for a Controlled Drug Delivery. *Journal of the American Chemical Society, 130*(21), 6774-6780. https://doi.org/10.1021/ja710973k

Horcajada, P., Serre, C., Vallet-Regí, M., Sebban, M., Taulelle, F., & Férey, G. (2006). Metal–Organic Frameworks as Efficient Materials for Drug Delivery. *Angewandte Chemie International Edition, 45*(36), 5974-5978. https://doi.org/10.1002/anie.200601878

Hu, J., Cai, H., Ren, H., Wei, Y., Xu, Z., Liu, H., & Hu, Y. (2010). Mixed-Matrix Membrane Hollow Fibers of Cu3(BTC)2 MOF and Polyimide for Gas Separation and Adsorption. *Industrial & Engineering Chemistry Research, 49*(24), 12605-12612. https://doi.org/10.1021/ie1014958

Hu, J., Wu, W., Qin, Y., Liu, C., Wei, P., Hu, J., Seeberger, P. H., & Yin, J. (2020). Fabrication of Glyco-Metal-Organic Frameworks for Targeted Interventional Photodynamic/Chemotherapy for Hepatocellular Carcinoma through Percutaneous Transperitoneal Puncture. *Advanced Functional Materials, 30*(19), 1910084. https://doi.org/10.1002/adfm.201910084

Hu, Q., Yu, J., Liu, M., Liu, A., Dou, Z., & Yang, Y. (2014). A Low Cytotoxic Cationic Metal–Organic Framework Carrier for Controllable Drug Release. *Journal of Medicinal Chemistry, 57*(13), 5679-5685. https://doi.org/10.1021/jm5004107

Hu, X., Liu, S., Wang, Y., Huang, X., Jiang, J., Cong, H., Lin, H., & Han, S. (2021). Hierarchical CuCo2O4@CoS-Cu/Co-MOF core-shell nanoflower derived from copper/cobalt bimetallic metal–organic frameworks for supercapacitors. *Journal of Colloid and Interface Science, 600*, 72-82. https://doi.org/10.1016/j.jcis.2021.05.008

Huang, H., Li, J.-R., Wang, K., Han, T., Tong, M., Li, L., Xie, Y., Yang, Q., Liu, D., & Zhong, C. (2015). An in situ self-assembly template strategy for the preparation of hierarchical-pore metal-organic frameworks. *Nature Communications, 6*(1), 8847. https://doi.org/10.1038/ncomms9847

Huang, P., Li, Z., Lin, J., Yang, D., Gao, G., Xu, C., Bao, L., Zhang, C., Wang, K., Song, H., Hu, H., & Cui, D. (2011). Photosensitizer-conjugated magnetic nanoparticles for in vivo simultaneous magnetofluorescent imaging and targeting therapy. *Biomaterials, 32*(13), 3447-3458. https://doi.org/10.1016/j.biomaterials.2011.01.032

Huang, P., Lin, J., Wang, S., Zhou, Z., Li, Z., Wang, Z., Zhang, C., Yue, X., Niu, G., Yang, M., Cui, D., & Chen, X. (2013). Photosensitizer-conjugated silica-coated gold nanoclusters for fluorescence imaging-guided photodynamic therapy. *Biomaterials, 34*(19), 4643-4654. https://doi.org/10.1016/j.biomaterials.2013.02.063

Huang, P., Lin, J., Wang, X., Wang, Z., Zhang, C., He, M., Wang, K., Chen, F., Li, Z., Shen, G., Cui, D., & Chen, X. (2012). Light-Triggered Theranostics Based on Photosensitizer-Conjugated Carbon Dots for Simultaneous Enhanced-Fluorescence Imaging and Photodynamic Therapy. *Advanced Materials, 24*(37), 5104-5110. https://doi.org/10.1002/adma.201200650

Huguenin, J., Ould Saad Hamady, S., & Bourson, P. (2015). Monitoring deprotonation of gallic acid by Raman spectroscopy. *Journal of Raman Spectroscopy, 46*(11), 1062-1066. https://doi.org/https://doi.org/10.1002/jrs.4752

Huo, J., Brightwell, M., El Hankari, S., Garai, A., & Bradshaw, D. (2013). A versatile, industrially relevant, aqueous room temperature synthesis of HKUST-1 with high space-time yield. *Journal of Materials Chemistry A, 1*(48), 15220-15223. https://doi.org/10.1039/C3TA14409G

Hyun, H., Park, M. H., Jo, G., Kim, S. Y., Chun, H. J., & Yang, D. H. (2019). Photo-Cured Glycol Chitosan Hydrogel for Ovarian Cancer Drug Delivery. *Marine Drugs, 17*(1). https://doi.org/10.3390/md17010041

Ibrahim, S. A., Yang, H., & Seo, C. W. (2008). Antimicrobial activity of lactic acid and copper on growth of Salmonella and Escherichia coli O157:H7 in laboratory medium and carrot juice. *Food Chemistry, 109*(1), 137-143. https://doi.org/10.1016/j.foodchem.2007.12.035

Inoue, M., Suzuki, R., Koide, T., Sakaguchi, N., Ogihara, Y., & Yabu, Y. (1994). Antioxidant, Gallic Acid, Induces Apoptosis in HL-60RG Cells. *Biochemical and Biophysical Research Communications, 204*(2), 898-904. https://doi.org/10.1006/bbrc.1994.2544

Jeremias, F. (2015). *Synthesis and Characterization of Metal-Organic Frameworks for Heat Transformation Applications*

Jhung, S. H., Lee, J. H., Yoon, J. W., Serre, C., Férey, G., & Chang, J. S. (2007). Microwave Synthesis of Chromium Terephthalate MIL-101 and Its Benzene Sorption Ability. *Advanced Materials, 19*(1), 121-124. https://doi.org/10.1002/adma.200601604

Jia, Q., Li, Z., Guo, C., Huang, X., Song, Y., Zhou, N., Wang, M., Zhang, Z., He, L., & Du, M. (2019). A γ-cyclodextrin-based metal–organic framework embedded with graphene quantum dots and modified with PEGMA via SI-ATRP for anticancer drug delivery and therapy. *Nanoscale, 11*(43), 20956-20967. https://doi.org/10.1039/C9NR06195A

Jiang, J., Huang, L., Liu, X., & Ai, L. (2017). Bioinspired Cobalt–Citrate Metal–Organic Framework as an Efficient Electrocatalyst for Water Oxidation. *ACS Applied Materials & Interfaces, 9*(8), 7193-7201. https://doi.org/10.1021/acsami.6b16534

Jin, S., Qi, X., Wang, T., Ren, L., Yang, K., & Zhong, H. (2018). In vitro study of stimulation effect on endothelialization by a copper bearing cobalt alloy. *Journal of Biomedical Materials Research Part A, 106*(2), 561-569. https://doi.org/10.1002/jbm.a.36263

Juaid, N., Amin, A., Abdalla, A., Reese, K., Alamri, Z., Moulay, M., Abdu, S., & Miled, N. (2021). Anti-Hepatocellular Carcinoma Biomolecules: Molecular Targets Insights. *International Journal of Molecular Sciences, 22*(19). https://doi.org/10.3390/ijms221910774

Jung, K.-W., Choi, B. H., Lee, S. Y., Ahn, K.-H., & Lee, Y. J. (2018). Green synthesis of aluminum-based metal organic framework for the removal of azo dye Acid Black 1 from aqueous media. *Journal of Industrial and Engineering Chemistry, 67*, 316-325. https://doi.org/10.1016/j.jiec.2018.07.003

Kang, M.-S., Oh, J.-S., Kang, I.-C., Hong, S.-J., & Choi, C.-H. (2008). Inhibitory effect of methyl gallate and gallic acid on oral bacteria. *The Journal of Microbiology, 46*(6), 744-750. https://doi.org/10.1007/s12275-008-0235-7

Kar, A. K., & Srivastava, R. (2018). An efficient and sustainable catalytic reduction of carbon–carbon multiple bonds, aldehydes, and ketones using a Cu nanoparticle decorated metal organic framework. *New Journal of Chemistry, 42*(12), 9557-9567. https://doi.org/10.1039/C8NJ01704B

Karimi-Khouzani, O., Heidarian, E., & Amini, S. A. (2017). Anti-inflammatory and ameliorative effects of gallic acid on fluoxetine-induced oxidative stress and liver damage in rats. *Pharmacological Reports, 69*(4), 830-835. https://doi.org/10.1016/j.pharep.2017.03.011

Katsoulidis, A. P., Antypov, D., Whitehead, G. F. S., Carrington, E. J., Adams, D. J., Berry, N. G., Darling, G. R., Dyer, M. S., & Rosseinsky, M. J. (2019). Chemical control of structure and guest uptake by a conformationally mobile porous material. *Nature, 565*(7738), 213-217. https://doi.org/10.1038/s41586-018-0820-9

Kawamori, T., Nakatsugi, S., Ohta, T., Sugimura, T., & Wakabayashi, K. (2002). Chemopreventive effects of nimesulide, a selective cyclooxygenase-2 inhibitor, against PhIP-induced mammary carcinogenesis. *Adv Exp Med Biol, 507*, 371-376. https://doi.org/10.1007/978-1-4615-0193-0_57

Ke, F., Yuan, Y.-P., Qiu, L.-G., Shen, Y.-H., Xie, A.-J., Zhu, J.-F., Tian, X.-Y., & Zhang, L.-D. (2011). Facile fabrication of magnetic metal–organic framework nanocomposites for potential targeted drug delivery. *Journal of Materials Chemistry, 21*(11), 3843-3848. https://doi.org/10.1039/C0JM01770A

Keating, G. M., & Santoro, A. (2009). Sorafenib. *Drugs, 69*(2), 223-240. https://doi.org/10.2165/00003495-200969020-00006

Keshet, R., & Erez, A. (2018). Arginine and the metabolic regulation of nitric oxide synthesis in cancer. *Disease Models & Mechanisms, 11*(8), dmm033332. https://doi.org/10.1242/dmm.033332

Keter, F. K., Guzei, I. A., Nell, M., Zyl, W. E. v., & Darkwa, J. (2014). Phosphinogold(I) Dithiocarbamate Complexes: Effect of the Nature of Phosphine Ligand on Anticancer Properties. *Inorganic Chemistry, 53*(4), 2058-2067. https://doi.org/10.1021/ic4025926

Kim, C.-k., Ghosh, P., & Rotello, V. M. (2009). Multimodal drug delivery using gold nanoparticles. *Nanoscale, 1*(1), 61-67.

Kim, K., Lee, S., Jin, E., Palanikumar, L., Lee, J. H., Kim, J. C., Nam, J. S., Jana, B., Kwon, T.-H., Kwak, S. K., Choe, W., & Ryu, J.-H. (2019). MOF × Biopolymer: Collaborative Combination of Metal–Organic Framework and Biopolymer for Advanced Anticancer Therapy. *ACS Applied Materials & Interfaces, 11*(31), 27512-27520. https://doi.org/10.1021/acsami.9b05736

Kirchon, A., Day, G. S., Fang, Y., Banerjee, S., Ozdemir, O. K., & Zhou, H.-C. (2018). Suspension Processing of Microporous Metal-Organic Frameworks: A Scalable Route to High-Quality Adsorbents. *iScience, 5*, 30-37. https://doi.org/https://doi.org/10.1016/j.isci.2018.06.009

Kodaira, H., Kusuhara, H., Ushiki, J., Fuse, E., & Sugiyama, Y. (2010). Kinetic Analysis of the Cooperation of P-Glycoprotein and Breast Cancer Resistance Protein in Limiting the Brain and Testis Penetration of Erlotinib, Flavopiridol, and Mitoxantrone. *Journal of Pharmacology and Experimental Therapeutics, 333*(3), 788. https://doi.org/10.1124/jpet.109.162321

Koo, J., Hwang, I.-C., Yu, X., Saha, S., Kim, Y., & Kim, K. (2017). Hollowing out MOFs: hierarchical micro- and mesoporous MOFs with tailorable porosity via selective acid etching. *Chemical Science, 8*(10), 6799-6803. https://doi.org/10.1039/C7SC02886E

Kooti, M., Sedeh, A. N., Motamedi, H., & Rezatofighi, S. E. (2018). Magnetic graphene oxide inlaid with silver nanoparticles as antibacterial and drug delivery composite. *Applied Microbiology and Biotechnology, 102*(8), 3607-3621. https://doi.org/10.1007/s00253-018-8880-1

Koshiyama, M., Matsumura, N., & Konishi, I. (2017). Subtypes of Ovarian Cancer and Ovarian Cancer Screening. *Diagnostics (Basel), 7*(1). https://doi.org/10.3390/diagnostics7010012

Kuo, C.-Y., Chao, Y., & Li, C.-P. (2014). Update on treatment of gastric cancer. *Journal of the Chinese Medical Association, 77*(7), 345-353. https://doi.org/10.1016/j.jcma.2014.04.006

Küsgens, P., Zgaverdea, A., Fritz, H.-G., Siegle, S., & Kaskel, S. (2010). Metal-Organic Frameworks in Monolithic Structures. *Journal of the American Ceramic Society, 93*(9), 2476-2479. https://doi.org/10.1111/j.1551-2916.2010.03824.x

Laha, D., Pal, K., Chowdhuri, A. R., Parida, P. K., Sahu, S. K., Jana, K., & Karmakar, P. (2019). Fabrication of curcumin-loaded folic acid-tagged metal organic framework for triple negative breast cancer therapy in in vitro and in vivo systems. *New Journal of Chemistry, 43*(1), 217-229. https://doi.org/10.1039/C8NJ03350A

Langley, S., & Beveridge, T. J. (1999). Effect of O-Side-Chain-Lipopolysaccharide Chemistry on Metal Binding. *Applied and Environmental Microbiology, 65*(2), 489-498. https://doi.org/10.1128/AEM.65.2.489-498.1999

Latroche, M., Surblé, S., Serre, C., Mellot-Draznieks, C., Llewellyn, P. L., Lee, J.-H., Chang, J.-S., Jhung, S. H., & Férey, G. (2006). Hydrogen Storage in the Giant-Pore Metal–Organic Frameworks MIL-100 and MIL-101. *Angewandte Chemie International Edition, 45*(48), 8227-8231. https://doi.org/10.1002/anie.200600105

Lebok, P., Öztürk, M., Heilenkötter, U., Jaenicke, F., Müller, V., Paluchowski, P., Geist, S., Wilke, C., Burandt, E., Lebeau, A., Wilczak, W., Krech, T., Simon, R., Sauter, G., & Quaas, A. (2016). High levels of class III β-tubulin expression are associated with aggressive tumor features in breast cancer. *Oncology letters, 11*(3), 1987-1994. https://doi.org/10.3892/ol.2016.4206

Lee, S. W., Cheon, S. A., Kim, M. I., & Park, T. J. (2015). Organic–inorganic hybrid nanoflowers: types, characteristics, and future prospects. *Journal of Nanobiotechnology, 13*(1), 54. https://doi.org/10.1186/s12951-015-0118-0

Lee, Y.-R., Kim, J., & Ahn, W.-S. (2013). Synthesis of metal-organic frameworks: A mini review. *Korean Journal of Chemical Engineering, 30*(9), 1667-1680. https://doi.org/10.1007/s11814-013-0140-6

Lei, B., Wang, M., Jiang, Z., Qi, W., Su, R., & He, Z. (2018). Constructing Redox-Responsive Metal–Organic Framework Nanocarriers for Anticancer Drug Delivery. *ACS Applied Materials & Interfaces, 10*(19), 16698-16706. https://doi.org/10.1021/acsami.7b19693

Lemire, J. A., Harrison, J. J., & Turner, R. J. (2013). Antimicrobial activity of metals: mechanisms, molecular targets and applications. *Nature Reviews Microbiology, 11*(6), 371-384. https://doi.org/10.1038/nrmicro3028

Leng, X., Dong, X., Wang, W., Sai, N., Yang, C., You, L., Huang, H., Yin, X., & Ni, J. (2018). Biocompatible Fe-Based Micropore Metal-Organic Frameworks as Sustained-Release Anticancer Drug Carriers. *Molecules, 23*(10). https://doi.org/10.3390/molecules23102490

Lestari, W. W., Arvinawati, M., Martien, R., & Kusumaningsih, T. (2018). Green and facile synthesis of MOF and nano MOF containing zinc(II) and benzen 1,3,5-tri carboxylate and its study in ibuprofen slow-release. *Materials Chemistry and Physics, 204*, 141-146. https://doi.org/10.1016/j.matchemphys.2017.10.034

Levina, A., Mitra, A., & Lay, P. A. (2009). Recent developments in ruthenium anticancer drugs. *Metallomics, 1*(6), 458-470. https://doi.org/10.1039/b904071d

Li, A., Chen, J., Zhu, W., Jiang, T., Zhang, X., & Gu, Q. (2007). Antibacterial activity of gallic acid from the flowers of Rosa chinensis Jacq. against fish pathogens. *Aquaculture Research, 38*(10), 1110-1112. https://doi.org/10.1111/j.1365-2109.2007.01745.x

Li, H.-T., Song, S.-J., Pei, X.-R., & Lu, D.-B. (2019). A InIII-MOF with Imidazole Decorated Pores as 5-Fu Delivery System to Inhibit Colon Cancer Cells Proliferation and Induce Cell Apoptosis in vitro and in vivo. *Zeitschrift für anorganische und allgemeine Chemie, 645*(11), 801-809. https://doi.org/10.1002/zaac.201900072

Li, H., Eddaoudi, M., O'Keeffe, M., & Yaghi, O. M. (1999). Design and synthesis of an exceptionally stable and highly porous metal-organic framework. *Nature, 402*(6759), 276-279. https://doi.org/10.1038/46248

Li, H., Lv, N., Li, X., Liu, B., Feng, J., Ren, X., Guo, T., Chen, D., Fraser Stoddart, J., Gref, R., & Zhang, J. (2017). Composite CD-MOF nanocrystals-containing microspheres for sustained drug delivery. *Nanoscale, 9*(22), 7454-7463. https://doi.org/10.1039/C6NR07593B

Li, J., Huo, M., Wang, J., Zhou, J., Mohammad, J. M., Zhang, Y., Zhu, Q., Waddad, A. Y., & Zhang, Q. (2012). Redox-sensitive micelles self-assembled from amphiphilic hyaluronic acid-deoxycholic acid conjugates for targeted intracellular delivery of paclitaxel. *Biomaterials, 33*(7), 2310-2320. https://doi.org/ 10.1016/j.biomaterials.2011.11.022

Li, J., Yu, X., Wang, Y., Yuan, Y., Xiao, H., Cheng, D., & Shuai, X. (2014). A Reduction and pH Dual-Sensitive Polymeric Vector for Long-Circulating and Tumor-Targeted siRNA Delivery. *Advanced Materials, 26*(48), 8217-8224. https://doi.org/10.1002/adma.201403877

Li, L., Xiang, S., Cao, S., Zhang, J., Ouyang, G., Chen, L., & Su, C.-Y. (2013). A synthetic route to ultralight hierarchically micro/mesoporous Al(III)-carboxylate metal-organic aerogels. *Nature Communications, 4*(1), 1774. https://doi.org/10.1038/ncomms2757

Li, P., Modica, Justin A., Howarth, Ashlee J., Vargas L, E., Moghadam, Peyman Z., Snurr, Randall Q., Mrksich, M., Hupp, Joseph T., & Farha, Omar K. (2016). Toward Design Rules for Enzyme Immobilization in Hierarchical Mesoporous Metal-Organic Frameworks. *Chem, 1*(1), 154-169. https://doi.org/10.1016/j.chempr.2016.05.001

Li, S.-D., & Huang, L. (2008). Pharmacokinetics and Biodistribution of Nanoparticles. *Molecular Pharmaceutics, 5*(4), 496-504. https://doi.org/10.1021/mp800049w

Li, S.-F., Guo, H., Huang, Y., Li, C.-M., Liu, Y., & Han, J. (2020). A porous Cu(II)-based metal-organic framework with one-dimensional hexagonal channels for solvent-free cyanosilylation and anti-ovarian cancer activity. *Journal of Polymer Research, 27*(3), 63. https://doi.org/10.1007/s10965-019-2002-3

Li, Y., Fei, X., Liang, L., Tian, J., Xu, L., Wang, X., & Wang, Y. (2016). The influence of synthesis conditions on enzymatic activity of enzyme-inorganic hybrid nanoflowers. *Journal of Molecular Catalysis B: Enzymatic, 133*, 92-97. https://doi.org/10.1016/j.molcatb.2016.08.001

Li, Y., Song, Y., Zhang, W., Xu, J., Hou, J., Feng, X., & Zhu, W. (2020). MOF nanoparticles with encapsulated dihydroartemisinin as a controlled drug delivery system for enhanced cancer therapy and mechanism analysis. *Journal of Materials Chemistry B, 8*(33), 7382-7389. https://doi.org/10.1039/D0TB01330G

Li, Y., & Yang, R. T. (2008). Hydrogen storage in metal-organic and covalent-organic frameworks by spillover. *AIChE Journal, 54*(1), 269-279. https://doi.org/10.1002/aic.11362

Li, Y., Zhou, J., Wang, L., & Xie, Z. (2020). Endogenous Hydrogen Sulfide-Triggered MOF-Based Nanoenzyme for Synergic Cancer Therapy. *ACS Applied Materials & Interfaces, 12*(27), 30213-30220. https://doi.org/10.1021/acsami.0c08659

Li, Z.-J., Liu, M., Dawuti, G., Dou, Q., Ma, Y., Liu, H.-G., & Aibai, S. (2017). Antifungal Activity of Gallic Acid In Vitro and In Vivo. *Phytotherapy Research, 31*(7), 1039-1045. https://doi.org/10.1002/ptr.5823

Li, Z.-Q., Qiu, L.-G., Xu, T., Wu, Y., Wang, W., Wu, Z.-Y., & Jiang, X. (2009). Ultrasonic synthesis of the microporous metal–organic framework Cu3(BTC)2 at ambient temperature and pressure: An efficient and environmentally friendly method. *Materials Letters, 63*(1), 78-80. https://doi.org/10.1016/j.matlet.2008.09.010

Li, Z., Wu, X., Wang, W., Gai, C., Zhang, W., Li, W., & Ding, D. (2021). Fe(II) and Tannic Acid-Cloaked MOF as Carrier of Artemisinin for Supply of Ferrous Ions to Enhance Treatment of Triple-Negative Breast Cancer. *Nanoscale Research Letters, 16*(1), 37. https://doi.org/10.1186/s11671-021-03497-z

Li, Z., Zhang, Y., Su, Y., Ouyang, P., Ge, J., & Liu, Z. (2014). Spatial co-localization of multi-enzymes by inorganic nanocrystal–protein complexes. *Chemical Communications, 50*(83), 12465-12468. https://doi.org/10.1039/C4CC05478D

Lian, X., Chen, Y.-P., Liu, T.-F., & Zhou, H.-C. (2016). Coupling two enzymes into a tandem nanoreactor utilizing a hierarchically structured MOF. *Chemical Science, 7*(12), 6969-6973. https://doi.org/10.1039/C6SC01438K

Liang, J., Xie, Y.-Q., Wang, X.-S., Wang, Q., Liu, T.-T., Huang, Y.-B., & Cao, R. (2018). An imidazolium-functionalized mesoporous cationic metal–organic framework for cooperative CO2 fixation into cyclic carbonate. *Chemical Communications, 54*(4), 342-345. https://doi.org/10.1039/C7CC08630J

Liang, S., Xiao, X., Bai, L., Liu, B., Yuan, M., Ma, P. a., Pang, M., Cheng, Z., & Lin, J. (2021). Conferring Ti-Based MOFs with Defects for Enhanced Sonodynamic Cancer Therapy. *Advanced Materials, 33*(18), 2100333. https://doi.org/10.1002/adma.202100333

Liang, Z., Yang, Z., Yuan, H., Wang, C., Qi, J., Liu, K., Cao, R., & Zheng, H. (2018). A protein@metal–organic framework nanocomposite for pH-triggered anticancer drug delivery. *Dalton Transactions, 47*(30), 10223-10228. https://doi.org/10.1039/C8DT01789A

Lin, Z., Xiao, Y., Yin, Y., Hu, W., Liu, W., & Yang, H. (2014). Facile Synthesis of Enzyme-Inorganic Hybrid Nanoflowers and Its Application as a Colorimetric Platform for Visual Detection of Hydrogen Peroxide and Phenol. *ACS Applied Materials & Interfaces, 6*(13), 10775-10782. https://doi.org/10.1021/am502757e

Liu, M., Liu, B., Liu, Q., Du, K., Wang, Z., & He, N. (2019). Nanomaterial-induced ferroptosis for cancer specific therapy. *Coordination Chemistry Reviews, 382*, 160-180. https://doi.org/10.1016/j.ccr.2018.12.015

Liu, Y., Jia, Q., Zhai, X., Mao, F., Jiang, A., & Zhou, J. (2019). Rationally designed pure-inorganic upconversion nanoprobes for ultra-highly selective hydrogen sulfide imaging and elimination in vivo. *Chemical Science, 10*(4), 1193-1200. https://doi.org/10.1039/C8SC04464C

Livage, C., Egger, C., & Férey, G. (2001). Hydrothermal versus Nonhydrothermal Synthesis for the Preparation of Organic−Inorganic Solids: The Example of Cobalt(II) Succinate. *Chemistry of Materials, 13*(2), 410-414. https://doi.org/10.1021/cm001148k

Lohe, M. R., Rose, M., & Kaskel, S. (2009). Metal–organic framework (MOF) aerogels with high micro- and macroporosity. *Chemical Communications*(40), 6056-6058. https://doi.org/10.1039/B910175F

Lu, X.-C., Wang, H.-L., Wang, X., Li, Q.-Z., & Liao, L. (2019). A New Zn(II)-Diisophthalate MOF for Solvent-Free Cyanosilylation of Aldehydes and Anti-colon Cancer Activity Study. *Journal of Cluster Science, 30*(6), 1673-1681. https://doi.org/10.1007/s10876-019-01614-8

Lu, Y., Yue, Z., Xie, J., Wang, W., Zhu, H., Zhang, E., & Cao, Z. (2018). Micelles with ultralow critical micelle concentration as carriers for drug delivery. *Nature Biomedical Engineering, 2*(5), 318-325. https://doi.org/10.1038/s41551-018-0234-x

Lucky, S. S., Soo, K. C., & Zhang, Y. (2015). Nanoparticles in Photodynamic Therapy. *Chemical Reviews, 115*(4), 1990-2042. https://doi.org/10.1021/cr5004198

Luo, W., Zhu, C., Su, S., Li, D., He, Y., Huang, Q., & Fan, C. (2010). Self-Catalyzed, Self-Limiting Growth of Glucose Oxidase-Mimicking Gold Nanoparticles. *ACS Nano, 4*(12), 7451-7458. https://doi.org/10.1021/nn102592h

Lv, C., Liu, Y., Meng, G., Li, J., & Ti, Z. (2020). A new Er(III)-based MOF showing anti-colon cancer activity by inhibiting IL-6-STAT3 signaling pathway and reducing TNF-α and IL-1β production. *Journal of Coordination Chemistry, 73*(9), 1478-1489. https://doi.org/10.1080/00958972.2020.1780216

Manna, L., Milliron, D. J., Meisel, A., Scher, E. C., & Alivisatos, A. P. (2003). Controlled growth of tetrapod-branched inorganic nanocrystals. *Nature Materials, 2*(6), 382-385. https://doi.org/10.1038/nmat902

Massoumi, R. (2011). CYLD: a deubiquitination enzyme with multiple roles in cancer. *Future Oncology, 7*(2), 285-297. https://doi.org/10.2217/fon.10.187

Mathieu, K. B., Bedi, D. G., Thrower, S. L., Qayyum, A., & Bast, R. C., Jr. (2018). Screening for ovarian cancer: imaging challenges and opportunities for improvement. *Ultrasound Obstet Gynecol, 51*(3), 293-303. https://doi.org/10.1002/uog.17557

Meng, F., Hennink, W. E., & Zhong, Z. (2009). Reduction-sensitive polymers and bioconjugates for biomedical applications. *Biomaterials, 30*(12), 2180-2198. https://doi.org/10.1016/j.biomaterials.2009.01.026

Meng, H., Liong, M., Xia, T., Li, Z., Ji, Z., Zink, J. I., & Nel, A. E. (2010). Engineered Design of Mesoporous Silica Nanoparticles to Deliver Doxorubicin and P-Glycoprotein siRNA to Overcome Drug Resistance in a Cancer Cell Line. *ACS Nano, 4*(8), 4539-4550. https://doi.org/10.1021/nn100690m

Meyers, J. D., Cheng, Y., Broome, A.-M., Agnes, R. S., Schluchter, M. D., Margevicius, S., Wang, X., Kenney, M. E., Burda, C., & Basilion, J. P. (2015). Peptide-Targeted Gold Nanoparticles for Photodynamic Therapy of Brain Cancer. *Particle & Particle Systems Characterization, 32*(4), 448-457. https://doi.org/10.1002/ppsc.201400119

Mignani, S., El Kazzouli, S., Bousmina, M., & Majoral, J.-P. (2013). Expand classical drug administration ways by emerging routes using dendrimer drug delivery systems: A concise overview. *Advanced Drug Delivery Reviews, 65*(10), 1316-1330. https://doi.org/10.1016/j.addr.2013.01.001

Mignani, S., Shi, X., Rodrigues, J., Roy, R., Muñoz-Fernández, Á., Ceña, V., & Majoral, J.-P. (2020). Dendrimers toward Translational Nanotherapeutics: Concise Key Step Analysis. *Bioconjugate Chemistry, 31*(9), 2060-2071. https://doi.org/10.1021/acs.bioconjchem.0c00395

Miller, S. R., Heurtaux, D., Baati, T., Horcajada, P., Grenèche, J.-M., & Serre, C. (2010). Biodegradable therapeutic MOFs for the delivery of bioactive molecules. *Chemical Communications, 46*(25), 4526-4528. https://doi.org/10.1039/C001181A

Mills, G. B., & Moolenaar, W. H. (2003). The emerging role of lysophosphatidic acid in cancer. *Nature Reviews Cancer, 3*(8), 582-591. https://doi.org/10.1038/nrc1143

Mitra, D., Kang, E.-T., & Neoh, K. G. (2020). Antimicrobial Copper-Based Materials and Coatings: Potential Multifaceted Biomedical Applications. *ACS Applied Materials & Interfaces, 12*(19), 21159-21182. https://doi.org/10.1021/acsami.9b17815

Miyazaki, M., Yuba, E., Hayashi, H., Harada, A., & Kono, K. (2018). Hyaluronic Acid-Based pH-Sensitive Polymer-Modified Liposomes for Cell-Specific Intracellular Drug Delivery Systems. *Bioconjugate Chemistry, 29*(1), 44-55. https://doi.org/10.1021/acs.bioconjchem.7b00551

Moghimi, R., Aliahmadi, A., McClements, D. J., & Rafati, H. (2016). Investigations of the effectiveness of nanoemulsions from sage oil as antibacterial agents on some food borne pathogens. *LWT - Food Science and Technology, 71*, 69-76. https://doi.org/10.1016/j.lwt.2016.03.018

Mokari, T., Zhang, M., & Yang, P. (2007). Shape, Size, and Assembly Control of PbTe Nanocrystals. *Journal of the American Chemical Society, 129*(32), 9864-9865. https://doi.org/10.1021/ja074145i

Mosmann, T. (1983). Rapid colorimetric assay for cellular growth and survival: Application to proliferation and cytotoxicity assays. *Journal of Immunological Methods, 65*(1), 55-63. https://doi.org/10.1016/0022-1759(83)90303-4

Mozzetti, S., Ferlini, C., Concolino, P., Filippetti, F., Raspaglio, G., Prislei, S., Gallo, D., Martinelli, E., Ranelletti, F. O., Ferrandina, G., & Scambia, G. (2005). Class III beta-tubulin overexpression is a prominent mechanism of paclitaxel resistance in ovarian cancer patients. *Clin Cancer Res, 11*(1), 298-305.

Mu, J., He, L., Fan, W., Tang, W., Wang, Z., Jiang, C., Zhang, D., Liu, Y., Deng, H., Zou, J., Jacobson, O., Qu, J., Huang, P., & Chen, X. (2020). Cascade Reactions Catalyzed by Planar Metal–Organic Framework Hybrid Architecture for Combined Cancer Therapy. *Small, 16*(42), 2004016. https://doi.org/10.1002/smll.202004016

Mukherjee, P., Kumar, A., Bhamidipati, K., Puvvada, N., & Sahu, S. K. (2020). Facile Strategy to Synthesize Magnetic Upconversion Nanoscale Metal–Organic Framework Composites for Theranostics Application. *ACS Applied Bio Materials, 3*(2), 869-880. https://doi.org/10.1021/acsabm.9b00949

Nagaraja, C. M., Haldar, R., Maji, T. K., & Rao, C. N. R. (2012). Chiral Porous Metal–Organic Frameworks of Co(II) and Ni(II): Synthesis, Structure, Magnetic Properties, and CO2 Uptake. *Crystal Growth & Design, 12*(2), 975-981. https://doi.org/10.1021/cg201447c

Nagata, S., Kokado, K., & Sada, K. (2020). Metal–organic framework tethering pH- and thermo-responsive polymer for ON–OFF controlled release of guest molecules. *CrystEngComm, 22*(6), 1106-1111. https://doi.org/10.1039/C9CE01731C

Nakatsugi, S., Ohta, T., Kawamori, T., Mutoh, M., Tanigawa, T., Watanabe, K., Sugie, S., Sugimura, T., & Wakabayashi, K. (2000). Chemoprevention by nimesulide, a selective cyclooxygenase-2 inhibitor, of 2-amino-1-methyl-6-phenylimidazo[4,5-b]pyridine (PhIP)-induced mammary gland carcinogenesis in rats. *Jpn J Cancer Res, 91*(9), 886-892. https://doi.org/10.1111/j.1349-7006.2000.tb01030.x

Naskar, A., & Kim, K.-s. (2019). Nanomaterials as Delivery Vehicles and Components of New Strategies to Combat Bacterial Infections: Advantages and Limitations. *Microorganisms, 7*(9). https://doi.org/10.3390/microorganisms7090356

Nathan, C. (2004). Antibiotics at the crossroads. *Nature, 431*(7011), 899-902. https://doi.org/10.1038/431899a

Nejadshafiee, V., Naeimi, H., Goliaei, B., Bigdeli, B., Sadighi, A., Dehghani, S., Lotfabadi, A., Hosseini, M., Nezamtaheri, M. S., Amanlou, M., Sharifzadeh, M., & Khoobi, M. (2019). Magnetic bio-metal–organic framework nanocomposites decorated with folic acid conjugated chitosan as a promising biocompatible targeted theranostic system for cancer treatment. *Materials Science and Engineering: C, 99*, 805-815. https://doi.org/10.1016/j.msec.2019.02.017

Nivetha, R., Sajeev, A., Mary Paul, A., Gothandapani, K., Gnanasekar, S., Bhardwaj, P., Jacob, G., Sellappan, R., Raghavan, V., N, K. C., Pitchaimuthu, S., Jeong, S. K., & Nirmala Grace, A. (2020). Cu based Metal Organic Framework (Cu-MOF) for electrocatalytic hydrogen evolution reaction. *Materials Research Express, 7*(11), 114001. https://doi.org/10.1088/2053-1591/abb056

Nohynek, L. J., Alakomi, H.-L., Kähkönen, M. P., Heinonen, M., Helander, I. M., Oksman-Caldentey, K.-M., & Puupponen-Pimiä, R. H. (2006). Berry Phenolics: Antimicrobial Properties and Mechanisms of Action Against Severe Human Pathogens. *Nutrition and Cancer, 54*(1), 18-32. https://doi.org/10.1207/s15327914nc5401_4

Ogawara, K.-i., Un, K., Tanaka, K.-i., Higaki, K., & Kimura, T. (2009). In vivo anti-tumor effect of PEG liposomal doxorubicin (DOX) in DOX-resistant tumor-bearing mice: Involvement of cytotoxic effect on vascular endothelial cells. *Journal of Controlled Release, 133*(1), 4-10. https://doi.org/10.1016/j.jconrel.2008.09.008

Ouyang, B., Ouyang, P., Shi, M., Maimaiti, T., Li, Q., Lan, S., Luo, J., Wu, X., & Yang, S.-T. (2021). Low toxicity of metal-organic framework MOF-199 to bacteria Escherichia coli and Staphylococcus aureus. *Journal of Hazardous Materials Advances, 1*, 100002. https://doi.org/10.1016/j.hazadv.2021.100002

Pan, Y., Liu, Y., Zeng, G., Zhao, L., & Lai, Z. (2011). Rapid synthesis of zeolitic imidazolate framework-8 (ZIF-8) nanocrystals in an aqueous system. *Chemical Communications, 47*(7), 2071-2073. https://doi.org/10.1039/C0CC05002D

Patel, D. K., Rana, D., Aswal, V. K., Srivastava, S., Roy, P., & Maiti, P. (2015). Influence of graphene on self-assembly of polyurethane and evaluation of its biomedical properties. *Polymer, 65*, 183-192. https://doi.org/10.1016/j.polymer.2015.03.076

Peng, X., Manna, L., Yang, W., Wickham, J., Scher, E., Kadavanich, A., & Alivisatos, A. P. (2000). Shape control of CdSe nanocrystals. *Nature, 404*(6773), 59-61. https://doi.org/10.1038/35003535

Pfeilschifter, W., Czech, B., Hoffmann, B. P., Sujak, M., Kahles, T., Steinmetz, H., Neumann-Haefelin, T., & Pfeilschifter, J. (2010). Pyrrolidine Dithiocarbamate Activates p38 MAPK and Protects Brain Endothelial Cells From Apoptosis: A Mechanism for the Protective Effect in Stroke? *Neurochemical Research, 35*(9), 1391-1401. https://doi.org/10.1007/s11064-010-0197-0

Pooresmaeil, M., Asl, E. A., & Namazi, H. (2021). A new pH-sensitive CS/Zn-MOF@GO ternary hybrid compound as a biofriendly and implantable platform for prolonged 5-Fluorouracil delivery to human breast cancer cells. *Journal of Alloys and Compounds, 885*, 160992. https://doi.org/10.1016/j.jallcom.2021.160992

PramilaDevamani, R. H., & Alagar, M. (2013). Synthesis and characterization of Copper (II) Phosphate nano particles. *Elixir NanoTechnology 2229-712X*, 16917-16921.

Proserpio, I., Rausei, S., Barzaghi, S., Frattini, F., Galli, F., Iovino, D., Rovera, F., Boni, L., Dionigi, G., & Pinotti, G. (2014). Multimodal treatment of gastric cancer. *World journal of gastrointestinal surgery, 6*(4), 55-58. https://doi.org/10.4240/wjgs.v6.i4.55

Qin, W., Cao, W., Liu, H., Li, Z., & Li, Y. (2014). Metal–organic framework MIL-101 doped with palladium for toluene adsorption and hydrogen storage. *RSC Advances, 4*(5), 2414-2420. https://doi.org/10.1039/C3RA45983G

Qiu, L.-G., Xu, T., Li, Z.-Q., Wang, W., Wu, Y., Jiang, X., Tian, X.-Y., & Zhang, L.-D. (2008). Hierarchically Micro- and Mesoporous Metal–Organic Frameworks with Tunable Porosity. *Angewandte Chemie International Edition, 47*(49), 9487-9491. https://doi.org/10.1002/anie.200803640

Rajkumar, T., Kukkar, D., Kim, K.-H., Sohn, J. R., & Deep, A. (2019). Cyclodextrin-metal–organic framework (CD-MOF): From synthesis to applications. *Journal of Industrial and Engineering Chemistry, 72*, 50-66. https://doi.org/10.1016/j.jiec.2018.12.048

Rawla, P., Sunkara, T., & Gaduputi, V. (2019). Epidemiology of Pancreatic Cancer: Global Trends, Etiology and Risk Factors. *World J Oncol, 10*(1), 10-27. https://doi.org/10.14740/wjon1166

Rawla, P., Sunkara, T., Muralidharan, P., & Raj, J. P. (2018). Update in global trends and aetiology of hepatocellular carcinoma. *Contemp Oncol (Pozn), 22*(3), 141-150. https://doi.org/10.5114/wo.2018.78941

Ren, G., Hu, D., Cheng, E. W. C., Vargas-Reus, M. A., Reip, P., & Allaker, R. P. (2009). Characterisation of copper oxide nanoparticles for antimicrobial applications. *International Journal of Antimicrobial Agents, 33*(6), 587-590. https://doi.org/10.1016/j.ijantimicag.2008.12.004

Ren, H., Zhang, L., An, J., Wang, T., Li, L., Si, X., He, L., Wu, X., Wang, C., & Su, Z. (2014). Polyacrylic acid@zeolitic imidazolate framework-8 nanoparticles with ultrahigh drug loading capability for pH-sensitive drug release. *Chemical Communications, 50*(8), 1000-1002. https://doi.org/10.1039/C3CC47666A

Ren, J., Xiao, Y.-j., Singh, L. S., Zhao, X., Zhao, Z., Feng, L., Rose, T. M., Prestwich, G. D., & Xu, Y. (2006). Lysophosphatidic Acid Is Constitutively Produced by Human Peritoneal Mesothelial Cells and Enhances Adhesion, Migration, and Invasion of Ovarian Cancer Cells. *Cancer Research, 66*(6), 3006. https://doi.org/10.1158/0008-5472.CAN-05-1292

Ren, L., Wong, H. M., Yan, C. H., Yeung, K. W. K., & Yang, K. (2015). Osteogenic ability of Cu-bearing stainless steel. *Journal of Biomedical Materials Research Part B: Applied Biomaterials, 103*(7), 1433-1444. https://doi.org/10.1002/jbm.b.33318

Reynolds, J. G., Geretti, E., Hendriks, B. S., Lee, H., Leonard, S. C., Klinz, S. G., Noble, C. O., Lücker, P. B., Zandstra, P. W., Drummond, D. C., Olivier, K. J., Nielsen, U. B., Niyikiza, C., Agresta, S. V., & Wickham, T. J. (2012). HER2-targeted liposomal doxorubicin displays enhanced anti-tumorigenic effects without associated cardiotoxicity. *Toxicology and Applied Pharmacology, 262*(1), 1-10. https://doi.org/10.1016/j.taap.2012.04.008

Rezaei-Seresht, H., Cheshomi, H., Falanji, F., Movahedi-Motlagh, F., Hashemian, M., & Mireskandari, E. (2019). Cytotoxic activity of caffeic acid and gallic acid against MCF-7 human breast cancer cells: An in silico and in vitro study. *Avicenna journal of phytomedicine, 9*(6), 574-586. https://doi.org/10.22038/AJP.2019.13475

Rodríguez, H. S., Hinestroza, J. P., Ochoa-Puentes, C., Sierra, C. A., & Soto, C. Y. (2014). Antibacterial activity against Escherichia coli of Cu-BTC (MOF-199) metal-organic framework immobilized onto cellulosic fibers. *Journal of Applied Polymer Science, 131*(19). https://doi.org/10.1002/app.40815

Rojas, S., Colinet, I., Cunha, D., Hidalgo, T., Salles, F., Serre, C., Guillou, N., & Horcajada, P. (2018). Toward Understanding Drug Incorporation and Delivery from Biocompatible Metal–Organic Frameworks in View of Cutaneous Administration. *ACS Omega, 3*(3), 2994-3003. https://doi.org/10.1021/acsomega.8b00185

Rojas, S., Devic, T., & Horcajada, P. (2017). Metal organic frameworks based on bioactive components. *Journal of Materials Chemistry B, 5*(14), 2560-2573. https://doi.org/10.1039/C6TB03217F

Rosenberg, M., Ilić, K., Juganson, K., Ivask, A., Ahonen, M., Vinković Vrček, I., & Kahru, A. (2019). Potential ecotoxicological effects of antimicrobial surface coatings: a literature survey backed up by analysis of market reports. *PeerJ, 7*, e6315. https://doi.org/10.7717/peerj.6315

Rowsell, J. L. C., & Yaghi, O. M. (2006). Effects of Functionalization, Catenation, and Variation of the Metal Oxide and Organic Linking Units on the Low-Pressure Hydrogen Adsorption Properties of Metal−Organic Frameworks. *Journal of the American Chemical Society, 128*(4), 1304-1315. https://doi.org/10.1021/ja056639q

Roy, D., Brooks, W. L. A., & Sumerlin, B. S. (2013). New directions in thermoresponsive polymers. *Chemical Society Reviews, 42*(17), 7214-7243. https://doi.org/10.1039/C3CS35499G

Ruparelia, J. P., Chatterjee, A. K., Duttagupta, S. P., & Mukherji, S. (2008). Strain specificity in antimicrobial activity of silver and copper nanoparticles. *Acta Biomaterialia, 4*(3), 707-716. https://doi.org/10.1016/j.actbio.2007.11.006

Santo, C. E., Quaranta, D., & Grass, G. (2012). Antimicrobial metallic copper surfaces kill Staphylococcus haemolyticus via membrane damage. *MicrobiologyOpen, 1*(1), 46-52. https://doi.org/https://doi.org/10.1002/mbo3.2

Santo Christophe, E., Taudte, N., Nies Dietrich, H., & Grass, G. (2008). Contribution of Copper Ion Resistance to Survival of Escherichia coli on Metallic Copper Surfaces. *Applied and Environmental Microbiology, 74*(4), 977-986. https://doi.org/10.1128/AEM.01938-07

Schlichte, K., Kratzke, T., & Kaskel, S. (2004). Improved synthesis, thermal stability and catalytic properties of the metal-organic framework compound Cu3(BTC)2. *Microporous and Mesoporous Materials, 73*(1), 81-88. https://doi.org/10.1016/j.micromeso.2003.12.027

Seibt, T. M., Proneth, B., & Conrad, M. (2019). Role of GPX4 in ferroptosis and its pharmacological implication. *Free Radical Biology and Medicine, 133*, 144-152. https://doi.org/10.1016/j.freeradbiomed.2018.09.014

Senapati, S., Mahanta, A. K., Kumar, S., & Maiti, P. (2018). Controlled drug delivery vehicles for cancer treatment and their performance. *Signal Transduction and Targeted Therapy, 3*(1), 7. https://doi.org/10.1038/s41392-017-0004-3

Senthil Raja, D., Luo, J.-H., Chang, T.-G., Lo, S.-H., Wu, C.-Y., & Lin, C.-H. (2013). Synthesis, Crystal Structure, and Luminescence Properties of a New Calcium(II) Coordination Polymer Based on L-Malic Acid. *Journal of Chemistry, 2013*, 980243. https://doi.org/10.1155/2013/980243

Sexton, R. E., Al Hallak, M. N., Diab, M., & Azmi, A. S. (2020). Gastric cancer: a comprehensive review of current and future treatment strategies. *Cancer and Metastasis Reviews, 39*(4), 1179-1203. https://doi.org/10.1007/s10555-020-09925-3

Shams, S., Ahmad, W., Memon, A. H., Shams, S., Wei, Y., Yuan, Q., & Liang, H. (2020). Cu/H3BTC MOF as a potential antibacterial therapeutic agent against Staphylococcus aureus and Escherichia coli. *New Journal of Chemistry, 44*(41), 17671-17678. https://doi.org/10.1039/D0NJ04120C

Shao, D., Li, J., Li, J., Tang, R., Liu, L., Shi, J., Huang, Q., & Yang, H. (2015). Inhibition of Gallic Acid on the Growth and Biofilm Formation of Escherichia coli and Streptococcus mutans. *Journal of Food Science, 80*(6), M1299-M1305. https://doi.org/10.1111/1750-3841.12902

Sharma, S., Mittal, D., Verma, A. K., & Roy, I. (2019). Copper-Gallic Acid Nanoscale Metal–Organic Framework for Combined Drug Delivery and Photodynamic Therapy. *ACS Applied Bio Materials, 2*(5), 2092-2101. https://doi.org/10.1021/acsabm.9b00116

Shen, S., Wang, S., Zheng, R., Zhu, X., Jiang, X., Fu, D., & Yang, W. (2015). Magnetic nanoparticle clusters for photothermal therapy with near-infrared irradiation. *Biomaterials, 39*, 67-74. https://doi.org/10.1016/j.biomaterials.2014.10.064

Shi, Q., Wu, Q., Li, H., Shi, D., Zhao, Y., & Jiao, Q. (2020). Enhanced catalytic performance of UiO-66 via a sulfuric acid post-synthetic modification strategy with partial etching. *Applied Catalysis A: General, 602*, 117733. https://doi.org/10.1016/j.apcata.2020.117733

Shooto, N., & Dikio, E. (2015). Synthesis, Morphology and Lead Ion Adsorption Properties of Metal Organic Frameworks of Copper and Cobalt. *Chemical Sciences Journal, 06*. https://doi.org/10.4172/2150-3494.1000113

Siegel, R., Naishadham, D., & Jemal, A. (2012). Cancer statistics, 2012. *CA: A Cancer Journal for Clinicians, 62*(1), 10-29. https://doi.org/10.3322/caac.20138

Sinha, R., & El-Bayoumy, K. (2004). Apoptosis is a Critical Cellular Event in Cancer Chemoprevention and Chemotherapy by Selenium Compounds. *Current Cancer Drug Targets, 4*(1), 13-28. https://doi.org/10.2174/1568009043481614

Slavin, Y. N., Asnis, J., Häfeli, U. O., & Bach, H. (2017). Metal nanoparticles: understanding the mechanisms behind antibacterial activity. *Journal of Nanobiotechnology, 15*(1), 65. https://doi.org/10.1186/s12951-017-0308-z

Smaldone, R. A., Forgan, R. S., Furukawa, H., Gassensmith, J. J., Slawin, A. M. Z., Yaghi, O. M., & Stoddart, J. F. (2010). Metal–Organic Frameworks from Edible Natural Products. *Angewandte Chemie International Edition, 49*(46), 8630-8634. https://doi.org/10.1002/anie.201002343

Society, T. A. C. *Cancer Statistics Center*. Retrieved June 16, 2021 from cancerstatisticscenter.cancer.org

Souza, B. E., Donà, L., Titov, K., Bruzzese, P., Zeng, Z., Zhang, Y., Babal, A. S., Möslein, A. F., Frogley, M. D., Wolna, M., Cinque, G., Civalleri, B., & Tan, J.-C. (2020). Elucidating the Drug Release from Metal–Organic Framework Nanocomposites via In Situ Synchrotron Microspectroscopy and Theoretical Modeling. *ACS Applied Materials & Interfaces, 12*(4), 5147-5156. https://doi.org/10.1021/acsami.9b21321

Stock, N., & Biswas, S. (2012). Synthesis of Metal-Organic Frameworks (MOFs): Routes to Various MOF Topologies, Morphologies, and Composites. *Chemical Reviews, 112*(2), 933-969. https://doi.org/10.1021/cr200304e

Stout, J. E., & Yu, V. L. (2003). Experiences of the First 16 Hospitals Using Copper-Silver Ionization for Legionella Control: Implications for the Evaluation of Other Disinfection Modalities. *Infection Control & Hospital Epidemiology, 24*(8), 563-568. https://doi.org/10.1086/502251

Stuehr, D. J. (2004). Enzymes of the L-Arginine to Nitric Oxide Pathway. *The Journal of Nutrition, 134*(10), 2748S-2751S. https://doi.org/10.1093/jn/134.10.2748S

Su, H., Sun, F., Jia, J., He, H., Wang, A., & Zhu, G. (2015). A highly porous medical metal–organic framework constructed from bioactive curcumin. *Chemical Communications, 51*(26), 5774-5777. https://doi.org/10.1039/C4CC10159F

Su, M., Zhang, R., Li, H., Jin, X., Li, J., Yue, X., & Qin, D. (2019). In situ deposition of MOF199 onto hierarchical structures of bamboo and wood and their antibacterial properties. *RSC Advances, 9*(69), 40277-40285. https://doi.org/10.1039/C9RA07046J

Sun, C.-Y., Liu, S.-X., Liang, D.-D., Shao, K.-Z., Ren, Y.-H., & Su, Z.-M. (2009). Highly Stable Crystalline Catalysts Based on a Microporous Metal−Organic Framework and Polyoxometalates. *Journal of the American Chemical Society, 131*(5), 1883-1888. https://doi.org/10.1021/ja807357r

Sun, L.-L., Li, Y.-H., & Shi, H. (2019). A Ketone Functionalized Gd(III)-MOF with Low Cytotoxicity for Anti-Cancer Drug Delivery and Inhibiting Human Liver Cancer Cells. *Journal of Cluster Science, 30*(1), 251-258. https://doi.org/10.1007/s10876-018-1482-3

Sun, L., Xu, Y., Gao, Y., Huang, X., Feng, S., Chen, J., Wang, X., Guo, L., Li, M., Meng, X., Zhang, J., Ge, J., An, X., Ding, D., Luo, Y., Zhang, Y., Jiang, Q., & Ning, X. (2019). Synergistic Amplification of Oxidative Stress–Mediated Antitumor Activity via Liposomal Dichloroacetic Acid and MOF-Fe2+. *Small, 15*(24), 1901156. https://doi.org/10.1002/smll.201901156

Sun, R. W.-Y., Zhang, M., Li, D., Zhang, Z.-F., Cai, H., Li, M., Xian, Y.-J., Ng, S. W., & Wong, A. S.-T. (2015). Dinuclear Gold(I) Pyrrolidinedithiocarbamato Complex: Cytotoxic and Antimigratory Activities on Cancer Cells and the Use of Metal–Organic Framework. *Chemistry – A European Journal, 21*(51), 18534-18538. https://doi.org/10.1002/chem.201503656

Sun, S., Murray, C. B., Weller, D., Folks, L., & Moser, A. (2000). Monodisperse FePt Nanoparticles and Ferromagnetic FePt Nanocrystal Superlattices. *Science, 287*(5460), 1989. https://doi.org/10.1126/science.287.5460.1989

Sun, X., He, G., Xiong, C., Wang, C., Lian, X., Hu, L., Li, Z., Dalgarno, S. J., Yang, Y.-W., & Tian, J. (2021). One-Pot Fabrication of Hollow Porphyrinic MOF Nanoparticles with Ultrahigh Drug Loading toward Controlled Delivery and Synergistic Cancer Therapy. *ACS Applied Materials & Interfaces, 13*(3), 3679-3693. https://doi.org/10.1021/acsami.0c20617

Sun, Y., Jin, H., Jiang, X., & Gui, R. (2020). Assembly of Black Phosphorus Nanosheets and MOF to Form Functional Hybrid Thin-Film for Precise Protein Capture, Dual-Signal and Intrinsic Self-Calibration Sensing of Specific Cancer-Derived Exosomes. *Analytical Chemistry, 92*(3), 2866-2875. https://doi.org/10.1021/acs.analchem.9b05583

Sutphen, R., Xu, Y., Wilbanks, G. D., Fiorica, J., Grendys, E. C., LaPolla, J. P., Arango, H., Hoffman, M. S., Martino, M., Wakeley, K., Griffin, D., Blanco, R. W., Cantor, A. B., Xiao, Y.-j., & Krischer, J. P. (2004). Lysophospholipids Are Potential Biomarkers of Ovarian Cancer. *Cancer Epidemiology Biomarkers &amp; Prevention, 13*(7), 1185. https://doi.org/10.1158/1055-9965.1185.13.7

Szabo, C., Coletta, C., Chao, C., Módis, K., Szczesny, B., Papapetropoulos, A., & Hellmich, M. R. (2013). Tumor-derived hydrogen sulfide, produced by cystathionine-β-synthase, stimulates bioenergetics, cell proliferation, and angiogenesis in colon cancer. *Proceedings of the National Academy of Sciences, 110*(30), 12474. https://doi.org/10.1073/pnas.1306241110

Taddei, M., McPherson, M. J., Gougsa, A., Lam, J., Sewell, J., & Andreoli, E. (2019). An Optimised Compaction Process for Zr-Fumarate (MOF-801). *Inorganics, 7*(9), 110. https://www.mdpi.com/2304-6740/7/9/110

Takahashi, T., Saikawa, Y., & Kitagawa, Y. (2013). Gastric Cancer: Current Status of Diagnosis and Treatment. *Cancers, 5*(1). https://doi.org/10.3390/cancers5010048

Tan, G., Zhong, Y., Yang, L., Jiang, Y., Liu, J., & Ren, F. (2020). A multifunctional MOF-based nanohybrid as injectable implant platform for drug synergistic oral cancer therapy. *Chemical Engineering Journal, 390*, 124446. https://doi.org/10.1016/j.cej.2020.124446

Taylor, K. M. L., Rieter, W. J., & Lin, W. (2008). Manganese-Based Nanoscale Metal−Organic Frameworks for Magnetic Resonance Imaging. *Journal of the American Chemical Society, 130*(44), 14358-14359. https://doi.org/10.1021/ja803777x

Tian, H., Zhang, M., Jin, G., Jiang, Y., & Luan, Y. (2021). Cu-MOF chemodynamic nanoplatform via modulating glutathione and H2O2 in tumor microenvironment for amplified cancer therapy. *Journal of Colloid and Interface Science, 587*, 358-366. https://doi.org/0.1016/j.jcis.2020.12.028

Tian, Z., Yao, X., Ma, K., Niu, X., Grothe, J., Xu, Q., Liu, L., Kaskel, S., & Zhu, Y. (2017). Metal–Organic Framework/Graphene Quantum Dot Nanoparticles Used for Synergistic Chemo- and Photothermal Therapy. *ACS Omega, 2*(3), 1249-1258. https://doi.org/10.1021/acsomega.6b00385

Tonigold, M., Lu, Y., Bredenkötter, B., Rieger, B., Bahnmüller, S., Hitzbleck, J., Langstein, G., & Volkmer, D. (2009). Heterogeneous Catalytic Oxidation by MFU-1: A Cobalt(II)-Containing Metal–Organic Framework. *Angewandte Chemie International Edition, 48*(41), 7546-7550. https://doi.org/10.1002/anie.200901241

Tranchemontagne, D. J., Hunt, J. R., & Yaghi, O. M. (2008). Room temperature synthesis of metal-organic frameworks: MOF-5, MOF-74, MOF-177, MOF-199, and IRMOF-0. *Tetrahedron, 64*(36), 8553-8557. https://doi.org/10.1016/j.tet.2008.06.036

Uemura, N., Okamoto, S., Yamamoto, S., Matsumura, N., Yamaguchi, S., Yamakido, M., Taniyama, K., Sasaki, N., & Schlemper, R. J. (2001). Helicobacter pylori Infection and the Development of Gastric Cancer. *New England Journal of Medicine, 345*(11), 784-789. https://doi.org/10.1056/NEJMoa001999

Umezu-Goto, M., Tanyi, J., Lahad, J., Liu, S., Yu, S., Lapushin, R., Hasegawa, Y., Lu, Y., Trost, R., Bevers, T., Jonasch, E., Aldape, K., Liu, J., James, R. D., Ferguson, C. G., Xu, Y., Prestwich, G. D., & Mills, G. B. (2004). Lysophosphatidic acid production and action: Validated targets in cancer?. *Journal of Cellular Biochemistry, 92*(6), 1115-1140. https://doi.org/10.1002/jcb.20113

Urtasun, N., Vidal-Pla, A., Pérez-Torras, S., & Mazo, A. (2015). Human pancreatic cancer stem cells are sensitive to dual inhibition of IGF-IR and ErbB receptors. *BMC Cancer, 15*(1), 223. https://doi.org/10.1186/s12885-015-1249-2

van-Dam, G. M., Themelis, G., Crane, L. M., Harlaar, N. J., Pleijhuis, R. G., Kelder, W., Sarantopoulos, A., de Jong, J. S., Arts, H. J., van der Zee, A. G., Bart, J., Low, P. S., & Ntziachristos, V. (2011). Intraoperative tumor-specific fluorescence imaging in ovarian cancer by folate receptor-α targeting: first in-human results. *Nat Med, 17*(10), 1315-1319. https://doi.org/10.1038/nm.2472

Vaughan, S., Coward, J. I., Bast, R. C., Berchuck, A., Berek, J. S., Brenton, J. D., Coukos, G., Crum, C. C., Drapkin, R., Etemadmoghadam, D., Friedlander, M., Gabra, H., Kaye, S. B., Lord, C. J., Lengyel, E., Levine, D. A., McNeish, I. A., Menon, U., Mills, G. B., Nephew, K. P., Oza, A. M., Sood, A. K., Stronach, E. A., Walczak, H., Bowtell, D. D., & Balkwill, F. R. (2011). Rethinking ovarian cancer: recommendations for improving outcomes. *Nature Reviews Cancer, 11*(10), 719-725. https://doi.org/10.1038/nrc3144

Wang, C., Li, W., & Hu, B. (2017). The anti-tumor effect of folate-targeted liposome microbubbles loaded with oridonin as ultrasound-triggered tumor-targeted therapeutic carrier system. *J Drug Target, 25*(1), 83-91. https://doi.org/10.1080/1061186x.2016.1200588

Wang, H., Zhang, J., & Yu, H. (2007). Elemental selenium at nano size possesses lower toxicity without compromising the fundamental effect on selenoenzymes: Comparison with selenomethionine in mice. *Free Radical Biology and Medicine, 42*(10), 1524-1533. https://doi.org/10.1016/j.freeradbiomed.2007.02.013

Wang, L., Qu, X., Zhao, Y., Weng, Y., Waterhouse, G. I. N., Yan, H., Guan, S., & Zhou, S. (2019). Exploiting Single Atom Iron Centers in a Porphyrin-like MOF for Efficient Cancer Phototherapy. *ACS Applied Materials & Interfaces, 11*(38), 35228-35237. https://doi.org/10.1021/acsami.9b11238

Wang, M., Hu, M., Li, Z., He, L., Song, Y., Jia, Q., Zhang, Z., & Du, M. (2019). Construction of Tb-MOF-on-Fe-MOF conjugate as a novel platform for ultrasensitive detection of carbohydrate antigen 125 and living cancer cells. *Biosensors and Bioelectronics, 142*, 111536. https://doi.org/10.1016/j.bios.2019.111536

Wang, P., Yuan, Y., Xu, K., Zhong, H., Yang, Y., Jin, S., Yang, K., & Qi, X. (2021). Biological applications of copper-containing materials. *Bioactive Materials, 6*(4), 916-927. https://doi.org/10.1016/j.bioactmat.2020.09.017

Wang, Q., de Oliveira, E. F., Alborzi, S., Bastarrachea, L. J., & Tikekar, R. V. (2017). On mechanism behind UV-A light enhanced antibacterial activity of gallic acid and propyl gallate against Escherichia coli O157:H7. *Scientific Reports, 7*(1), 8325. https://doi.org/10.1038/s41598-017-08449-1

Wang, S., Wu, H., Sun, K., Hu, J., Chen, F., Liu, W., Chen, J., Sun, B., & Hossain, A. M. S. (2021). A novel pH-responsive Fe-MOF system for enhanced cancer treatment mediated by the Fenton reaction. *New Journal of Chemistry, 45*(6), 3271-3279. https://doi.org/10.1039/D0NJ05105E

Wang, S., Yu, G., Wang, Z., Jacobson, O., Lin, L.-S., Yang, W., Deng, H., He, Z., Liu, Y., Chen, Z.-Y., & Chen, X. (2019). Enhanced Antitumor Efficacy by a Cascade of Reactive Oxygen Species Generation and Drug Release. *Angewandte Chemie International Edition, 58*(41), 14758-14763. https://doi.org/10.1002/anie.201908997

Wang, X., Shi, J., Li, Z., Zhang, S., Wu, H., Jiang, Z., Yang, C., & Tian, C. (2014). Facile One-Pot Preparation of Chitosan/Calcium Pyrophosphate Hybrid Microflowers. *ACS Applied Materials & Interfaces, 6*(16), 14522-14532. https://doi.org/10.1021/am503787h

Wang, X., Zhong, X., Lei, H., Geng, Y., Zhao, Q., Gong, F., Yang, Z., Dong, Z., Liu, Z., & Cheng, L. (2019). Hollow Cu2Se Nanozymes for Tumor Photothermal-Catalytic Therapy. *Chemistry of Materials, 31*(16), 6174-6186. https://doi.org/10.1021/acs.chemmater.9b01958

Wang, Y., Liu, X., Liu, G., Guo, H., Li, C., Zhang, Y., Zhang, F., Zhao, Z., & Cheng, H. (2016). Novel galactosylated biodegradable nanoparticles for hepatocyte-delivery of oridonin. *Int J Pharm, 502*(1-2), 47-60. https://doi.org/10.1016/j.ijpharm.2016.02.025

Wang, Y., Wang, K., Zhao, J., Liu, X., Bu, J., Yan, X., & Huang, R. (2013). Multifunctional Mesoporous Silica-Coated Graphene Nanosheet Used for Chemo-Photothermal Synergistic Targeted Therapy of Glioma. *Journal of the American Chemical Society, 135*(12), 4799-4804. https://doi.org/10.1021/ja312221g

Wang, Z., & Cohen, S. M. (2009). Postsynthetic modification of metal–organic frameworks. *Chemical Society Reviews, 38*(5), 1315-1329. https://doi.org/10.1039/B802258P

Wang, Z., Feng, C., Zhao, H., Ren, X., Peng, S., & Zuo, Z. (2015). Autoregulation of inducible nitric oxide synthase expression by RNA interference provides neuroprotection in neonatal rats. *Theranostics, 5*(5), 504-514. https://doi.org/10.7150/thno.10441

Wang, Z., Luo, T., Sheng, R., Li, H., Sun, J., & Cao, A. (2016). Amphiphilic Diblock Terpolymer PMAgala-b-P(MAA-co-MAChol)s with Attached Galactose and Cholesterol Grafts and Their Intracellular pH-Responsive Doxorubicin Delivery. *Biomacromolecules, 17*(1), 98-110. https://doi.org/10.1021/acs.biomac.5b01227

Warsame, R., & Grothey, A. (2012). Treatment options for advanced pancreatic cancer: a review. *Expert Review of Anticancer Therapy, 12*(10), 1327-1336. https://doi.org/10.1586/era.12.115

Watanabe, M., Kawano, K., Yokoyama, M., Opanasopit, P., Okano, T., & Maitani, Y. (2006). Preparation of camptothecin-loaded polymeric micelles and evaluation of their incorporation and circulation stability. *International Journal of Pharmaceutics, 308*(1), 183-189. https://doi.org/10.1016/j.ijpharm.2005.10.030

Weaver, L., Michels, H. T., & Keevil, C. W. (2008). Survival of Clostridium difficile on copper and steel: futuristic options for hospital hygiene. *Journal of Hospital Infection, 68*(2), 145-151. https://doi.org/10.1016/j.jhin.2007.11.011

Wei, D., Xin, Y., Rong, Y., Li, Y., Zhang, C., Chen, Q., Qin, S., Wang, W., & Hao, Y. (2020). A Mesoporous Gd-MOF with Lewis Basic Sites for 5-Fu Delivery and Inhibition of Human Lung Cancer Cells In Vivo and In Vitro. *Journal of Inorganic and Organometallic Polymers and Materials, 30*(4), 1121-1131. https://doi.org/10.1007/s10904-019-01305-x

Wheeldon, L. J., Worthington, T., Lambert, P. A., Hilton, A. C., Lowden, C. J., & Elliott, T. S. J. (2008). Antimicrobial efficacy of copper surfaces against spores and vegetative cells of Clostridium difficile: the germination theory. *Journal of Antimicrobial Chemotherapy, 62*(3), 522-525. https://doi.org/10.1093/jac/dkn219

Wilhelm, S. M., Adnane, L., Newell, P., Villanueva, A., Llovet, J. M., & Lynch, M. (2008). Preclinical overview of sorafenib, a multikinase inhibitor that targets both Raf and VEGF and PDGF receptor tyrosine kinase signaling. *Molecular Cancer Therapeutics, 7*(10), 3129. https://doi.org/10.1158/1535-7163.MCT-08-0013

Williford, J.-M., Wu, J., Ren, Y., Archang, M. M., Leong, K. W., & Mao, H.-Q. (2014). Recent Advances in Nanoparticle-Mediated siRNA Delivery. *Annual Review of Biomedical Engineering, 16*(1), 347-370. https://doi.org/10.1146/annurev-bioeng-071813-105119

World Cancer Research Fund. *Breast Cancer Statistics*. Retrieved March 3, 2020 from https://www.wcrf.org/dietandcancer/breast-cancer-statistics/

World Cancer Research Fund. *Continuous Update Project Report: Diet, Nutrition, Physical Activity and Stomach Cancer* Retrieved June 16, 2021 from https://www.wcrf.org/wp-content/uploads/2021/02/stomach-cancer-report.pdf

World Cancer Research Fund. *Colorectal cancer statistics*. Retrieved on December 5, 2021 from https://www.wcrf.org/cancer-trends/colorectal-cancer-statistics/

World Cancer Research Fund. *Ovarian cancer*. Retrieved December 14, 2021 from https://www.wcrf.org/dietandcancer/ovarian-cancer/

World Health Organization.*Cancer*. Retrieved October 10, 2021 from https://www.who.int/news-room/fact-sheets/detail/cancer

World Health Organization. *Cervical Cancer*. Retrieved October 10, 2021 from https://www.who.int/health-topics/cervical-cancer#tab=tab_1

World Health Organization. *Estimated Cancer Incidence, Mortality and Prevalence Worldwide*. Retrieved June 16, 2021 from https://gco.iarc.fr/

Wright, A. A., Bohlke, K., Armstrong, D. K., Bookman, M. A., Cliby, W. A., Coleman, R. L., Dizon, D. S., Kash, J. J., Meyer, L. A., Moore, K. N., Olawaiye, A. B., Oldham, J., Salani, R., Sparacio, D., Tew, W. P., Vergote, I., & Edelson, M. I. (2016). Neoadjuvant chemotherapy for newly diagnosed, advanced ovarian cancer: Society of Gynecologic Oncology and American Society of Clinical Oncology Clinical Practice Guideline. *Gynecol Oncol, 143*(1), 3-15. https://doi.org/10.1016/j.ygyno.2016.05.022

Wu, L., Sun, Y., Sugimoto, K., Luo, Z., Ishigaki, Y., Pu, K., Suzuki, T., Chen, H.-Y., & Ye, D. (2018). Engineering of Electrochromic Materials as Activatable Probes for Molecular Imaging and Photodynamic Therapy. *Journal of the American Chemical Society, 140*(47), 16340-16352. https://doi.org/10.1021/jacs.8b10176

Wu, S.-Y., Chou, H.-Y., Yuh, C.-H., Mekuria, S. L., Kao, Y.-C., & Tsai, H.-C. (2018). Radiation-Sensitive Dendrimer-Based Drug Delivery System. *Advanced Science, 5*(2), 1700339. https://doi.org/10.1002/advs.201700339

Wu, Y.-Y., Fan, H.-Q., Chen, H.-J., Jiang, L.-X., & Zhang, W.-P. (2021). A Zn(II)-MOF with Suitable Pore Surroundings for Cyanosilylation Reaction and Protective Effect on Bladder Cancer Cells by Regulating miR-130 and CYLD. *Journal of Inorganic and Organometallic Polymers and Materials, 31*(2), 520-527. https://doi.org/10.1007/s10904-020-01694-4

Wu, Z.-F., Wang, Z., Zhang, Y., Ma, Y.-L., He, C.-Y., Li, H., Chen, L., Huo, Q.-S., Wang, L., & Li, Z.-Q. (2016). Amino acids-incorporated nanoflowers with an intrinsic peroxidase-like activity. *Scientific Reports, 6*(1), 22412. https://doi.org/10.1038/srep22412

Xi, Y.-M., Ma, Z.-Z., Wang, L.-N., Li, M., & Li, Z.-J. (2019). Three-Dimensional Ni(II)-MOF Containing an Asymmetric Pyridyl-Carboxylate Ligand: Catalytic Cyanosilylation of Aldehydes and Inhibits Human Promyelocytic Leukemia Cancer Cells. *Journal of Cluster Science, 30*(6), 1455-1464. https://doi.org/10.1007/s10876-019-01589-6

Xiang, X., Pang, H., Ma, T., Du, F., Li, L., Huang, J., Ma, L., & Qiu, L. (2021). Ultrasound targeted microbubble destruction combined with Fe-MOF based bio-/enzyme-mimics nanoparticles for treating of cancer. *Journal of Nanobiotechnology, 19*(1), 92. https://doi.org/10.1186/s12951-021-00835-2

Xiang, Z., Qi, Y., Lu, Y., Hu, Z., Wang, X., Jia, W., Hu, J., Ji, J., & Lu, W. (2020). MOF-derived novel porous Fe3O4@C nanocomposites as smart nanomedical platforms for combined cancer therapy: magnetic-triggered synergistic hyperthermia and chemotherapy. *Journal of Materials Chemistry B, 8*(37), 8671-8683. https://doi.org/10.1039/D0TB01021A

Xiao, D.-R., Sun, D.-Z., Liu, J.-L., Zhang, G.-J., Chen, H.-Y., He, J.-H., Yan, S.-W., Yuan, R., & Wang, E.-B. (2011). Two Unprecedented Entangled Metal–Olsalazine Complexes with Coexistence of 2D → 3D Polycatenation and meso-Helix. *European Journal of Inorganic Chemistry, 2011*(24), 4656-3663. https://doi.org/10.1002/ejic.201100366

Xiao, Y., Huang, W., Zhu, D., Wang, Q., Chen, B., Liu, Z., Wang, Y., & Liu, Q. (2020). Cancer cell membrane-camouflaged MOF nanoparticles for a potent dihydroartemisinin-based hepatocellular carcinoma therapy. *RSC Advances, 10*(12), 7194-7205. https://doi.org/10.1039/C9RA09233A

Xiong, X.-B., & Lavasanifar, A. (2011). Traceable Multifunctional Micellar Nanocarriers for Cancer-Targeted Co-delivery of MDR-1 siRNA and Doxorubicin. *ACS Nano, 5*(6), 5202-5213. https://doi.org/10.1021/nn2013707

Xu, C., Li, J., Yang, L., Shi, F., Yang, L., & Ye, M. (2017). Antibacterial activity and a membrane damage mechanism of Lachnum YM30 melanin against Vibrio parahaemolyticus and Staphylococcus aureus. *Food Control, 73*, 1445-1451. https://doi.org/10.1016/j.foodcont.2016.10.048

Xu, Y., Fei, J., Li, G., Yuan, T., Xu, X., & Li, J. (2019). Nanozyme-Catalyzed Cascade Reactions for Mitochondria-Mimicking Oxidative Phosphorylation. *Angewandte Chemie International Edition, 58*(17), 5572-5576. https://doi.org/10.1002/anie.201813771

Xu, Y., Shen, Z., Wiper, D. W., Wu, M., Morton, R. E., Elson, P., Kennedy, A. W., Belinson, J., Markman, M., & Casey, G. (1998). Lysophosphatidic Acid as a Potential Biomarker for Ovarian and Other Gynecologic Cancers. *JAMA, 280*(8), 719-723. https://doi.org/10.1001/jama.280.8.719

Yaghi, O. M., O'Keeffe, M., Ockwig, N. W., Chae, H. K., Eddaoudi, M., & Kim, J. (2003). Reticular synthesis and the design of new materials. *Nature, 423*(6941), 705-714. https://doi.org/10.1038/nature01650

Yan, Z., Li, X., Fan, Q., Bai, H., Wu, S., Zhang, Z.-F., & Pan, L. (2020). A water-stable and biofriendly Zn-MOF with pyrazine decorated pores as 5-Fu delivery system to induce human ovarian cancer cells apoptosis and abrogate their growth. *Journal of Molecular Structure, 1204*, 127477. https://doi.org/10.1016/j.molstruc.2019.127477

Yang, B., Chen, Y., & Shi, J. (2019). Reactive Oxygen Species (ROS)-Based Nanomedicine. *Chemical Reviews, 119*(8), 4881-4985. https://doi.org/10.1021/acs.chemrev.8b00626

Yang, B., Ding, L., Yao, H., Chen, Y., & Shi, J. (2020). A Metal-Organic Framework (MOF) Fenton Nanoagent-Enabled Nanocatalytic Cancer Therapy in Synergy with Autophagy Inhibition. *Advanced Materials, 32*(12), 1907152. https://doi.org/10.1002/adma.201907152

Yang, J., Trickett, C. A., Alahmadi, S. B., Alshammari, A. S., & Yaghi, O. M. (2017). Calcium l-Lactate Frameworks as Naturally Degradable Carriers for Pesticides. *Journal of the American Chemical Society, 139*(24), 8118-8121. https://doi.org/10.1021/jacs.7b04542

Yang, J., & Yang, Y.-W. (2020). Metal–Organic Frameworks for Biomedical Applications. *Small, 16*(10), 1906846. https://doi.org/10.1002/smll.201906846

Yang, K., Feng, L., & Liu, Z. (2015). The advancing uses of nano-graphene in drug delivery. *Expert Opinion on Drug Delivery, 12*(4), 601-612. https://doi.org/10.1517/17425247.2015.978760

Yang, K. K., Zhang, L., Liao, P., Xiao, Z., Zhang, F., Sindaye, D., Xin, Z., Tan, C., Deng, J., Yin, Y., & Deng, B. (2020). Impact of Gallic Acid on Gut Health: Focus on the Gut Microbiome, Immune Response, and Mechanisms of Action. *Frontiers in Immunology, 11*.

Yang, L., Ruess, G. L., & Carreon, M. A. (2015). Cu, Al and Ga based metal organic framework catalysts for the decarboxylation of oleic acid. *Catalysis Science & Technology, 5*(5), 2777-2782. https://doi.org/10.1039/C4CY01609B

Yang, X., Sun, Y., Zhang, Y., & Han, S. (2020). Downregulation of miR-181b inhibits human colon cancer cell proliferation by targeting CYLD and inhibiting the NF-κB signaling pathway. *Int J Mol Med, 46*(5), 1755-1764. https://doi.org/10.3892/ijmm.2020.4720

Yang, X., Tang, Q., Jiang, Y., Zhang, M., Wang, M., & Mao, L. (2019). Nanoscale ATP-Responsive Zeolitic Imidazole Framework-90 as a General Platform for Cytosolic Protein Delivery and Genome Editing. *Journal of the American Chemical Society, 141*(9), 3782-3786. https://doi.org/10.1021/jacs.8b11996

Yang, Y., Hu, Q., Zhang, Q., Jiang, K., Lin, W., Yang, Y., Cui, Y., & Qian, G. (2016). A Large Capacity Cationic Metal–Organic Framework Nanocarrier for Physiological pH Responsive Drug Delivery. *Molecular Pharmaceutics, 13*(8), 2782-2786. https://doi.org/10.1021/acs.molpharmaceut.6b00374

Yao, H.-B., Fang, H.-Y., Wang, X.-H., & Yu, S.-H. (2011). Hierarchical assembly of micro-/nano-building blocks: bio-inspired rigid structural functional materials. *Chemical Society Reviews, 40*(7), 3764-3785. https://doi.org/10.1039/C0CS00121J

Yeh, J. J., Hsu, W. H., Wang, J. J., Ho, S. T., & Kao, A. (2003). Predicting Chemotherapy Response to Paclitaxel-Based Therapy in Advanced Non-Small-Cell Lung Cancer with P-Glycoprotein Expression. *Respiration, 70*(1), 32-35. https://doi.org/10.1159/000068411

Yellepeddi, V. K., Vangara, K. K., Kumar, A., & Palakurthi, S. (2012). Comparative Evaluation of Small-molecule Chemosensitizers in Reversal of Cisplatin Resistance in Ovarian Cancer Cells. *Anticancer Research, 32*(9), 3651-3658.

Yutkin, M. P., Zavakhina, M. S., Samsonenko, D. G., Dybtsev, D. N., & Fedin, V. P. (2013). Synthesis and characterization of expected and unexpected topologies of homochiral porous metal(II) malate frameworks. *Inorganica Chimica Acta, 394*, 367-372. https://doi.org/10.1016/j.ica.2012.08.012

Zavakhina, M. S., Samsonenko, D. G., Virovets, A. V., Dybtsev, D. N., & Fedin, V. P. (2014). Homochiral Cu(II) and Ni(II) malates with tunable structural features. *Journal of Solid State Chemistry, 210*(1), 125-129. https://doi.org/10.1016/j.jssc.2013.11.011

Zhang, B., Chen, L., Yang, X., Xu, T., Sun, T., Wang, L., & Zhang, Q. (2017). A luminescent Terbium-Succinate MOF fabricated by co-precipitation for sensing of Fe3+ in aqueous environment. *Journal of Materials Science: Materials in Electronics, 28*(10), 7326-7332. https://doi.org/10.1007/s10854-017-6419-3

Zhang, B., Li, P., Zhang, H., Wang, H., Li, X., Tian, L., Ali, N., Ali, Z., & Zhang, Q. (2016). Preparation of lipase/Zn3(PO4)2 hybrid nanoflower and its catalytic performance as an immobilized enzyme. *Chemical Engineering Journal, 291*, 287-297. https://doi.org/10.1016/j.cej.2016.01.104

Zhang, J.-H., Nong, R.-Y., Xie, S.-M., Wang, B.-J., Ai, P., & Yuan, L.-M. (2017). Homochiral metal-organic frameworks based on amino acid ligands for HPLC separation of enantiomers. *ELECTROPHORESIS, 38*(19), 2513-2520. https://doi.org/10.1002/elps.201700122

Zhang, J., Chen, S., Zingiryan, A., & Bu, X. (2008). Integrated Molecular Chirality, Absolute Helicity, and Intrinsic Chiral Topology in Three-Dimensional Open-Framework Materials. *Journal of the American Chemical Society, 130*(51), 17246-17247. https://doi.org/10.1021/ja8075692

Zhang, K., Meng, X., Yang, Z., Dong, H., & Zhang, X. (2020). Enhanced cancer therapy by hypoxia-responsive copper metal-organic frameworks nanosystem. *Biomaterials, 258*, 120278. https://doi.org/10.1016/j.biomaterials.2020.120278

Zhang, L., Gao, Y., Sun, S., Li, Z., Wu, A., & Zeng, L. (2020). pH-Responsive metal–organic framework encapsulated gold nanoclusters with modulated release to enhance photodynamic therapy/chemotherapy in breast cancer. *Journal of Materials Chemistry B, 8*(8), 1739-1747. https://doi.org/10.1039/C9TB02621E

Zhang, L., Liu, C., Gao, Y., Li, Z., Xing, J., Ren, W., Zhang, L., Li, A., Lu, G., Wu, A., & Zeng, L. (2018). ZD2-Engineered Gold Nanostar@Metal-Organic Framework Nanoprobes for T1-Weighted Magnetic Resonance Imaging and Photothermal Therapy Specifically Toward Triple-Negative Breast Cancer. *Advanced Healthcare Materials, 7*(24), 1801144. https://doi.org/10.1002/adhm.201801144

Zhang, S.-Y., Shi, W., Cheng, P., & Zaworotko, M. J. (2015). A Mixed-Crystal Lanthanide Zeolite-like Metal–Organic Framework as a Fluorescent Indicator for Lysophosphatidic Acid, a Cancer Biomarker. *Journal of the American Chemical Society, 137*(38), 12203-12206. https://doi.org/10.1021/jacs.5b06929

Zhang, Z., Zhang, Y., Song, R., Wang, M., Yan, F., He, L., Feng, X., Fang, S., Zhao, J., & Zhang, H. (2015). Manganese(II) phosphate nanoflowers as electrochemical biosensors for the high-sensitivity detection of ractopamine. *Sensors and Actuators B: Chemical, 211*, 310-317. https://doi.org/10.1016/j.snb.2015.01.106

Zhang, Z., Zhou, Y., Zhou, Z., Piao, Y., Kalva, N., Liu, X., Tang, J., & Shen, Y. (2018). Synthesis of enzyme-responsive phosphoramidate dendrimers for cancer drug delivery. *Polymer Chemistry, 9*(4), 438-449. https://doi.org/10.1039/C7PY01492A

Zhao, J., Lu, D., Moya, S., Yan, H., Qiu, M., Chen, J., Wang, X., Li, Y., Pan, H., Chen, G., & Wang, G. (2020). Bispecific T-cell engager (BiTE) immunotherapy of ovarian cancer based on MIL-88A MOF/MC gene delivery system. *Applied Materials Today, 20*, 100701. https://doi.org/10.1016/j.apmt.2020.100701

Zheng, H., Zhang, Y., Liu, L., Wan, W., Guo, P., Nyström, A. M., & Zou, X. (2016). One-pot Synthesis of Metal–Organic Frameworks with Encapsulated Target Molecules and Their Applications for Controlled Drug Delivery. *Journal of the American Chemical Society, 138*(3), 962-968. https://doi.org/10.1021/jacs.5b11720

Zheng, M., Liu, S., Guan, X., & Xie, Z. (2015). One-Step Synthesis of Nanoscale Zeolitic Imidazolate Frameworks with High Curcumin Loading for Treatment of Cervical Cancer. *ACS Applied Materials & Interfaces, 7*(40), 22181-22187. https://doi.org/10.1021/acsami.5b04315

Zheng, W., Cao, C., Liu, Y., Yu, Q., Zheng, C., Sun, D., Ren, X., & Liu, J. (2015). Multifunctional polyamidoamine-modified selenium nanoparticles dual-delivering siRNA and cisplatin to A549/DDP cells for reversal multidrug resistance. *Acta Biomaterialia, 11*, 368-380. https://doi.org/10.1016/j.actbio.2014.08.035

Zhou, G., Wang, Y. S., Jin, Z., Zhao, P., Zhang, H., Wen, Y., & He, Q. (2019). Porphyrin–palladium hydride MOF nanoparticles for tumor-targeting photoacoustic imaging-guided hydrogenothermal cancer therapy. *Nanoscale Horizons, 4*(5), 1185-1193. https://doi.org/10.1039/C9NH00021F

Zhou, H.-C., Long, J. R., & Yaghi, O. M. (2012). Introduction to Metal–Organic Frameworks. *Chemical Reviews, 112*(2), 673-674. https://doi.org/10.1021/cr300014x

Zhou, Q., Zhang, L., Yang, T., & Wu, H. (2018). Stimuli-responsive polymeric micelles for drug delivery and cancer therapy. *International journal of nanomedicine, 13*, 2921-2942. https://doi.org/10.2147/IJN.S158696

Zhuang, J., Kuo, C.-H., Chou, L.-Y., Liu, D.-Y., Weerapana, E., & Tsung, C.-K. (2014). Optimized Metal–Organic-Framework Nanospheres for Drug Delivery: Evaluation of Small-Molecule Encapsulation. *ACS Nano, 8*(3), 2812-2819. https://doi.org/10.1021/nn406590q

UAE UNIVERSITY DOCTORATE DISSERTATION NO. 2022:12

The research presented in this dissertation was carried out with the intention of improving the limitations and challenges faced with conventional chemotherapeutic drugs and to overcome the antibiotic resistance crisis that stems from overuse and lack of developing new antibiotics. The designed copper-based MOFs were successful in overcoming these hurdles while acting as stand-alone treatments. Furthermore, the stability and biological functions of these copper-based MOFs were enhanced by post-synthetic modifications creating a MOF core-shell nanoflower with dual intrinsic peroxidase activity.

Sandy Elmehrath received her PhD in Chemistry from the Department of Chemistry, College of Science at UAE University, UAE. She received her MSc in Chemistry from the College of Science, Purdue University, Indiana.

www.uaeu.ac.ae